ENERGY TRANSFER BETWEEN THULIUM AND HOLMIUM IN LASER HOSTS

by

Kenneth Michael Dinndorf

S.B. Physics with Electrical Engineering
Massachusetts Institute of Technology, 1989.

Submitted to the Department of Physics in
Partial Fulfillment of the Requirements
for the Degree of

Doctor of Philosophy

at the

Massachusetts Institute of Technology

September 1993

Signature of Author____
Department of Physics
August 30, 1993

Certified by____
Dr. Hans P. Jenssen
Director
Laboratory for Advanced Solid State Laser Materials
Thesis Advisor

Accepted by____
Prof. George F. Koster
Chairman, Department of Physics Graduate Committee

ENERGY TRANSFER BETWEEN THULIUM AND HOLMIUM IN LASER HOSTS

by

Kenneth M. Dinndorf

Submitted to the MIT Department of Physics on
30 September 1993 in partial fulfillment of the requirements
for the degree of Doctor of Philosophy in
Experimental Condensed Matter Physics

ABSTRACT

We derive equilibrium relations between the excited state manifolds of rare earth ions substitutionally doped into large band gap materials. We then apply these relations to Thulium-Holmium doped materials. We derive the distribution of excitations between excited manifolds under quasi-equilibrium conditions. We derive relationships between spectroscopic quantities such as the absorption cross-section and the quasi-equilibrium distribution at low excitation levels. We discuss the limits of validity of this relation. We confirm these relations with a series of steady-state experiments at room temperature. We extend the model for the distribution to high excitation densities and confirm it with dynamics measurements.

We then explore the relationships between transfer parameters with a series of dynamics experiments. We measure the transfer parameters for cross-relaxation and upconversion in singly doped Tm. We then measure transfer parameters in the codoped Tm-Ho system. We find that the process of migration complicates the application of the relation between transfer microparameters. The difference between average transfer parameters and microparameters is discussed. We find that the relation between the microparameters will limit the average transfer parameter.

We measure the lifetime and transition cross-sections for Tm, Ho in several materials. We identify and discuss other energy transfer processes in the codoped system. We discuss the implications of our results for the 2 μm Tm-Ho laser.

Acknowledgements

I wish to express my sincere appreciation to my thesis supervisor, Hans Jenssen, for the guidance he has given me in the years that I have worked in his laboratory. His vast knowledge of the field of solid state lasers started me on the path toward this thesis, and many portions of this document reflect the ideas, intuition, and advice which Hans has used to guide me. In the last four years I have learned not only how to design, conduct, and repair experiments; but also to how think critically about ideas and concepts. I feel that this is perhaps the most valuable skill that I have learned at MIT, and I thank Hans for constantly challenging me to think thoroughly about ideas.

Special thanks go to Arlete Cassanho for her instruction in the growth of BaY_2F_8, and for the growth of many of the materials used in support of this thesis.

I would like to thank and acknowledge fellow graduate students Gary Allen and Stefan Anderson, who have provided not only critical feedback on this thesis and other physics ideas, but who have also made my graduate life at MIT a lot more enjoyable. I would also like to acknowledge the help of other personnel of the laboratory - Dave Knowles, Vie-han Chan, Somnath Sengupta, and visiting scientists Yasu Yamaguchi and Mauro Tonelli. I would also like to acknowledge James Harrison of Schwartz Electro-Optics for assistance with the Ti:Sapphire laser used for much of the experimentation.

I would like to thank my family, who have been a constant source of support during the time I've spent at MIT. I would not have been able to complete this course of study without their encouragement. I would also like to thank my friends in the area who have helped me to pack a lot of fun into small amounts of free time.

Finally, I would like to dedicate this thesis to my wife. Her patience with the constraints imposed by graduate student life has been remarkable, and her encouragement has helped me through the rough times which occasionally occur in graduate school. This thesis is as much hers as it is mine.

Table of Contents

Figures

Tables

1. Introduction

Since the birth of the laser in the early 1960's[1, 2], lasers have evolved from an exotic laboratory technology to become tools which are used daily in a variety of applications. Early laser systems were difficult and inefficient to operate, but the intervening years have seen a steady improvement in the quality, efficiency, and ease of use of lasers. Increases in the efficiency and attainable power have come from not only better quality components and more efficient excitation techniques, but also as a result of a more thorough understanding of the processes which can occur in laser materials.

This thesis describes a series of experiments investigating processes which transfer energy between rare-earth ions doped into laser hosts. As materials such as these are the basic building blocks of solid-state lasers, an understanding of the relationships between these processes is of importance for the field of solid-state laser engineering. Processes which affect rare earth ions in solids occur on several different time scales; due to this, experiments can explore what effectively is a steady-state situation for some interactions when the overall system is far from equilibrium. In this thesis, we will establish a relationship between populations of different excited states of rare-earth ions under quasi-equilibrium conditions. We will then theoretically and experimentally explore the effects of various processes active in rare-earth doped materials upon the equilibrium relationships between ions, and conversely, explore what constraints the equilibrium relations place upon these processes. We will explore the equilibrium relationships between the Thulium and Holmium ions in laser host materials; these materials not only satisfy the necessary quasi-equilibrium conditions, but also present a currently unsolved problem of interest to the solid-state laser community.

We start with a brief review of the properties of rare-earth ions in solids and the basics of energy transfer theory. Following this, we quickly review the engineering background of the Tm-Ho doped laser system.

1.1. Properties of Rare-Earth Ions in Solids

The rare earth elements are characterized by the successive filling of the f shell and can be separated into two series of elements based on their electronic shell structure. The Lanthanide series consists of the elements Cerium-Lutetium; these elements all have

---

[1] A. L. Schalow and C. H. Townes, Phys. Rev., V112, (1958), P1940.

[2] T. H. Maiman, Nature, V187, (1960), P493.

the Xenon electronic shell structure as a core with two electrons in the 6s states in addition to the partially filled 4f shell. These elements are chemically similar to Yttrium ($4d^1$, $5s^2$) and Lanthanum ($5d^1$, $6s^2$) and can substitutionally replace these elements in materials. (An additional electron is occasionally found in the $5d^1$ state.) The +3 ionization state is dominant for lanthanide ions in crystals, although some can be found in the +2 state (Eu, Yb, Sm) or +4 state (Ce, Tb) under the proper conditions. The two 6s electrons and one additional electron (from the $5d^1$, when that state is occupied) are generally involved in the bonding.

As the 4f shell is filled with electrons, it contracts spatially; this contraction, known as the lanthanide contraction, arises from the imperfect screening of the central potential by the 4f electrons [3]. The 4f wave functions are naturally localized near the nuclei; this contraction only increases the localization. These orbitals behave in some respects as an inner shell and, in effect, are partially shielded from the outer environment by closed s^2p^6 shells; in general they have only small interactions with the surrounding environment.

The Actinide series of the rare earth ions consists of the elements Thorium-Lawrencium. These elements have a closed Radon shell structure with partially filled 5f shells. The 5f shell is not as localized as the 4f shell, and as a result elements of the actinide series are more sensitive to the nearby environment than those of the lanthanide series. They can be found in a variety of ionization states up to +6, although the +3 state seems to be favored by some of the heavier elements[3]. Most of this series is radioactive; the optical properties of these elements when doped into solids have not been studied in detail with the exception of some work with Uranium[4]. For now we will concentrate on the lanthanide series.

The Hamiltonian for rare-earth ions in a solid can be expressed as $H_{tot}=H_o+H_{coul}+H_{spin\text{-}orbit}+H_{crystal}$, where the first three terms comprise the free space Hamiltonian[5]. Here, H_o represents the contribution of the ionic central field, which establishes the energy of the $4f^n$ configuration. The coulomb interaction between the electrons, H_{coul}, removes the degeneracy of the $4f^n$ configuration and splits it into groups of configurations whose energies are separated on the order of 10^4 wavenumbers (cm^{-1}). The degeneracy of the ^{2s+1}L terms is further lifted by spin-orbit coupling ($H_{spin\text{-}orbit}$),

---

[3] B. G. Wybourne, Spectroscopic Properties of the Rare-Earths, Wiley, New York, 1965.

[4] See, for example, G. J. Quarles, L. Esterowitz, G. Rosenblatt, R. Uhrin, and R. Belt, in OSA Proc. of the Advanced Solid State Laser Conference (V 13), Ed. Chase and Pinto, Santa Fe, 1992, P 306-309, or P. P. Sorokin and M. J. Stevenson, "Stimulated Infrared Emission from Trivalent Uranium," Phys. Rev. Lett. 5, (1960), P 557-559.

[5] S. Hufner, Optical Spectra of Transparent Rare Earth Compounds, Academic Press, New York, 1978.

which splits the ^{2s+1}L multiplets further into $^{2s+1}L_J$ multiplets with separations of the order of tens of thousands of wavenumbers. In most rare earths the magnitude of the coulomb and the spin orbit interactions are roughly equal[5]; and the intermediate coupling scheme [6] is used to characterize the interaction. Russell-Saunder's notation, while not strictly valid, is generally used to describe the multi-electron configuration of each manifold state.

When the ions are doped into crystals, the interaction of the crystal field ($H_{crystal}$) must be included; this interaction lifts the m_j degeneracy of a manifold to a degree dependent on the site symmetry[7]. (The Kramer's degeneracy remains for ions with odd numbers of electrons.) Due to the partially shielded nature of the 4f shells, the magnitude of this interaction is smaller than the other interactions, and the splittings and shifts in the energy levels resulting from the crystal field are small perturbations in comparison to the splittings that the other interactions produce. The total splitting between the different levels within a 4f manifold is on the order of 100 cm^{-1}. Fig. 1.1.1 illustrates the interactions and typical splittings resulting from them. As a result of the relative weakness of the crystal field interactions, the positions of the energy levels of rare earth ions are similar in most materials; a good approximation of the energy levels in any material can be found from the Dieke chart[8], which summarizes the positions of energy levels of the rare-earths in $LaCl_3$. In fact, the energy levels of lanthanide ions in crystals are very similar to the energy levels of the +3 oxidation state of free ions.

---

[6] See, for example, E. U. Condon and G. H. Shortley, The Theory of Atomic Spectra, Cambridge University Press, Cambridge, 1957.

[7] See any crystal field or group theory text, such as L. M. Falicov, Group Theory and Its Physical Applications. University of Chicago Press, Chicago, 1989.

[8] H. M. Crosswhite and H. M. Moos, Optical Properties of Ions in Crystals, Interscience, New York, 1967.

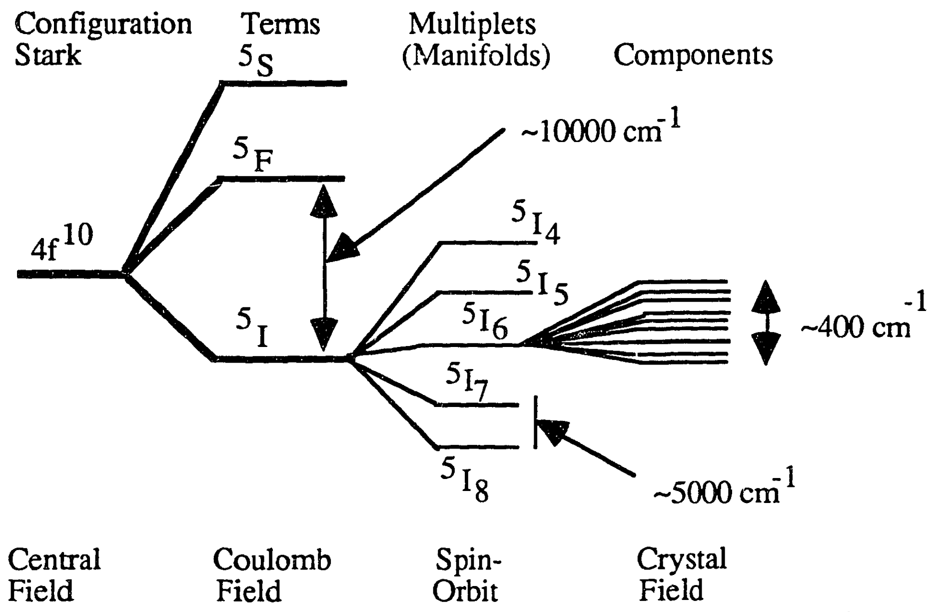

Fig. 1.1.1 Illustrative example of splittings caused by the different interactions.

As was mentioned earlier, the actinide series' 5f shells are not as tightly shielded as the lanthanide series' 4f shells. As a result, the 5f electrons interact more strongly with the crystal field and are more sensitive to the local environment than the 4f rare earths. The positions of actinide energy levels differ considerably from host to host, and there is no analog of the Dieke chart for these materials.

In contrast to the 4f rare-earths, where the energy levels are for the most part unaffected by the local environment, transition metals ions (with their partially filled d shell structure) show much more sensitivity to the local environment; not only their energy levels but also the character of their electronic wavefunctions are substantially determined by the local environment. The d orbitals of transition metals interact with the environment far more than the f orbitals because they are less localized. When working with these ions, the role of the crystal field and the spin-orbit interactions exchange positions, with the spin-orbit effects being handled as a perturbation of the electronic states produced by the crystal field interaction[9].

In theory, the energy levels for any material can be calculated from first principles using standard crystal field theory[10] or ligand field theory[11] (crystal field theory with extended charge distributions), but in practice the energy levels are most often

---

[9] C. A. Morrison, Host Materials for Transition-Metal Ions, Harry Diamond Laboratories, US Army Electronics Research and Development Command, Pub. HDL-Ds-89-1, 1989.

[10] C. A. Morrison, Lectures on Crystal Field Theory, Harry Diamond Laboratories, US Army Electronics Research and Development Command, Pub. HDL-SR-82-8, 1982.

[11] For example, C. J. Ballhausen, Introduction to Ligand Field Theory, McGraw-Hill, New York, 1962.

determined by fitting the parameters of crystal field theory with a few experimentally determined energy levels[12].

Due to the localized and shielded nature of 4f wavefunctions, the 4f energy levels of rare-earth dopants do not form a band structure. The 4f wavefunctions retain many of their atomic characteristics and appear more as those of trapped impurities in a solid regardless of dopant concentration; electrons in the 4f states have little mobility in the crystal. Excitations of these orbitals are localized and resemble, in some sense, tightly-bound excitons. When these ions are doped into solids, the presence of the 4f energy levels can be observed both above [13] and below the bandgap of the material.

1.1.1. Effect of the static crystal field.

The crystal field interaction, though small in magnitude, plays an important role as it not only lifts the degeneracy of the levels but also allows optical transitions to occur within the 4f configuration. Electric dipole transitions are normally forbidden between states of the same parity. However, when an ion is doped into a non-centrosymmetric site (one lacking inversion symmetry), wavefunctions of different parities mix. In the rare-earths, the inter-mixing of the $5d\text{-}4f^{n-1}$ and $4f^{n}$ wavefunctions allows electric dipole transitions to occur between different $4f^{n}$ shell configurations[14]. These normally forbidden transitions are often referred to as "forced" electric dipole transitions. In comparison to allowed electric dipole transitions, the oscillator strengths of these "forced" transitions are weak; as a result, some of the manifolds of the rare-earth ions are relatively long-lived (Some manifolds exhibit lifetimes greater than 10 ms.)[5]. The only general selection rule observed by these transitions is $\Delta J \le \pm 6$. Certain selection rules determined by the site symmetry exist for transitions between different energy levels, and can be determined from group theory[7]. Higher order transitions such as magnetic dipole and electric quadrupole are also allowed; and since these transitions are not parity forbidden for intra-f transitions their relative intensity can be much closer to that of the "forced" electric dipole transitions. The magnetic dipole selection rule of $\Delta J = \pm 1, 0$, but not 0->0, still holds.

---

[12] See, for example, E. D. Filer, C. A. Morrison, G. A. Turner, and N. P. Barnes, "Theoretical Branching Ratios for the $^5I_7 \rightarrow {}^5I_8$ Levels of Ho^{3+} in the Garnets $A_3B_2C_3O_{12}$," OSA Proc. on Advanced Solid-State Lasers, Santa Fe, Ed. L. L. Chase and A. A. Pinto, V13, 1992, P354.

[13] Levels above the bandgap can be observed with the techniques of double photon spectroscopy described in several references. For example, see Y. R. Shen, The Principles of Nonlinear Optics, Wiley, New York, 1984.

[14] J. H. Van Vleck, J. Phys. Chem., V4, (1937), P67.

1.1.2. Effect of the dynamic crystal field.

In actuality the crystal field is not static, but dynamic. The crystal field at a point in space will vary over time as the ions which generate the field change position. The field can be expressed as

$$V_{xtal}(t) = V_0 + \frac{\partial V}{\partial x_i} dx_i + \frac{\partial V}{\partial x_i}\frac{\partial V}{\partial x_j} dx_i dx_j + \cdots,$$

where dx is the change in the relative position of the ligands. The applied crystal field will change with the relative movement of the ions. The dynamic portion of the crystal field can be expressed as a sum over the normal modes of the crystal's vibration (the phonon states).

The phonons interact with the ions in a variety of ways. The fluctuating crystal field which the phonons create mixes the electronic wavefunctions of the system, which allows ions to make transitions between different states. Thus, the phonons interact with the excited ions to bring about an equilibrium distribution of excitations within the manifold by allowing ions in higher lying energy states to relax to energetically lower states. Both acoustical and optical phonons are involved in this process, and multiphonon processes are likely[15]. For this reason, transitions to upper lying energy levels are sometimes said to be phonon-broadened. Linewidths of these transitions are increased (in part) because of the electron-phonon interaction.

Phonon-assisted optical transitions can also occur. In these transitions, an ion makes a transition between different electronic states by photon emission or absorption coupled with the emission or absorption of a phonon[16]. A transition of this nature is in some sense a second-order process, and its cross-section may be expected to be low in comparison to a first order transition. However, the cross-section of these phonon-assisted transitions can be roughly comparable to "forced" transitions (the parity mixing of the ionic wavefunctions may be increased as the ionic motion may reduce site symmetry); and these "vibronic" interactions play an important role in many systems. Some optical transitions are strongly coupled to the phonon modes of the crystal. As the coupling between an energy level and a phonon mode will depend on the details of the

---

[15] L. A. Riseberg and M. J. Weber, "Relaxation Phenomena in Rare-Earth Luminescence," Progress In Optics, V14, Ed. E. Wolf, North-Holland, Amsterdam, 1976, P91-159.

[16] See, for example, M. Wagner, "Vibronic Spectra in Ionic Crystals," Optical Properties of Ions in Crystals, Ed. H. M. Crosswhite and H. W. Moos, Interscience, New York, 1967, P349-356.

crystal field interaction, the effective density of phonons can be different for vibronic transitions than would be measured by other methods.

These phonon-electron interactions can be driven by extended or local modes of the crystal. A rare-earth ion in a substitutional site represents a subtle break in the overall symmetry of the crystal, and therefore the local modes of the dopant site are important; these modes can generally be described as a superposition of extended lattice modes. A dopant ion in a crystal is spatially well-located; because of this it can couple to all of k space when interacting with phonons. The effect of the phonon interactions on the lineshape will depend on the details of the ion-lattice coupling. The 4f wavefunctions are not strongly coupled to the lattice, and $4f^n$-$4f^n$ phonon-assisted transitions tend to reflect the full spectrum of phonons which can couple to the ion[17]. This ion-lattice coupling is not only ion dependent, but is also sensitive to the host; and determining the exact details of a material's phonon-electron interaction is not a simple matter.

1.1.3. Multi-phonon relaxation.

Not only do phonons affect the optical transitions between manifolds and bring the excited ions within the manifold to equilibrium, they also can cause transitions between different manifolds. This process is called multi-phonon relaxation as an excitation can make a "non-radiative" transition (no photons emitted or absorbed) between two manifolds by emitting and absorbing phonons. This is a multi-phonon process; generally the optical phonons are thought to be involved in this process as the energy gaps bridged can be on the order of thousands of wavenumbers. A relationship has been empirically found to describe this process by Moos and others[18]; this relationship is

$$W_{nr} = Ce^{-\Delta/E_g},$$

where W_{nr} is the non-radiative relaxation rate, C is a host material dependent constant, E_g is the maximum energy of the host's effective phonon density, and Δ is the energy of the gap between the manifolds. The non-radiative relaxation rate is highly host dependent, and this relaxation process will limit the lifetimes of manifolds which lie energetically close to lower lying manifolds. It is clear that the lifetimes of the manifolds of a rare-earth ion are dependent on the phonon spectrum of the host.

---

[17] See, for example, H. P. Jenssen, "Phonon Assisted Laser Transitions and Energy Transfer in Rare Earth Crystals," PhD Dissertation, Mass. Inst. of Tech., 1971, and also [16] for a discussion of these issues.

[18] H. W. Moos, "Spectroscopic Relaxation Processes of Rare Earth Ions in Crystals," J. Lumin, V1, N2, (1970), P106.

1.2. Introduction to Energy Transfer.

We now review energy transfer between ions, a basic process of importance to optical materials that can occur when rare-earth ions are doped into solids. Comprehensive reviews of energy transfer can be found in [19, 20]. In energy transfer, some or all of the energy absorbed by one ion is transferred to a second ion. We now describe the theory qualitatively and delay a formal examination of the microscopic theory until Chapter 2.

When energy transfer occurs, an ion in an energetically high lying state makes a transition to a lower energy state while promoting another ion from a low energy state to a higher energy state. The ions can be of the same or different species. This process can be caused by either the electromagnetic interaction or the exchange interaction. When the electromagnetic interaction is mediated by a real photon (the ion emits a photon which is then absorbed by another ion), the transfer process is called radiative trapping or reabsorption, and the lifetime of the emitting state is generally not affected.

If the interaction is non-radiative (involving either the exchange interaction or the electromagnetic interaction mediated by virtual photons), it can affect the lifetime of the initial level. The magnitude of this effect depends on the distance between the ions; therefore, this interaction will be concentration-dependent.

The transfer process can be either resonant or non-resonant in nature. In a resonant process, the interaction occurs principally between the electronic wavefunctions of the ions. Energy is conserved during the actual transfer process, although other interaction mechanisms affecting the involved states may cause a net loss of energy. Thermalization of the manifold is an example of such a situation and will be discussed later. In a non-resonant process, energy transfer between the two ions is coupled with the emission or absorption of a phonon; therefore some of the electronic energy is lost to or obtained from the lattice. These two processes are illustrated in Figure 1.2.1.

---

[19] J. C. Wright., in Radiationless Processes in Molecules and Condense Phases, Ed. F.K. Fong, Topics in Applied Physics Series, V15, Springer-Verlag, Berlin, 1976, P. 239.

[20] V. M. Agranovich and M. D. Galanin, Electronic Excitation Energy Transfer in Condensed Matter, Modern Problems in Condensed Matter Sciences Series, V3, North-Holland, Amsterdam, 1982.

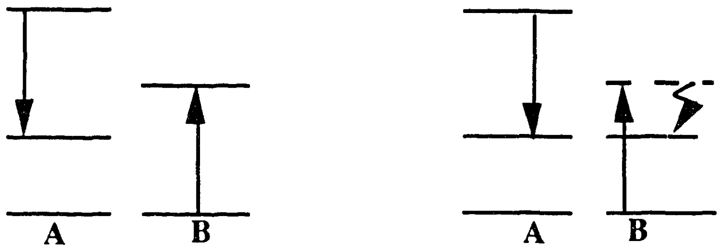

Resonant Transfer Non-resonant Transfer

Figure 1.2.1. Energy diagram for resonant and non-resonant energy transfer.

These are the underlying physical processes of energy transfer; however, the processes are historically grouped into a few different classes based on their macroscopic effects. In fact, often two different names will be used to refer to the same process depending on whether the process is thought desirable or undesirable. These different classifications are now described so that the reader is familiar with the nomenclature of the field.

Donor-acceptor transfer occurs when one ion (the donor) absorbs energy, which is subsequently transferred to another ion (the acceptor). An example of this is the "sensitization" of a laser material by the addition of an efficiently absorbing ion. In this type of transfer, the ion where the energy is desired is referred to as the acceptor ion, and the ion which has been included for the sole purpose of supplying energy to the acceptor ion is referred to as the donor ion. This is illustrated in Figure 1.2.2.

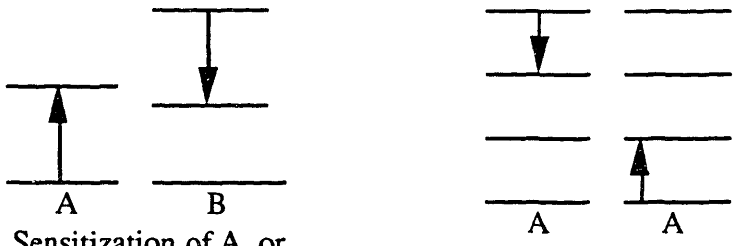

Sensitization of A or Quenching of B

Self-Quenching or Cross-relaxation

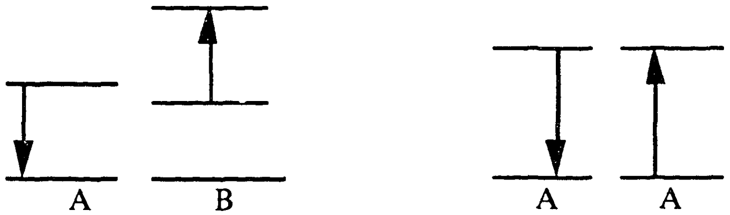

Upconversion Migration

Figure 1.2.2. Various energy transfer processes.

The same process is called quenching if the ion loosing the excitation (the donor) is of primary interest. This is sometimes viewed as a desirable process, (For example, if the terminal level of a laser is quenched[21]) and sometimes as an undesirable process (For example, when a laser's initial level is quenched). What processes are considered beneficial will depend on the engineering concerns of the problem.

Cross-relaxation (or self-quenching) is also illustrated in Figure 1.2.2. In this process, an ion in a high lying level falls to an intermediate level while promoting another ion from the ground state to a higher level. As can be seen, this is essentially the same process as donor-acceptor transfer. The term cross-relaxation is generally used when the intermediate levels populated by the transfer are of interest; while the term self-quenching is used when this energy transfer process considered to be loss acting on the upper level[22].

Upconversion, illustrated in Figure 1.2.2, is the reverse of cross-relaxation. Here an ion in an intermediate state falls to a lower state while promoting another ion in an intermediate state to a higher state. The final state of the promoted ion is typically higher in energy than either of the intermediate states. This is one the basic mechanisms currently being explored which can be used to produce efficient infrared[23] and visible[24] lasers; meanwhile, it is also considered to be the primary loss mechanism in some of the other infrared lasers currently being developed[25].

Migration (or diffusion) is the name used when an excitation is transferred resonantly between the same manifold of two ions. This mechanism, while not visibly changing the spectra or lifetimes of the manifold by itself, allows excitations to diffuse away from the location of the initial excitation. Thus migration can allow an excitation initially not near an accepting center to diffuse out until it finds an acceptor (or decays on

---

[21] D. S. Knowles and H. P. Jenssen, "Upconversion versus Pr-deactivation for Efficient 3 μm Laser Operation in Er", IEEE J. Quant. Elect., V28, N4, (1992), P1197.

[22] See, for example, R. Buisson and J. Q. Liu, "Fluorescence quenching of Nd^{3+} in LaF_3 studied by direct measurement of pairs," J. Physique, V45, (1984), P1523. or V. Lupei, A. Lupei, S. Georgescu, and W. M. Yen, "Effects of energy transfer on quantum efficiency of YAG:Nd," J. Appl. Phys., V66, N8, 1989, P3792.

[23] B. J. Dinerman and P.F. Moulton, "CW Laser Operation from Er:YAG, Er:GGG and Er:YSGG," OSA Proc. on Advanced Solid-State Lasers, Santa Fe, Ed. L.L. Chase and A.A. Pinto, V13, 1992, P152.

[24] T. Herbert, W. P. Risk, R. M. Macfarlane, and W. Lenth, "Diode-Laser-Pumped 551-nm Upconversion Laser in $YLiF_4:Er^{3+}$," OSA Proc. on Advanced Solid-State Lasers, Salt Lake City, ed. H. P. Jenssen and G. Dube, V6, 1990, P379.

[25] T. Y. Fan, G. Huber, R. L. Byer, and P. Mitzscherlich, "Spectroscopy and Diode Laser-Pumped Operation of Tm, Ho:YAG," IEEE J. Quant. Elect., V24, N6, (1988), P924.

its own) and, for this reason, is a very important mechanism in sensitized or upconversion lasers[26]. We will return to these processes in later chapters.

---

[26] See, for example, M. J. Weber, "Luminescence Decay by Energy Migration and Transfer: Observation of Diffusion-Limited Relaxation", Phys. Rev. B, V4, N9, (1971), P2932.

1.3. Review of the 2 μm Laser

In this section we review the engineering motivation behind our thesis problem. We first explain why an efficient 2 μm laser is desired, and then briefly review the development history of the Ho laser to illustrate how engineering concerns have suggested that the diode-pumped Tm-Ho laser system is the system of choice. We then present the problems currently observed in state of the art Tm-Ho laser systems.

1.3.1. Why do we want a 2 μm laser?

Lasers which operate in the mid-to-far infrared spectral region are of great interest to the technical community as the human eye is not transmissive to electromagnetic radiation of wavelengths longer than ≈1.5 μm. The eye is no more sensitive to these wavelengths than any other portion of the human body; therefore these lasers which operate in this spectral region are considered "eyesafe." This eyesafe quality is important for applications (such as atmospheric sensing) where potential human exposure hazards exist.

The 2 μm wavelength is desirable because there is a local minimum in the water vapor absorption in this region and atmospheric transmission of the light is possible. Additionally, this wavelength of light is above the cut-off wavelength of currently used optical materials and therefore is compatible with much existing technology. This system has potential applications in many diverse areas such as coherent laser radar[27] and Differential Absorption Lidar (DIAL) measurements of atmospheric gases[28], pump sources for frequency down-converters which span the 3 to 5 μm region[29], medical applications (due to strong liquid water absorption[25] in this region), and research applications. Presently, there is a great deal of interest in developing a practical device capable of generating coherent 2 μm radiation.

---

[27] S. W. Henderson, C. P. Hale, J. R. Magee, M. J. Kavaya, and A. V. Huffaker, "Eye-safe coherent laser radar system at 2.1 mm using Tm,Ho:YAG lasers," Optics Letters, V16, N 10, (May 1991), P 773-775.

[28] M. E. Storm and W. W. Rohrbach, "Single-longitudinal-mode lasing of Ho:Tm:YAG at 2.091 μm", Applied Optics, V 28, N 23, (Dec 89), P 4965.

[29] P. A. Budni, P. G. Schunemann, M. G. Knights, T.M. Pollak, and E.P. Chicklis,"Efficient, High Average Power Optical Parametric Oscillator Using $ZnGeP_2$.", in OSA Proc. of the Advanced Solid State Laser Conference (V 13), Ed. Chase and Pinto, Santa Fe, 1992, P 380-383.

1.3.2. Why the Ho^{3+} laser?

A variety of different systems are capable of producing coherent 2 μm radiation. The desire for reliability and durability has focused attention on all-solid-state devices. These include frequency down-converters (OPO's) for visible laser radiation[30], laser diodes, and conventional solid state lasers. OPO's, while broadly tunable devices, are complicated to operate and can not achieve the efficiencies of which diode and solid-state lasers are capable. Efficient 2μm diodes are not yet available and, for this and other reasons, much effort has been directed at diode-pumped solid state lasers. Additionally, in many ways diode-pumped solid state lasers have advantages over the direct use of diode lasers. Better beam quality, higher peak powers, and narrow and more stable frequency linewidths can be obtained with a diode-pumped solid state laser than with diodes operating alone[31]. In a sense, the solid state laser can serve as an optical energy integrator and a frequency converter for diode lasers.

Several solid state systems capable of generating 2 μm radiation have been explored, including Co:MgF_2[32, 33], Tm-doped systems [34, 35], and Ho-doped systems. Much work has concentrated on Ho^{3+} as it has a considerably higher cross-section in the 2 μm region than the other two materials. The system of choice for a high power 2 μm laser is currently a diode-pumped sensitized Ho-activated system. We will now review the development of the Ho-activated laser system to illustrate some of the concerns when working with the system.

---

[30] See, for example, K. L. Schepler, M. D. Turner, and P. A. Budni, "High-Average-Power Nonlinear Frequency Conversion in $AgGaSe_2$", OSA Proc. on Adv. Sol. State Laser, V10, ed G. Dube and L. Chase, Hilton Head, (1991), P325 for a discussion of the technology.

[31] T. Y. Fan and R. L. Byer, "Diode Laser-Pumped Solid State Lasers," IEEE J. Quant. Elect., V24, N6, (1988), P 895.

[32] P. F. Moulton, "An Investigation of the Co:MgF2 Laser System," IEEE J. Quant. Elect., V21, (1985), P1582.

[33] D. M. Rines, G. A. Rines, D. Welford, and P. F. Moulton, "High-Energy Operation of a Co:MgF_2 Laser," in OSA Proc. of the Advanced Solid State Laser Conference (V 13), Ed. Chase and Pinto, Santa Fe, 1992, P 161.

[34] G. J. Quarles, A. Rosenbaum, C. L. Marquardt, and L. Esterowitz, "Efficient room-temperature operation of a flash-lamp-pumped Cr,Tm:YAG laser at 2.01 μm," Optics Letters, V15, N1, (1990), P42.

[35] S. R. Bowman, G.J . Quarles, and B. J. Feldman, "Upconversion Studies of Flashlamp-Pumped Cr,Tm:YAG," in OSA Proc. of the Advanced Solid State Laser Conference (V 10), Ed. G. Dube and L. Chase, Hilton Head, 1991, P 169.

1.3.3. History of the Ho laser.

The Ho^{3+} $^5I_7$->$^5I_8$ transition was first lased by Johnson et. al.[36] in 1962. In this system, Ho:$CaWO_4$ was flash lamp pumped at liquid N_2 temperatures which allowed operation as a four-level laser. The general scheme under which the system operated is illustrated in Fig 1.3.1,

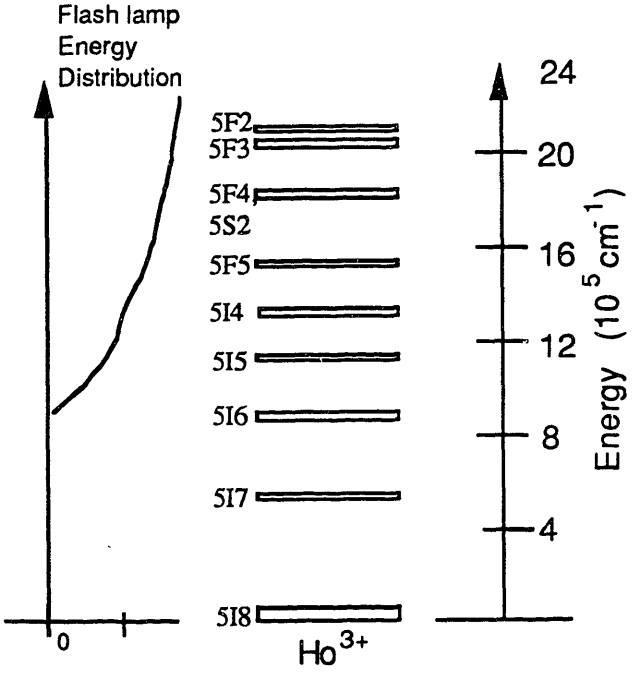

Figure 1.3.1. Diagram of the energy levels of Ho^{3+}.

Energy was absorbed by the higher-lying levels with absorption in the region of flashlamp emission. The energy absorbed "trickled" down via a variety of processes and eventually was deposited in the upper laser level. Laser oscillation then occurred between a lower-lying energy level of the $^5I_7$ manifold and an upper-lying level of $^5I_8$. This design, while able to demonstrate laser oscillation at the desired wavelengths, was not a practical device for several reasons.

First and foremost, the system operated at cryogenic temperatures, which considerably increased the system complexity but which made laser operation easier to obtain. This is because the Ho laser transition terminates at a higher lying level of the ground state manifold (See Fig. 1.3.2). At room temperature this level is substantially

---

[36] L. F. Johnson, G. D. Boyd, and K. Nassau, "Optical maser characteristics of Ho^{3+} in $CaWO_4$," Proc. IRE, V 50, (1962), P 87.

populated and the system resembles a 3 level laser[37]; but at cryogenic temperatures the terminal level is essentially unpopulated and the system resembles a 4 level laser. However, for many applications it is desirable to have simple and reliable devices; therefore, current research is driven to develop efficient all-solid state systems which operate at temperatures greater than 200K (the practical limit of solid state cooling devices). Overcoming the three-level nature of room temperature operation is one of the primary challenges in the quest for efficient systems.

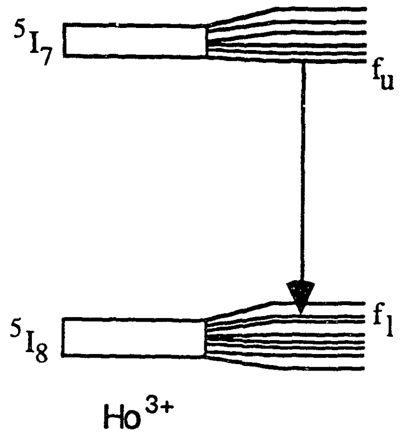

Figure 1.3.2. Illustration of typical manifold splittings for Ho^{3+}.To achieve laser oscillation the population in the initial state must exceed that of the population of the final state.

A second problem with flashlamp pumping of the singly-doped Ho system can be seen by comparing the spectrally broad flashlamp energy distribution with the Ho absorption, which consists of several spectrally narrow regions of absorption. It is apparent that much of the flashlamp energy is wasted and that the system efficiency is inherently low.

One final problem with singly-doped Ho which significantly affects laser performance is not apparent in the above figures. It was mentioned earlier that the energy deposited in the upper-lying manifolds "trickled" down and is collected in the $^5I_7$ manifold. What is now known is that the Ho levels are too far apart for efficient non-radiative relaxation. In some hosts the $^5I_6$, $^5F_5$, and $^5S_2$ manifolds are also metastable. Energy can collect in these levels during the trickle down process, forming "relaxation bottlenecks".

---

[37] See, for example, A. Yariv, Quantum Electronics, Wiley, New York, 1967, P245.

Codoping

One solution to the above mentioned problems is to add additional dopants to the material. Pump energy can be absorbed by a sensitizing dopant (an ion with complementary absorption) and then transferred to Ho by some of the processes described earlier. Codoping also allows independent optimization of ion concentrations for a given application; this can minimize some of the inherent problems of a three-level laser system. Finally, codopants can quench the metastable levels of Ho and ensure that most of the energy absorbed is deposited in the $^5I_7$ manifolds. It is clear that the proper choice of codopants is crucial for efficient room temperature operation.

The proper choice of host materials also is important. The host material will determine some aspects of the non-radiative processes as well as the detailed splitting of the energy levels of the dopants. As the manifold splitting is different in each host, it is possible to find materials which minimize the required inversion threshold.

There is no obvious choice of a "best" material for a 2 µm laser; the optimum choice will be determined by the desired application. Any chosen material represents a trade-off between transfer rates, manifold splittings, cross-sections, and other parameters. For this reason, many different combinations of hosts and sensitizers have been tried in an effort to optimize the system. Early work focused on the use of Cr^{3+} and Er^{3+} as sensitizers in several different hosts. However, neither of these systems performed as well as was expected from simple spectroscopic measurements.

The next significant step in the development of the system was the addition of Tm to the Cr and Er sensitized systems to facilitate energy transfer between the sensitizers and Ho[38,39]. Overall efficiencies improved considerably with the addition of Tm, and current schemes for flashlamp pumped systems use Cr, Tm or Er, Tm as codopants. Typical system efficiencies run on the order of 5% of applied power for room temperature systems[40]. However, these systems are still not as efficient as expected, and problems still exist with current models of this system.

---

[38] R. L. Remski and D. J. Smith, "Temperature dependence of pulsed laser threshold in YAG: Er^{3+}, Tm^{3+}, Ho^{3+}," IEEE J. Quant. Elect., V6, (1970), P750.

[39] E. P. Chicklis, C. S. Naiman, R. C. Folweiler, D. R. Gabbe, H. P. Jenssen, and A. Linz, "High-Efficiency Room-Temperature 2.06-µm Laser Using Sensitized Ho^{3+}:YLF," App. Phys. Let., V19, N4, (1971), P119.

[40] G. J. Quarles, A. Rosenbaum, C. L. Marquardt, and L Esterowitz, "High-efficiency 2.09 µm flashlamp-pumped Tm:Ho:YAG laser," Appl. Opt., V24, (1985), P940.

Laser-pumping

A second solution to the problems of the singly-doped Ho system has emerged with the advent of laser pumped lasers. Using a laser, it is now possible to efficiently pump the narrow absorption bands of rare-earth ions, and a wide variety of new laser operating schemes are now possible. Of particular interest is laser-diode pumping, which has already produced high-power all-solid-state systems [See, for example, 41, 42].

Direct pumping of the $^5I_7$ manifold is one possible approach. This approach would directly excite the upper laser manifold and eliminate many complications arising from energy transfer processes. Direct pumping is the most efficient way to couple optical energy into the system - the intrinsic efficiency of this process is roughly 90%. Recently, solid state lasers (Tm, Er-Tm) in the appropriate wavelength range (1.8-1.9 μm) have been demonstrated[43] and have even been used to pump a Ho^{3+} 2.0 μm laser [44]. Diode lasers in this wavelength range are also under development. However, there are practical problems with this scheme. The use of another solid state laser will require optimization of that system as well as the 2 μm system, while 1.9 μm diode lasers are still not optimized. For this reason it is sensible to look for alternatives to the direct pumping approach -- some combination of codoping and laser-pumping.

The system which has attracted the most attention is the codoped Tm-Ho system. The use of Tm as a sensitizer has several advantages as far as practical, affordable devices are concerned. First of all, it has absorption in a range (800 nm) where high-power diode lasers have been optimized (for use in pumping Nd lasers) and are therefore readily available and relatively inexpensive in comparison to other diode sources. Secondly, although the pumped absorption band is centered at ~800 nm, there is an energy transfer process that efficiently feeds the lower Tm manifold, following which there is efficient transfer from Tm to Ho. The intrinsic quantum efficiency of this process is roughly 80% in most materials. While this value is not as high as that of direct pumping, the practical advantages of using this scheme may more than offset the loss due to the lower optical efficiency. An additional advantage which results from using Tm as a sensitizer is that it can be pumped with near infrared tunable solid state sources (Ti:Sapphire, Alexandrite, and others) which are currently available.

---

41 N. P. Barnes, M. E. Storm, P. L. Cross, and M. W. Skolaut, Jr., "Efficiency of Nd laser materials with laser diode pumping," IEEE J. Quant. Elect., V26, (1990), P558.

42 L. E. Holder, C. Kennedy, L. Long, and G. Dube, "One Joule per Q-Switched Pulse Diode-Pumped Laser," IEEE J. Quant. Elect., V28, N4, (1992), P986.

43 T. S. Kubo and T. J. Kane, "Diode-Pumped Lasers at Five Eye-Safe Wavelengths," IEEE J. Quant. Elect., V28, N4, (1992), P1033.

44 R. C. Stoneman and L. Esterowitz, "Intracavity-pumped 2.09-μm Ho:YAG Laser," OSA Proc. on Adv. Sol. State Lasers, V13, ed. L. L. Chase and A. A. Pinto, Santa Fe, (1992), P115.

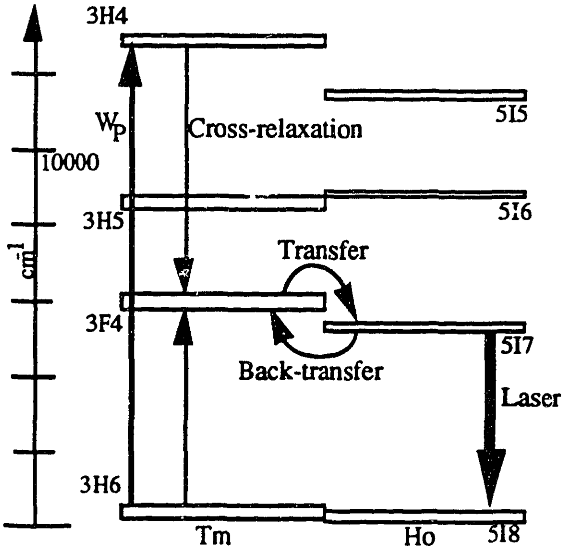

Figure 1.3.3. Model currently used for Tm, Ho 2.0 µm lasers.
The cross-relaxation processes shown leads to two excitations in the $^3F_4$-$^5I_7$ manifold for each pump photon absorbed. The transfer and back-transfer processes are thought to lead to equilibrium between the two manifolds.

The model for the Tm-Ho doped system is shown in Fig. 1.3.3. In this model, Tm ions are excited into the $^3H_4$ manifold by the absorption of pump radiation The $^3H_4$ state decays by a cross-relaxation process to produce two excitations in the $^3F_4$ manifold. The excitations in the $^3F_4$ then transfer to the Ho $^5I_7$ manifold. The reverse transfer process also can occur, and as these transfer processes occur at much higher rates than the relaxation processes effecting the $^3F_4$ and the $^5I_7$ manifolds, an equilibrium distribution of excitations between the $^3F_4$ and the $^5I_7$ manifolds develops.

The diode-pumping of a Tm-Ho laser was proposed but not demonstrated by Castleberry[45]. A diode pumped system was first lased at 77K by Allen et. al.[46]. CW room temperature operation was subsequently demonstrated in Tm, Ho:YAG by Fan et. al.[47]. Tm, Ho:YLF has also been lased at room temperature with diode pumping.

---

[45] D. E. Castleberry, "Energy transfer in sensitized rare earth lasers," Ph. D. dissertation, Mass. Inst. of Tech, Cambridge, MA, 1975.

[46] R. Allen, L. Esterowitz, L. Goldberg, J. F. Weller, and M. Storm, "Diode-pumped 2 µm holmium laser," Electron. Lett., V22, (1986), P947.

[47] T. Y. Fan, G. Huber, R. L. Byer, and P. Mitzscherlich, "Continuous wave operation at 2.1 µm of a diode laser pumped, Tm-sensitized Ho:$Y_3Al_5O_{12}$ laser at 300K," Opt. Lett., V12, (1987), P678.

1.3.4 Current Problems of the Tm-Ho system.

Although the Tm-Ho system has been successfully lased in a number of hosts, the model for this system is still not complete. These lasers do not perform as well as predicted from simple spectroscopic and dynamics measurements. Thresholds are higher than expected and the lifetime of upper laser level is shortened at high excitation densities[48]. These experimental facts indicate that a loss mechanism is present.

An upconversion process has been identified as one of the loss mechanisms for the $^5I_7$ manifold[25]. This process promotes an excitation from the $^5I_7$ to the $^5I_5$ manifold of Ho by accepting energy from an excitation in the $^3F_4$ manifold of Tm; the state of the Tm ion involved changes from the $^3F_4$ to the $^3H_6$ state in this process. This process is modeled as removing two excitations from the initial laser level as the $^3F_4$ manifold serves as a reservoir of excitations for the $^5I_7$. Several authors have attempted to measure the magnitude of this upconversion process; however, measurements made at high excitation densities often do not agree with predictions based on measurements made at lower excitation levels. The problems become pronounced at higher excitation densities, and less energy can be extracted from the system than expected. These facts indicates that the model for this system is still incomplete.

Additional loss processes have been suggested, such as excited state absorption[49] or other energy transfer processes[50, 51, 52]. While other mechanisms are certainly present and may eventually be incorporated into the current model, it is not clear that they can explain the observed deviations from this model. There is a definite need to develop a model with some predictive power in order to have a better understanding of the processes and the problem.

It may be possible that some of the observed deviations from this model are the result of an incorrect application of the model to the physical system and do not require additional mechanisms for their explanation. At the present time, it is generally assumed

---

48 S. R. Bowman, M. J. Winings, R. C. Y. Auyeung, J. E. Tucker, S. Searles, and B. J. Feldman, "Upconversion Studies of Flashlamp-Pumped Cr,Tm,Ho:YAG," in OSA Proc. of the Advanced Solid State Laser Conference (V 13), Ed. L. Chase and E. Pinto, Santa Fe, 1992, P 172.

49 M. G. Jani, R. R. Reeves, R.C . Powell, G. J. Quarles, and L. Esterowitz, "Alexandrite-laser excitation of a Tm:Ho:$Y_3Al_5O_{12}$ laser," J. Opt. Soc. Am. B, V8, N4, (1991), P741.

50 L. B. Shaw, X.B . Jiang, R. S. F. Chang, and N. Djeu, "Upconversion of 5I7 to 5I6 and 5I5 in Ho:YAG and Ho:YLF," in OSA Proc. of the Advanced Solid State Laser Conference (V 13), Ed. L. Chase and E. Pinto, Santa Fe, 1992, P 174.

51 M. A. Noginov, G. K. Sarkissian, V. A. Smirnov, and I. A. Shcherbakov, "Cross-relaxation depletion of the ground state of rare-earth ions in crystals", OSA Proc. of the Adv. Solid State Laser Conf, V6, Ed. H. P. Jenssen and G. Dube, Salt Lake City, (1990), P375.

52 C. Hauglie-Hanssen and N. Djeu, "Pump saturation for the 2 μm Tm laser", OSA Proc. of the Advanced Solid State Laser Conference, Ed. E. Pinto and T. Y. Fan, New Orleans, 1993, In press.

that the equilibrium distribution of excitations between the $^3F_4$-$^5I_7$ manifolds is a canonical distribution which can be calculated from the energy levels of these manifolds. However, this model for the distribution has never been experimentally verified. The $^5I_5$ upconversion rates can not be found without knowledge of either the $^3F_4$-$^5I_7$ transfer and back-transfer rates or the equilibrium distribution between the $^3F_4$ and $^5I_7$ manifolds. Without an accurate knowledge of these quantities, the values for the upconversion parameters can not be determined and it is not possible to make accurate predictions of the systems behavior. If, in fact, the distribution is not a simple canonical distribution over the $^3F_4$-$^5I_7$ manifolds, many of the observed results may be explained. The prediction and measurement of this distribution will be the central goal of this thesis. We will also explore the implications of this equilibrium distribution for energy transfer rates in the system.

1.4. Thesis Overview

In the following chapter, we will review the basic theory crucial to the understanding of this thesis. We present concepts and results which are used throughout the thesis and are necessary for data interpretation. In this review, we will highlight only important results as the amount of work done in this field is extremely large. We will cover microscopic energy transfer theory, generalizations of the Einstein relations, and electron-phonon interactions in a unifying manner so that the common points between these theories are evident.

In Chapter 3, we present our thesis problem and detail the underlying assumptions. We discuss the model assumed to apply to the system and present what is generally assumed to be the correct description of the energy distribution between the $^3F_4$ and the $^5I_7$ manifolds. We then establish a connection between energy transfer theory and generalized Einstein relations for two state systems, and using this connection, rigorously derive an expression for the distribution. We find that our description of the distribution varies from that generally assumed. In this derivation we also develop useful analysis tools. We confirm our theoretical results with a second derivation which relies on simple statistical mechanics and a qualitative description. The limits of validity of the theory developed in this chapter and the potential reasons for its breakdown are discussed.

Chapter 4 reviews the experimental tools used in the study. The various experiments and apparatus used for sample characterization are described. Sample preparation techniques and physical properties of the materials used are then reviewed. A summary of the basic material parameters produced by these measurements is provided.

Chapter 5 describes in detail steady-state measurements which test the theory developed in Chapter 3. The equilibrium distribution is determined by several different measurement techniques and found to confirm the predictions of Chapter 3. The measurement theory and procedure are described in detail, as are necessary aspects of the equipment. Systematic and statistical uncertainties are discussed.

In Chapter 6, we extend the theory developed in Chapter 3 to systems that have not come to equilibrium. We use the relationship established by connecting energy transfer theory to the generalized Einstein relations to examine the relationship between the average transfer parameters for forward and reverse transfer processes. We perform a set of dynamics measurements on singly-doped and co-doped samples of Tm and Ho in various hosts. Energy transfer rates for upconversion and cross-relaxation processes are obtained in several materials. A potential breakdown of the theory presented in Chap. 3 is identified. Additional energy transfer processes in these materials are identified and discussed.

In Chapter 7 we discuss the implications of the measurements of Chapters 5 and 6 on the theory presented in Chapter 3. We discuss the role of the migration process as a possible reason for the deviations found in our measurements. We then raise general concerns of the theory and discuss still-unresolved questions. Finally, we discuss the implications of this thesis for the Tm-Ho system. We discuss how our measurements may explain some of the problems observed in the model for the Tm-Ho system.

In Chapter 8, we summarize the experimental and theoretical results of this thesis. We will discuss the practical implications of these results for the 2 μm laser. We also discuss some of the implications of the theory for energy transfer theory and suggest future measurements.

The appendixes contain a variety of information, such as details regarding mathematical proofs and computer programs which are necessary for completeness but which distract from the flow of the thesis. Also included is the spectroscopic data used to generate the results summarized in the main body of the work, but which, by itself, is not necessary for the main points of the thesis.

2. Theory Review

In this chapter, we will review the basic theory underlying this thesis. We present concepts and results which are used throughout the thesis and are necessary for data interpretation.

In this review, we have tried to present the current theory in a manner which will lead to a thorough and natural understanding of the thesis problem. In doing so, we have neglected the actual historical development of the different theories; instead presenting the theory in a manner which hindsight allows us. Additionally, we have tried to unify concepts of several different bodies of work so that common points between them are evident. Here we present only a summary of important results and concepts; detailed derivations of several of the results can be found in Appendix A.

We start with an overview of energy transfer theory, first explaining the underlying concept and then introducing the interactions which cause energy transfer. We then cover the various complications which inhibit the straightforward interpretation of energy transfer data and develop relations which we later use for data analysis. Following our review of energy transfer theory, we move to the Einstein relations and the generalizations needed to relate them to experiment. Finally, we cover the effects of the electron-phonon interaction between rare-earth ions and the lattice.

2.1 Review of Basic Energy Transfer Theory.

In this section we will review the basic mechanisms behind energy transfer. We start with a simplified model to illustrate the concepts.

Assume we have a pair of two-level ions which interact through a process which can be described with a Hamiltonian H_{int}. Let ϕ_0 correspond to the ground state electronic wavefunction of ion A and ϕ_1 correspond to the excited state of the same ion. The primed ϕ's will designate the corresponding electronic wavefunctions of ion B.

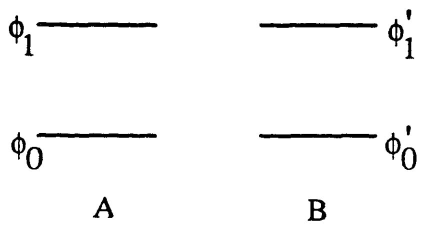

Figure 2.1.1. Energy diagram of simple system.

This model of energy transfer processes was initially proposed by Davydov[53] and has been summarized by [54] and [20]. In this model, the total unperturbed ground state wave function of the system can be expressed as $\psi_0 = \phi_0\phi_0'$, where ϕ_0 and ϕ_0' are the ground state electronic wavefunctions of the ions. Let us assume that the interaction only affects the ions when one is in an excited state and the other in the ground state--of the four possible states of the total system, only two interact. The two states which can interact can be expressed as $\psi_1 = \phi_1\phi_0'$ and $\psi_2 = \phi_0\phi_1'$.

Confining our attention to only the two interacting states, we can think of this as a typical two-state problem, with one state given by ψ_1 and the other by ψ_2. The interaction will cause a mixing of these states so that neither state is stationary. The resulting mixed state can be described as

$$\psi^{ex} = c_1\psi_1 + c_2\psi_2. \tag{2.1.1}$$

It has been shown that for a periodic perturbation[55], the probability of finding the system in either one of the basis states (ψ_1 and ψ_2) can be expressed as

$$|c_1(t)|^2 = \frac{1}{2}\left(1+\cos\left[\frac{2\langle H_{int}\rangle t}{\hbar}\right]\right), \tag{2.1.2a}$$

and

$$|c_2(t)|^2 = \frac{1}{2}\left(1-\cos\left[\frac{2\langle H_{int}\rangle t}{\hbar}\right]\right). \tag{2.1.2b}$$

Here, $|c_1(t)|^2$ and $|c_2(t)|^2$ respectively represent the probability of finding the system in state ψ_1 or ψ_2. In this solution it is has been assumed that the system was initially in state ψ_1, i.e., $|c_1(0)|^2=1$ and $|c_2(0)|^2=0$. The probability of finding the system in a state oscillates as is typical of two-state systems[56]. For this situation, we can say that an excitation has transferred from A to B when the probability of finding the system in state ψ_2 is greater than that for finding it in state ψ_1.

---

[53] A. S. Davydov, "The Radiationless Transfer of Energy of Electronic Excitation Between Impurity Molecules in Crystals," Phys. Stat. Sol., V30, (1968), P357.

[54] O. K. Alimov, M. K. Ashurov, T. T. Basiev, E. O. Kirpichenkova, and V. B. Murav'ev, in Selective Laser Spectroscopy of Activated Crystals and Glasses, Ed. by V.V. Osiko, Proc. of the Inst. of Gen. Phys. Acad. of Sciences of the USSR, Vol. 9., Nova, New York, (1990), P69.

[55] L. D. Landau and E. M. Lifshitz, Quantum Mechanics, 3rd Ed., Pergamon, Oxford, 1977.

[56] J. J. Sakurai, Modern Quantum Mechanics, Addison-Wesley, Redwood City, (1985), P320.

The above relationships are valid for a two level system. However, it must be kept in mind that we have merely rewritten a portion of the problem as a two state system - our initial problem was more complex, consisting of two additional states which could interact via other mechanisms. In addition, considerable complications develop when this simple model is applied to real materials.

Interactions which cause transitions between the other states of system will not necessarily destroy the oscillating energy transfer between states described by Eq. 2.1.2. However, any interaction which causes the system to loose phase coherence at a high rate relative to the energy transfer process will prevent these oscillations from occurring. This is true whether or not the interactions cause a transition between other states of the system. This can be shown using a density operator approach[57]. In a real material, a rare earth ion will couple to the lattice vibrations. Interactions with these vibrations have been estimated to occur at a rate of $\sim 10^{11}$ s^{-1}[5]. As the largest energy transfer rates for rare-earth ions are on the order of $\sim 10^{7}$ s^{-1}, it is apparent that the lattice-ion interactions will cause a loss of coherence and energy transfer oscillations will be suppressed. Although the transfer will not coherently oscillate, the process is still microscopically reversible in that transfer can occur from A to B and from B to A.. It can be shown that coherent oscillations and incoherent transfer are limiting results of the two state problem with a density matrix approach[See, for example, 20]. Dexter and others[58] have argued that since the final state actually is a distribution of many different states due to phonon interactions, the transfer can be described as incoherent.

In the case of incoherent transfer, it is appropriate to use Fermi's Golden Rule to describe the transfer probabilities. This can be expressed as

$$W(E) = \frac{2\pi}{\hbar} \left| \langle \psi_1 | H_{int} | \psi_2 \rangle \right|^2 \rho(E), \qquad (2.1.3)$$

where W(E) is the transfer rate, $\hbar$ is Plank's constant, and $\rho(E)$ is just the density of states at the appropriate energy. This equation is the traditional starting point for discussions of energy transfer theory. As the theory evolved from studies of essentially non-reversible transfer processes, this relation is a natural approach to the problem. However, the fundamental energy transfer problem can be thought of as a two-state problem which constantly loses phase coherence.

---

[57] See, for example, R. Loudon, The Quantum Theory of Light, 2nd Ed., Oxford Science, New York,1983.

[58] D. L. Dexter, T. Forster, and R. S. Knox, Phys. Stat. Sol., V34, (1969), K159.

2.2. The Transfer Interaction.

The Hamiltonian for two interacting ions ($H_{\text{ion-ion}}$) is basically electromagnetic in nature. It can be expressed as

$$H_{\text{ion-ion}} = \frac{1}{2\kappa}\sum_{i,j}\frac{e^2}{|\vec{r}_i - \vec{r}_j|}, \tag{2.2.1}$$

where r_i is the position of the i^th^ electron of ion a and r_j is the j^th^ electron of ion b. Here κ is a constant related to the polarizability of the medium, and e is the electron charge. By using a multipole expansion of $H_{\text{ion-ion}}$ and Fermi's Golden rule the energy transfer rate can be related to experimentally measurable quantities. The interaction rate between two ions separated by $R = |\vec{r}_i - \vec{r}_j|$ can now be expressed as[59, 60]

$$W = \frac{C^{d-d}}{R^6} + \frac{C^{d-q}}{R^8} + \frac{C^{q-q}}{R^{10}} + \dots \tag{2.2.2}$$

Here C^{d-d} is the interaction parameter for dipole-dipole coupling, C^{d-q} for dipole-quadrupole, etc. The characteristic distance for the expansion is the ion size[61]. Dexter has shown that the expression for C^{d-d} can be related to measurable quantities such as the cross-section[60]. It can be shown that C for dipole-dipole transfer from ion 1 to ion 2 can be expressed as

$$C_{12} = \frac{9\chi^2 c}{16\pi^4 n^2}\int \sigma^{(2)}_{\text{abs}}(\lambda)\sigma^{(1)}_{\text{emit}}(\lambda)d\lambda, \tag{2.2.3}$$

where σ_{emit} is the emission cross-section of ion 1 and σ_{abs} is the absorption cross-section for ion 2. n is the index of refraction of the material and χ^2 is a quantity which expresses the orientational average (this is generally assumed to be 2/3 in most early treatments). The higher order terms can be expressed in a similar manner.

As ion concentrations increase, the average distance between ions decreases and higher-order interactions become more important. It has been suggested that interactions such as the quadrupole-dipole and quadrupole-quadrupole must also be considered[19].

---

[59] T. Forster, Ann. Physik, V2, (1948), P55.

[60] D. L. Dexter, "A Theory of Sensitized Luminescence in Solids," J. Chem. Phys., V21, N5, (1953), P836.

[61] R. J. Birgeneau, "Mechanisms of energy transport between rare-earth ions," App. Phys. Lett., V13, N5, (1968), P193.

In relating the energy transfer rate to measurable quantities, some terms have been dropped due to convenient simplifications of the problem. First, the magnetic dipole interaction has been neglected. As magnetic dipole transitions can be of comparable magnitude to electric-dipole transitions in rare-earth systems, it is logical to assume that this mechanism could make measurable contributions. This has the same dependence on distance as electric dipole transfer.

In the typical process of evaluating the expansion of Eq. 2.2.2, the ion wavefunctions are simplified and terms are dropped. The overall wavefunction must be anti-symmetric with respect to electron exchange since electrons are fermions. As only simple wavefunctions are used in the standard derivation, the effects of wavefunction anti-symmetrization are lost. These must be included and will give rise to an exchange interaction rate which can be expressed as [60]

$$W = 2\pi Z^2 \int f_{ab}(\omega) f_{em}(\omega) d\omega, \qquad (2.2.4)$$

where Z is the wavefunction overlap and is defined by

$$Z^2 = A \int Q(\bar{r}_1) \frac{1}{r} Q(\bar{r}_2) d\bar{r}_1 d\bar{r}_2 . \qquad (2.2.5)$$

Here, Q is the charge cloud made of the ground state of one ion and the excited state of another ion. These exchange interactions can occur and will contribute when the average ion-ion distance is small[62]. The magnitude of the exchange interaction relative to the electric dipole interaction is expected to be small in rare-earths due to the shielded nature of their wavefunctions. Exchange interactions are generally not considered at low ion concentrations; however, they may be of importance at higher ion concentrations when substantial numbers of ions have near-neighbors. The relative magnitude of the exchange and higher-order multipole interactions is still open to debate[19].

2.3. Environments and Averaging

Considering for the moment only electric dipole transfer, we can say that the energy transfer rate between two ions separated by a distance vector $\bar{r}_{ij} = \bar{r}_i - \bar{r}_j$ is given by

---

[62] R. J. Birgeneau, M.T. Hutchings, J.M. Baker, and J.D. Riley, "High-Degree Electrostatic and Exchange Interactions in Rare-Earth Compounds," J. Appl. Phys., V40, N3, (1969), P1070.

$$W_{ij} = \frac{C_{ij}}{\left|\vec{r}_{ij}\right|^6}. \tag{2.3.1}$$

However, it is not appropriate to simply apply the relationship given by Eq. 2.3.1 to experimental data as a macroscopic experiment does not actually measure the energy transfer rate between an isolated set of ions. Instead, an experiment produces an ensemble averaged measurement over all the different ion environments in the material. The necessary averaging considerably complicates data analysis.

We examine a typical energy transfer experiment to illustrate the necessary concerns. In this experiment, a sample is excited with a short laser pulse and the resulting transient fluorescence recorded. A short laser pulse is defined as a pulse with a duration that is short when compared with the transfer times and decay times of the system being studied; therefore, we can approximate the excitation process as a delta-function that produces a random distribution of excited ions. For experiments where pulses of comparable duration to the relevant time scales of the system, the relations derived in this section and the following section can be integrated with respect to time to produce the proper transient[63]. For now, we restrict our discussion to low excitation densities.

With this restriction, the total decay probability for a donor ion in an excited state separated from an acceptor by $\vec{r}_{ij}$ is given by

$$P_{ij} = \left(\frac{1}{\tau_0} + f(\vec{r}_{ij})\right), \tag{2.3.2}$$

where τ_0 is the intrinsic lifetime of the donor manifold material as measured in a singly-doped material with low concentrations of ions and $f(\vec{r}_{ij})$ is a function describing the energy transfer probability between the two ions.

We now separate out the intrinsic decay probability and also restrict ourselves to only one interaction process to find the dynamics due to energy transfer. This is possible due to the linear nature of these process; the solutions for each interaction can be found separately and then added to produce a total solution once we have found the partial

---

[63] N. Krasutsky and H. W. Moos, "Energy transfer between the low-lying energy levels of Pr3+ and Nd3+ in LaCl3", Phys. Rev. B, V8, N3, (1973), P1010.

solutions[64]. Considering only one interaction mechanism, the total transfer probability for an ion i can be expressed as

$$P_i = \sum_k^{N_a} f(\bar{r}_{ik}), \tag{2.3.3}$$

where the index k represents a summation over the number of acceptors (N_a). The transfer dynamics of the donor ion now appear as

$$\rho_i(t) = \prod_k^{N_a} \exp\left(-tf(\bar{r}_{ik})\right). \tag{2.3.4}$$

Now, we wish to average this relation over the different donor environments to find the experimentally observable transient,

$$\bar{\rho}_i(t) = \frac{1}{N_d} \sum_i^{N_d} \prod_k^{N_a} \exp\left(-tf(\bar{r}_{ik})\right). \tag{2.3.5}$$

Here we have the total energy transfer dynamic; not surprisingly, the resulting average is a summation of exponential decays containing all possible combinations of transfer and decay rates. This relationship will in principle describe the energy transfer dynamics accurately if the distribution of ions and the interactions are known. However, this explicit expression is not useful as this information is usually lacking; therefore, it is useful to approximate this relation in order to get a understanding of the system that can be compared with physical measurements. Using the simple approach outlined by Cellarius[65], it can be shown that Eq. 2.3.5 can be transformed to

$$\bar{\rho}_i(t) = \prod_k^{N_a} \int_0^{\infty} 4\pi r^2 dr \exp(-tf(r)) = \left[\int_0^{\infty} 4\pi r^2 dr \exp(-tf(r)) \right]^{N_a}. \tag{2.3.6}$$

To develop Eq. 2.3.6 from Eq. 2.3.5, only two approximations were required: (1) that the distributions of donors and acceptors is completely random and can be described

---

[64] See, for example, C.H. Edwards, Jr. and D.E. Penney, Elementary Differential Equations with Applications, Prentice-Hall Englewood Cliffs, (1985).

[65] R. A. Cellarius, "Excitation Energy Transfer in Systems of Many Molecules," Photochemistry and Photobiology, V6, (1967), P91.

with a constant density, and (2) that the interaction depends only on distance, not orientation. Thus, we have approximated the discrete structure of a crystal as amorphous. Many different methods of approximating Eq. 2.3.5 exist and will be discussed shortly.

To proceed further, we must know the nature of the interaction. If we assume an interaction of the form $W = C/r^s$, (the appropriate form for the multipole expansion), it can be shown that the dynamics can be expressed as

$$I(t) = I_o \exp\left(-\frac{t}{\tau_0} - \frac{4\pi}{3}\Gamma\left[1-\frac{3}{s}\right]N_a(Ct)^{3/s}\right), \tag{2.3.7}$$

where s=6 for dipole-dipole, 8 for quadrupole-dipole, etc. and Γ is the gamma function. Here we have added the intrinsic lifetime, τ_0, to produce the final solution. The various energy transfer processes can be included by simply adding terms in the exponential. The exchange interaction can also be expressed in this manner[19].

Eq. 2.3.6 relies on two major approximations. The first approximation (constant spatial density) can be partially removed. Here we have approximated the distribution of ions as a constant density, where $\rho(r)=\rho_0 4\pi r^2$ and ρ_0 is constant. In actuality, $\rho(r)$ is determined by the lattice sites in the crystal structure and is a discrete function. As the transfer rates are largest at small distances, the first obvious correction is to restrict the minimum transfer distance to be the distance to nearest neighbor, (R_0). This can be accomplished by changing the lower limit on the integral of Eq. 2.3.6 from zero to the minimum transfer distance. With this correction, Eq. 2.3.7 becomes[66]

$$I(t) = I_o \exp\left(-\frac{t}{\tau_0} - \frac{4\pi}{3}\Gamma\left[1-\frac{3}{s}\right]N_a(Ct)^{3/s}\left(\frac{\exp[-W_0 t]}{(W_0 t)^{3/s}} + \mathrm{Erf}\left[(W_0 t)^{3/s}\right]\right)\right), \tag{2.3.8}$$

where Erf is the error function and $W_0 = C/R_0^s$ is the transfer rate for transfer to the nearest neighbor.

A more rigorous correction can be obtained by summing over the discrete lattice sites. This procedure is equivalent to using Eq. 2.3.5 with the assumption of isotropic transfer probabilities and has been applied successfully in low concentration samples. A final refinement to this solution would be to lift the second approximation used to generate Eq. 2.3.7 and to drop the approximation that the transfer probability is

---

[66] D. S. Knowles, "Energy Transfer Under Strong Pumping in High Concentration Rare Earth Doped Laser Crystals", PhD dissertation, MIT, Sept 1991.

independent of the relative orientation of the sites, which in effect is simply using Eq. 2.3.5. Approximations which include the effects of the differing relative orientations between sites without the use of Eq. 2.3.5 are possible, but a rigorous derivation has not been done to date (or at least not published). For energy transfer processes in anisotropic materials such solutions are desirable; we will return to this topic in Chapter 7.

Although many exact solutions are possible for a variety of different interactions, in practice these are not useful due to the similarity of the dynamics for the interactions. Any measured dynamic will be a sum of the different dynamics and can be quite complicated to interpret. Although it may appear to be possible to sort out the different processes by using higher concentration samples, this is not as straight forward an approach as it may appear. Transfer processes that can be described with the above model are generally referred to as "static" energy transfer processes in the literature. The model just derived is only applicable for low concentrations of donors; at higher concentrations other processes further complicate the interpretation of energy transfer measurements.

2.4. Migration

As donor concentrations increase, a second energy transfer process can occur which will effect the measured donor-acceptor transfer dynamics. Excitations can be transferred from donor to donor as well as from donor to acceptor. These donor-donor interactions complicate the analysis of data by allowing an excitation to move or "migrate" among the donor ions before transferring to an acceptor or decaying. This process partially averages the different local environments of each donor ion as an excitation can sample the environment of each donor. In the limiting case where donor-donor transfer rates are much greater than donor-acceptor transfer rates, the decay of the donor will become a simple exponential as the donor ions see only one effective transfer rate, i.e.[67]

$$I(t) = I_0 \exp(-W_{tot} t), \text{ where } W_{tot} = W_{ma} + {}^{1}\!/_{\tau_0}. \qquad (2.4.1)$$

Here, W_{tot} is the total decay rate seen by manifold and W_{ma} is the migration assisted energy transfer rate. This case is often seen at high concentrations of donors - a rough lower limit on the concentration is ≈10-15% in most rare-earth doped materials.

---

[67] For a quick review, see [19]. For a thorough discussion, see W.J.C. Grant, "Role of Rate Equations in the Theory of Luminescent Energy Transfer," Phys. Rev. B, V4, N2, (1971), P648.

The situation at intermediate concentrations is interesting as the decay dynamic contains elements of both static and migration-assisted energy transfer. In this situation, donors with nearby acceptor ions decay by static energy transfer (no migration before transfer), but donors with far-lying acceptors will transfer their excitations to other donors before transferring to an acceptor. Under these circumstances, the decay can be described as

$$I(t) = I_0 \exp\left[-W_{tot}t - B\sqrt{t}\right] \qquad (2.4.2)$$

for the case of dipole-dipole coupling. With a mixed decay such as this, it is possible to find the interaction micro-parameters for not only C_{da}, but also C_{dd}.

A great deal of theoretical effort has been devoted to the proper way to extract C_{dd} from the migration assisted transfer rate[68]. The general approach is to model the migration as a random walk problem with complications. The complications which must be considered are the following:

(1) Steps taken in different directions are of different sizes and have different probabilities of occurring.

(2) "Long" steps can be taken where the excitation hops to a second or third nearest neighbor due to the nature of the interaction.

(3) For most concentrations, the sites are randomly occupied. This means that the random walk occurs on a disordered lattice--some steps are not allowed.

(4) Other interactions can enter the problem -- for very short distances, exchange or higher-order multipole interactions may be important, while for longer distances dipole-dipole coupling will be the predominant mechanism causing transfer to occur.

The standard approach is to model the problem as a diffusion process[69]. The migration assisted transfer rate is then given by

$$W_{ma} = \frac{dn}{dt} = -D\nabla^2 n - n\sum_i \frac{C_{da}}{\left|\vec{r} - \vec{r}_i\right|^6}. \qquad (2.4.3)$$

With a few assumptions this relation can be solved to yield

$$W_{ma} = 4\pi N_a D\rho. \qquad (2.4.4)$$

---

[68] See, for example, H. C. Chow, and R. C. Powell, "Models for energy transfer in solids," Phys. Rev. B, V21, N9, (1980), P3785.

[69] See, for example, M. Yokota and O. Tanimoto, "Effects of diffusion on energy transfer by resonance", J. Phys. Soc. of Japan, V22, N3, (1967), P779.

Here, ρ is a physically significant length scale defined to be the characteristic distance where the average time required to directly transfer is equal to the time required to reach the acceptor by diffusion. It can be shown that the migration assisted transfer rate for this model can be expressed as

$$W_{ma} = kN_aN_dC_{da}^{1/4}C_{dd}^{3/4}, \qquad (2.4.5)$$

where k is dependent on the details of the model[70]. Different approximations used will lead to different values of k, but the general form remains the same. Implicit in this model is the assumption that transfer to the acceptor can occur from anywhere. This implies that C_{da} is larger that C_{dd}.

Another model has been developed by Burshtein[71] which may be appropriate for situations where the probability of donor-donor transfer is much greater than that for donor-acceptor transfer. In this model the migration process is still diffusive, but donor-acceptor transfer is restricted to occur in only a small volume around the acceptor. In the limiting case, a diffusing excitation will pass through this volume in only one step; the transfer to the acceptor must occur before the excitation steps again. For dipole-dipole transfer, the migration-assisted transfer rate will be

$$W_{ma} = \frac{2\pi}{3}N_a\left(\frac{C_{da}}{\tau_s}\right)^{1/2}. \qquad (2.4.6)$$

Here, τ_s is the average step time. Applying similar relations as used to generate Eq. 2.4.5, this relation becomes

$$W_{ma} = k'N_dN_aC_{da}^{1/2}C_{dd}^{1/2}, \qquad (2.4.7)$$

where k' is again a constant dependent on the exact details of the modeling.

These two models are the limiting cases for migration-assisted energy transfer. In the diffusion model, donor-acceptor transfer can occur from any donor ion, while for the hopping model transfer will only occur when an excitation is within a certain distance of an acceptor. We have solved the above models for the case of dipole-dipole coupling.

---

[70] A. I. Burshtein, "Concentration quenching of noncoherent excitation in solutions," Sov. Phys. Usp., V27, N8, (1984), P579.

[71] A. I Burshtein, "Hopping Mechanism of Energy Transfer," Sov. JETP Phys., V35, N5, (1972), P882.

The relationships for higher order multipole interactions and the exchange interaction can also be derived. It must be mentioned now that many derivations in the literature neglect the effect of back transfer between the donor ions. Burshtein has shown that including donor back-transfer leads to a change in the constant k predicted by the modeling[70]. As of the present, no one has analyzed a system for which there is substantial back-transfer from the acceptor ions, which is the appropriate case for Tm and Ho.

We have presented these models as they are necessary for understanding some of the processes affecting our experimental results. These processes can also lead to deviations from the predictions of the theory we will present in Chap. 3. We will return to both static transfer and migration-assisted transfer in the discussion of Chap. 7.

2.5. Einstein relations and their generalizations.

We now shift our focus from energy transfer theory to a second area of theory which we will use repeatedly in the rest of this document. We start with a review of the basic Einstein relations for spectroscopic transitions. Einstein's model is illustrated in Fig. 2.5.1.

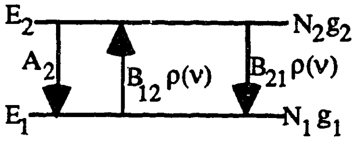

Figure. 2.5.1. Diagram of relevant processes for two level system.

In this model, N_1 and N_2 are the populations of the energy levels, g_1 and g_2 are the degeneracies, E_1 and E_2 are the energies, and $\rho(\nu)$ is the density of radiation at the frequency ν. A_2 is the probability per unit time that an ion in state 2 would spontaneously decay to state 1 by the emission of a photon of energy $h\nu$. $B_{12}\rho(\nu)$ and $B_{21}\rho(\nu)$ are the probabilities per unit time that a transition will occur between the levels 1 and 2 due to the interaction with the radiation field. By using Planck's distribution for black body radiation and applying detailed balance arguments to the above system, it can be shown[72] that

$$\frac{A_2}{B_{21}} = \frac{8\pi\upsilon^2 h\upsilon}{c^3}, \tag{2.5.1}$$

and

$$B_{21} = \frac{g_1 B_{12}}{g_2}. \tag{2.5.2}$$

The existence of B_{21} (the stimulated emission coefficient) was surmised by Einstein[73] and is the basis behind laser operation. By considering the amount of energy absorbed as a beam of light passes through a material, the B coefficients can be related to the cross-sections (σ) for absorption and stimulated emission. The relationship is

$$\sigma_{21} = \frac{h\upsilon B_{21}}{c}, \tag{2.5.3}$$

---

[72] W. Koechner, Solid-State Laser Engineering, 2nd Ed., Springer-Verlag, New York, 1985.

[73] A. Einstein, Phys. Zeits. V18, (1917), P121.

and is presented here as it can be easily related to measurable quantities.

Both the A and the B coefficients were shown to arise from the same basic mechanism by Dirac, who demonstrated that the process of spontaneous emission could be modeled as stimulated emission triggered by a virtual photon[74]. Thus, the prefactor in Eq. 2.5.1 can be viewed as the density of spatial modes for photons with frequency ν. An elegant test of this relationship in optical materials has been provided by Christensen and Jenssen[75].

In an actual material, the levels in Fig. 2.5.1 are not well-defined single energy states; rather they are generally manifolds composed of several energy levels. McCumber[76,77] generalized the Einstein relations to account for the splitting of the manifolds. We briefly outline the physical logic of their derivations here as we will refer to this later.

Let us start with a simple model of interacting levels. Assume that we initially have a system consisting of energy levels which can be grouped into two manifolds (m,n). This system is illustrated schematically in Fig. 2.5.2.

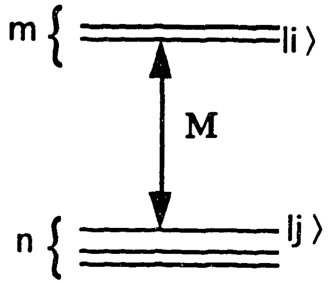

Figure 2.5.2. Multiply-split manifolds.

The m and n manifolds are respectively composed of individual levels i and j. A state in the upper manifold will be represented by $|i\rangle$, where the label m is understood. We assume that there is an interaction M which leads to transitions between levels of the two manifolds. We want to generalize the relationship given by Eq. 2.5.2 to transition rates between the two manifolds.

---

[74] See, for example, J.J. Sakurai, Advanced Quantum Mechanics, Addison-Wesley, Redwood City, 1967.

[75] H. P. Christensen, D.R. Gabbe, and H.P. Jenssen, "Fluorescence lifetimes for neodymium-doped yttrium aluminum garnet and yttrium oxide powders," Phys. Rev. B, V25, N3. (1982), P1467.

[76] D. E. McCumber, "Theory of Vibrational Structure in Optical Spectra of Impurities in Solids. I. Singlets," J. Math. Phys., V5, N2, (1964), P221.

[77] D. E. McCumber, "Theory of Vibrational Structure in Optical Spectra of Impurities in Solids. II. Multiplets," J. Math. Phys., V5, N4, (1964), P508.

We assume that there is a mechanism which brings about equilibrium between the levels within a manifold on a time scale much faster than the transition rate between manifolds. Therefore, we can assume that the levels in each manifold are populated in some sort of equilibrium distribution such that the population of the i^{th} level can be expressed as $N_m f_i$, where N_m is the total number of ions whose states can be grouped into the m manifold and f_i (the occupation factor) is the probability that such an ion is in a state i. This requires a mechanism which can cause intra-manifold transitions and interacts with the ions much more often than the ions make transitions out of manifold. This mechanism is generally assumed to be the coupling of the electronic states to phonons.[78]

Using Fermi's Golden Rule, we find the rate to be

$$r(\omega) = \frac{2\pi}{\hbar} \sum_{i,j} |M_{ij}|^2 \delta(\varepsilon_i - \varepsilon_j - \hbar\omega) \rho(\omega), \qquad (2.5.4)$$

where $\rho(\omega)$ is the joint density of states, $\hbar$ is Planck's constant, $r(\omega)$ is the frequency-dependent transition rate, and M_{ij} is the matrix element for the interaction between the states i and j. $|M_{ij}|^2$ is the probability of a transition between the i and j states[79]. Here, ε_i and ε_j are the energies of states i and j, respectively. The delta function is necessary for energy conservation.

We now concentrate on the relationship between the transition probability per unit time for an i -> j transition to that for a j -> i transition. The rate of transitions between states is directly proportional to the probability of the transition occurring and to the density of states able to make the transition. If we identify the density of states for a i->j transition to be $f_i N_m$, then we can express the transition probability per unit time as

$$p_{ji} = \frac{2\pi}{\hbar} |M_{ji}|^2 f_i. \qquad (2.5.5)$$

This expression is analogous to $B_{ji}\rho(\nu)$ in Einstein's model. Taking the ratio of the i->j and j->i transition probabilities, we find

---

[78] D. E. McCumber, "Einstein relations connecting broadband emission and absorption spectra", Phys. Rev., V136, (1964), PA954.

[79] See, for example, K. Gottfried, Quantum Mechanics I. Fundamentals, Addison-Wesley, Redwood City, 1989.

$$\frac{p_{ji}}{p_{ij}} = \frac{f_i}{f_j}\frac{\langle M_{ij}\rangle^2}{\langle M_{ji}\rangle^2} = \frac{f_i}{f_j}. \tag{2.5.6}$$

Assuming $|M_{ij}|^2 = |M_{ji}|^2$, we can cancel these matrix elements and find that the ratio of transition rates between any two levels is merely the ratio of the level's occupation factors. If we assume that the distribution of excitations between the levels within a manifold is a simple Boltzmann distribution, the occupation factors can be expressed as

$$f_i = \frac{e^{-\beta\varepsilon_i}}{z_m}, \tag{2.5.7}$$

where β is 1/kT (k being the Boltzmann constant and T being the system temperature), ε_i is the energy of the ith level, and z_m is the partition function of the m manifold. We can now say

$$\frac{p_{ji}}{p_{ij}} = \frac{f_i}{f_j} = \frac{e^{-\beta\varepsilon_i}}{z_m}\frac{z_n}{e^{-\beta\varepsilon_j}}. \tag{2.5.8}$$

If we identify $e^{-\beta\mu}$ as z_m/z_n[80] (μ being the chemical potential), we have

$$\frac{p_{ji}}{p_{ij}} = e^{-\beta[(\varepsilon_i-\varepsilon_j)-\mu]} = e^{-\beta[\hbar\omega-\mu]} \tag{2.5.9}$$

where $\hbar\omega=(\varepsilon_i-\varepsilon_j)$. Here, $\hbar\omega$ also represents the amount of energy absorbed or emitted during the transition. The above relationship depends upon only upon μ and $\hbar\omega$; it is independent of the initial and final state energies. As only the energy difference is significant in this relationship, it is straight-forward to generalize this relationship for transition probabilities between specific states to a relationship for the entire manifold. We can say,

$$\frac{p_{nm}(\omega)}{p_{mn}(\omega)} = \sum_{i,j} e^{-\beta[(\varepsilon_i-\varepsilon_j)-\mu]}\delta(\varepsilon_i - \varepsilon_j - \hbar\omega) = e^{-\beta[\hbar\omega-\mu]}. \tag{2.5.10}$$

---

[80] See, for example, F. Reif, Fundamentals of Statistical and Thermal Physics, McGraw-Hill, New York, 1965.

If we let **M** be the electric dipole operator, then we can identify p_{nm} as proportional to the emission cross-section and p_{mn} as proportional to the absorption cross-section. In this case we have

$$\frac{\sigma_{em}(\omega)}{\sigma_{ab}(\omega)} = e^{-\beta[\hbar\omega-\mu]}, \tag{2.5.11}$$

which is one of McCumber's basic relationships. This relationship has been confirmed and extended by many authors[81, 82]

The relationship between transition probabilities given in Eq. 2.5.11 rests on two assumptions: (1) that the probability of making an ion in state i making a transition to state j is the same as an ion in state j making a transition to state i, i.e, $|M_{ij}|^2 = |M_{ji}|^2$ holds; and (2) that the population of the initial level can be described with a occupation factor f_i determined from the energy levels of the manifold.

2.6. Phonon-Electron Interactions.

Up to now, we have assumed a static crystal lattice in our theory review, with the exception of our reliance on phonons for manifold thermalization in the derivation of McCumber's relations. In reality, the lattice is not static but dynamic; in the following sections, we show how phonon-ion interactions can affect our previous results. We start by finding the wavefunction for a coupled phonon-photon, or "vibronic", state.

We follow the general approach outlined by Cohen and Moos[83] and model the ion-phonon interaction as a perturbing interaction on the ionic wavefunctions. Using standard perturbation theory, we can find the perturbed wavefunctions and use them to calculate various quantities. Modeling the problem in this manner is justified as the rare-earths interact only weakly with the lattice.

We start by expressing the Hamiltonian for the entire crystal. Let H_0 be the unperturbed Hamiltonian for the ion, and H_{vib} be the unperturbed Hamiltonian for the crystal. H_0 is taken to be $H_{free}+V_0$, where H_{free} is the Hamiltonian for the ion's electrons

---

[81] J. C. Walling, O. G. Peterson, H. P. Jenssen, R. C. Morris, and E. W. O'Dell, "Tunable Alexandrite Lasers," IEEE J. Quant. Elect., V16, N12, (1980), P1302.

[82] Y. B. Band and D. F. Heller, "Relationships between the absorption and emission of light in multilevel systems," Phys. Rev. A, V38, N4, (1988), P1885.

[83] E. Cohen and H. W. Moos, "Vibronic Transitions of Hexagonal Rare-Earth Trichlorides. I. Pr^{3+} and Nd^{3+} in $NdCl_3$," Phys. Rev., V161, N2, (1967), P258.

in free space (discussed in the introduction) and V_0 is the contribution from the static crystal field. The unperturbed Hamiltonian is $H_{tot}=H_0+H_{vib}$; $H_0|\psi_i\rangle=E_i|\psi_i\rangle$ and $H_{vib}|\phi_x\rangle=E_x|\phi_x\rangle$ define the unperturbed eigenstates and eigenenergies. These wavefunctions for the system are separable if there is no coupling between electronic energy states and the lattice, and the complete state of the system (Ψ) can be expressed as $\Psi_{ix}=\psi_i\phi_x$. Now, including the coupling between the states, the total Hamiltonian becomes

$$H_{tot}=H_0+H_{vib}+H_P, \tag{2.6.1}$$

where H_P represents the electronic-phonon interaction responsible for the coupling.

H_P will produce a new set of eigenstates (χ_{ix}) by mixing the original states. Using non-degenerate time-independent perturbation theory[84], these can be expressed as

$$|\chi_{ix}\rangle=|\Psi_{ix}\rangle+\sum_{\substack{j\neq i\\ r\neq x}}\frac{|\Psi_{jr}\rangle\langle\Psi_{jr}|H_P|\Psi_{ix}\rangle}{E_{ix}-E_{jr}}. \tag{2.6.2}$$

H_P can be approximated as

$$H_P=\frac{\partial V}{\partial x_i}dx_i+\frac{\partial V}{\partial x_i}\frac{\partial V}{\partial x_j}dx_i dx_j+\cdots\approx\frac{\partial V}{\partial x_i}dx_i=\sum_q v_q\Omega_q, \tag{2.6.3}$$

where we have dropped the higher-order terms of the expansion and expressed ionic displacements as summations over phonon modes Ω_q. Here v_q is the coupling coefficient for the phonon mode. Expressing ϕ_x in terms of phonons, we find

$$|\phi_x\rangle=\prod_q|q,n_q^x\rangle. \tag{2.6.4}$$

Here $|q, n_q^x\rangle$ is the state ket for a mode q with n_q^x phonons. n_q^x is the number of phonons in mode q when the crystal is in a state ϕ_x. From now on we express $|\psi_i\rangle$ as $|i\rangle$ for notational convenience.

---

[84] See, for example, K. Gottfried, Quantum Mechanics I, Fundamentals, Addison-Wesley, Redwood City, 1989.

With these relations, it can now be shown that the wavefunction for a "vibronic" state can be expressed as

$$\left|\chi_{ix}\right\rangle = |i\rangle \prod_{q} \left|q, n_q^x\right\rangle + \sum_{\substack{j\neq i \\ q}} \sqrt{\frac{\hbar}{2\omega_q}} |j\rangle\langle j|v_q|i\rangle \left[\frac{\sqrt{n_q^x+1}\left|q, n_q^x+1\right\rangle}{E_i - E_j - \hbar\omega_q} + \frac{\sqrt{n_q^x}\left|q, n_q^x-1\right\rangle}{E_i - E_j + \hbar\omega_q} \right] \prod_{q'\neq q} \left|q', n_{q'}^x\right\rangle . \qquad (2.6.5)$$

Here, $\hbar\omega_q$ is the energy of the phonon in mode q. We now have an expression for the vibronic wavefunction corresponding to the unperturbed electronic state ψ_i coupled to the lattice state ϕ_X. This expression is similar to that obtained by Cohen and Moos, with the exception that their relation is for only one phonon in a mode q and no phonons in the other modes; while our expression is for n_q phonons in each mode q. As can be seen from Eq. 2.6.5, the wavefunction for a vibronic state is the original wavefunction plus a correction term which couples the original wavefunction to the other states and is weighted by the phonon mode occupation number.

2.7 Multi-phonon Relaxation.

Phonons can induce transitions between electronic states as they can intermix these states. As was mentioned earlier, the electron-phonon interaction is thought to cause the equilibrium distribution between the energy states within a manifold to develop. Just as the intra-manifold relaxation and thermalization can occur because of multiple-phonon interactions, so can relaxation between different manifolds. This process is often called non-radiative relaxation as excitations deposited in a manifold can relax to lower-lying manifolds without photon emission via this mechanism. This is the reason that many manifolds of rare-earth ions do not fluoresce when doped into solids[85].

The process can be modeled theoretically by retaining the full expression for the electron-phonon coupling interaction H_p (Eq. 2.6.3) and using Fermi's golden rule. However, detailed theoretical models have had limited success; and in practice a simple

---

[85] L. A. Riseberg, H. W. Moos, and W. D. Partlow, "Multiphonon Relaxation in Laser Materials and Applications to the Design of Quantum Electronic Devices," IEEE J. Quant. Elect., V4, N10, (1968), P609.

phenomenological approach based on Fermi's golden rule is used to determine multiphonon relaxation rates from measured parameters.

The general logic can be shown with a single phonon energy model. Here the energy difference is bridged by multiple phonons of the same energy $p(\hbar\omega_i) = \Delta E$, where p is the number of phonons. With this approximation, it can be shown that the transition rate can be expressed as[86]

$$W(T) = W_0(n+1)^p, \qquad (2.7.1)$$

where W_0 is the spontaneous transition rate at 0 K ($W(0)=W_0$), n is the occupation number. Substituting in the Bose-Einstein average for n, we find

$$W^p(T) = W_0\left[\frac{e^{\beta\hbar\omega}}{e^{\beta\hbar\omega}-1}\right]^p \qquad (2.7.2)$$

A plot of this relationship is shown in Fig. 2.7.1.

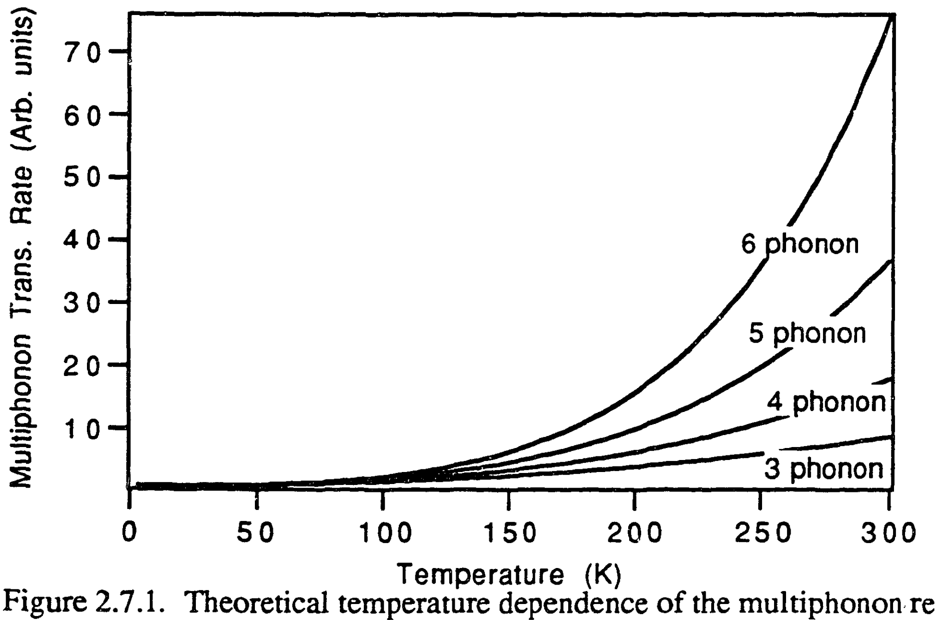

Figure 2.7.1. Theoretical temperature dependence of the multiphonon relaxation rate from Eq. 2.7.2. The energy gap has been held constant.

---

[86] H. W. Moos, "Spectroscopic Relaxation Processes of Rare Earth Ions in Crystals", J. Lumin, V1, N2, (1970), P106.

It can be seen that the behavior at higher temperatures depends on the order of the process. This model can be extended to multiple levels, but in practice Eq. 2.7.2 is sufficient for a qualitative description of the temperature dependence of the multiphonon relaxation rate. Studies of the temperature dependence of the multiphonon rate are often used to identify the order of process.[87]

The success of this simple approach depends on several things. First of all, the coupling between the ion and the lattice must be relatively weak. This makes the resulting vibronic spectrum be relatively smoothly varying -- no pronounced spikes or intense absorptions. When the smoothly varying effective density of phonon states for coupling is convolved several times to account for the multiphonon nature of the problem, most of the details are averaged out. The energy gap between the multiplets must be large enough that the process can be described as multi-phonon so that the averaging can occur.

The energy gap dependence of the multiphonon relaxation rate has also been treated and been shown to be

$$W^p = A\varepsilon^p, \tag{2.7.3}$$

for a pth order process. Here, A is a constant and ε is the ratio of the rate for a pth order process over a p-1th order process. $\varepsilon = W^p/W^{p-1}$ and is indicative of the speed of convergence of the perturbation expansion used to generate Eq. 2.7.1,

It has been observed that the lowest order process consistent with energy conservation is generally dominant[86]. In the limiting case, Eq. 2.7.2 and Eq. 2.7.3 can be combined to yield

$$W = Ce^{-\alpha\Delta E}. \tag{2.7.4}$$

The above relation has been experimentally confirmed for a number of systems satisfying the required conditions. However, when a system displays very strong coupling to some phonon modes, this relationship will not work quite as well[15]. For this situation, the energies of these phonons must also be considered and the analysis becomes more complicated.

---

[87] See, for example, E.D. Reed, Jr. and H.W. Moos, "Multiphonon Relaxation of Excited States of Rare-Earth Ions in YVO_4, $YAsO_4$, and YPO_4," Phys. Rev. B, V8, N3, (1973), P980.

2.8 Non-Resonant Energy Transfer.

Just as multi-phonon relaxation can occur when an ion makes an inter-manifold transition by emitting the excess energy as phonons, so can energy transfer. It is possible to observe energy transfer even in situations where the overlap integral of Eq. 2.2.3 appears to be vanishingly small. Miyakawa and Dexter[88] have used the method described above to derive an analog of Eq. 2.7.4 for energy transfer. They found the non-resonant energy transfer rate to be

$$W_{et} = C' e^{-\beta \Delta E}, \tag{2.8.1}$$

where β is related to the α of Eq. 2.7.4 by the relationship

$$\beta = \alpha - \frac{1}{\hbar \omega_i} \ln\left(1 + \frac{g_b}{g_a}\right). \tag{2.8.2}$$

Here g_a and g_b are the electron-lattice coupling parameters for ions A and B. Qualitative agreement between this expression and measured energy transfer rates have been obtained, but the exact relationship between α and β has not been confirmed.[89]

2.9 Phonon-assisted transitions

Earlier we modeled the ion-phonon interaction as a perturbation and found the first order correction to the electronic wavefunctions. We will now use these wavefunctions to calculate the resulting energy level shifts and the transition probabilities between the perturbed states. Selected results of this section will not be required until the discussion of Chapter 7, but we present a brief derivation of the pertinent results now so that we will not need to digress in the discussion section of the thesis.

---

[88] T. Miyakawa and D. L. Dexter, " Phonon sidebands, multiphonon relaxation of excited states, and phonon-assisted energy transfer between ions in solids", Phys. Rev. B, V1, N7, (1970), P2961.

[89] For example, contrast the results of N.S. Yamada, S. Shionoya, and T. Kushida, J. Phys. Soc. Japan, V32, (1972), P1577 and H.P. Jenssen in [17].

2.9.1. Energy level shifts due to phonon coupling.

We first examine the change in energy of the state Ψ_{ix} from the electron-phonon interaction. The first order correction to the energy of the system can be expressed as

$$E_{ix}^{(1)} = \sum_{q} \langle i|v_q|i\rangle \langle q, n_q^x| \sqrt{\frac{\hbar}{2\omega_q}} \left(b_q^\dagger + b_q\right) |q, n_q^x\rangle . \tag{2.9.1}$$

Here $b_q^\dagger$ is the phonon creation operator and b_q the phonon annihilation operator. This correction vanishes due to the properties of the creation and annihilation operators.

As the first order correction to the energy vanishes with this approximation, we look to the second-order correction. It can be shown that the second order shift in the energy can be expressed as

$$E_{ix}^{(2)} = \sum_{q} \frac{\hbar}{2\omega_q} \left|\langle i|v_q|j\rangle\right|^2 \left(\frac{n_q + 1}{E_i - E_j - \hbar\omega_q} + \frac{n_q}{E_i - E_j + \hbar\omega_q} \right). \tag{2.9.2}$$

As can be seen, a second-order shift in the energy of a level is theoretically allowed. This shift is dependent upon the phonon population and therefore will be temperature dependent.

2.9.2. Vibronic Transition Probabilities

We now evaluate the matrix element for a photon induced transition between vibronic states in two different cases. We first find the matrix element for a transition between vibronic states with no net change in the number of phonons, following which we examine a transition which involves phonon emission or absorption.

In the first case, an interaction M causes an ion to make a transition between vibronic states χ_{ix} and χ_{kx} with no net emission of phonons. To find the probability of a transition occurring, we start by finding the matrix element for the process, which is

$$\langle \chi_{kx}|M|\chi_{ix}\rangle = \langle k|M|i\rangle + \sum_{\substack{j,j' \\ q}}^{\substack{j\neq k, \\ j'\neq i}} \frac{\hbar}{2\omega_q} \langle k|v_q|j\rangle \langle j|M|j'\rangle \langle j'|v_q|i\rangle F(E_k, E_i, j, j', q), \tag{2.9.3}$$

where

$$F(E_k,E_i,j,j',q)=\left[\frac{n_q^x+1}{(E_k-E_j-\hbar\omega_q)(E_i-E_{j'}-\hbar\omega_q)}+\frac{n_q^x}{(E_k-E_j+\hbar\omega_q)(E_i-E_{j'}+\hbar\omega_q)}\right].$$

Dropping F(E_i, E_k, j, j', q) for now, we can express the transition probability p_{ki} as

$$p_{ki}^{n_q,n_q}\propto|\langle\chi_{kx}|M|\chi_{ix}\rangle|^2=|\langle k|M|i\rangle|^2. \qquad (2.9.4)$$

To first order, the probability for transitions between vibronic states with phonon number conservation is unchanged from that for purely electronic states.

We now examine the transition probability when the electronic state of an ion changes from i to k with the emission of a phonon into mode q. The situation to be discussed is illustrated schematically in Fig. 2.9.1.

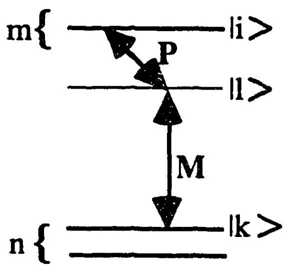

Figure 2.9.1. Energy diagram for a phonon-assisted transition.

In Fig. 2.9.1, i is the initial electronic state, k is the final state, and l can be thought of as an intermediate state. Starting with the matrix element between the vibronic states χ_{ix} with n^x_q phonons in mode q and χ_{kr} with n^x_q+1 phonons in mode q, it can be shown that the probability for a transition is

$$p_{ki}^{n_q+1,n_q}=\frac{\hbar}{2\omega_q}(n_q+1)\left[\sum_{j\neq i}\frac{|\langle k|M|j\rangle\langle j|v_q|i\rangle|^2}{(E_i-E_j+\hbar\omega_q)^2}+\sum_{j\neq k}\frac{|\langle k|v_q|j\rangle\langle j|M|i\rangle|^2}{(E_k-E_j-\hbar\omega_q)^2}\right], \qquad (2.9.5)$$

where we have assumed that no degeneracies exist between the phonon-assisted transition energy and other energy levels. Here, v_q is the phonon coupling constant between the electronic states. The terms of Eq. 2.9.5 correspond to two different processes. The first term corresponds to the process where an ion in state i emits a phonon and then makes an electronic transition between manifolds; while the second term corresponds to a situation where the ion first makes the transition and then emits a phonon.

This interaction is reciprocal, i.e., the probability for an ion in electronic state i with n phonons in mode q to make a transition to electronic state k with n+1 phonons in mode q is equal to that for an ion in electronic state k with n+1 mode q phonons to make a transition to electronic state i with n mode q phonons. In other words, $p_{ki}^{n_q+1,n_q} = p_{ik}^{n_q,n_q+1}$. It is therefore tempting to say that the transition probabilities for a phonon assisted transition between electronic states i and k are equal.

However, this is not true. The above relationship is for a certain number of phonons in the mode q, namely n when the ion is in state i and n+1 when the ion is in the state k. However, for incoherent processes such as these, the phonon population will be in equilibrium and the number of phonons initially in the mode q will be independent of the ionic state. In that case, the probability for a transition between i and k coupled with a q phonon emission will be proportional to n_q+1, while the probability for the reverse process will be proportional to n_q. The relationship between transition probabilities is

$$p_{ik}^{n_q-1,n_q} = \frac{n_q}{n_q+1} p_{ki}^{n_q+1,n_q}. \tag{2.9.6}$$

This case is clearly seen in low temperature emission and absorption cross-sections, where reciprocal transitions involving phonon absorption are not seen although the transitions are clearly observable when phonon emission occurs. McCumber has included vibronic transitions in his theory by modeling the manifold as a continuous distribution of vibronic energy levels created by the phonon distribution. By substituting the Bose-Einstein average for n_q, it can be shown that the relation between the transition probabilities given in Eq. 2.9.6 becomes $p_{ik}^{n_q-1,n_q} = e^{-\beta\hbar\omega_q} p_{ki}^{n_q+1,n_q}$. Using this relationship, it can be shown that McCumber's relation should hold for phonon-assisted transitions[77]. A large amount of experimental evidence in systems with substantial electron-phonon interactions would seem to support this approximation[81, 90].

This relationship is valid except when there is a match between the phonon energies and the energy difference between the electronic states i and j. In this case, the denominators of Eq 2.9.3 and Eq. 2.9.5 are undefined. These degeneracies could affect the relationship between the transition probabilities. We will return to this topic in the discussion of Chap. 7.

---

[90] D. E. McCumber, "Theory of phonon-terminated optical masers", Phys. Rev., V134, (1964), PA299.

3. Implications of Current Theories

Now that we have reviewed the theory which we will use throughout the thesis, we would like to examine what these theories imply for the equilibrium distribution of excitations between the excited state manifolds of different ions. Additionally, we will examine the implications of these theories for the energy transfer parameters.

We start with a review of the problem, and then present what has in the past been assumed to be the correct expression for the excitation distribution between two interacting excited state manifolds. We then establish a connection between the relations of energy transfer theory and McCumber's generalization of the Einstein relations, and show that the distribution of excitations between excited rare earth ions differs from that generally assumed as a natural consequence of the link between these two theories. In these derivations we develop useful relationships between experimentally measurable quantities; these relationships can be used to confirm and simplify the experimental process necessary for determining the equilibrium distribution. We then use a different approach using only statistical mechanics to rigorously confirm our expression for the distribution. Finally, we discuss the limits of our theory -- basically where and why it may break down or fail to be a complete solution. We start with an overview of the problem.

3.1. Conditions for Equilibrium.

For an equilibrium situation to develop between manifolds of dopant ions, the lifetimes of the manifolds involved must be substantially longer than the transfer times between the manifolds. Additionally, an interaction which causes each transferred excitation to equilibrate within the manifold before transferring a second time is also required. We will use the Tm-Ho system as an example. Not only does this system satisfy the necessary conditions for equilibrium to develop, it also is of great interest to the solid state laser community. For this reason, there is a large amount of data available for comparison.

The typical material for laser diode pumped 2 μm lasers uses Ho as the active ion and Tm as a sensitizer ion. In this system, optical energy at $\approx$800 nm is absorbed by Tm ions, causing the ions to make transitions from the ground state to the $^3H_4$ manifold. Following a cross-relaxation step where one $^3H_4$ excitation is converted to two $^3F_4$ excitations, the excitation is transferred to the Ho $^5I_7$ manifold. Due to the proximity in energy of the Tm $^3F_4$ manifold to the Ho $^5I_7$ manifold, there will also be reverse energy transfer from Ho to Tm. These transfers occur at a high enough rate to ensure that an equilibrium distribution will develop between the $^3F_4$ and the $^5I_7$ manifolds. It has generally been assumed that this distribution can be described by a canonical ensemble of the combined energy levels of the Tm $^3F_4$ and the Ho $^5I_7$ manifolds[45].

We wish to rigorously derive the distribution of excitations between the excited states of the Tm $^3F_4$ manifold and the Ho $^5I_7$ manifold. The model to be used is illustrated in Fig. 3.1.1. For the moment we consider only the lower energy levels of the system.

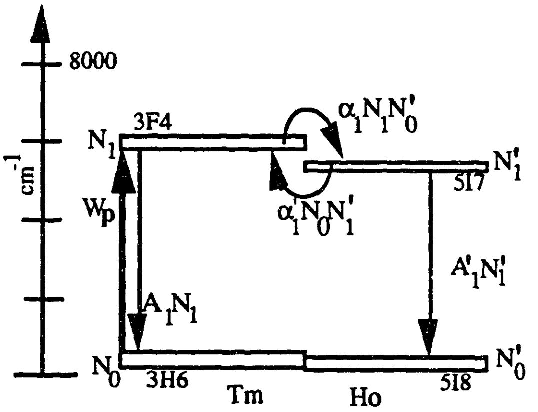

Figure 3.1.1. Simplified sketch of Tm-Ho energy transfer dynamics at low excitation densities.

In this model, A_1 and A'_1 are Einstein A coefficients, and α_1 and α'_1 are the transfer parameters. N denotes a manifold in Tm, while N' denotes a manifold in Ho. Each manifold is actually composed of several different energy levels; N_x is the total population density of manifold x with the populations of all the levels included. It has been established that the levels within each manifold come to thermal equilibrium within ~10^{-10} s[78]. This model can be described with the simple set of rate equations shown below.

$$\dot{N}_0 = -\dot{N}_1$$
$$\dot{N}'_0 = -\dot{N}'_1$$
$$\dot{N}_1 = W_P - A_1 N_1 - \alpha_1 N'_0 N_1 + \alpha'_1 N_0 N'_1$$
$$\dot{N}'_1 = -A'_1 N'_1 + \alpha_1 N'_0 N_1 - \alpha'_1 N_0 N'_1$$

For the concentrations of Tm and Ho typically used in lasers, the transfer probabilities ($\alpha_1 N'_0$ and $\alpha'_1 N_0$) are much larger than the spontaneous emission decay probabilities (A_1 and A'_1). The equilibration time for the two manifolds has been demonstrated to be on the order of 10-100 μs[91, 92] for concentrations of interest (Tm concentrations in the range of 5-6% Tm and Ho concentration in the range of 0.2 to 1.7%) , while the spontaneous emission lifetimes are on the order of 10 ms; together these imply that the transfer rates are much faster than the spontaneous emission loss rates. Therefore, we can say that the $^3F_4$ and $^5I_7$ manifolds are effectively in equilibrium when the rate of transfer between the two manifolds is equal. Mathematically, the equilibrium conditions can be expressed as

$$\alpha_1 N'_0 N_1 = \alpha'_1 N_0 N'_1 \qquad (3.1.1)$$

It follows from Eq. 3.1.1 that

$$\frac{N'_1}{N_1} = \theta \frac{N_{Ho}}{N_{Tm}} \frac{\left(1 - {N'_1}/{N_{Ho}}\right)}{\left(1 - {N_1}/{N_{Tm}}\right)}, \qquad (3.1.2)$$

where

$$\theta = \frac{\alpha_1}{\alpha'_1}. \qquad (3.1.3)$$

Here we neglect the presence of other levels and use the constraints $N_0+N_1=N_{Tm}$ and $N'_0+N'_1=N_{Ho}$ (N_{Tm} and N_{Ho} are concentrations of Tm and Ho in the crystal). θ is the temperature dependent ratio of the $^5I_7$ <-> $^3F_4$ transfer parameters. We have dropped A_1N_1 and $A'_1N'_1$ as these rates are much smaller than the transfer rates. For now we drop the pump rate (W_p) and restrict our discussion to the period immediately following a pump pulse[†]. Thus, if α_1 and α'_1 are known, the distribution at any excitation level can be determined.

A first step in our investigation is the exploration of this problem at low excitation density, i.e., when there are very few excitations stored in the upper state manifolds and we do not have to be concerned with effects such as depletion of the ground states or

---

91 A. Brenier, J. Rubin, R. Moncorge and C. Pedrini, "Excited-state dynamics of the Tm^{3+} ions and Tm^{3+}->Ho^{3+} energy transfers in $LiYF_4$", J. Phys. France, V50, (1989), P1463.

92 G. Armagan, A. M. Buoncristiani, A. T. Inge, and B. DiBartolo, "Comparison of Spectroscopic Properties of Tm and Ho in YAG and YLF Crystals", OSA Proc. on Adv. Sol. State Lasers, V10, Ed. G. Dube and L. Chase, Hilton Head, (1991), P222.

[†] W_p is necessary to excite the system; however we will show that the effects of the pumping process will be neglible (<1%) for our experimental conditions. We return to this term at the end of this chapter when we discuss the applicability of this theory.

upconversion. Under these conditions, we can make the approximation of undepleted ground states and find

$$\frac{N_1'}{N_1} = \theta \frac{N_{Ho}}{N_{Tm}} \frac{\left(1 - N_1'/N_{Ho}\right)}{\left(1 - N_1/N_{Tm}\right)} \cong \theta \frac{N_{Ho}}{N_{Tm}}. \qquad (3.1.4)$$

Here θ is seen to be proportional to the excited state populations at low pump intensities. It must be kept in mind that Eq. 3.1.4 is an approximation and is only applicable at low excitation densities. One common source of errors found in the literature is the neglect of this ground state depletion when performing calculations on this system

3.2. Methods of calculating the θ coefficient.

The correct calculation of θ is the goal of this portion of the research. Various methods have been used to calculate θ and will now be discussed.

3.2.1. Castleberry's Approach

The method generally used to calculate the distribution of excitations between the $^3F_4$ and the $^5I_7$ is a summation over all the energy levels of the excited state manifolds using the canonical distribution. For the Tm-Ho system, this leads to

$$N_1 = \frac{N_{Tm} \sum_i g_i e^{-\beta \varepsilon_i}}{N_{Tm} \sum_i g_i e^{-\beta \varepsilon_i} + N_{Ho} \sum_j g_j e^{-\beta \varepsilon_j}}, \qquad (3.2.1)$$

and

$$N_1' = \frac{N_{Ho} \sum_j g_j e^{-\beta \varepsilon_j}}{N_{Tm} \sum_i g_i e^{-\beta \varepsilon_i} + N_{Ho} \sum_j g_j e^{-\beta \varepsilon_j}}, \qquad (3.2.2)$$

where ε_i and ε_j are, respectively ,the energy of levels in the $^3F_4$ and $^5I_7$ multiplets and g_i and g_j are the degeneracies. Here $\beta = 1/kT$, where k is the Boltzmann constant, and T is the temperature of the sample in Kelvin. This implies

$$\theta = \frac{\sum_{j}^{5I7} g_j e^{-\beta\varepsilon_j}}{\sum_{i}^{3F4} g_i e^{-\beta\varepsilon_i}}. \qquad (3.2.3)$$

Here the terms keep their earlier definitions.

This model was initially suggested by Castleberry[45] and has been used by the majority of authors[†]. This model is presented for comparison with our results due to its widespread use in the field. However, it has never been rigorously derived or experimentally confirmed. Experiment confirmation has been claimed, but in general these experiments have been directed at establishing the existence of equilibrium and have made only rough measurements of the distribution[93].

3.2.2. Chemical Potential Approach.

We will now theoretically develop the description of the distribution. This approach uses results from energy transfer theory[19] and from McCumber's generalization of the Einstein relations[77] which were reviewed in the preceding chapter. We first recall Eq. 3.1.3, where θ was defined to be the ratio of the energy transfer parameters α_1 and α'_1. It can be argued that, for systems with rapid transfer rates in comparison to the manifold relaxation rates

$$\theta = \frac{\alpha_1}{\alpha_1'} \cong \frac{C_{Tm\text{->}Ho}}{C_{Ho\text{->}Tm}} \qquad (3.2.4)$$

where the C_{ij} represents the energy transfer microparameter for the transfer of excitation from ion i to ion j. These microparameters can be found with energy transfer theory. The approximation of Eq. 3.2.4 relies on certain assumptions about the transfer process (essentially that the transfer is assisted by fast migration); we will return to this approximation in the discussion of Chap. 7. Recalling the expression for dipole-dipole energy transfer (Eq. 2.2.3), which is

---

[†] For examples, review the proceedings of any of the various topical meetings on mid-infrared laser systems. The assumption of the simple Boltzmann distribution is one of the basic starting points of almost all anaylsis of these systems.

[93] See, for example, G. Armagan, A. M. Buoncristiani, A. T. Inge, and B. Di Bartolo, "Comparison of Spectroscopic Properties of Tm and Ho in YAG and YLF Crystals", OSA Proc. on Adv. Sol. State Lasers, V10, Ed. G. Dube and L. L. Chase, Hilton Head, (1991), P222.

$$C_{ij}=\frac{9\chi^2 c}{16\pi^4 n^2}\int_0^\infty \overset{(i)}{\sigma}_{em}(\lambda)\,\overset{(j)}{\sigma}_{abs}(\lambda)\,d\lambda\,,$$

and by using McCumber's extensions of the Einstein relations (Eq. 2.5.11)

$$\sigma_{em}(\lambda)=\sigma_{ab}(\lambda)e^{-\beta(E(\lambda)-\mu)}.$$

we can relate the C_{ij} micro-parameters for $^3F_4$ <-> $^5I_7$ transfer and back-transfer. Here $E(\lambda)$ is the energy of the transition at a given wavelength and μ is the chemical potential. The two above relations can be combined with Eq. 3.2.4 to show

$$\theta\cong\frac{C_{Tm->Ho}}{C_{Ho->Tm}}=e^{\beta(\mu_{Tm}-\mu_{Ho})},\qquad(3.2.5)$$

where μ_{Tm} is the chemical potential of the $^3F_4$ manifold and μ_{Ho} is that of the $^5I_7$ manifold. The θ coefficient is now determined by the difference of the chemical potentials. As was mentioned earlier, μ is rigorously defined by the ratio of the excited state population to the ground state population when the system is in true thermal equilibrium[80], i.e.,

$$e^{-\beta\mu}=\frac{N_{ex}}{N_g}=\frac{\sum_i^{ex} g_i e^{-\beta\varepsilon_i}}{\sum_j^{g} g_j e^{-\beta\varepsilon_j}}\qquad(3.2.6)$$

With this relation we can express the chemical potential in terms of the energy levels. If Eq. 3.2.6 is substituted into the Eq. 3.2.5, we find the following expression for θ.

$$\theta=\frac{\sum_i^{5I7} g_i e^{-\beta\varepsilon_i}\;\sum_k^{3H6} g_k e^{-\beta\varepsilon_k}}{\sum_j^{3F4} g_j e^{-\beta\varepsilon_j}\;\sum_l^{5I8} g_l e^{-\beta\varepsilon_l}}\qquad(3.2.7)$$

We have now expressed the distribution in terms of the energy levels of the material. A similar expression was proposed by Zubenko et. al.[94] based on assumptions regarding energy transfer rates but was not experimentally confirmed. This relation will reduce to Eq. 3.2.3 when each of the ground states are singlet states. It is clear that this approach can be easily generalized for any transfer process which can be expressed in terms of overlap integrals, and therefore should hold for any of the energy transfer processes discussed in Chapter 2.

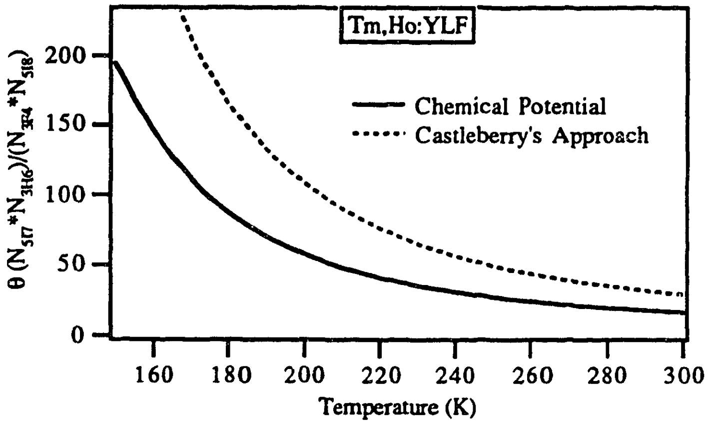

Figure 3.2.1. Difference between predictions of chemical potential approach (Eq. 3.2.7) and Castleberry's approach (Eq. 3.2.3).

Although the correction factor of Eq. 3.2.7 may seem like a trivial correction to the description generally assumed (Castleberry's approach - Eq. 3.2.3), the quantitative differences between the two relations are dramatic at temperatures of interest. Figure 3.2.1 graphically illustrates the differences between these two relations in the temperature range of 300 to 150 K.

3.2.3 Two-State Approach.

Remembering our initial description of the energy transfer process (Sec. 2.1), it was established that we could model the problem as a reduced two state problem where phase coherence was constantly lost. In this description, we considered only two of four possible states of the complete system, and showed how these two composite states paired to produce a mixed state of the system. The energy transfer process was modeled as a change in the probability of finding a specific basis state in the mixed state.

---

[94] D. A. Zubenko, M. A. Noginov, S. G. Serenkov, V. A. Smirnov, and I. A. Shcherbakov, Sov. J. Quant. Elect., V22, N2, (1992), P133-138.

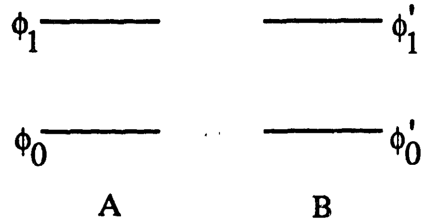

Figure 3.2.1. Energy level diagram for simple two state system.

Let us now simply apply the canonical distribution to this problem. Examining first a single two-state system, our composite basis states are given by $\psi_1 = \phi_1\phi_0'$ and $\psi_2 = \phi_0\phi_1'$, and the energies for these states are given by $E_1 = \varepsilon_1 + \varepsilon_0'$ and $E_2 = \varepsilon_0 + \varepsilon_1'$. The probability ($p_1$) of a system being in state ψ_1 is expressed as

$$p_1 = \frac{e^{-\beta E_1}}{e^{-\beta E_1} + e^{-\beta E_2}} = \frac{e^{-\beta(\varepsilon_1 + \varepsilon_0')}}{e^{-\beta(\varepsilon_1 + \varepsilon_0')} + e^{-\beta(\varepsilon_0 + \varepsilon_1')}}. \tag{3.2.8}$$

A similar expression exists for the probability of finding the system in ψ_2. By taking the ratio of p_2 to p_1, we find

$$\frac{p_2}{p_1} = \frac{e^{-\beta(\varepsilon_0 + \varepsilon_1')}}{e^{-\beta(\varepsilon_1 + \varepsilon_0')}} \tag{3.2.9}$$

This relation can be generalized to include the multiple levels of a manifold by simply summing over the different possible state combinations for two ions, in which case Eq. 3.2.9 becomes

$$\frac{P_2}{P_1} = \frac{\sum_{\{\varepsilon_1'\}} g_1' e^{-\beta\varepsilon_1'} \sum_{\{\varepsilon_0\}} g_0 e^{-\beta\varepsilon_0}}{\sum_{\{\varepsilon_1\}} g_1 e^{-\beta\varepsilon_1} \sum_{\{\varepsilon_0'\}} g_0' e^{-\beta\varepsilon_0'}} = \theta, \tag{3.2.10}$$

where P_1 is the probability that ion A is in a state that belongs to it's upper manifold (1) and ion B is in a state belonging to it's lower manifold of levels (0'). P_2 is the probability that the opposite situation occurs; specifically, ion A in a state belonging to the (0) manifold and ion B in a state belonging to the (1').

Identifying θ as the ratio of the probabilities of finding the system in one of the two composite excited states, we find the same relationship which we derived in Eq. 3.2.7. However, in this derivation we have used nothing but our definition of the basis states and basic statistical mechanics. As our first derivation is based on McCumber's theory and energy transfer theory, any assumptions made in the development of these theories were also implicit assumptions of our first derivation. Additionally, we made the approximation that the ratio of the average transfer parameters was equal to the ratio of the transfer microparameters (Eq. 3.2.4) This second derivation requires only that the underlying assumptions of statistical mechanics are satisfied; i.e., that the manifolds involved have long lifetimes in comparison to the transfer times, and that the interaction which equilibrates the internal states of each manifold occurs much faster than the transfer process.

3.2.4 Other Approaches.

It must be mentioned that we could have also developed the relationship simply by following the formulation of McCumber's theory (Sect. 2.5) and substituting the composite two-ion state kets used above in place of the single-ion states. By following this approach, we would have been able to derive Eq. 3.2.5 without the use of the overlap integrals for energy transfer. However, such a derivation would still maintain the assumptions of McCumber's theory; and little insight would be gained except for generalized rewrite of the theory. By including the energy transfer relations in our derivation, we have established a link between McCumber's relation and energy transfer theory. By exploiting this connection, we can now relate experimentally measurable quantities such as the transition cross-sections and the energy transfer microparameters to the distribution of excitations. Additionally, the first derivation implies relationships between the energy transfer rates and parameters which would not have been apparent in the strict statistical mechanics approach of Sect. 3.2.3.

It must be mentioned that the relations of Sect. 3.2.2 can also be obtained by multiplying the single ion partition functions together and grouping the terms which contain an excitation in either of the ion's first excited states to create a restricted partition function. Explicitly,

$$z_{tot} = z_1 z_2 = \left(\sum_{k}^{3H6} g_k e^{-\beta\varepsilon_k} + \sum_{j}^{3F4} g_j e^{-\beta\varepsilon_j} + \cdots \right) \left(\sum_{l}^{5I8} g_l e^{-\beta\varepsilon_l} + \sum_{i}^{5I7} g_i e^{-\beta\varepsilon_i} + \cdots \right).$$

Expanding this relation and grouping the terms which have one excitation in either of the first excited states, we find

$$z' = \sum_{k}^{3H6} g_k e^{-\beta\varepsilon_k} \sum_{i}^{5I7} g_i e^{-\beta\varepsilon_i} + \sum_{l}^{5I8} g_l e^{-\beta\varepsilon_l} \sum_{j}^{3F4} g_j e^{-\beta\varepsilon_j} .$$

This will also lead directly to Eq. 3.2.7.

3.3 Implications at higher excitation densities.

So far our discussion of the equilibrium distribution has been directed at low excitation levels where we could use the undepleted ground state approximation. In the regions of interest for practical room-temperature applications, however, this assumption is not appropriate. For instance, to achieve threshold for 2 μm operation at room temperature, roughly 20% of the Ho ions must be inverted in most materials; for energy storage applications the desired inversion density will be even higher. We will now examine the implications of equilibrium at higher pump intensities. Rearranging Eq. 3.1.4 we find

$$\frac{N_1'}{N_{Ho}} = \theta \frac{N_1}{N_{Tm}} \frac{1}{1+(\theta-1)N_1/N_{Tm}} \qquad (3.3.1)$$

where N'_1/N_{Ho} (the fraction of Ho ions excited) is expressed as a function of θ and N_1/N_{Tm} (the fraction of Tm ions excited). From this relationship it can be seen that the $^5I_7$ population is not a linear function of the $^3F_4$ population[†]; instead there will be a θ dependent roll-off with increasing population. Plots of this relationship for values of θ corresponding to various temperatures in Tm-Ho:YLF are shown in Fig. 3.3.1.

[†] This is the equivalent to ground state depletion. A frequent cause of errors in the literature results from approximating the lower manifolds as undepleted.

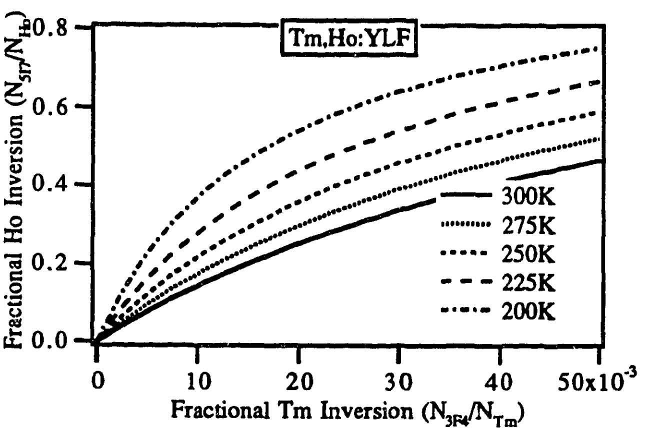

Figure 3.3.1. Fraction of Ho ions inverted plotted against the fraction of Tm ion inverted.

The total excitation density required to obtain a given Ho inversion can be determined from Eq. 3.3.1 if N_{Tm}, N_{Ho}, and θ are known. Note that this relation is concentration invariant. The fraction of Ho ions in the $^5I_7$ manifold is determined solely by θ and the fraction of Tm ions in the $^3H_4$ manifold.

Although the essential physics of this model is contained in Eq. 3.3.1, it is useful to convert this relationship to explicitly contain the concentration and the excited state density. This will allow us to more easily compare our expression and its predictions with the experiment. In our present model, all excitations will be in either the Tm $^3F_4$ level (N_1) or the Ho $^5I_7$ level (N'_1); therefore we can impose the constraint $N_{ex}=N_1+N'_1$. Combining this constraint with Eq. 3.3.1, we can solve for N_1,

$$N_1 = \frac{-[N_{Tm} + N_{Ho}\theta_0 - N_{ex}(\theta_0 - 1)]}{2(\theta_0 - 1)} + \frac{\sqrt{[N_{Tm} + N_{Ho}\theta_0 - N_{ex}(\theta_0 - 1)]^2 + 4(\theta_0 - 1)N_{Tm}N_{ex}}}{2(\theta_0 - 1)}. \qquad (3.3.2)$$

We can find the value of N'_1 from the relationship $N_{ex}=N_1+N'_1$. A normalized plot of N'_1/N_1 for different concentrations of Tm and Ho in YLF is shown in Figure 3.3.2.

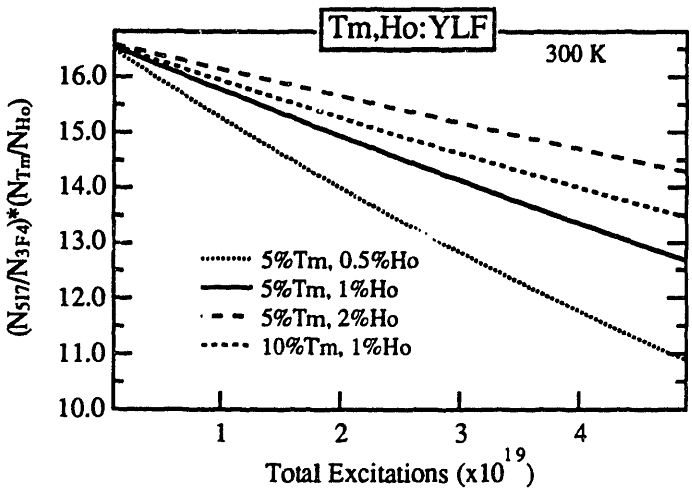

Figure 3.3.2. $(N_1/N_1)(N_{Tm}/N'_{Ho})$ versus excitations stored in Tm, Ho:YLF. Here the results of Eq. 3.3.2 have been normalized to account for the difference in concentration for each material. There is still an observable difference between systems with different concentrations at a fixed excitation level. This graphically illustrates a complication which must be considered when working with these systems at higher excitation levels.

As can be seen in the above plot, the ratio of $(N'_1/N_1)(N_{Tm}/N_{Ho})$ is very sensitive to the amount of excitations stored in the system and to the ion concentrations. It is apparent that θ can not be determined merely by finding the ratio $(N'_1/N_1)(N_{Tm}/N_{Ho})$ at arbitrary excitation levels as any result will be highly dependent on the excitation level and would vary for different concentrations. This depletion of the ground state will result in a ratio of Ho excitations to Tm excitations that is lower than what would be expected from naively applying Eq. 3.1.4.

3.4. Regions of applicability.

We have derived the relationship between the equilibrium distribution of the two manifolds in several different manners. In these derivations we have made some implicit assumptions which may not always be valid. We now discuss why these assumptions may break down and what effect the breakdown of these assumptions may have upon our measurements.

The crucial assumptions of all of our derivations depend on the relative time scales of the interactions. We have assumed that the manifold self-equilibrates much faster than transfer occurs, and also that transfer occurs much faster than the manifold's decay. These requirements on the transfer time will allow us to set rough limits on the applicable ranges of this theory.

The requirement that the intra-manifold equilibration time be much faster than the transfer time allows us to describe the distribution of excitations within the manifold with the canonical ensemble. If the transfer time is faster than or comparable to the equilibration time, the manifold will not come to equilibrium and we cannot use this description[†]. This will not be a problem in applications to rare earth doped materials as the maximum transfer times measured between rare earth ions are $\sim 10^7$ s^{-1}; therefore we will not discuss this further.

The requirement that the transfer rates be much larger that the decay rates will set a limit on the maximum energy gap between manifolds that will allow thermalization Recalling Sec. 2.8, we discussed non-resonant energy transfer and found that the transfer rate between manifolds varied exponentially with the energy gap between the manifolds. Therefore, for energy gaps which are too large, energy transfer will not occur quickly enough to allow equilibration.

A similar limit can be imposed on the concentrations based on microscopic concerns. The energy transfer rate between manifolds will vary with the ion concentrations. As can be seen from Eq. 2.2.2, the transfer rate will be determined by the distance between Tm and Ho ions. For low concentrations of Ho, direct excitation transfer from a Tm ion to a Ho ion may not occur at a high enough rate to allow equilibration of the manifolds. An excitation deposited in Tm must therefore migrate among the Tm ions until it is close enough to a Ho ion for transfer to occur. If equilibration is to occur, either the density of Tm ions must be large enough to allow fast migration and transfer, or the density of Ho ions must be high enough to allow direct transfer. Payne et al[95] has conducted a study of energy transfer between Tm and Ho in YLF and found that the equilibration time lengthens considerably at low dopant concentrations. We will return to this topic in the discussion in Chap. 7.

In our derivation of the relationship between the equilibrium populations, we dropped both the pump rate and the spontaneous emission rates. The inclusion of the pump term will cause a difference between the population predicted by Eq. 3.1.2 and the actual population as the system will not come to complete equilibrium. The difference between these populations will be on the order of τ_{trans}/τ_{life}. Based on the transfer times reported in [91, 92], this population difference should be negligible (<1%) for the $^5I_7$ and $^3F_4$ manifolds for the concentrations of Tm and Ho typically used in lasers.

[†] For these conditions, it would be appropriate to use the density matrix formalism discussed in Chap. 2.

[95] S. A. Payne, L. K. Smith, W. L. Kway, and W. F. Krupke, "Tm->Ho Energy Transfer in $LiYF_4$," Proc. Adv. Solid State Lasers, Sante Fe, 1992, Ed. Chase and Pinto, P166.

4. Experimental Apparatus and Samples

In this chapter, we provide some of the experimental background required for interpretation of this thesis. We review the standard experiments used for materials characterization, then briefly discuss our sample preparation techniques. Following this, we comment on the specific materials used in this study and summarize pertinent materials properties.

4.1. Experimental Measurements

Here we discuss some of the experiments used for basic characterization of a material's spectroscopic properties. We will refer to these experiments and their results throughout the remainder of this thesis. As the measurements discussed in this chapter are standard in the field, only aspects specific to our apparatus or pertinent to this thesis will be covered. A basic review of the techniques and apparatus can be found in several references on spectroscopic measurements[96].

4.1.1. Absorption

Absorption measurements refer to measurements of the attenuation of light as it passes through a material. They can be used not only to find the absorption cross-section of a dopant, but also to determine the position of energy levels and to measure dopant concentrations.

Absorption measurements were performed with a Perkin-Elmer Lambda 9 Spectrophotometer. The instrument is a dual-beam comparator device, with the signal taken to be the ratio of intensities of the sampling beam and the reference beam. The response time of the instrument can be varied and was in the 0.5 s to 2.0 s range for all measurements performed. The data scans were controlled and stored with a PC compatible computer. The minimum data interval was 0.01 nm; any interval longer than this could be selected in 0.01 nm steps. The minimum usable interval was set by the scan speed. Due to instrumental limitations, there was a maximum data transmission rate of

---

[96] See, for instance, K. Lark-Horovitz and V. A. Johnson, Solid State Physics, Methods in Experimental Physics Series, V6, Ed L. Marton, Academic Press, New York, 1959.

approximately 300 data points/min. Scan speeds varied from 30 nm/min to 0.9 nm/min depending on the desired resolution and the response time of the instrument.

The slit size could be held constant for measurements in the 200 nm to 870 nm range by setting the instrument's spectral resolution. The measured resolution was similar to the theoretical resolution at most wavelengths. The spectral resolution was generally set in the 0.5-0.3 nm range for room temperature measurements, while at cryogenic temperatures it was typically in the range of 0.12-0.2 nm to resolve the narrowed linewidths. The signal noise became prohibitively large for set resolutions smaller than 0.12 mm. At wavelengths longer than 870 nm the instrument ran in a constant gain mode, where reference signal strength was relatively constant throughout the scan. As such, the slit width varied with both the response of the PbS detector and the output power of the lamp; and spectra with constant resolution could not be obtained for lengthy scans. However, for short scans (~≤ 300 nm in length), the slit width was relatively constant and spectra of nearly constant resolution could be obtained. In the 2 μm region, the spectral resolution could be varied from ~0.6 nm to over 3 nm depending on the gain setting; the set resolution was constant to ~0.2 nm over the spectra.

For small samples, an aperture was used to restrict the probe beam so that it passed only through the sample; a similar aperture was also placed in the reference beam. Polarized measurements were made by placing a matched set of Glan-Thompson polarizers in the sample and reference beams. The extinction ratio of these polarizers was measured to be greater than 100:1. The system performed a self-calibration at start up; and the response for any particular configuration of the sample compartment (polarizers, apertures, etc.) was corrected for by performing a background calibration scan.

Spectra were measured by the instrument in dimensionless units of absorption (A), where A was given by the relationship $I_S/I_r=10^{-A}$. Here I_S is the intensity of the beam passing through the sample and I_r is the intensity of the reference beam. The spectra were corrected for Fresnel reflection losses. For values of $A > 3$, the response of the instrument became slightly non-linear, and the instrument saturated at $A \geq 5$. Care was taken to make sure that the instrument was operating in a linear region for measurements where the peak intensity and lineshape were important. The resulting spectra were converted to yield the absorption coefficient α by the relationship $\alpha = A \ln(10)/t$, where t is the sample thickness in cm. The absorption coefficient could be converted to the absorption cross-section if the concentration of absorbing dopants was known.

Low temperature measurements could be made by mounting a flowing-type cryostat in the sample chamber. These measurements, when combined with low temperature fluorescence measurements, could be used to determine the position of energy levels. The cryostats were stable to ±0.5 K in the 5-15 K range, ±3 K in the 15-40 K range, and ±1 K at temperatures greater than ~40 K. A calibrated Si diode was used to measure the sample temperature.

4.1.2. Fluorescence

The fluorescence spectra of a material is a measure of the spontaneous emission intensity (the Einstein A coefficient) as a function of wavelength (or energy). It can be transformed into the stimulated emission cross-section via an analog of Eq. 2.5.1. It can also be used to determine the position of energy levels and to calculate energy transfer parameters. It can serve as a check of sample purity as fluorescence from impurity ions can be identified in fluorescence spectra.

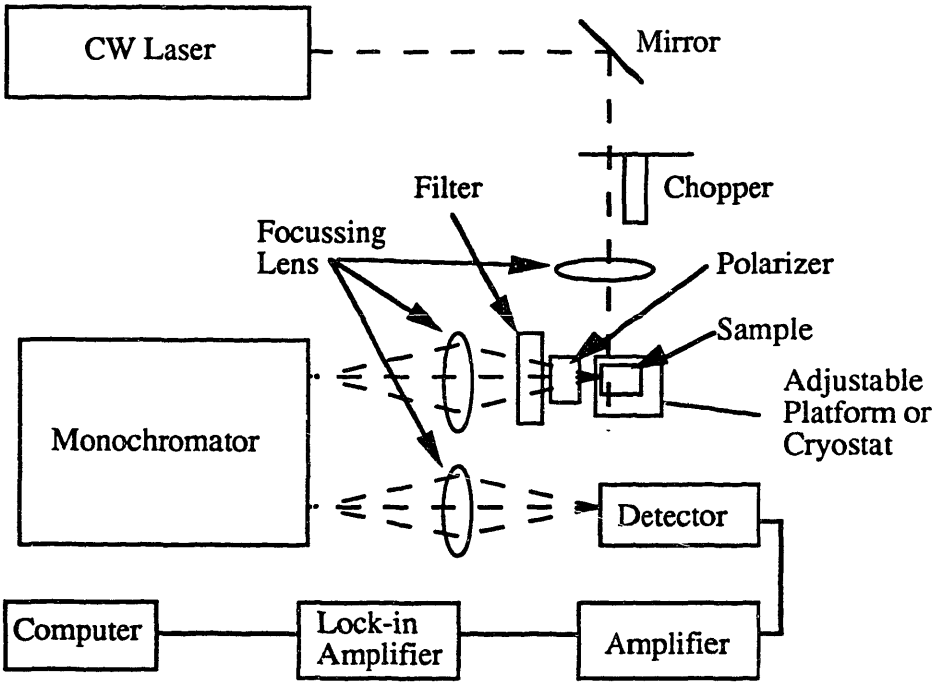

Figure 4.1.1. Experimental apparatus for a typical fluorescence measurement.

A typical fluorescence experiment is shown in Fig. 4.1.1. Samples were mounted and pumped with a cw laser source tuned to an absorption line. The sample mount and the pump focusing lens were 3 axis translationally adjustable, and also had the tilt and swivel adjustments of the typical optical mount. Fluorescence from the sample was focused with a lens onto the entrance slit of the monochromator. A polarizer and a filter were placed between the sample and the monochromator when required. The usable slit sizes ranged from ~50 µm to 2 mm. The slit used depended on the characteristics of the material and the purpose of the experiment. Both a MacPherson 1 m monochromator and 0.3 m monochromator were used for the experiments. The 1 m monochromator was capable of higher resolution, but the 0.3 m monochromator had a higher optical throughput. The gratings available for the monochromators allowed scans in the 100-1075 nm (1200 grvs/mm), 200-2150 nm (600 grvs/mm), and 400-4300 nm (300 grvs/mm) ranges. The monochromators could be purged with a dry gas (usually N_2) when necessary. Photomultiplier tubes were used for fluorescence detection in the 500-1100 nm range. A cooled Ge detector was used in the 1000 nm-1700 nm range, while InSb and InAs detectors operating at 77 K were used for wavelengths beyond 1500 nm. When necessary, a trans-impedance amplifier was used with the diode detectors to reduce the dark current.

Data collection was accomplished by a computer with a fast-sampling (up to 55,000 samples/sec) analog-to-digital converter card installed. Scan speeds ranged from 0.5 nm/min to 20 nm/min for the measurements, while the response time (for exponential averaging) of the lock-in amplifier ranged from 300 ms to 3 s and was the longest time constant of the system. The chopper frequency ranged from 110 to 400 Hz; and an electronic bandpass filter centered at this frequency was often used to cut down noise from other sources.

Crystal position for each measurement was optimized by scanning the monochromator to a transition with high signal strength and then adjusting both the crystal and the pump position until the signal was maximized. Transitions susceptible to reabsorption were used for position optimization to minimize the effects of this reabsorption on the spectra. The sample mount was rotationally adjustable about the vertical axis, which allowed a sample to be adjusted so that its face was ~±1° normal to the fluorescence collection system.

The wavelength of the system was calibrated from Ne and Ar ion lamp lines in the regions of interest. In general, the wavelength correction ranged from 0 to 3 nm depending on the grating, monochromator, and spectral region of interest. The spectral response of the system was determined from comparison of a calibrated source with the measured signal of that source. Uncorrected fluorescence spectra were multiplied by the system response to produce the actual fluorescence spectra.

For many measurements, a polarizer was used in the system. When working with anisotropic materials this polarizer was often rotated between measurements (in order to keep the absorbed power constant in the sample while observing different polarization spectra). When the polarizer was rotated, the beam path would shift slightly and the crystal position would need to be re-optimized. A separate system response was required for each polarization.

Low temperature measurements could be conducted with a sample-in-vapor dewar style cryostat. The cryostat was stable to ±1 K in the 5-15 K range, ±3 K in the 15-40 K range, and ±2 K at temperatures greater than ~40 K. A calibrated Si diode was used to measure the sample temperature.

4.1.3. Lifetime measurements

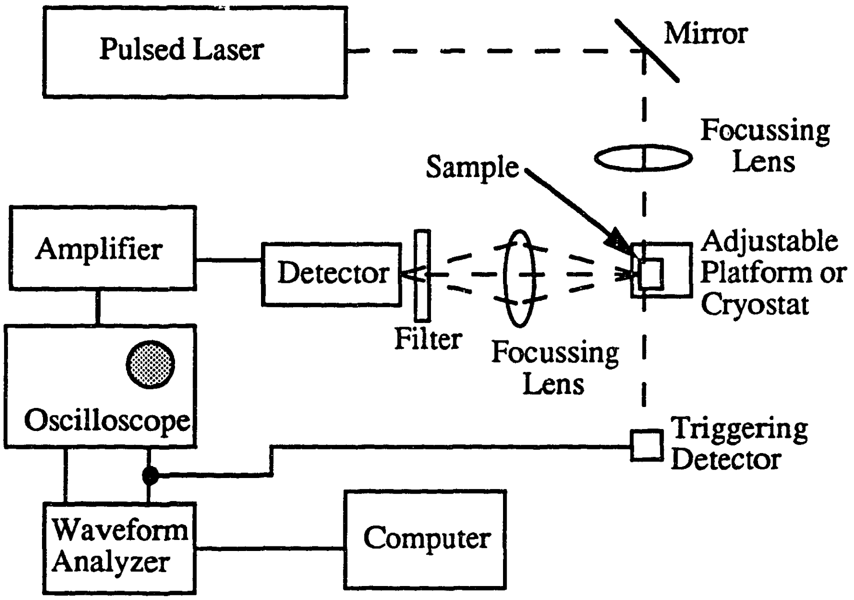

Figure 4.1.2. Experimental apparatus for lifetime measurements.

A typical lifetime measurement apparatus is illustrated in Fig. 4.1.2. In the diagram, a pulse from the laser propagates through a series of mirrors to be focused into the sample. Fluorescence from the sample is collected by a lens, passes through a filter and is focused onto a detector. The signal from the detector is amplified and digitized by a fast digitizer, which collects and averages a number of shots to produce a transient. The signal was also monitored on an oscilloscope for experiment alignment and optimization.

Samples were excited with a short (~20-30 ns) pulse. Two sources were used for excitation; either a pulsed dye laser (400 nm-650 nm) or a Ti:Sapphire laser (750 nm-950 nm). Fluorescence from the sample was observed with the same detectors described earlier with the exception that the biasing was adjusted so that the response time of the detector was much faster than the lifetime being measured. Whenever possible, the upper state was directly pumped, and the fluorescence to a level other than the ground state was monitored. Direct pumping made the interpretation of the time-resolved fluorescence much simpler as there were no "coupled decays"; while observation at a wavelength far away from the pump greatly cut down the amount of scattered pump radiation incident on the detector. The samples were all pumped as close to the absorption edge as possible to minimize the reabsorption lengthening of the lifetime.

When it was not possible to directly pump the upper state, a level with a known lifetime was pumped and the observed decay was analyzed as a coupled exponential decay and buildup. Band pass filters were used in all cases to cut down on the scattered pump radiation. A monochromator was occasionally used in addition to the band pass filter to provide additional scattered light rejection; this was sometimes necessary when observing fluorescence close in wavelength to the pump wavelength. Time-dependent fluorescence data for Ho and Tm were collected and averaged using a DATA 6000 waveform analyzer. Lifetimes were interpreted as the 1/e time of the linear portion of the logarithm of the time-dependent fluorescence intensity. Typical data can be seen in Figure 4.1.8.

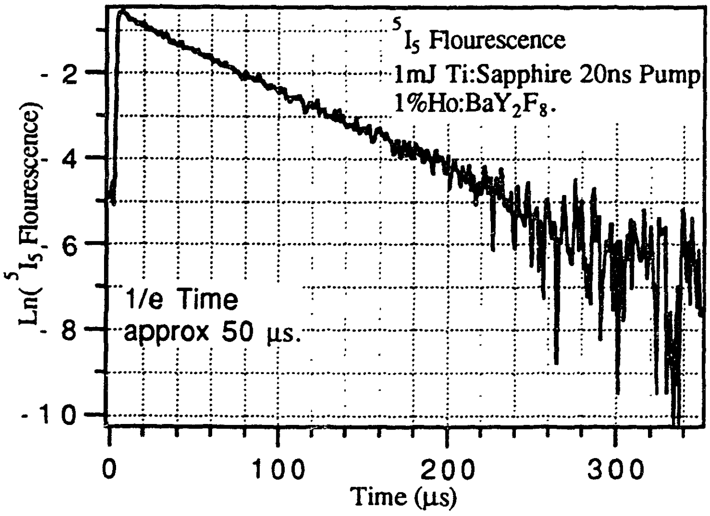

Figure 4.1.8. Natural logarithm of the fluorescence emission of the $^5I_5$ level in Ho doped BaY_2F_8. All reported lifetimes are taken from the linear portion of such plots.

4.2. Sample Preparation

Sample preparation and characterization is an important part of any experiment. We will now briefly summarize the techniques used to produce, orient, and polish samples.

4.2.1. Orientation

Due to the anisotropic nature of some of the materials studied, it was necessary to make measurements at specific orientations relative to the crystallographic axes. This required careful orientation of the samples. Both x-ray diffraction and optical identification of the axes were used for orientation. The x-ray diffraction method allowed the user to determine the crystallographic orientation of a sample by scattering x-rays. These scattered x-rays produced a Laue pattern of reflected spots on a photographic film. This technique is in common use and has been described by a number of authors.[97]. What must be kept in mind when using this technique is that a Laue pattern is produced by reflections from planes of atoms in the crystal, and will therefore identify vectors in reciprocal space. Thus, when a Laue pattern is produced at an orientation normal to the crystallographic b and c axes, it indicates the [1 0 0] direction and not the a axis of the material. While there is no difference between [1 0 0] and the crystallographic a axis for crystals of orthogonal symmetries, there is a difference for materials where the angle between the crystallographic axes is ≠ 90°. In materials with these symmetries, care must be taken to ensure that you have the proper orientation of the sample. The difference between [1 0 0] and a for BaY_2F_8 is illustrated in Fig. 4.2.1.

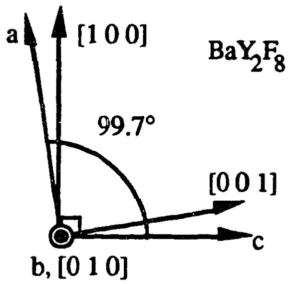

Figure 4.2.1. Crystal axes and reciprocal axes for BaY_2F_8.

When working with optically anisotropic materials, it is possible to align the crystal by locating the "extinction" directions for the material and using that as a reference. By placing the sample between two crossed polarizers, an anisotropic crystal will rotate the polarization of the light and therefore allow some light to pass through the polarizers except when the polarization is parallel to an axis of the index ellipsoid--these axes are called extinction directions.

---

[97] See, for example, C. Kittel, Introduction to Solid State Physics, 6th Ed, Wiley, Brisbane, 1986.

For orientation with the x-ray technique, samples were mounted in a goniometer which allowed a point of the sample to be rotated about a point in space. A Laue pattern of the sample was produced and the orientation was adjusted. This process was repeated until the orientation was satisfactory, then the crystal was cut. When polarized light was used as an orientation technique, the extinction axes were located and all cuts were performed in reference to these axes.

4.2.2. Cutting and Polishing

Following crystal orientation, the materials and mounts were affixed to translationally adjustable holders. Saws with diamond edged blades were used to cut the crystals. A cut could be made to roughly ±1° of the desired orientation. Following a cut, samples were mounted with wax on the flat end of a brass cylinder. The samples were then lapped to the desired thickness by placing the cylinders inside a polishing jig (which held the flat end of the cylinder parallel to a surface), placing the jig on a flat glass plate on which alumina grit and water had been applied, and then grinding the crystal. Grit sizes between 40 and 9 μm were used for lapping. The sample was polished using the same techniques, but with grit sizes in the 9 μm to 1 μm range. A spinning rotary wheel with 0.3 μm grit was substituted for the glass plates in the final finishing step.

Some of these materials are prone to cracking during preparation. For these materials, low cutting speeds ($\leq$ 5 mm/min or less) were used, and only the smaller sizes of lapping grit ($\leq$ 20 μm) were used to prevent cracking the crystal. Samples prepared with these techniques were oriented within ±2° of the desired orientation, with opposing faces parallel to within ±1°.

4.2.3. Growth Methods

Most of the fluoride materials used in this study were grown by the Czochralski growth technique in sealed growth atmospheres in the MIT CMSE crystal growth laboratories[†]. A stochiometric melt of feed materials was used for BaY_2F_8, while a non-stochiometric melt was used for $YLiF_4$ and $NaYF_4$. The feed materials for the fluoride crystals were produced by hydrofluorinating oxides of 99.99% or higher purity. The oxide samples were obtained from several different sources.

[†] Nearly all of the crystal growth was performed by A. Cassanho. Some crystal growth of BaY_2F_8 was performed by the author following the techniques developed by A. Cassanho. The crystal growth techniques are detailed in several publications by A. Cassanho and H. P. Jenssen.

4.3. Sample Materials and Characteristics

In this section we summarize the observed physical properties of the samples used in this study. YLiF$_4$ and Y$_3$Al$_5$O$_{12}$ are well characterized materials and a large amount of information can be found in the literature; we merely summarize the pertinent properties of these materials

4.3.1. BaY$_2$F$_8$

BaY$_2$F$_8$ is a birefringent material that is optically transparent from its infrared absorption edge at 9 μm to beyond 200 nm in the ultraviolet[98]. Its phonon spectra is relatively low energy, with a maximum phonon energy of 415 cm^{-1}[99], and it has low non-radiative relaxation rates (in comparison to garnets)[100]. BaY$_2$F$_8$ has been used successfully as a laser host for a number of rare-earth dopants, including Nd[101], Pr[102], Dy[100], Ho[103], and Er[99].

BaY$_2$F$_8$ crystallizes in the b-BaTm$_2$F$_8$ structure and is isostructural with BaLn$_2$F$_8$, with Ln->{Dy, Ho, Er, Tm, and Yb}[104]. The unit cell is monoclinic (space group C$_2$/m) with unit cell parameters a=6.935±0.001Å, b=10.457±0.002Å, c=4.243±0.001Å, and β=99°40'±2'[105]; each unit cell contains 2 formula units of BaTm$_2$F$_8$. Rare earths enter substitutionally into the Y^{3+} site, which has site symmetry C$_2$. Other rare earths can be substituted into the system in small concentrations, but a lattice strain develops with increasing rare-earth concentration due to the size mismatch

---

[98] H. P. Christensen, H. P. Jenssen, and D. R. Gabbe, "BaY$_2$F$_8$ as a Host For Ln Ions, I: Optical Properties of the Crystal and Spectroscopic Results for Pr, Dy, Ho, and Er Doping", Unpublished.

[99] A. A. Kaminskii, S. E. Sarkisov, F. Below, and H. J. Eichler, "Spectroscopic and laser properties of Er^{3+}-doped monoclinic BaY$_2$F$_8$ single crystals," Optical and Quant. Elect., 22, S95,(1990).

[100] L. F. Johnson and H. J. Guggengeim, "Laser emission at 3 μm from Dy^{3+} in BaY$_2$F$_8$," Appl. Phys. Lett., V23, N2, P96, (1973).

[101] A. A. Kaminskii and B. N. Sobolev, Neorg.Mat., V19, N11, (Nov 83), P1947-1950.

[102] A. A. Kaminskii, and S. E. Sarkisov,"Stimulated-Emission Spectroscopy of Pr^{3+} Ions in Monoclinic BaY$_2$F$_8$ Flouride", Phys. Stat. Sol. (a) 97, K163 (1986).

[103] L. F. Johnson and H. J. Guggenheim, "Electronic- and Phonon- Terminated Laser Emission from Ho^{3+} in BaY$_2$F$_8$," IEEE J. of Quant. Elect., V10, N4, P442, (1974)

[104] A. A. Kaminskii, B. P. Sobolev, S. E. Sarkisov, G. A. Denisnko, V. V. Byabchenkov, V. A. Fedorov, and T. V. Uvarova, "Physiochemical Aspects of the Preparation, Spectroscopy, and Stimulate Emission of Single Crystals of BaLn$_2$F$_8$-Ln^{3+}," Neorg. Mat., V18, N3, P482, (1982).

[105] O. E. Izotova and V. B. Aleksandrov, "The Crystal Structure of BaTm$_2$F$_8$," Sov. Phys. Doklady, V15, N6, P525, (1970).

between the Y^{3+} ion and the rare earth ion. This strain makes the crystal liable to cracking.

Due to its monoclinic crystal structure, BaY_2F_8 is a biaxial material that also exhibits dispersion in the orientation of its optical axes in the a-c plane. No dispersion of the axes is allowed in the b-a or b-c plane due to symmetry constraints[106]. Therefore, three different indices of refraction are needed to describe the dielectric properties of BaY_2F_8 as well as an angle, ρ, describing the angular difference between the orientation of the optical axes and the crystallographic axes of the crystal[107].

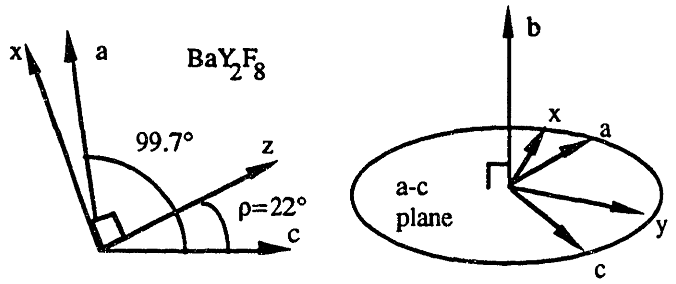

Figure 4.3.1. Crystallographic (a, b, c) and optical (x, y, z) axes in BaY_2F_8.

In addition to the dispersion exhibited by the indices of refraction, dispersion of the imaginary portion of the dielectric tensor is also allowed in the a-c plane of this crystal structure. This means that the minima and maxima of the absorption cross-section tensor need not coincide with the crystallographic or optical axes of the crystal[108]. It has been experimentally determined that the angular orientation of the absorption cross-section differs from the crystallographic and optical axes in these crystals[109].

For ions with odd numbers of electrons there are no selection rules for electric dipole transitions, while for ions with an even number of electrons, the energy levels can be decomposed into two sets of different symmetries (Γ_1 and Γ_2). For electric dipole transitions, transitions between states of the same symmetry will be seen in E//b spectra,

---

[106] For a discussion of these issues, see, for example, M. Born and E. Wolf, Principles of Optics, 6th ed., (Pergamon, 1980), P667-679, P708, or J. J. Nye, Physical Properties of Crystals, (Oxford, London, 1960), P3-49, P305-309.

[107] W. L. Bond, J. Apple. Phys., 36, P1674, (1965).

[108] For a discussion of these issues, see, for example, M. Born and E. Wolf, Principles of Optics, 6th ed., (Pergamon, 1980), P667-679, P708, or J.J. Nye, Physical Properties of Crystals, (Oxford, London, 1960), P3-49, P305-309.

[109] K. M. Dinndorf, D. S. Knowles, M. Gojer, C. J. Taylor, and H. P. Jenssen, "Where are the principal axes for transitions in monoclinic crystals?", Proc. of the Adv. Solid State Laser Conf., Santa Fe, NM, Feb 17-19, 1992.

while transitions between states of different symmetries will be seen only in E⊥b spectra. The energy levels for Tm and Ho in BaY_2F_8 can be found in Tables 4.3.1 and 4.3.2.

Man.	En. Levels		Energy (cm^{-1})
	The.	Exp.	
$^3H_6$	13	11	0, 1.5, 146, 160, 278, 284, 291, 302, 310, 457*, 467*, 479*, 568*
$^3F_4$	9	9	5681, 5796, 5851, 5902, 5937, 6044, 6054, 6084*, 6088*
$^3H_5$	11	10	8292, 8293, 8438*, 8514, 8528, 8540, 8578*, 8594*, 8605, 8642
$^3H_4$	9	8	12666, 12667, 12741, 12808, 12845, 12887, 12919, 12956*, 12982*, 13012*
$^3F_3$	7	7	14583, 14640, 14665, 14670, 14674, 14704, 14725
$^3F_2$	5	4	15205, 15239, 15321, 15342
$^1G_4$	9	9	21052, 21206, 21369, 21376, 21386, 21607, 21623, 21656, 21696 *Data should be refined.

Table 4.3.1. Partial listing of energy levels of Tm^{+3} in BaY_2F_8. No other energy level data for Tm:BaY_2F_8 has been located. Accuracy is ±2 cm^{-1} for the $^3F_4$, $^3H_4$, $^3F_3$, $^3F_2$, and $^1G_4$ multiplets. All other multiplets have an uncertainty of ±5 cm^{-1}.

Man.	En. Levels		Energy (cm^{-1})
	The.	Exp.	
$^5I_8$	17	14	0@, 37, 39, 54, 57, 88, 119, 238*, 272*, 311*, 321*, 349*, 377*, 386*
$^5I_7$	15	12	5171, 5175, 5180, 5188, 5196, 5213, 5227, 5253, 5266, 5271, 5275, 5356
$^5I_6$	13	8	8687, 8696, 8700, 8704, 8711, 8717, 8739, 8746, 8753, 8757, 8855
$^5I_5$	11	7	11254, 11262, 11273, 11280, 11285, 11287, 11310
$^5F_5$	11	7	15495, 15499, 15529, 15579, 15621, 15654, 15685, 15697, 15713 *Data should be refined. @ a quasi-doublet with 0.24 cm^{-1} separation.[110]

Table 4.3.2. Partial listing of energy levels of Ho^{+3} in BaY_2F_8 from [98]. Uncertainty of ±5 cm^{-1} for all multiplets with the exception of $^5I_7$, $^5I_8$ which have uncertainty of ±1 cm^{-1}.

4.3.2. $YLiF_4$

$YLiF_4$ (YLF) is an uniaxial material that is optically transparent throughout the visible and much of the infrared (cutoff $\lambda \approx 5$ μm). It is a popular host material because of its low index refraction, low phonon energies, and its negative coefficient for thermal lensing. Laser operation has been demonstrated in YLF for Ce, Pr, Nd, Tb, Ho, Er, and Tm dopants[111]. $YLiF_4$ crystallizes in the scheelite ($CaWO_4$) structure and forms solid

---

[110] I. N. Kurkin, K. P. Chernov, and Yu. K. Chirkin, Sov. Phys. Solid St., V21, P521, (1979).

[111] A. Linz, H. P. Jenssen, C. S. Naiman, and E. P. Chickliss, "$LiYF_4$ (YLF): A Spectrally Diverse Laser Host and Electro-Optical Material", unpublished, 1980.

solutions of the compounds $LiLnF_4$, with Ln ranging through the rare earth from Eu through Yb[112]. The unit cell is tetragonal with lattice cell parameters a=5.26Å and c=10.94Å[113] and contains 4 formula units per unit cell. Rare earths substitute into the Y^{3+} site, which has site symmetry S_4. Although the point symmetry is S_4, the selection rules and energy levels are generally determined for D_{2d} symmetry[114]. The energy levels of Tm:YLF are shown in Table 4.3.3 and of Ho:YLF in Table 4.3.4.

Man.	En. Levels		Energy (cm^{-1})
	The.	Exp.	
$^3H_6$	10	5	0, 31*, 56, 282, 310, 324, 327*, 374, 375*, 509
$^3H_4$	7	7	5605, 5760*, 5757, 5827, 5944, 5967, 5997*
$^3H_5$	9	9	8285, 8285*, 8295, 8500*, 8497, 8500*, 8508, 8532
$^3H_4$	7	5	12621, 12619, 12644*, 12741, 12825, 12831*, 12938
$^3F_3$	5	5	14531*, 14561, 14605*, 14605, 14616
$^3F_2$	4	2	15104, 15189, 15218*, 15235

Table 4.3.3 Energy levels of Tm:YLF from [114]. * denotes doubly degenerate levels.

Man.	En. Levels		Energy (cm-1)
	The.	Exp.	
$^5I_8$	13	13	0, 7, 23, 48, 56, 72, 217, 270, 276, 283, 290, 303, 315
$^5I_7$	11	10	5153, 5157*, 5164,5185*, 5207, 5229*, 5233, 5291, 5293*, 5293
$^5I_6$	10	10	8670, 8670, 8680*, 8686*, 8687, 8696, 8701, 8768, 8783*, 8796
$^5I_5$	8	8	11240*, 11240, 11248*, 11245, 11252, 11298, 11327*, 11333
$^5F_5$	8	8	15485, 15491*, 15508, 15555, 15620*, 15627, 15632, 15654*

Table 4.3.4. Energy levels of Ho:YLF from [115]. * denotes doubly degenerate levels.

4.3.3. $Y_3Al_5O_{12}$.

$Y_3Al_5O_{12}$ (YAG) is an isotropic material which possesses the cubic structure characteristic of garnets. It is perhaps the most widely used host material for solid state lasers; a review of its physical properties can be found in [72]. A discussion of its

---

[112] D. R. Gabbe, A. Linz, M. Douma, C. S. Naiman, and R. C. Folweiler, "Growth of single crystals of pure and rare earth doped $LiYF_4$ for laser applications", presented and 169th ACS Nat. Meet., Philadelphia, Apr 6-11, 1975.

[113] A. L. Harmer, A. Linz, and D. R. Gabbe, "Fluorescence of Nd3+ in Lithium Yttrium Fluoride", J. Phys. Chem. Solids, V30, (1989), P1483.

[114] H. P. Jenssen, A. Linz, R. P. Leavitt, C. A. Morrison, and D. E. Wortman,"Analysis of the optical spectrum of Tm^{3+} in $LiYF_4$, " Physical Review B, V 11, N 1, (Jan 1975), P 92-101.

[115] N. Karayianis, D.E. Wortman, and H.P. Jenssen, "Analysis of the optical spectrum of Ho^{3+} in $LiYF_4$, " J. Phys. Chem. Solids, V 37, (1976), P675-682.

structure can be found in Bogomolova et al[116]. The site symmetry is assumed to be D_2 for the purposes of calculating the energy levels[117]. The energy levels for Tm and Ho in YAG can be found in Tables 4.3.5 and 4.3.6.

	En. Levels		
Man.	The.	Exp.	Energy (cm^{-1})
$^3H_6$	13	10	0, 27, 218, 228, 256, 266, 520, 613, 652, 687, 701, 754, 767
$^3H_4$	9	9	5539, 5760, 5813, 5915, 6043, 6114, 6166, 6231, 6246
$^3H_5$	11	9	8339, 8345, 8516, 8530, 8524, 8556, 8711, 8773, 8800, 8873, 8882
$^3H_4$	9	7	12607, 12679, 12747, 12818, 12824, 12954, 13072, 13139, 13159
$^3F_3$	7	5	14659, 14649, 14661, 14679, 14705, 14720, 14741
$^3F_2$	5	3	15245, 15264, 15302, 15433, 15440

Table 4.3.5. Energy levels of Tm:YAG from [118].

	En. Levels		
Man.	The.	Exp.	Energy (cm-1)
$^5I_8$	17	15	0, 4, 41, 51, 138, 145, 151, 160, 399, 418, 448, 457, 498, 506, 520, 531, 536
$^5I_7$	15	14	5229, 5232, 5243, 5250, 5303, 5312, 5320, 5341, 5352, 5375, 5395, 5404, 5418, 5455, 5490
$^5I_6$	13	13	8721, 8726, 8735, 8741, 8745, 8763, 8773, 8819, 8844, 8854, 8869, 8940, 8954
$^5I_5$	11	11	11301, 11311, 11322, 11328, 11332, 11355, 11382, 11391, 11422, 11477, 11485

Table 4.3.6. Energy levels of Ho:YAG from [119].

4.3.4 $NaYF_4$.

$NaYF_4$ (NYF) is a uniaxial material currently under development. Its structure is a derivative of the basic CaF_2 structure[120]; some details of the structure are still not

---

116 G. A. Bogomolova, L. A. Bumagina, A. A. Kaminskii, and B. Z. Malkin, "Crystal field in laser garnets with TR^{3+} ions in the exchange charge model", Sov. Phys. Solid State, V19, N8, (1977), P1428.

117 C. A. Morrison, E. D. Filer, and N. P. Barnes, "Energy levels and branching ratios of Tm^{3+} in ten garnet laser materials", Harry Diamond Laboratories, Adelphi MD, HDL-TR-2196, (1991).

118 J. B. Gruber, M. E. Hills, R. M. Macfarlane, C. A. Morrison, G. A. Turner, G. J. Quarles, G. J. Kintz, and L. Esterowitz, "Spectra and Energy Levels of Tm3+:Y3Al5O12", Phys. Rev. B, V40, (1989), P9464.

119 J. B. Gruber, M. E. hills, M. D. Seltzer, S. B. Stevens, C. A. Morrison, G. A. Turner, and M. R. Kokta, "Energy levels and crystal quantum states of trivalent holmium in yttrium aluminum garnet", J. Appl. Phys., V69, N12, (1991), P8183.

120 S. Aleonard, M. Labeau, Y. Le Fur and M. Gorius, Mat. Res. Bull., V8, (1973), P605.

established[121]. The space group for the structure is C^1_{3h} and the lattice constants of the material are a=5.967 Å and c=3.523 Å. The structure has two different Y^{3+} sites; each site has symmetry S_6. There are 1.5 formula units per unit cell. One site is always occupied by Y^{3+} ion;the other site has a 50% probability of being occupied by a Y^{3+} ion (if the site is not occupied by a Y^{3+} ion, then a Na^+ ion occupies the site). Optical transitions at room temperature are relatively broad in comparison to other rare earth doped materials as a result of overlapping transitions from the differing energy levels of the different sites. The presence of two sites complicates the identification of the energy levels; selective pumping techniques[122] must be used to excite sites of only one symmetry. The resulting fluorescence spectra can be compared with the absorption spectra to determine to which site the energy levels (between which the optical transitions are observed) belong. Selective pumping techniques have been successfully applied to Nd:$NaYF_4$ [123]; identification of the energy levels of Tm and Ho in $NaYF_4$ is currently being pursued. This material is thought to be a vary desirable host due to its low multiphonon relaxation rates, which are apparent in the long lifetimes of $NaYF_4$ in comparison to similiar materials (See Table 4.3.7 below.)

4.3.5. Summary of some basic material parameters

We have conducted the basic experiments detailed in Section 4.1 on the materials just described. A brief summary of the results of these measurements can be found in Table 4.3.7 on the following page. For comparison, we have included the results of previous measurements of these quantities when available. We will use these values throughout the rest of this thesis.

---

[121] See, for instance, J. H. Burns, "Crystal Structure of Hexagonal Sodium Neodymium Fluoride and Related Compounds", Inorg. Chem., V4, (1965), P1005; B. P. Sobolev, D. A. Mineev, and V. P. Pashutin, "Low-temperature hexagonal modification of NaYF4 having the gagarinite structure", Dokl. Akad. Nauk. SSSR, V150, (1963), P791, and A. A. Voronkov, N. G. Shumyatskay, and Y. A. Pyatenko, "Crystal Structure of Gagarinite", Zh. Strukt. Khim., V3, (1962), P691.

[122] See, for example, Y. Yamaguchi, K. M. Dinndorf, H. P. Jenssen, and A. Cassanho, "Spectroscopy of Nd:KYF_4", OSA Proc. of Adv. Solid State Laser Conf., Ed. E. Pinto and T. Y. Fan, New Orleans, (1993), In press.

[123] D. S. Knowles, A. Cassanho, and H. P. Jenssen, OSA Proc. on Tunable Solid State Lasers, (1989), V5. P139. and M. F. Joubert, C. Linares, B. Jacquier, A. Cassanho, and H. P. Jenssen, J. Lumin., V51, (1992), P175.

Physical Quantity	$Y_3Al_5O_{12}$	$YLiF_4$	BaY_2F_8	$NaYF_4$
3F4 lifetime (ms)	11	14±0.5	17.5±0.7	10.5±0.7
3H4 lifetime (ms)	0.83^	2.10±.1	2.33±0.1	1.5± 0.1
5I7 lifetime (ms)	9	13.5±0.5	17 (16 †)	12
5I6 lifetime (ms)	*	(2.05 ¥)	5.4±0.3 (5 †)	*
5I5 lifetime (ms)	*	18±2 (18 ¥)	50±3	130±5
5F5 lifetime (μs)	*	30 ¥	39±2 ®	*
Ref. ind. (Ave)	1.81	1.48	1.52	≈1.5
Y sites density ($x10^{22}$)	1.28	1.39	1.30	1.38
$\hbar\omega_{eff}$ (cm-1)	700	400	*	
C (s-1)	9.7x107	3.5x107	4.5x107	
a(cm)	3.1x10-3	3.8x10-3	4.1x10-3	
e	0.045	0.22	*	

Table 4.3.7. Summary of basic material parameters. For anisotropic materials we have listed the average of the different indices of refraction for the axes. * denotes data from which has not been measured. Data from others are denoted by parentheses. ¥ are from [124], † are from [103], ® are from [98], and ^ are from [92]. The last four rows of data for multiphonon relaxation processes are from [15]

---

[124] H. Chou, "Energy Transfer in Codoped Ho, Er:YLF and Its Potential for Improving the Efficiency of 3 Micron Lasers", S. M. Dissertation, Mass. Inst. of Tech., May 1983.

5. Steady State Distribution Measurements

We now experimentally determine the distribution of excitations between the Ho $^5I_7$ and the Tm $^3F_4$ in the steady-state limit. Our method is to measure the normalized ratio of the excitations stored in each manifold, θ, under steady state conditions. We use some of the various approaches suggested by the derivations of Chap. 3 to indirectly determine θ from spectroscopic measurements and material parameters, following which we directly measure this ratio. We compare the results of the different measurement techniques and extend these measurements to lower temperatures. Finally we discuss the potential sources of experimental uncertainty.

In the following section, most of the experimental work presented has been performed with YLF and YAG as these two materials are firmly established and well known experimentally.

5.1. Indirect Measurements of the Population Ratio.

In Chap. 3, we saw that the value of θ can be obtained if the energy levels of the $^5I_7$, $^5I_8$, $^3F_4$, and $^3H_6$ manifolds are known (Eq. 3.2.7). At 293 K we would expect θ to be 17.8 for Tm, Ho:YLF. We would like to compare the value of θ predicted by the energy levels with the value of θ determined from simple measurements.

5.1.1. Spectral Cross-sections

It is clear from Eq. 3.2.5 that θ is determined by the difference in the manifolds' chemical potentials. These chemical potentials can be determined from crossing points of the emission and absorption cross-sections as a direct consequence of McCumber's relation (Eq. 2.5.11). An example of how the chemical potential can be read directly from spectra is illustrated in Fig. 5.1.1.

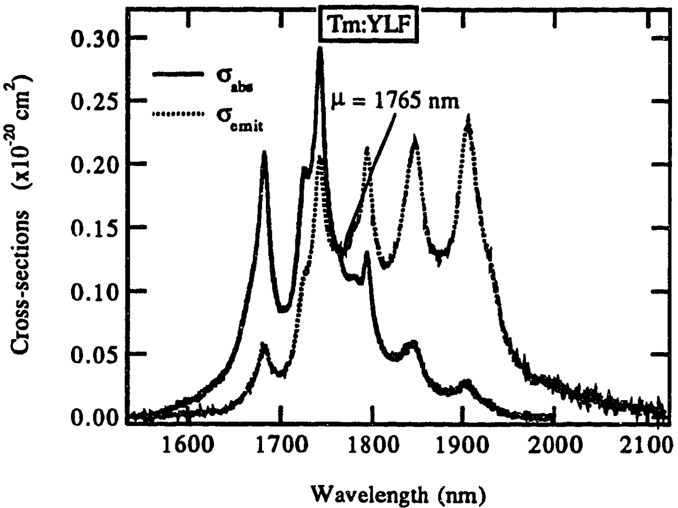

Figure 5.1.1. Absorption and effective emission cross-sections for the 3F4 manifold of Tm:YLF for the E//a polarization. The chemical potential can be read from the crossing point of the two spectra.

The absorption spectra was produced with a Perkin-Elmer Lambda 9 Spectrophotometer. The effective emission cross-section, σ^{em}, was produced from fluorescence spectra using the relationship[125]

$$\sigma_i^{em}(\lambda)=\frac{\lambda^5 I_i(\lambda)}{8\pi n^2 c\tau_R \frac{1}{3}\sum_j \int \lambda I_j(\lambda)d\lambda}, \qquad (5.1.1)$$

where I_i is the fluorescence intensity for polarization i in units of [W/nm]. Here n is the index of refraction of the material, c is the speed of light, and τ_R is the radiative lifetime of the manifold. The chemical potentials measured from the spectra for Tm, Ho:YLF can be found in Table 5.1.1.

Quantity	E//a	E//c	Ave	En. Levels
μ_{Tm}	5688±15	5675±20	5681.5±10	5689.5
μ_{Ho}	5116±10	5110±10	5113±5	5107.4

Table 5.1.1. Measured μ from spectra compared with μ expected from energy levels for the $^3F_4$-$^3H_6$ and the $^5I_8$-$^5I_7$ transitions.

The method of finding the chemical potentials just described is somewhat simplified from the procedure actually used to read the chemical potentials from cross-

---

[125] B. F. Aull and H. P. Jenssen, "Vibronic Interactions in Nd:YAG Resulting in Nonreciprocity of Absorption and Stimulated Emission Cross Sections", IEEE J. Quant. Elect., V18, N5, (1982), P925.

sections. The above approach assumes that the both of the spectra have been recorded at the same resolution and additionally requires that the spectra have very little noise. We obtained the chemical potentials listed in Table 5.1.1 by fitting McCumber's relation to a spectra produced by dividing the emission cross-section spectra by the absorption cross-section spectra, and then finding the point where the resulting fit was equal to unity. This technique does not require that the spectra have the same resolution and also can more easily accommodate noisy data. The simple method described earlier serves to illustrate the fundamental ideas of this section; the actual procedure used to produce the chemical potentials is detailed in Appendix D.

In Table 5.1.1, a measured value of μ has been reported for each polarization. The difference between the two polarizations is indicative of a systematic error in our system response. This effects and magnitude of this error will be discussed later. For now we simply average the two values to produce μ for each manifold. The value of θ implied by these measurements is 16.6 ± 1.5 in comparison to the value of 17.8 which we would expect from the energy levels.

Values of the chemical potential are generally not reported for measurements of cross-sections; however, quantities such as the peak cross-section often are reported and can be compared to our measurements to give a idea of the accuracy of our results. We measure the peak effective emission cross-section for the Ho $^5I_7$-$^5I_8$ transition to be $(1.45 \pm 0.1) \times 10^{-19}$ cm^2. Reported values in the literature range from 1.8×10^{-19} cm^2[126] to 1.5×10^{-19} cm^2[127]. As typical uncertainties on these measurements are on the order of 15-20%, we consider these values to be in agreement with our value.

The values for θ and for the chemical potentials produced by these measurements comprise an independent check on the values predicted for these quantities by the energy levels. Within the experimental uncertainties, the values for these quantities produced by this method agree with the predictions from the energy levels.

5.1.3. Overlap Integrals.

By examining our derivation of Sec. 3.2.2, one additional relation is useful for finding θ. Recalling Eq. 3.2.5, $\theta = C_{Tm \rightarrow Ho}/C_{Ho \rightarrow Tm}$, we see that θ can be determined from the energy transfer microparameters . In Chapter 2, we discussed the different ways

---

126 S. A. Payne, L. L. Chase, L. K. Smith, W. L. Kway, and W. F. Krupke, "Infrared cross-section measurements for crystals doped with Er^{3+}, Tm^{3+}, and Ho^{3+}", IEEE J. Quant. Elect., V28, N11, (1982), P2619.

127 M. E. Storm, "Holmium YLF amplifier performance and the prospects for multi-joule energies using diode-laser pumping", IEEE J. Quant. Elect., V29, N2, (1993), P440.

of that C_{da} could be obtained from experimental data. C_{da} can be determined from dynamic decay data with Eq. 2.3.5, or from the overlap of transition cross-sections with Eq. 2.2.3.

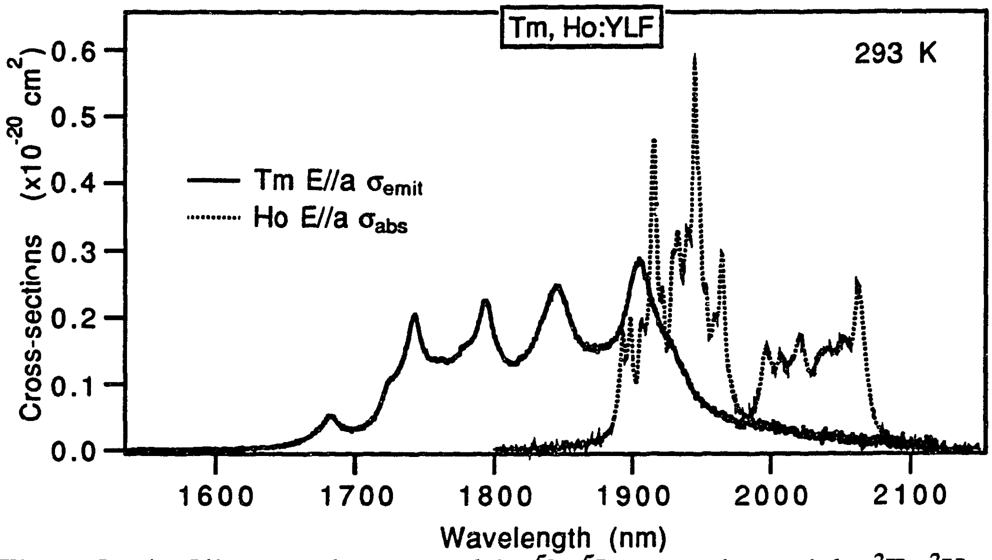

Figure 5.1.4. E//a spectral overlap of the $^5I_8$-$^5I_7$ absorption and the $^3F_4$-$^3H_6$ emission. The overlap of these spectra is proportional to the probability of $^3F_4$-$^5I_7$ energy transfer.

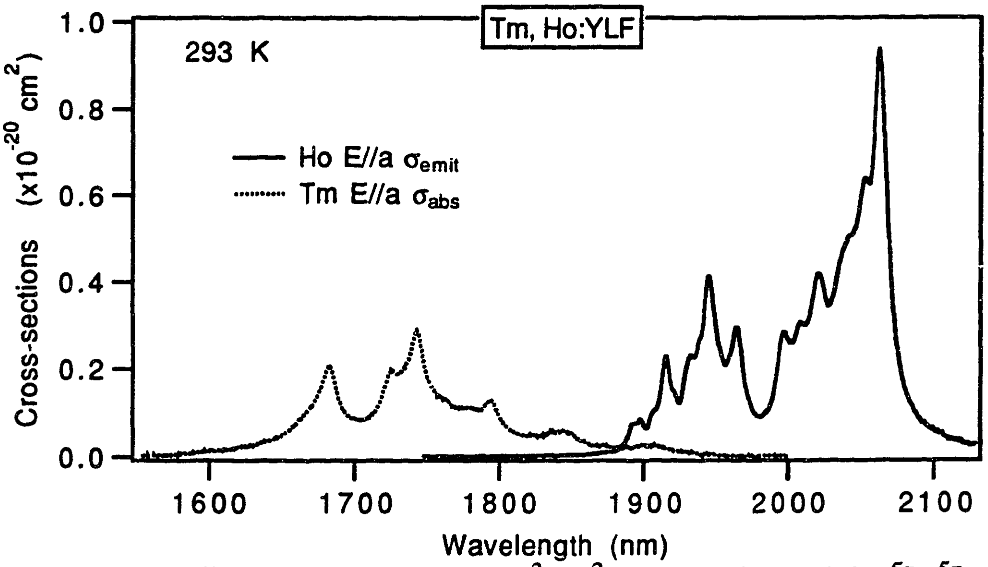

Figure 5.1.5. E//a spectral overlap of the $^3H_6$-$^3F_4$ absorption and the $^5I_7$-$^5I_8$ emission. The overlap of these spectra is proportional to the probability of $^5I_7$-$^3F_4$ energy transfer.

Figure 5.1.4 displays the overlap of the Tm $^3F_4$ emission and the Ho $^5I_7$ absorption cross-sections, while Fig. 5.1.5 displays the overlap of the Ho $^5I_7$ emission and the Tm $^3F_4$ absorption cross-sections. C_{da} for energy transfer from Tm to Ho can be calculated from the overlap in Fig. 5.1.4 and for back-transfer from Ho to Tm from that in Fig. 5.1.5. The calculated transfer micro-parameters are summarized in Table 5.1.2.

Quantity	E//a	E//c	Ave
$C_{Tm\text{->}Ho}$	$(26.4\pm2)\times10^{-40}$ cm^{3}s^{-1}	$(36.8\pm2)\times10^{-40}$ cm^{3}s^{-1}	$(29.9\pm2)\times10^{-40}$ cm^{3}s^{-1}
$C_{Ho\text{->}Tm}$	$(1.2\pm0.2)\times10^{-40}$ cm^{3}s^{-1}	$(2.3\pm0.3)\times10^{-40}$ cm^{3}s^{-1}	$(1.6\pm0.2)\times10^{-40}$ cm^{3}s^{-1}
Ratio (θ)	21±4	16±3	18.7±3

Table 5.1.2. Energy transfer microparameters for $^3F_4$-$^5I_7$ transfer and back transfer calculated from overlap integrals. Values are for Tm and Ho in YLF at 293K. θ is dimensionless.

As can be seen, there is a substantial difference between the microparameters for different polarizations. This is not surprising as YLF is uniaxial; and, by themselves, these differences are not a direct indication of error. The ratio of the transfer parameters, however, should be independent of polarization; and these agree within experimental uncertainty. The value of θ we find for these measurements agrees with the value expected from the energy levels, which is 17.8.

The average value of the transfer parameter was obtained by averaging two times the E//a microparameter plus the E//c microparameter. The E//a parameter was weighted twice as high since there are two a axes in YLF. We have only assumed that we can average in this manner, however. The proper way to treat some details of the energy transfer process in anisotropic materials is still open to debate; we will return to this subject in the discussion of Chapter 7.

5.2. Direct Measurement of the Distribution at Room Temperature.

We can directly determine θ by measuring the relative population of $^5I_7$ and $^3F_4$ in the steady state. The intensity of fluorescence from a manifold is proportional to the Einstein A coefficient and the population of the manifold, i.e., $I_x=A_xN_x$, where I_x is the total integrated intensity of the fluorescence spectra. The ratio of the emission from two different species of ions is

$$\frac{I_1'}{I_1}=\frac{A_1'N_1'}{A_1N_1}\Rightarrow\frac{N_1'}{N_1}=\frac{A_1I_1'}{A_1'I_1}=\frac{\tau_1'^R I_1'}{\tau_1^R I_1}, \qquad (5.2.1)$$

Here we have used the standard relationship between the Einstein A coefficient and the radiative lifetime. ($A=1/\tau$) The above expression can be related to θ with Eq. 3.1.4. to yield

$$\frac{N_1'}{N_1}=\frac{\tau_1'^R I_1'}{\tau_1^R I_1}=\theta\frac{N_{Ho}}{N_{Tm}}\Rightarrow\theta=\frac{\tau_1'^R I_1' N_{Tm}}{\tau_1^R I_1 N_{Ho}}. \qquad (5.2.2)$$

As can be seen from Eq. 5.2.2, we can determine θ with a knowledge of the ionic concentrations, the single ion radiative lifetimes, and the relative fluorescence intensity of the two ions. The concentrations in our materials are known to ±2%. The radiative lifetimes were determined from a standard lifetime measurement (described in Chap. 4) and are known to ~5% accuracy. We have assumed that $\tau^R \equiv \tau_{meas}$ as the relaxation from $^3F_4$ and $^5I_7$ should be primarily radiative in lightly doped materials.

The relative photon flux was determined from fluorescence spectra obtained with the experimental arrangement described in Chap. 4. The excitation density was less than 1×10^{18} ions/cm^3, ensuring that the conditions necessary for the approximation (low excitation densities) which yielded Eq. 3.1.4 were satisfied for the materials considered. The crystal position was optimized for each measurement in the manner described earlier.

The contribution of each ion to the fluorescence was found by fitting the measured single-ion spectra to the fluorescence spectra measured from the co-doped system. This was accomplished in the following manner. The fluorescence spectra from singly doped materials were obtained and used as standards. Spectra from codoped materials were then recorded in the same experimental configuration. Intense fluorescence peaks unique to each ion were identified in regions where there were minimal contributions from the other ion. For Tm, these peaks were found in the 1600-1850 nm region, while for Ho this region was for wavelengths > 2000 nm. Comparison of peak intensities in the codoped materials with those in the singly doped samples allowed a scaling factor for each ion's contribution to the total fluorescence spectra to be obtained. Typical fluorescence spectra are shown in Fig. 5.2.1.

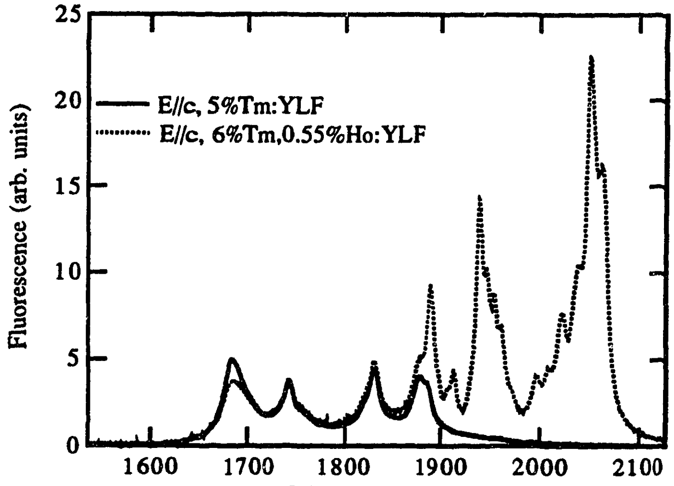

Figure 5.2.1. Typical corrected fluorescence spectra.
Some reabsorption is evident in this spectra for singly-doped Tm. The spectra have been scaled to overlay each other in the manner used to produce the relative fluorescence intensities.

Spectra were converted from units of power/nm to units of photons/nm by multiplication by the wavelength. (This was required as the spectral response function used to correct the spectra was in units of power per nm, while the relation between I_x, A_x, and N_x is for a photon flux. The relationship between energy and wavelength for photons is given by $E=hc/\lambda$, where h is Planck's constant, E is the energy of a photon, c is the speed of light, and λ is the wavelength of the photon. Therefore, we must multiply all spectra by a factor proportional to $1/\nu$, or λ, to convert from units of power to units of photons per second)

By integrating the spectra we obtained a number proportional to the total number of photons emitted. We could scale the values for our standard spectra with the scaling factors previously determined to find the contribution of each ion to the flux from the codoped sample. The ratio of each ion's total flux gave the ratio of intensities; which could then be scaled by the lifetimes and concentrations to produce θ. For anisotropic materials, the flux contributions of the independent polarizations were summed together before taking this ratio. The results of these measurements for a number of samples of Tm,Ho:YLF at 293 K are presented in Fig. 5.2.2.

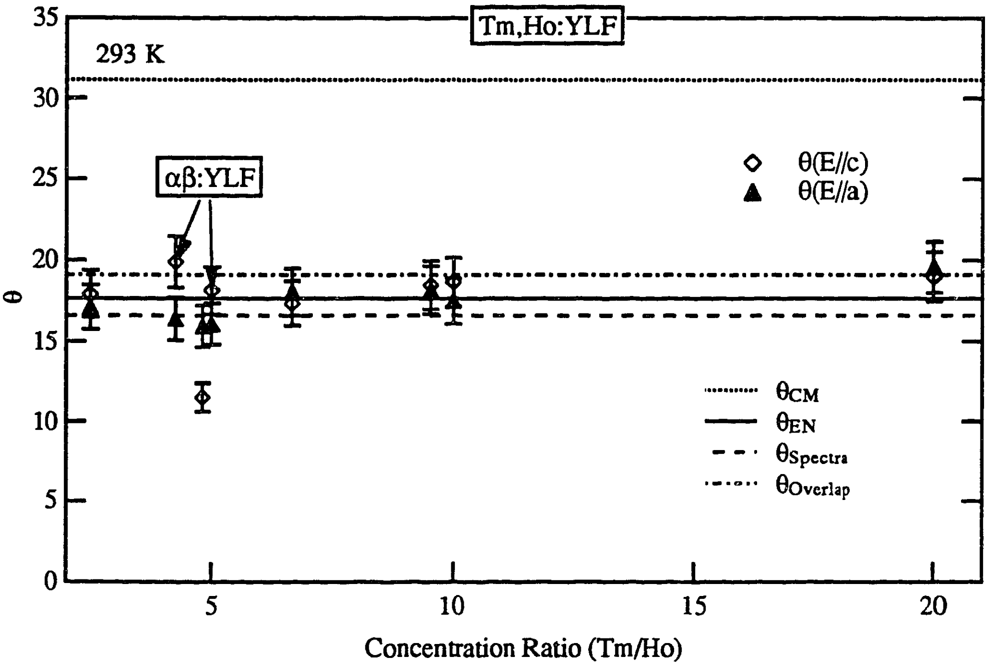

Figure 5.2.2. Measured θ for Tm, Ho: YLF at 293 K. Data are presented for measurements taken in both polarizations.

In the above figures, θ_{CM} represents the value which would be expected by applying the canonical ensemble to only the $^5I_7$ and $^3F_4$ manifolds (Castleberry's method - Eq. 3.2.3). θ_{EN} represents the chemical potential approach and is calculated from Eq. 3.2.7 using the energy level data available in the literature[114, 115]. $\theta_{Spectra}$ represents the value calculated with chemical potentials read directly from the emission and absorption cross-sections; while $\theta_{Overlap}$ is the value calculated directly from transfer microparameters determined from the overlap of the cross-sections. The values for $\theta_{Spectra}$ and $\theta_{Overlap}$ were calculated in Section 5.1. The values obtained by both the indirect and the direct measurements agree within the bounds of experimental uncertainty. Note the large difference between the measured values for θ and the predictions of the canonical ensemble when only the $^5I_7$ and $^3F_4$ manifolds are included in the summation.

The direct measurements were conducted on Tm, Ho:YLF samples with Tm concentrations in the range of 5-6% and Ho concentrations in the range of 0.3%-1.25%. A single sample of 2% Tm, 2% Ho:YLF was also used. In addition, Er, Tm, Ho:YLF samples were measured; the measurements from these samples are marked αβ:YLF in Figure 5.2.2. The Tm concentrations in the αβ:YLF samples were in the 7.2-7.5% range, and the Ho concentrations ranged between 1.5-1.7%. Additionally, we use the lifetimes reported in Chapter 4 for the scaling of Eq. 5.2.2 (τ'_R=13.5 ± 0.5 ms and τ_R=14.0 ± 0.5 ms for YLF).

Two values, denoted E//a and E//c, have been reported for each sample. These measurements were produced using scaling factors derived from the measured peak intensities in their respective polarizations; the total integrated intensity scaled by these values includes both the contribution of the E//c and the E//a polarizations in YLF. Each polarization is an independent check on the value of θ, and the difference between the values obtained for each polarization indicates either an error in orientation of the sample or a systematic error in our measured response. These measurements have also been conducted for Tm,Ho:YAG and are shown in Fig. 5.2.3

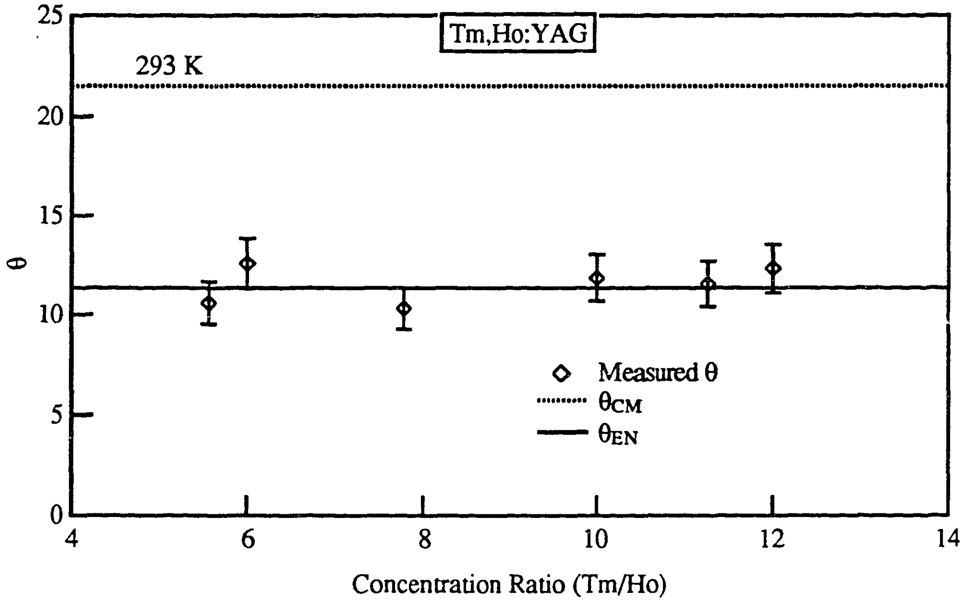

Figure 5.2.3. Measured θ for Tm, Ho:YAG at 293K. Energy levels are from [118, 119].

Note that the results for YAG also support our model of the distribution. In Tm, Ho:YAG at room temperature, the value expected for θ using the chemical potential approach is 11.3, in contrast to the value of 21.7 as would be expected using Castleberry's method. Thus it can be seen that the Castleberry's method will considerably overestimate the amount of excitation stored in the $^5I_7$ manifold for a given excitation level.

The quantitative difference between the Castleberry's method (Eq. 3.2.3) and the chemical potential approach becomes more pronounced at lower temperatures, although the qualitative behavior is similar. We have applied the methods described above to measurements of the distribution performed at lower temperatures. Figure 5.2.4 displays data from Tm, Ho: YLF as the sample is cooled from 293 K to 175 K.

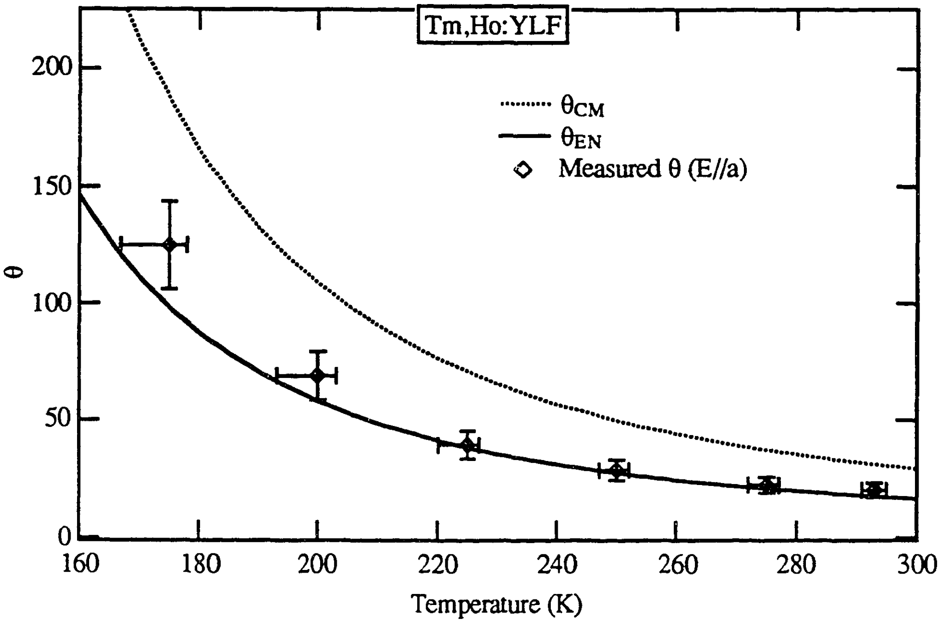

Figure 5.2.4. θ coefficient as a function of temperature for Tm, Ho: YLF.

As can be seen in Fig. 5.2.4, there is good agreement between the predictions by the chemical potential approach and the measured $^3F_4$ and $^5I_7$ population distribution over a wide range of temperatures. The uncertainty in these measurements increases as the temperature is decreased since the population stored in the $^3F_4$ drops considerably.

The results presented in this section support the proposed model of the quasi-equilibrium distribution for various concentrations of Tm and Ho in YLF and YAG. The predictions of the simple Boltzmann distribution typically assumed are not consistent with these results.

5.3 Uncertainty Analysis.

In our measurements, there are 3 basic sources of experimental uncertainty; the dopant concentrations, the manifold lifetimes, and the system response and calibration of the fluorescence measurement system. Uncertainties in these quantities will affect each of our measurements in different ways.

Dopant concentrations for all samples were calibrated against a standard sample in each material. Most samples were found to be with ±2% of their stated concentrations relative to the concentration of the reference standard. The absorption cross-sections using samples with calibrated concentrations were measured, and the results agree well with previously reported values. The uncertainty in our concentrations is roughly ±1%. Errors in the dopant concentrations will be reflected linearly as scaling errors in the absorption cross-section and the directly measured values of θ. Scaling errors in the cross-section will shift the chemical potential and linearly scale the values of the energy transfer microparameters calculated with Eq. 2.2.3. Thus, uncertainties in these concentrations will contribute roughly 2% to the total statistical uncertainty for each measurement.

The radiative lifetimes for each material (τ_R) were determined in a separate set of measurements using the lifetime apparatus detailed in Chapter 4. The measurements were performed on low concentration (<1% doping) samples, so the lifetimes should be relatively free of reabsorption lengthening of the lifetimes. The measured lifetimes can be interpreted as the radiative lifetimes since there will be negligible multiphonon quenching of the $^5I_7$ and $^3F_4$ manifolds because of the large energy difference between these manifolds and the ground states. Several samples were measured (when available); the reported lifetimes represent the average of the several different measurements. Variations of ±3% in the measured lifetime were observed dependent on the configuration of the experiment. Impurity quenching was evident in some samples; the lifetimes of these samples were not used to produce the average lifetime. Values for lifetimes reported in the literature vary considerably. As an example, measurements of the Tm $^3F_4$ lifetime in YLF range from 12 ms to 16 ms[126]. Our value, 14.0±0.5 ms, is consistent with the bulk of the reported values for YLF. The uncertainty in our lifetimes for the $^3F_4$ and $^5I_7$ manifolds is roughly 5%, which enter the results as a systematic uncertainty since any error will shift all values in the same manner.

The chief source of uncertainty in our measurements comes from the uncertainty in the system response. As absolute intensity measurements are very difficult to perform, our analysis techniques have been designed to use only the shape of the spectra and their relative intensities. We are not sensitive to the absolute magnitude of the system response as we effectively cancel the magnitude of this response by using intensity ratios. Our techniques are sensitive to the shape of the response, however. Errors in the shape of the response will be reflected as errors in the shapes of the fluorescence spectra.

The response function for any configuration of optics, monochromator, and detectors was produced by measuring the emission of a calibrated source. The calibrated spectra of that source was then divided by the measured spectra to produce the response function. Our calibration source was a calibrated tungsten bulb placed a specific distance from the monochromator entrance slit.

The shape of the response function could be roughly checked with McCumber's relation. Taking the emission cross-section produced from corrected fluorescence spectra, we divide by the absorption cross-section measured in the same polarization at the same temperature. The resulting exponential should be described by $e^{-\beta(\mu-E(\lambda))}$. By fitting to the ratio of the cross-sections to this exponential, we should be able to find the temperature at which the spectra were recorded from the exponent. Figure 5.3.1 contains a plot of the result of this procedure for the E//a spectra in Tm:YLF.

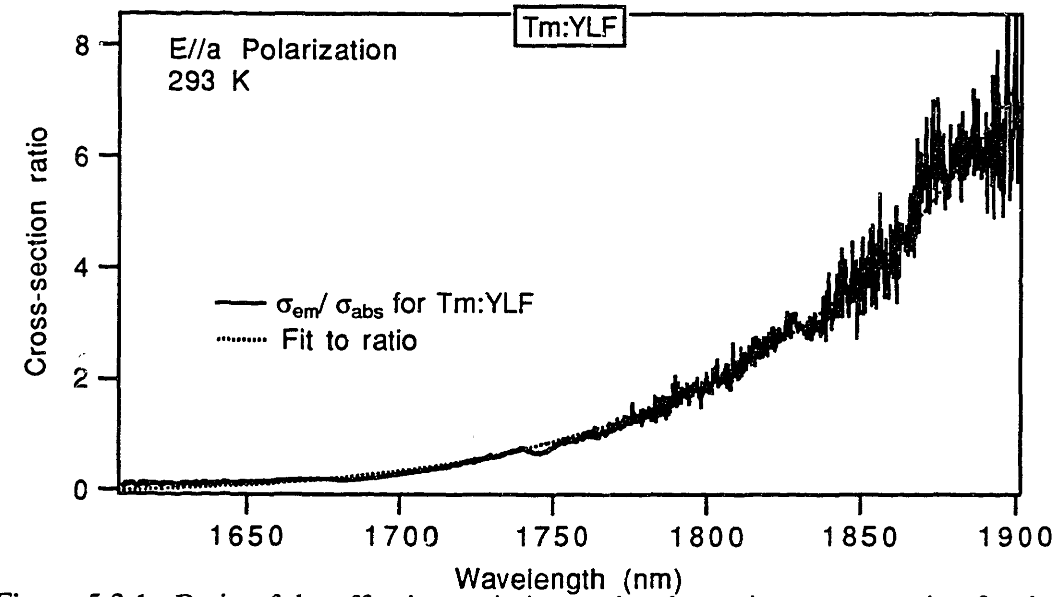

Figure 5.3.1. Ratio of the effective emission to the absorption cross-section for the E//a polarization of Tm:YLF. The temperature implied by the exponent of the fit is 310±25K.

An exponent which indicates a different temperature from the known temperature of the measurement indicates an error in the response function which will weight the ion fluorescence disproportionately. A response function which produces an exponential temperature less than the known temperature will weight long-wavelength emission more than short wavelength emission. By comparing the measured run temperatures with the known run temperatures in the manner just described for our spectra, we estimate that not more than a 10% weighting error will exist in the 1600-2100 nm region. This weighting error would result in a systematic shift of all data presented; this systematic shift would not exceed ~5% of the reported values.

It is apparent that no gross errors exist in the shape of the response function--errors would show up as bumps or dips in Fig. 5.3.1. However, measurements of anisotropic samples are also sensitive to the relative magnitude of the response function for the different polarizations used. The relative scaling and shapes of the response function for the different polarizations were checked by comparison of the corrected fluorescence spectra of isotropic samples taken in each polarization. The response functions produced spectra which overlaid one another fairly well, with only small apparent discrepancies. These discrepancies give rise to the slightly different values of θ apparent in Fig. 5.2.2 for measurements performed in the different polarizations for the same sample. The relative scaling of these spectra was also checked by comparison with absorption data.

The net systematic uncertainty from these sources would results in at most a 15-20% shift in the average value of θ. It is clear that the difference between the predictions of Castleberry's approach and our measurements can not be explained as a systematic error.

5.4. Summary.

In this chapter, we have determined the distribution of excitations between the $^3F_4$ and the $^5I_7$ manifolds with three different measurement techniques. These measurements confirm our model for the distribution of excitations between the $^5I_7$ and $^3F_4$ manifolds as the exponential difference of the manifolds' chemical potentials. The chemical potential of each manifold can be determined from the material's energy levels or from measurements of the emission and absorption cross-sections for transitions between the manifold and the ground state. These measurements reject Castleberry's method of calculating the distribution by using a canonical summation over only the $^3F_4$ and $^5I_7$ manifolds.

6. Transfer Processes Between Other Levels.

In the preceding chapter we confirmed the steady-state distribution of excitations between manifolds which we predicted in Chap. 3. In our derivation of this relationship, we also derived a relation between the energy transfer micro-parameters for forward and reverse transfer processes (Eq. 3.2.5). This relationship should allow us to connect different types of measurements to one another, and we would like to test this relationship in a variety of experimental settings.

For many situations of interest, the populations of the manifolds involved in the energy transfer will not come to equilibrium. This will occur when the energy transfer rates are less than or comparable to the intrinsic relaxation rates of the manifolds involved or when the time scale of the experiment is less than the equilibration time. In these situations, it is clear that we can not apply the relationships between equilibrium populations of the manifolds which we confirmed in Chapter 5.

However, the relationship between the transfer and back-transfer microparameters (Eq. 3.2.5) derived in Chapter 3 requires only that the manifold self-equilibrates rapidly in comparison to the energy transfer processes. For rare-earth doped systems this relationship should be valid since the manifold equilibrates in $\approx 10^{-10}$ s, whereas the minimum time scale for energy transfer is $\approx 10^{-7}$ s. We therefore expect that $C_{da} = \theta\, C_{ad}$. However, the relation between the energy transfer microparameters (C_{da}'s) and the average transfer parameters (α's) used in the derivation of Chapter 3 was only an approximation, and it is not clear that the average transfer parameters for forward and reverse transfer processes can be described by $\alpha_1 = \theta\alpha'_1$ for time scales short in comparison to the equilibration time. The average transfer parameters will depend on the details of the transfer process and are sensitive to such processes as migration. If we can establish under which conditions a relation between the average transfer parameters exists (and if such a relation actually exists), we will be able to simplify measurements of these transfer parameters. Specifically, if the relationship $\alpha = \theta\alpha'$ holds for the Tm-Ho system (where the α is the average transfer parameter for a process and α' the parameter for the reverse process), we will be able to determine the upconversion parameters from measurements of the cross-relaxation parameters. Measurements of the upconversion parameter are difficult and complicated; additionally, the results are often model dependent. In contrast, cross-relaxation measurements are fairly straightforward to perform and interpret. Therefore, the establishment of a relationship between the average transfer parameters for forward and reverse processes holds the promise of greatly simplifying experimentation.

We will explore these relationships in the Tm-Ho doped system. The measurements of this chapter serve a dual purpose. Not only will the measurements allow us to explore the relationships between the transfer parameters, but they will also provide values of the transfer parameters required for the modeling of 2 μm Tm-Ho lasers.

We will first explore the rate relationship in singly-doped Tm. This is a simpler system than the Tm-Ho doped system and will serve to illustrate the basic techniques used to measure the cross-relaxation and upconversion parameters. Additionally, it will give us information on the process which feeds the $^3F_4$ manifold when the $^3H_4$ manifold is excited by direct pumping. The goal of these measurements is to find if the expected relationship between average transfer parameters applies.

6.1. Energy transfer processes in Tm^{3+}.

The energy level diagram for Tm is shown if Fig. 6.1. Earlier it was mentioned that an efficient cross-relaxation process turns an excitation deposited in the $^3H_4$ level into two $^3F_4$ excitations. The reverse of this process is also possible, although the energy mismatch between the $^3H_4$ and the $^3F_4$ does not favor the process.

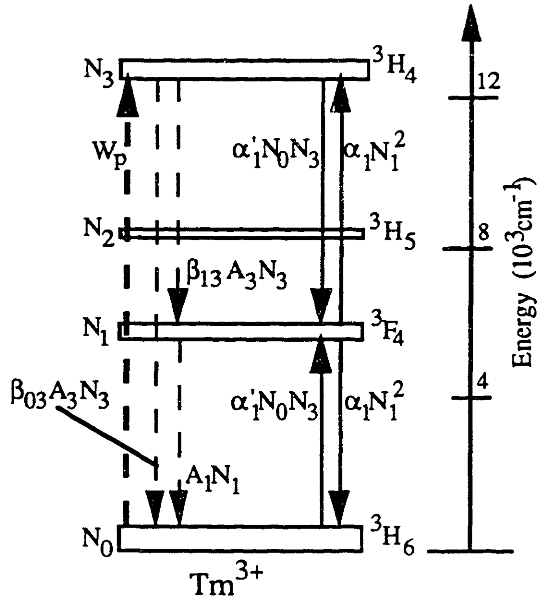

Figure 6.1.1. Energy transfer processes in singly-doped Tm. Solid arrows represent energy transfer processes, while the dotted arrows represent radiative processes.

In Fig. 6.1.1, N_0, N_1, N_2, and N_3 are respectively the populations of the $^3H_6$, $^3F_4$, $^3H_5$, and $^3H_4$ levels. α_1 is the transfer parameter for $^3H_4$-$^3F_4$ upconversion and α_1' is the cross-relaxation parameter. A_3 and A_1 are the Einstein A coefficients of the respective manifolds, and β_{13} and β_{03} are respectively the branching ratios for emission from the $^3H_4$ manifold to the $^3F_4$ and the $^3H_6$ manifold. We have made the assumption that the transfer processes can be described with an average transfer parameter, α. The rate equations for this simplified model are expressed below.

$$\begin{aligned}\dot{N}_3 &= W_p - A_3N_3 - \alpha_1'N_3N_0 + \alpha_1N_1^2 \\ \dot{N}_1 &= \beta_{13}A_3N_3 + 2\alpha_1'N_3N_0 - 2\alpha_1N_1^2 - A_1N_1 \\ \dot{N}_0 &= -\dot{N}_1 - \dot{N}_3\end{aligned}$$

Here we have assumed that the $^3H_5$ manifold is primarily quenched by multiphonon relaxation to the $^3F_4$ and therefore dropped this manifold from the rate equations. This approximation is justified as little fluorescence is observed from this manifold in most materials (at room temperature). As the energy gap between these manifolds is ~2400 cm^{-1}, it can easily be bridged by a multiphonon relaxation process in most materials. For now we neglect the $^3H_5$, although this manifold may be of importance for some transfer processes and will be discussed later.

In our original derivation of the equilibrium relations, we placed no restrictions on which manifolds were connected by the energy transfer processes. Therefore, we would expect these relations to be valid for any set of manifolds. We can relate the upconversion parameter (α_1) to the cross-relaxation parameter (α'_1). If the system shown in Fig. 6.1.1 came to equilibrium, we could say

$$\alpha_1N_1^2 = \alpha_1'N_0N_2. \tag{6.1.1}$$

This implies

$$\frac{N_2}{N_1} = \theta_1\frac{N_1}{N_0}. \tag{6.1.2}$$

Carrying out some manipulations, we find

$$\theta_1 = \frac{\alpha_1}{\alpha_1'} = \frac{N_0 N_2}{N_1^2}, \text{ where}$$

$$\theta_1 = \frac{\sum_i^{3H6} g_i e^{-\beta\varepsilon_i} \sum_j^{3H4} g_j e^{-\beta\varepsilon_j}}{\left(\sum_k^{3F4} g_k e^{-\beta\varepsilon_k}\right)^2}. \tag{6.1.3}$$

For the energy levels in BaY_2F_8, this yields a ratio between the transfer microparameters of 3.1×10^{-3}. Although the manifold populations will not be in equilibrium for the following experiments, the manipulations performed above are a convenient way of figuring out the ratio between the two transfer microparameters (See Appendix B). We could also obtain this relation by using the difference in the chemical potential between the $^3H_4$ and the $^3F_4$ manifolds as one of the chemical potentials in Eq. 3.2.5[†]. The relationship between the microparameters (Eq. 3.2.5) should be applicable whenever the manifolds are internally in equilibrium. We assume that the average transfer parameters will also follow this relationship. To see if this relationship holds, we now measure the cross-relaxation and upconversion parameters independently.

6.1.1. Measurement of the cross-relaxation parameter.

The cross-relaxation rate, $\alpha_1'N_0$, can be determined by observing the change in the lifetime of the $^3H_4$ manifold with changing Tm concentration. Using the lifetime apparatus described in Chap. 4, we directly pump the $^3H_4$ manifold with a pulsed Ti:Sapphire laser and monitor the fluorescence to the ground state. The manifold was pumped at ≈780 nm and the fluorescence was measured through a bandpass filter centered at 840 nm. An S-1 type photomultiplier with a measured response time of <200 ns was used for the measurements. The pulse length of the pump laser was on the order of 20 ns.

The unquenched lifetime of the $^3H_4$ manifold was found to be 2.33±0.05 ms in a low concentration sample. As the concentration of Tm was increased, this lifetime shortened. By examination of the rate equation for the $^3H_4$ manifold, we attribute this shortening to cross-relaxation . The $\alpha'N_1^2$ term in the rate equation can be neglected (for

---

[†] Actually, the chemical potentials used in Eq. 3.2.5 to calculate the $^3F_4$-$^5I_7$ equilibrium distribution are the differences in the chemical potential of the $^3F_4$ and the $^3H_6$ manifolds and of the $^5I_7$ and $^5I_8$ manifolds. As all the chemical potentials have been calculated relative to the ground state, there is no difference for these quantities when one of the manifolds is the ground state.

now) as excitation densities are low and α' should be small in comparison to α. Plots of the $^3H_4$ fluorescence are shown in Fig. 6.1.2. for different concentrations of Tm:BaY_2F_8.

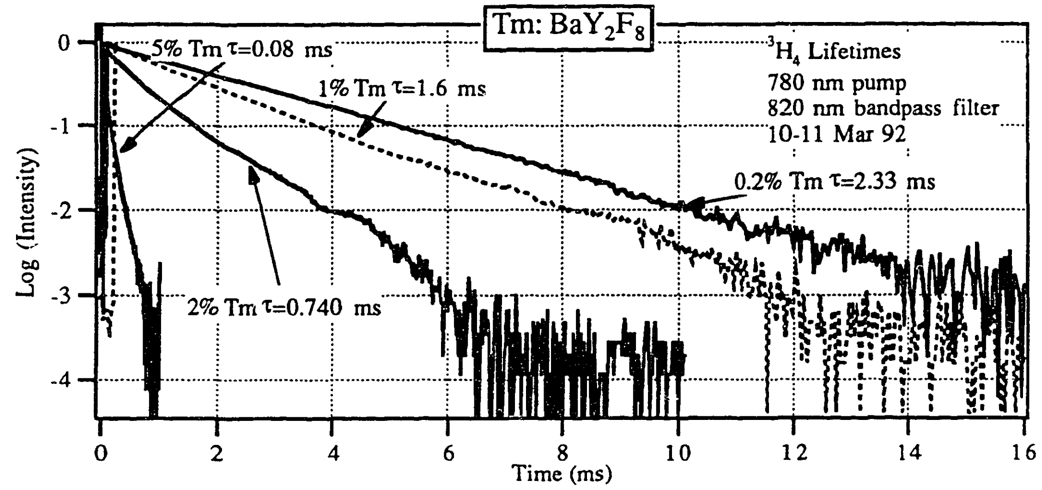

Figure 6.1.2. $^3H_4$ decay dynamics of Tm:BaY_2F_8 for varying Tm concentration.

As can be seen, the lifetime decreases dramatically with increasing Tm concentration. An average cross-relaxation rate can be found from these measurements with the relation $W=W_{cr}+W_{in}$, where the total relaxation rate (W) is the inverse of the lifetime of the decay as found by approximating the decay as linear. W_{in} is the intrinsic single-ion relaxation rate for low concentration materials. ($W_{in}=A_3$, or 4.3×10^2 s^{-1} in this case). The values for W_{cr} calculated with this relationship are found in Fig. 6.1.3.

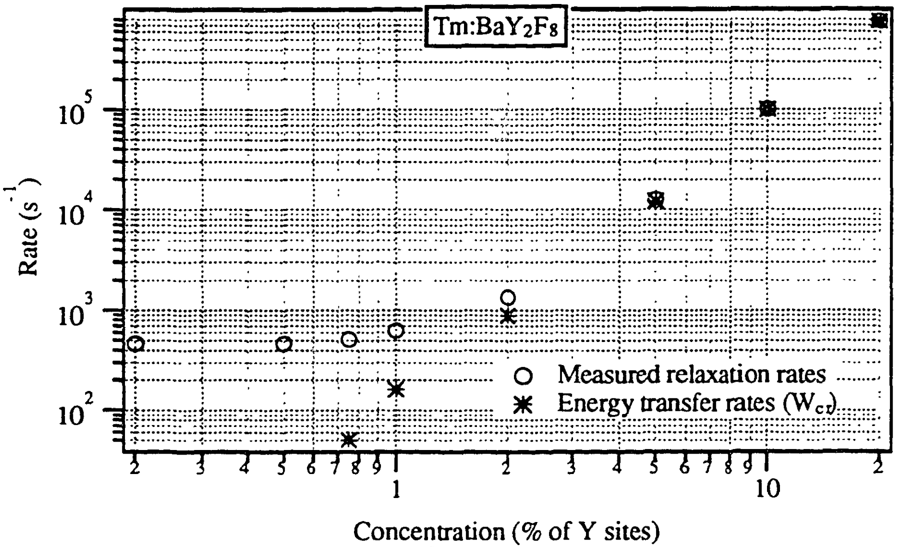

Figure 6.1.3. Relaxation rates of the $^3H_4$ manifold of Tm:BaY_2F_8 as a function of concentration and the cross-relaxation rates calculated from these measurements.

Note how the cross-relaxation rates increase linearly with ion concentration. This is an indication that only one type of energy transfer process is active in the system. We suspect that the cross-relaxation process is a static-type process. The cross-relaxation parameter α_1', can be calculated from the average cross-relaxation rates using the relation $W_{cr}=\alpha_1' N_0$. Figure 6.1.4 displays the calculated values of α_1' for varying Tm concentrations.

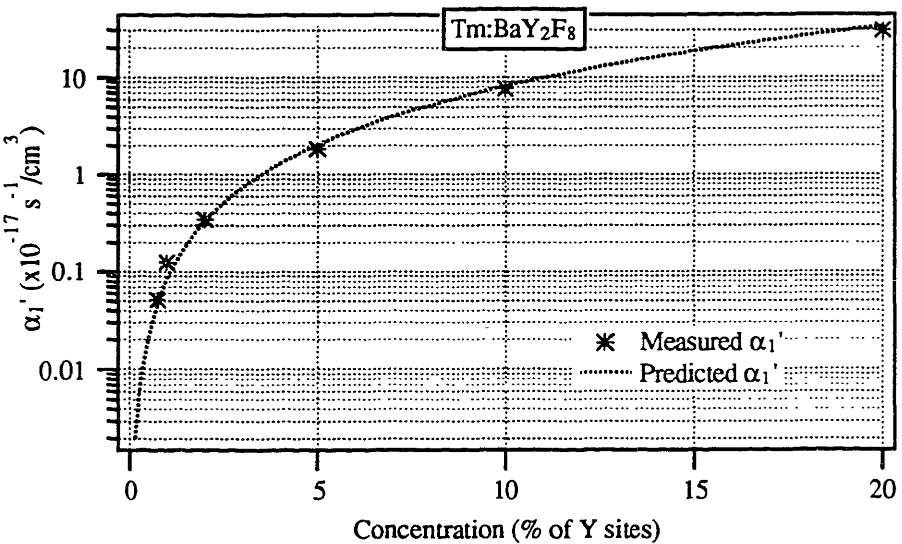

Figure 6.1.4. Average cross-relaxation parameter as a function of concentration. Values for the cross-relaxation parameter have been calculated from the cross-relaxation rates.

In Figure 6.1.4, we have plotted the concentration dependence that would be expected for the static dipole-dipole quenching[128], i.e.

$$\alpha(C) \cong \alpha(C_0)\left(\frac{C}{C_0}\right)^2 . \tag{6.1.4}$$

This approximate concentration dependence arises as the average distance between ions is inversely proportional to the cubic root of the concentration; while the transfer parameter is proportional to the average of the sixth power of the distance between ions. In short, we have approximated α_1 for static processes as

---

[128] This is equivalent to the concentration-lifetime relationship of D. L. Dexter and J. H Schulman, "Theory of Concentration Quenching in Inorganic Phosphors", J. Chem. Phys., V22, N4, (1954), P1063, and confirmed for Tm, Ho:YLF in G. Armagan, IBID.

$$\alpha_{da} = \frac{1}{N_d N_a} \sum_{i,j} \frac{C_{da}}{r_{ij}^6} = C_{da} \left\langle \frac{1}{r_{da}^6} \right\rangle \cong C_{da} \left\langle \frac{1}{r_{da}} \right\rangle^6 . \qquad (6.1.5)$$

By substituting $\langle r_{da} \rangle = C^{-1/3}$ into Eq. 6.1.5 (and selecting a reference concentration C_0), Eq. 6.1.4 results. In principle the energy transfer microparameters for this process could also be determined by fitting the transients with the static quenching relation discussed in Section 2.3, but our data lacks adequate resolution to provide an accurate fit. However, for our purposes only the average transfer parameters are required. These relations are only approximations; we will return to this approximation in the discussion. Various quantities derived from these measurements are summarized in Table 6.1.1.

Conc.(Tm)	$^3F_4$ τ (ms)	$^3H_4$ τ (μs)	W_{cr} (s^{-1})	α_1'(cm^3s^{-1})	χ_{cr}	Predicted α_1 (cm^3s^{-1})
0.2%	*	2.33×10^3	*	*	*	
0.5%	17±0.7	2.16×10^3	28	4.3×10^{-19}	0.06	1.3×10^{-21}
0.75%	17.2±0.7	1.95×10^3	78	8.0×10^{-19}	0.15	2.5×10^{-21}
1%	17.5±0.7	1.6×10^3	1.9×10^2	1.4×10^{-18}	0.30	4.3×10^{-21}
2%	17.5±0.7	740	9.2×10^2	3.5×10^{-18}	0.68	1.1×10^{-20}
5%	14.5±0.6	80	1.2×10^4	1.8×10^{-17}	0.96	5.6×10^{-20}
10%	14.4±0.6	~10	1.0×10^5	7.7×10^{-17}	~1.00	2.4×10^{-19}
20%	6±0.6	~1.5	6.7×10^5	2.6×10^{-16}	~1.00	8.1×10^{-19}

Table 6.1.1. Lifetimes and energy transfer parameters in BaY_2F_8 at room temperature.

For the higher Tm concentrations, the cross-relaxation rate is much larger than the spontaneous relaxation rate, and most of the excitations deposited in the $^3H_4$ manifold will relax by cross-relaxation to the $^3F_4$. We can define the quantum efficiency of this cross-relaxation process to be

$$\chi_{cr} = \frac{\alpha_1' N_0}{\alpha_1' N_0 + A_3}, \qquad (6.1.6)$$

where χ_{cr} is the probability that an excitation placed in the $^3H_4$ will decay by cross-relaxation to the $^3F_4$. In Table 6.1.1, we have tabulated the values of χ_{cr} for the different Tm concentrations. We have also calculated the value of a1 which would be expected from $\alpha_1 = \theta\alpha_1'$.

We are actually interested in comparing several materials. Table 6.1.2. summarizes the same parameters for YLF, YAG, and NYF.

Material	$^3H_4$ τ (μs)	W_{cr} (s^{-1})	a_1' (cm^3s^{-1})	χ_{cr}
0.25% Tm:YLF	2.10×10^3	*	*	*
0.5%	2.05×10^3	10	1.4×10^{-19}	0.02
1%	1.34×10^3	2.7×10^2	2.0×10^{-18}	0.36
5%	66	1.5×10^4	2.2×10^{-17}	0.97
6% *	37±4	2.7×10^4	3.2×10^{-17}	0.99
7%	25	3.9×10^4	4.0×10^{-17}	~1.00
10%	8.5	1.2×10^5	8.6×10^{-17}	~1.00
0% Tm:YAG	830	*	*	
.75	450	1.0×10^3	1.04×10^{-19}	0.45
2	200	3.8×10^3	1.5×10^{-17}	0.76
3.5	100	8.8×10^3	1.9×10^{-17}	0.88
6%	10	9.9×10^4	1.2×10^{-16}	0.99
0.9% Tm:NYF	1.5×10^3	*	*	
2.64% Tm:NYF	670	8.3×10^2	2.3×10^{-18}	0.55
5.56% Tm:NYF	90	1.0×10^4	1.4×10^{-17}	0.90

Table 6.1.2. Lifetimes and energy transfer parameters for $^3H_4$-$^3F_4$ transfer. Values for YLF are from [129] (except *), while values for YAG are from [92].

As can be seen, the values of the cross-relaxation parameters are roughly similar (for similar concentrations of Tm) for the materials listed for this process. The fastest cross-relaxation rate was found in YAG and the lowest in NYF. This is not surprising as the multiphonon relaxation rates are largest in YAG; we would expect the cross-relaxation rates to vary as the multiphonon rates since this cross-relaxation process is non-resonant. For the concentrations of Tm which were used in our codoped samples, the quantum efficiency of cross-relaxation will be greater than 95%. It can be seen from Eq. 6.1.6 that this quantum efficiency will fall as the Tm ground state becomes depleted; however, for operating conditions typical in Tm-Ho lasers this reduction will be small. A plot of the transfer parameters for various concentration of Tm in the different materials can be found below.

---

129 G. La Rosa, "Spectroscopy of Tm^{3+}:YLF as a Laser Material for Diode Laser Pumping," M.S. dissertation, Mass. Inst. of Tech., Aug. 1988.

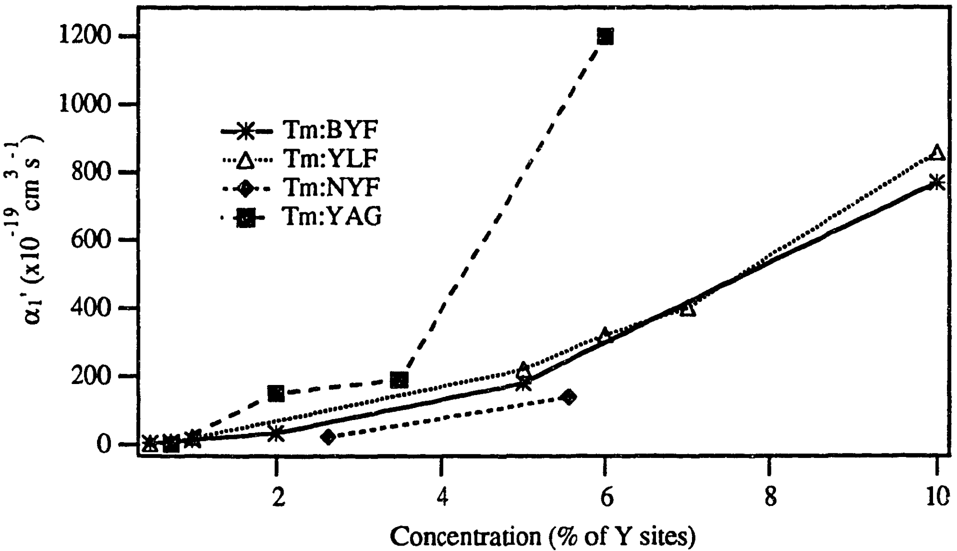

Figure 6.1.7. Cross-relaxation parameters for the various materials as a function of concentration. The parameters for YLF were calculated from La Rosa[129], while the parameters for YAG were calculated with values from G. Armagan[92].

6.1.2. $^3F_4$->$^3H_4$ Upconversion.

We have found the α_1's for $^3H_4$-$^3F_4$ cross-relaxation. We now find α_1 by another method to see if the relationship between the average transfer parameter is valid. While this measurement will be difficult to make because of the expected small value of the upconversion coefficients, it will serve to illustrate the necessary concerns of upconversion measurements with a simple system before we attempt the more complicated Tm-Ho system. Our experimental apparatus is pictured in Fig. 6.1.8.

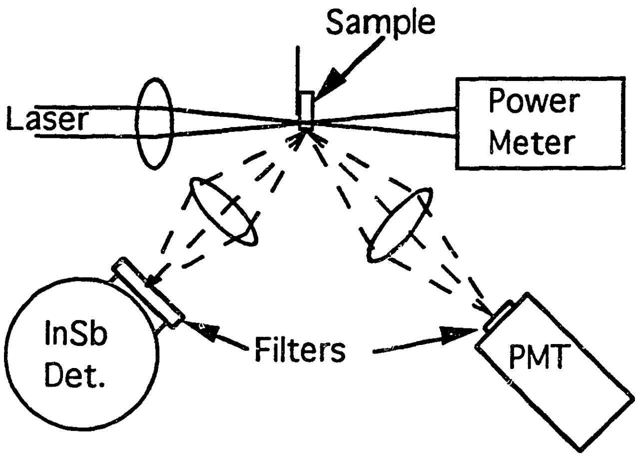

Figure 6.1.8. Apparatus used for the measurement of the $^3F_4$->$^3H_4$ upconversion.

In Figure 6.1.8, the pump beam from a cw Ti:Sapphire laser passes through a set of lenses and is focused to a small diameter spot in the sample. The sample mount had a razor edge for characterization of the pump beam profile. The sample and lenses were three-axis translationally adjustable. The pump was chopped to produce approximately square pulses with respect to time, and fluorescence transients were obtained. We use a thin sample to reduce the difference in the power absorbed over the length of the sample.

Due to the expected small value of the upconversion constant, we expect that we will need to obtain a high inversion density in order to see any measurable effects on the fluorescence of the material. Typical transients at high excitation densities (between 4%-18% inversion of the Tm ions) are shown in Fig. 6.1.9. Upconversion measurement techniques rely on precise knowledge of the excitation density in the material; uncertainties in the excitation density are directly reflected in the uncertainty of the upconversion parameter. By working at high enough excitation densities to partially deplete the ground state, we can measure the excitation density directly and eliminate some of the typical uncertainties in these measurements.

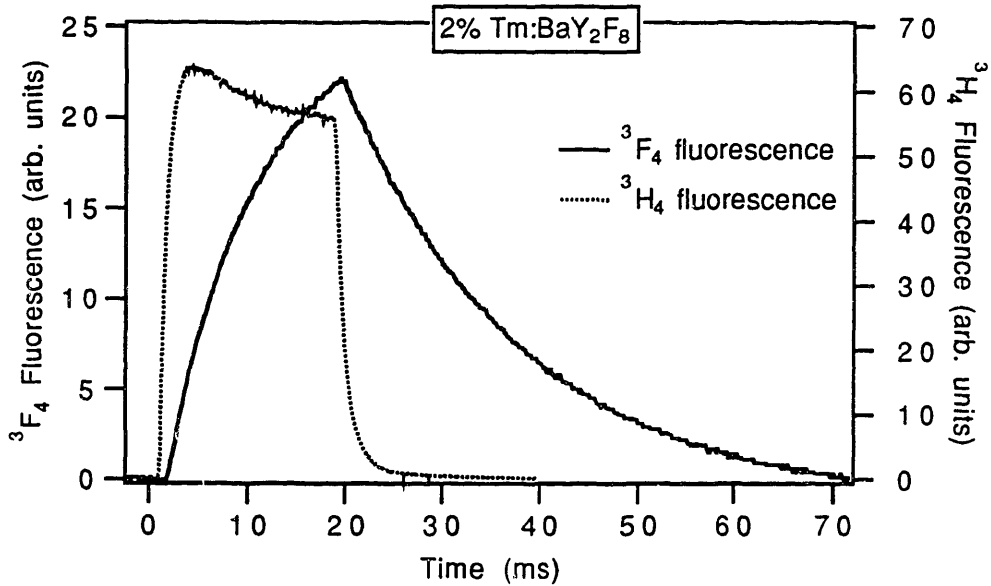

Figure 6.1.9 Plot of the $^3H_4$ and the $^3F_4$ fluorescence vs time in 2%Tm:BaY$_2$F$_8$ at high excitation levels.

A close examination of the above data reveals a lengthened decay tail in the $^3H_4$ transient which is indicative of upconversion feeding of the level. The lifetime of this exponential tail should be roughly half that of the $^3F_4$ lifetime. An expanded portion of the tail of the $^3H_4$ fluorescence transient is shown in Figure 6.1.10.

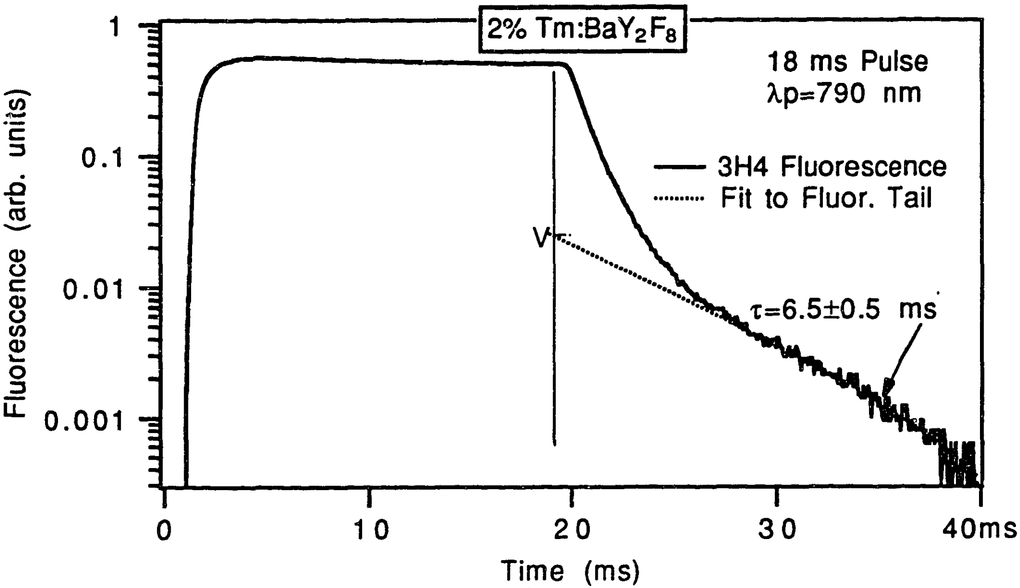

Figure 6.1.10. Logarithmic plot of the $^3H_4$ fluorescence transient. A long exponential tail is clearly visible. The lifetime of this tail is ~6.5 ms, roughly half that of the $^3F_4$ manifold. The initial component of the decay has a lifetime of ~850 μs.

Several different analysis techniques can be used to find α_1 from data such as that shown in Figures 6.1.9 and 6.1.10. Our method is to determine the population of the $^3F_4$ and the amount of upconversion resulting from that population at various of excitation levels. The technique is illustrated in Figure 6.1.11.

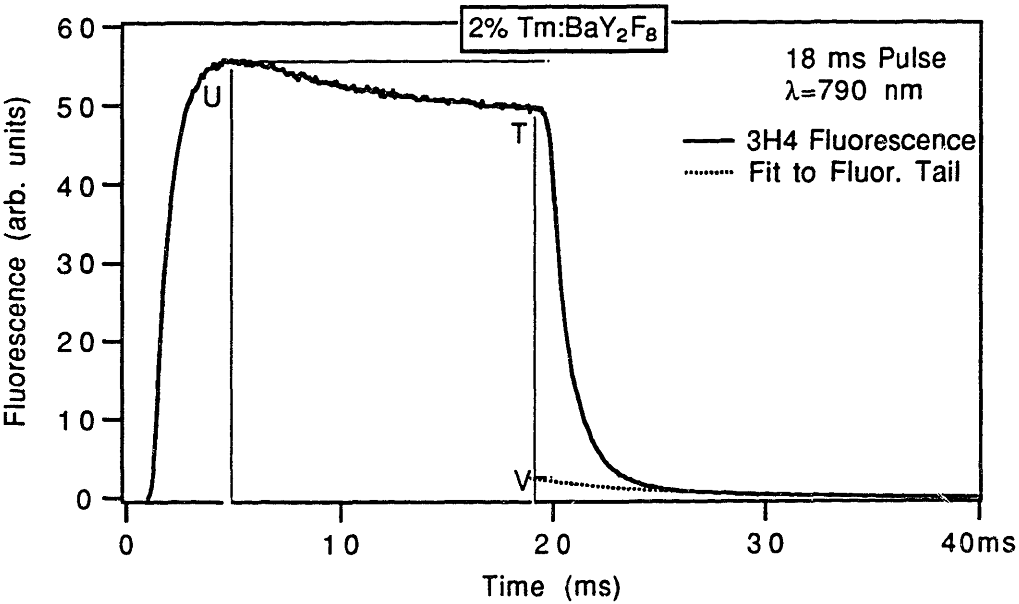

Figure 6.1.11. Plot of $^3H_4$ fluorescence transient to illustrate analysis technique. The values U, T, and V can be read from the transient and used to calculate the upconversion parameter.

The upconversion parameter can be determined from data in the following manner. We use a variation of the technique used by Chou[130] and Knowles[131] to measure the upconversion constants in Er:YLF and Er:BYF. Chou and Knowles measure the upconversion parameter by directly pumping the manifold to which upconversion occurs with a pulse long relative to the lifetimes of the manifolds involved in the upconversion. The amount of upconverted population is determined by the ratio of the signal at the pulse cutoff to the maximum signal immediately following the signal buildup. The upconversion parameter can be determined from this ratio by solving the rate equations in the steady-state for a given excitation density. The excitation density of the lower levels involved in the upconversion process is calculated from measurements of the absorbed power and the systems feeding efficiencies. Our technique differs from their approach in that we can directly measure the excited state population by monitoring the ground state depletion and thereby eliminate many of the uncertainties of their method. Additionally, this technique does not require the system to be in equilibrium at the termination of the pump pulse. The $^3H_4$ population resulting from direct pumping of the manifold, U, is given by,

$$U = P_0 N_0 \tau. \tag{6.1.7}$$

Here P_0 is the pump rate per ion, N_0 is the ground state population, and τ is the lifetime of the $^3H_4$ manifold. The population increase of the $^3H_4$ manifold due to upconversion, V, can be expressed as

$$V = \alpha_1 N_1^2 \tau. \tag{6.1.8}$$

V can not be directly determined from the data in Fig. 6.1.11, but its value can be estimated by fitting to the long lifetime exponential tail and extrapolating back to the point where the pump pulse cuts off. By taking the ratio of Eq. 6.1.7 and Eq. 6.1.8, we find

---

[130] H. Chou and H.P. Jenssen, in OSA Proceedings on Tunable Solid State Lasers, Vol. 5, ed. M.L. Shand and H.P. Jenssen, Cape Cod, (1989), P167; and H. Chou, Upconversion Processes and Cr-sensitization of Er- and Er, Ho-activated Solid State Laser Materials, Ph.D. dissertation, Mass. Ins. of Tech, Feb. 1989.

[131] D.S. Knowles, Energy Transfer Under Strong Pumping in High Concentration Rare Earth Doped Laser Crystals, Ph.D. dissertation, MIT, Sept. 1991, and in [21].

$$\frac{V}{U}=\frac{\alpha_1 N_1^2}{P_0 N_0}. \qquad (6.1.9)$$

The values of this ratio are displayed in Fig. 6.1.11.

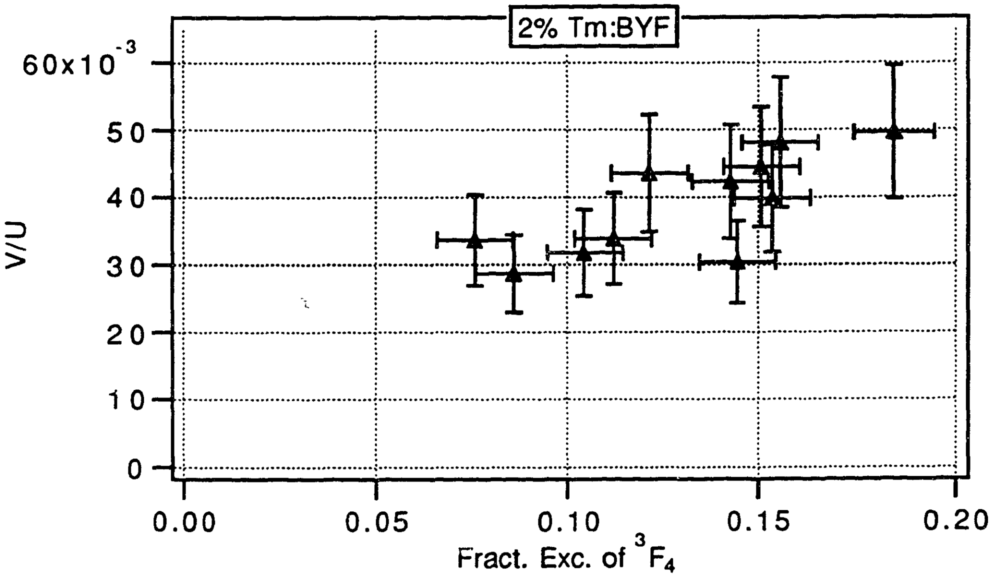

Figure 6.1.12. Ratio of upconverted population to directly pumped population for the $^3F_4$ manifold in 2% Tm:BYF at room temperature.

We need to know N_1 and P_0 to determine α_1. These two quantities are related. Neglecting the effects of upconversion upon the $^3F_4$ population, we can relate N_1 to the pump intensity with the following relation,

$$N_1(t)=W_{eff}\left(1-e^{-A_1 t}\right)=P_0 N_0 \chi_{13}\left(1-e^{-A_1 t}\right), \qquad (6.1.10)$$

where W_{eff} is an effective pump rate determined by the pump rate into the $^3H_4$ and the feeding efficiency from the $^3H_4$ to the $^3F_4$. This feeding efficiency, χ_{13}, is determined in the same manner as the cross-relaxation efficiency of Eq. 6.1.6 by including the term $A_3\beta_{13}$ in the numerator and recalculating the efficiency. This term must be included for the 2% Tm sample as the quantum efficiency for cross-relaxation to the $^3F_4$ is only ≈0.68.

Solving for P_0, we substitute this relation into Eq. 6.1.9 to find

$$\alpha=\frac{V}{U}\frac{1}{\chi_{13}\left(1-e^{-A_1 t_0}\right)N_1}. \qquad (6.1.11)$$

N_1 can be determined from the drop in the fluorescence intensity of the $^3H_4$ manifolds by recognizing that the drop in the $^3H_4$ fluorescence results from ground state depletion and that the states of most of the excited Tm ions belong to the $^3F_4$ manifold. The fraction of Tm ions in the $^3F_4$ manifold is given by (U-T+V)/U from Figure 6.1.11. We have determined the fraction of inverted ions as a function of applied pump power.

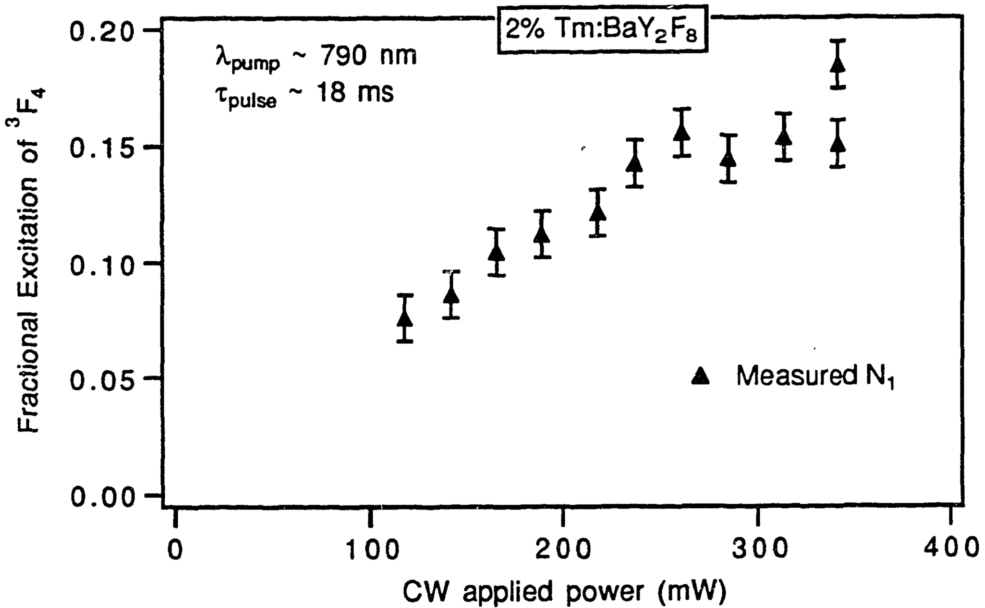

Figure 6.1.13. Fraction inversion of the $^3F_4$ manifold as a function of applied pump. Power levels were measured under cw conditions. The pump pulse was roughly 18 ms long with a duty cycle of 25%. The three slightly lower points at higher applied power were measured in a different sequence of measurements than the other points and give an estimate of the systematic uncertainties of the experiment.

As can be seen from Fig. 6.1.13, the fractional inversion level rises in roughly a linear manner with the pump power at lower intensities; some deviations are apparent at the higher applied powers. From the data, we have determined α_1 at a number of excitation levels in 2% Tm:BaY$_2$F$_8$. Values for α_1 are shown in Fig. 6.1.14.

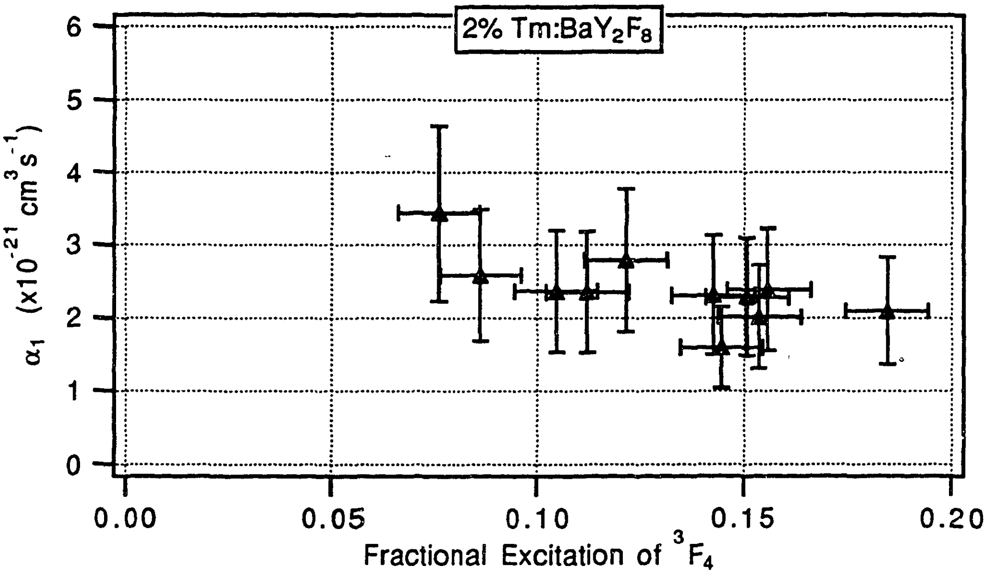

Figure 6.1.14. Measured value of the upconversion parameter α_1 for 2% Tm:BaY$_2$F$_8$ at room temperature.

As can be seen in the above plot, the value of the upconversion parameter is roughly $(2.4\pm1)\times10^{-21}$ cm^{3}s^{-1}. This is considerably less than the value of $(1.1\pm0.2)\times10^{-20}$ cm^{3}s^{-1} expected from the cross relaxation measurements. It appears that the relationship between the transfer parameters ($\alpha_1=\theta\ \alpha_1'$) is not valid for 2% Tm:BaY$_2$F$_8$.

In the derivation just described, we have made several approximations which may effect the accuracy of our results. In the above analysis, we have assumed that the pumped volume is uniformly excited. Due to the small diameter of the pumped spot ($\leq$ 10 μm) necessary to produce the high excitation densities required for ground state depletion, we were unable to accurately measure the profile of the pump beam. When the pump was profiled at larger pump diameters, the profile was approximately gaussian. If the pump beam is gaussian, a systematic correction factor must be applied to Eq. 6.1.11. This correction enters as the fluorescence signal which contributes to U is averaged differently over the volume than the signal (V) resulting from upconversion. We will return to this topic in Section 6.3 and in the discussion of Chapter 7. Additionally, even though we have used thin samples to reduce the difference in the absorbed power in the length of the sample, a small difference still remains in the absorbed power from one side of the sample to the other. We can also correct for the resulting difference in the excitation density along the length of the material. Under these circumstances, Eq. 6.1.11 becomes

$$\alpha = \frac{V}{U}\frac{2e^{-\alpha_{abs}x_0}}{\chi_{13}\left(1-e^{-A_1t_0}\right)N_1}, \qquad (6.1.12)$$

where the factor of 2 comes from the Gaussian distribution and the exp($\alpha_{abs}x_0$) factor is the correction for the exponential drop in the absorption. This factor could be calculated from measurements of applied and transmitted power; here α_{abs} is the absorption coefficient at the pump wavelength and x_0 is the thickness of the sample. For the 2% Tm:BaY_2F_8 sample, the total correction factor is 2.05±0.01.

This yields an average value for α_1 of $(4.9 \pm 1.6)x10^{-21}$ cm^3s^{-1} for a Gaussian excitation in contrast to a value of $(2.4 \pm 0.8)x10^{-21}$ cm^3s^{-1} for a uniform excitation density. Both of these values are less than the value of α_1 which we would expect from the cross-relaxation measurements, $(1.1 \pm 0.1)x10^{-20}$ cm^3s^{-1}; even the uncertainties for these measurements do not overlap. These data imply that the expected relationship between the transfer parameters is not valid for 2%Tm:BaY_2F_8.

This naturally brings into question the accuracy of our data. A close examination of the expression for α_1 (Eq. 6.1.11) will give use some idea of the accuracy of the reported values. Experimentally, the most sensitive term in Eq. 6.1.11 is the ratio of the upconverted fluorescence to the directly pumped fluorescence, V/U. As the amount of upconverted fluorescence is small in comparison to the total signal, it is difficult to accurately determine the value of V. Additionally, V must be determined by fitting to the long-lived fluorescence tail and extrapolating . By observation of the sensitivity of V to variations in U and the lifetime of the fit to the tail, we estimate the uncertainty in the value of V/U to be roughly 20%. The uncertainty in V also affects the measured inversion density and results in a ~5% uncertainty in N_1.

The second major source of uncertainty is the lifetime ($1/A_3$) used in the expression (1-exp($-A_1t_0$)). In the direct pumping measurement described earlier, we measured the lifetime of the $^3F_4$ to be ~17 ms (Table 6.1.1). In the upconversion measurements just described, the fits to the $^3H_4$ fluorescence tail indicated an upconversion-fed signal with lifetimes in the range of ~ 6.5 - 7 ms. As the lifetime of the $^3H_4$ fluorescence resulting from upconversion should be roughly half that of the $^3F_4$ manifold, this would imply that the lifetime of the $^3F_4$ is in the range of 13 - 14 ms. The difference in these lifetimes contributes an uncertainty of ~10% to the values of α_1 reported.

Some uncertainty enters through the feeding efficiency, χ_{13}. When fitting the decay with a double exponential, we find that the measured lifetime of the $^3H_4$ level lengthens with increasing excitation density from ~ 830 to ~900 μs. Recalling the expression for the cross-relaxation rate, this is not surprising as this rate depends on the number of ions in the ground state; as excitation densities increase, the number of ions in the ground state will fall from depletion. There is also an uncertainty in the branching ratio, β_{13}, which has a small effect on the uncertainty of the feeding efficiency. The feeding efficiency uncertainty contributes ≈ 5% to the total uncertainty.

One assumption we have made is that no other processes affect the system. Other processes would be expected to change the lifetimes of the $^3H_4$ and the $^3F_4$ manifolds if they had a substantial effect on these populations of these manifolds. It was mentioned that the $^3H_4$ lifetime lengthened at high excitation densities; within the limits of our experimental uncertainties, this can be explained as a reduction in the cross-relaxation rate due to ground state depletion and therefore is not evidence of another process. It was also mentioned that the data on the tail of the $^3H_4$ decay indicated that the lifetime of the $^3F_4$ manifold is shortened to ~13-14 ms at high excitation densities. This is not a direct indication of another process, however, as each excitation promoted to the $^3H_4$ by upconversion could decay by a process other than cross-relaxation; in our model, the probability of this occurring is $1-\chi_{13}$. The net result would be a shortening of the $^3F_4$ lifetime; however, the small value of the upconversion coefficient restricts this shortening to be at most ~0.5 ms in our experiments. Observations of the $^3F_4$ fluorescence indicate only minor shortening in the lifetime of the manifold (The observed shortening is within the previously stated uncertainties of the directly pumped cross-relaxation measurements -Table 6.1.1). The discrepancy between the measured $^3F_4$ lifetime and the lifetime implied by the $^3H_4$ tail may indicate the presence of another process affecting one of these manifolds at high excitation densities. However, the magnitude of these process are most likely small (due to the position of energy levels); and, in any case, the effects of these processes upon α_1 are included in the uncertainties discussed earlier.

As we have ruled out additional processes as a reason for the disagreements between the values of the directly measured upconversion coefficient and the cross-relaxation measurement, we conclude that this disagreement results from some other problem with the model for Tm. We suspect that the reason for the disagreement in the value of the upconversion parameter predicted by cross-relaxation and the value measured by the upconversion results from the approximation used to generate the relation. We will return to these results in the discussion of Chapter 7.

6.1.3. Other processes in singly-doped Tm.

In the model for Tm presented earlier, we neglected a few additional transfer processes that could be present in the system. As mentioned, these processes can not explain the discrepancy in the values of α_1; however, they are of interest for other reasons. The energy level diagram for Tm^{3+} is shown in Fig. 6.1.15.

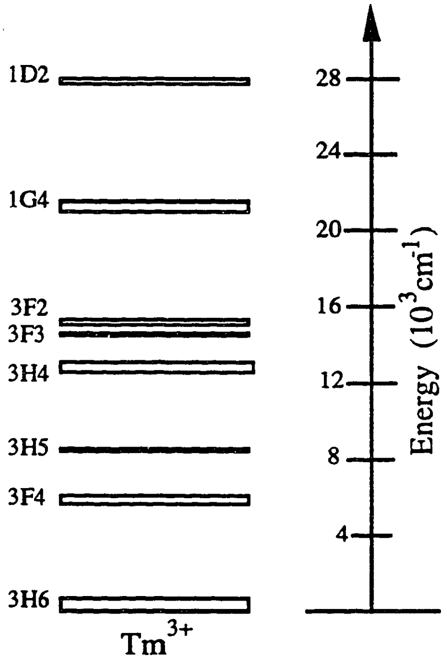

Figure 6.1.15. Energy levels of the manifolds of Tm^{3+}.

The $^3F_3$ and the $^3F_2$ manifolds have extremely short lifetimes because of multiphonon relaxation to the $^3H_4$ manifold; emission from these levels has not been observed in our materials at room temperatures. The existence of these manifolds may be of importance for energy transfer processes and other processes[132] involving the absorption of excitation by ions making transitions into these manifolds; however, these manifolds are rapidly depopulated by multiphonon relaxation and will not contribute to processes which require donation of energy from these manifolds. Therefore, these manifolds can act as acceptors but not donors for energy transfer.

Upconversion from the $^3F_4$ to the $^3H_5$ is possible and has been suggested to be a loss mechanism at high excitation densities[51, 52]. This process is certainly possible, but if it had a substantial effect it would show up as a shortening in the $^3F_4$ lifetime. This

---

[132] For example, the $^3F_3$ pumping of Tm with 681 nm diodes. This was discussed by Stoneman, Pinto, and L. Esterowitz at the OSA annual conference, Boston, 1992, as a possible technique for pumping 2 μm lasers.

was not observed in measurements of the $^3F_4$ transient, but it could be responsible for the shortened lifetime of the upconversion fed fluorescence observed in the tail of the $^3H_4$ transient.

The $^1G_4$ manifold is relatively long lived at low concentrations but shortens with increasing Tm concentration. We have measured the lifetime of the $^1G_4$ manifold as a function of concentration by directly pumping the level; data are tabulated in Table 6.1.5.

Conc. (Tm)	$^1G_4$ Lifetime	W_{cr} (s^{-1})	α_{eff} (cm^3s^{-1})
0.2%	820±30 μs	0	0
0.5%	740±30 μs	132 s^{-1}	3.9x10-19
0.75%	630±20 μs	368 s^{-1}	1.1x10-18
1%	460±20 μs	9.5×10^2 s^{-1}	2.81x10-18
2%	220±15 μs	3.3×10^3 s^{-1}	9.7x10-18
5%	~40 μs	2.4×10^4 s^{-1}	7.1x10-18
10%	~5.5 μs	1.8×10^5 s^{-1}	5.3x10-16
20%	~250 ns	4.0×10^6 s^{-1}	1.2x10-15

Table 6.1.5. Lifetime and other quantities for the $^1G_4$ manifold for varying concentrations of $Tm:BaY_2F_8$.

The rapid reduction in lifetime with increasing Tm concentration indicates that a cross-relaxation process is present. This $^1G_4$ cross-relaxation process can occur through a variety of channels - ($^1G_4$->$^3H_4$, $^3H_6$->$^3F_4$), ($^1G_4$-$^3H_4$, $^3F_4$-$^3H_4$), and ($^1G_4$-$^3F_3$, $^3H_6$-$^3H_5$) as well as others. An effective cross-relaxation parameter for these processes has been determined and is tabulated in Table 6.1.5 for the different concentrations. The existence of this cross-relaxation process implies that upconversion processes can also populate the $^1G_4$ manifold. However, the majority of these upconversion mechanisms are not favored energetically, (values of $\theta<0.01$). The only process energetically favored is a coupled $^3H_4$-$^1G_4$, $^3H_4$-$^3H_6$ upconversion process. This process would in principal have a N_3^2 (or N_1^4) dependence. Emission from the $^1G_4$ has been observed when the $^3H_4$ is pumped; in fact, upconversion to the $^1G_4$ is being used to attempt to produce upconversion lasers in Yb, Tm codoped systems[133]. The same methods described earlier could, in principle, be applied to measure this upconversion process; but without further process identification this technique is not useful. In singly doped Tm upconversion to the $^1G_4$ is unlikely as the only process energetically favored is ($^3H_4$->$^3H_6$, $^3H_4$->$^1G_4$)

---

[133] For a discussion of the process, see F. E. Auzel, "Materials and Devices Using Double-Pumped Phosphors with Energy Transfer", Proc. of the IEEE, V61, N6, (1973), P758.

upconversion. This process is highly unlikely as it requires two excitations in the $^3H_4$ to interact.

6.2. Energy transfer processes in singly-doped Ho^{3+}.

A energy level diagram for singly-doped Ho is shown in Fig. 6.2.1.

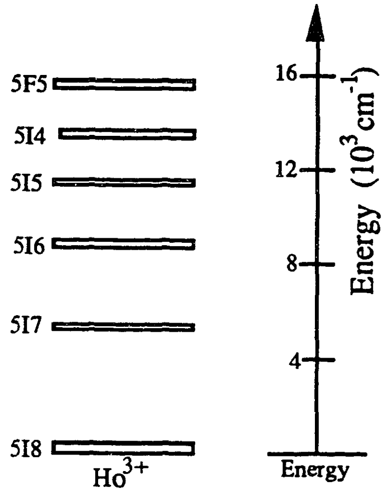

Figure 6.2.1. Energy levels of the lower levels of singly-doped Ho^{3+}.

We can apply the techniques used for singly-doped Tm to determine the cross-relaxation and upconversion parameters for Ho. We first directly pump the $^5I_5$ manifold and measure the $^5I_5$ lifetime. This manifold shows considerable quenching due to multiphonon relaxation. In fact, a measurable lifetime was not found for Ho:YAG. The lifetime of this manifold has been estimated to be ≈1 μs in Ho:YAG[134].

We find no measurable change in the lifetime of the $^5I_5$ manifold in YLF for Ho concentrations in the range of 1% to 10%. This implies that the $^5I_5$ does not cross-relax efficiently in Ho:YLF. Defining θ for this process in the same manner as for Tm (Eq. 6.1.3), we find that the expected ratio of the upconversion parameter to the cross-relaxation parameter is ≈0.01 for ($^5I_7$-$^5I_8$, $^5I_7$-$^5I_5$) upconversion. This implies that there is minimal $^5I_7$-$^5I_5$ upconversion in singly-doped Ho:YLF; We would expect similar results in BaY_2F_8 and $NaYF_4$ as the multiphonon relaxation rates in these materials are smaller than in YLF for similar energy gaps. Based on these arguments, it appears that we can rule out ($^5I_7$-$^5I_8$, $^5I_7$-$^5I_5$) upconversion as a significant loss mechanism in YLF, BYF, or NYF. This is inconsistent with the results reported in [50]; our results place an

---

[134] K. H. Kim, Y. S. Choi, R. V. Hess, C. H. Blair, P. Brockman, N. P. Barnes, G. W. Henderson, and M. R. Kokta, "Experiments and Theory for Tm:Ho:YAG Laser End Pumped by a Cr:GSAG Laser", OSA Proc. Adv. Sol. State Lasers, V6, Ed. H. P. Jenssen and G. Dube, Salt Lake City, (1990), P155.

upper limit of the $^5I_7$-$^5I_8$, $^5I_7$-$^5I_5$ upconversion parameter in YLF of $\approx 10^{-20}$ cm^{3}s^{-1} based on the lack of lifetime shortening at concentrations of 10% Ho:YLF We can not rule out this upconversion process in Ho:YAG as we do not have adequate measurements of the concentration dependence of the $^5I_7$ lifetime. Upconversion to the $^5I_6$ manifold can not be ruled out based on consideration of energy level positions; in fact, a ($^5I_7$-$^5I_8$, $^5I_7$-$^5I_5$) upconversion process would be energetically favored.

However, as these upconversion processes require two excitations in the $^5I_7$ manifold to combine to produce one excitation in a higher lying level, we can effectively rule them out at the low concentrations of Ho used in 2.0 μm laser materials. We expect the effects of these strictly Ho upconversion processes to be small relative to the Tm-Ho processes affecting these manifolds in laser hosts.

Material	$^5I_5$ τ (μs)	W_{nr} (s^{-1})	E_{gap}
1% Ho:YLF	19±1.5	5.2×10^4	≈2450
10% Ho: YLF	18.5±1.5	5.3×10^4	≈2450
1% Ho: BYF	52±4	1.8×10^4	≈2400
0.5%Ho:NYF	120±10	7.3×10^3	?

Table 6.2.1. Lifetimes and non-radiative relaxation rates for Ho in various materials. The non-radiative relaxation rates can be calculate with a knowledge of the Einstein A coefficient for the $^5I_5$ manifold.

6.3. Upconversion in Tm-Ho.

We now concentrate on the energy transfer processes which occur in the codoped Tm-Ho system. Earlier the energy transfer processes leading to the $^3F_4$ and $^5I_7$ steady-state equilibrium were explored. We further examine these processes, as well as explore the upconversion process thought to be the primary loss mechanism from the upper laser level at high excitation densities.

The lower energy levels of the Tm-Ho system are displayed in Fig. 6.3.1.

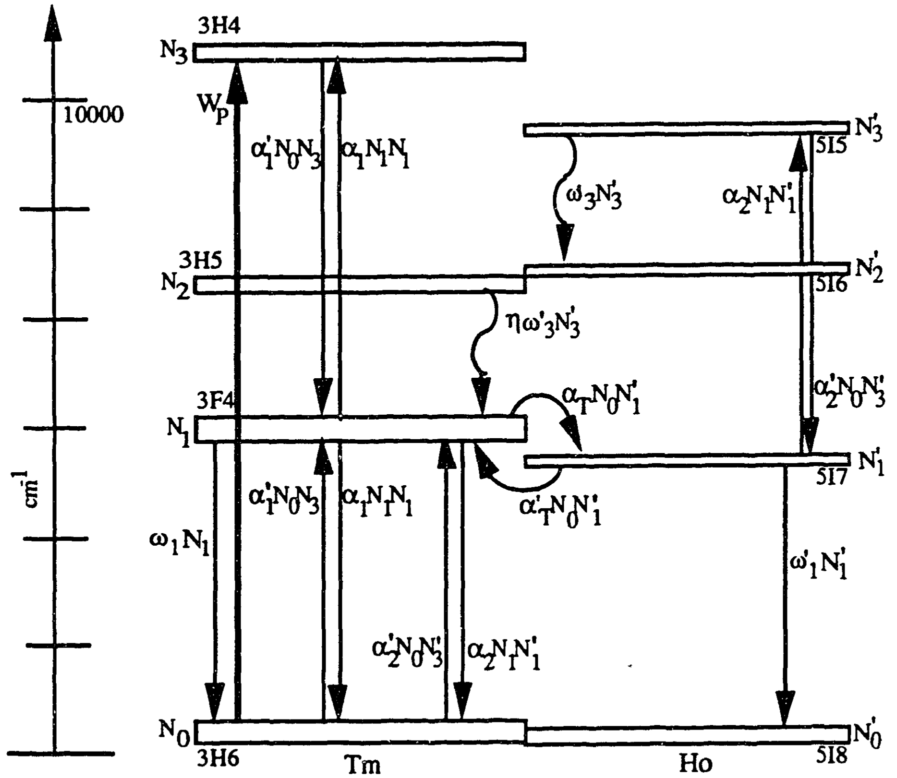

Figure 6.3.1. Model for the Tm-Ho system. Spontaneous emission processes from higher-lying levels are omitted.

In the above figure, W_p is the pumping rate of the $^3H_4$ level, α_T and α_T' are the parameters for transfer and back-transfer from Tm($^3F_4$) to Ho($^5I_7$). As before, α_1 and α_1' are the energy transfer parameters for $^3H_4$-$^3F_4$ upconversion and cross-relaxation. Here α_2 is the energy transfer parameter for $^5I_7$-$^5I_5$, $^3F_4$-$^3H_6$ upconversion, and α_2' the parameter for cross-relaxation. ω_1, ω_1', and ω_3' are the single-ion relaxation probabilities in singly-doped crystals. The dominant contributions to ω_1 and ω_1' come from radiative relaxation, while the primary process contributing to ω_3' is multi-phonon relaxation. The rate equations for this model are expressed below.

$$\dot{N}_1 = 2\alpha_1' N_0 N_3 - 2\alpha_1 N_1^2 - \alpha_T N_0' N_1 + \alpha_T' N_0 N$$

$$- \alpha_2 N_1 N_1' + \alpha_2' N_0 N_3' - \omega_1 N_1 + \eta \omega_3' N_3'$$

$$\dot{N}_3 = W_p - \alpha_1' N_0 N_3 + \alpha_1 N_1^2 - \omega_3 N_3$$

$$\dot{N}_0 = -\dot{N}_1 - \dot{N}_3$$

$$\dot{N}_1' = \alpha_T N_0' N_1 - \alpha_T' N_0 N_1' - \alpha_2 N_1 N_1' + \alpha_2' N_0$$

$$\dot{N}_3' = \alpha_2 N_1 N_1' - \alpha_2' N_0 N_3' + \omega_3' N_3'$$

$$\dot{N}_0' = -\dot{N}_1' - \dot{N}_3'$$

Some simplifying assumptions have been made and will now be detailed. We have dropped many of the inter-manifold radiative relaxation processes for the higher-lying manifolds as their effects will be small in comparison to those of the non-radiative and energy transfer processes. Secondly, we do not (for the moment) consider processes which may occur at extremely high excitation densities. (For example, additional upconversion mechanisms are not currently included.)

This model has an additional term in comparison to the models typically used for these materials.[See, for example, 25, 26] Most models consider only the upconversion process ($^3F_4$->$^3H_6$, $^5I_7$->$^5I_5$) and neglect the relaxation processes which affect the $^5I_5$ manifold. This model includes both the cross-relaxation and multiphonon processes that can relax this manifold.[135] We have assumed that any excitation lost from the $^5I_5$ manifold by multi-phonon relaxation to the $^5I_6$ manifold transfers to the $^3H_5$ and non-radiatively relaxes to the $^3F_4$ manifold with efficiency η. The energy levels of the $^5I_6$ and the $^3H_5$ manifolds are well matched for energy transfer. At most, one excitation can return to the $^5I_7$-$^3F_4$ manifolds if the $^5I_5$ relaxes by multiphonon relaxation to the $^5I_6$ manifold in comparison to the two that would return via cross-relaxation of the $^5I_5$ manifold. The actual value of η will depend on the processes which affect the $^5I_6$ and should be close to unity. This is an upper limit on the efficiency of the non-radiative relaxation in returning an excitation to these levels. For now, we eliminate the $^5I_6$ and the $^3H_5$ manifolds from the rate equations.

---

[135] K.M. Dinndorf, M. Tonelli, A. Cassanho, Y. Yamaguchi, and H.P. Jenssen, "Relative Upconversion Rates in Tm-Ho doped crystals," in <u>OSA Proc. of the Adv. Sol. State Laser Conf. V16</u>, ed A.A. Pinto and T.Y. Fan, New Orleans, (1993), P.

Once again, we have made the assumption that we can describe the energy transfer between manifolds with an average transfer parameter, α. As mentioned earlier, this may not always be appropriate; we will return to this topic in the discussion of Chap. 7.

6.3.1 Measurement of the cross-relaxation rate.

We start by examining the shortening of the $^5I_5$ lifetime that occurs with increasing Tm concentration in a Tm-Ho doped material; we attribute this shortening to a $^5I_5$-$^5I_7$, $^3H_6$-$^3F_4$ cross-relaxation process.

In our experiment, we directly pump the $^5I_5$ manifold and observe the fluorescence decay with the lifetime apparatus described in Chap. 4. We use a pulsed Ti:Sapphire laser to produce 884 nm, ~1mJ pulses of duration ~20 ns. The maximum $^5I_5$ fluorescence signal was between 910 and 917 nm in these materials; this close spectral match between pump wavelength and fluorescence wavelength combined with the weak $^5I_5$-$^5I_8$ absorption complicated this experiment. The signal from the $^5I_5$ was small in comparison to the scattered pump signal; a 20 nm bandpass filter centered at 920 nm was not able to sufficiently filter the pump pulse from the fluorescence. A monochromator and lens combination was also not sufficient as enough scattered pump light entered the monochromator to obscure the fluorescence from the $^5I_5$. A combination of filters, apertures, and lenses was used with the monochromator to produce a $^5I_5$ signal free of pump contamination. This arrangement sufficiently blocked the scattered pump so that a fluorescence signal was only observable when the monochromator was tuned to an emission peak of the $^5I_5$ manifold. The light collection system used is shown in Fig. 6.3.2.

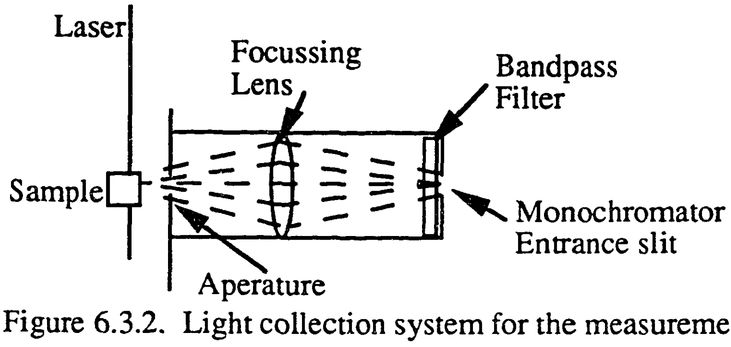

Figure 6.3.2. Light collection system for the measurement of $^5I_5$ fluorescence.

The fluorescence dynamics were measured at room temperature for various concentrations of Tm and Ho in YLF, NYF, and BYF. As was mentioned earlier, the fluorescence lifetime of the $^5I_5$ manifold was not measured in YAG as its lifetime was less than our experimental resolution. Figure 6.3.3. shows the reduction in $^5I_5$ lifetime for Tm, Ho:YLF. Note that the dynamics show no resolvable sensitivity to the Ho concentration in the codoped samples.

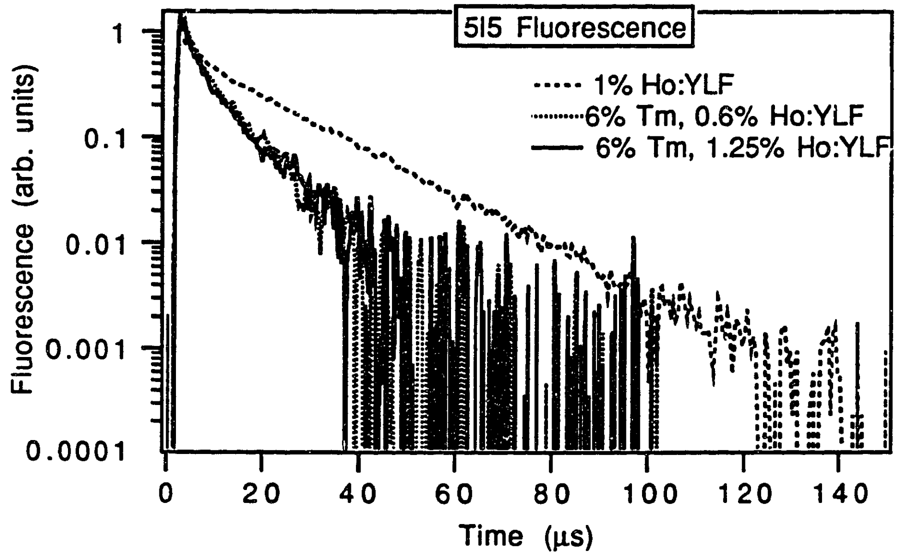

Figure 6.3.3. $^5I_5$ fluorescence dynamics in YLF. Note that the lifetime is roughly insensitive to the Ho concentration.

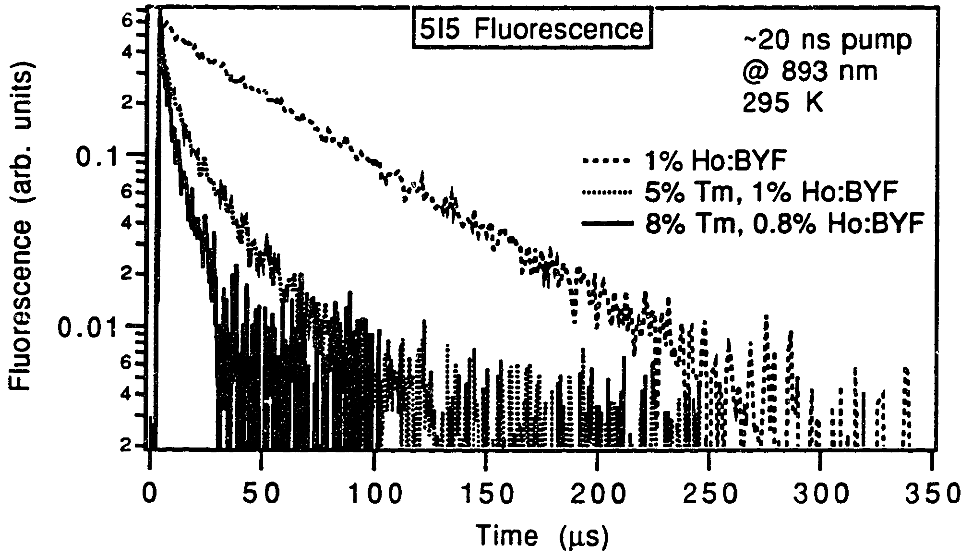

Figure 6.3.4. $^5I_5$ fluorescence dynamics as a function of Tm concentration in BaY_2F_8. Note that the cross-relaxation rate increases with increasing Tm concentration.

Fig. 6.3.4 shows the reduction of lifetime with increasing Tm concentration in Tm, Ho:BaY_2F_8. These decays are slightly non-linear; this is expected as the quenching mechanism is most likely a static process (discussed in Sec. 2.3). It is improbable that migration could occur among the $^5I_5$ manifold due to its short lifetime and the low concentrations of Ho involved.

By approximating these dynamics as linear, we can determine an average energy transfer parameter for cross-relaxation. This cross-relaxation parameter can be related to the upconversion parameter in the same manner as for the Tm upconversion process. The equilibrium condition for this energy transfer process is

$$\theta_2 = \frac{\alpha_2}{\alpha_2'} = \frac{N_0 N_3'}{N_1 N_1'}, \tag{6.3.1}$$

where these terms retain their earlier definitions. This leads to

$$\theta_2 = \frac{\sum_{i}^{3H6} g_i e^{-\beta\varepsilon_i} \sum_{k}^{5I5} g_k e^{-\beta\varepsilon_k}}{\sum_{l}^{3F4} g_l e^{-\beta\varepsilon_l} \sum_{j}^{5I7} g_j e^{-\beta\varepsilon_j}}, \tag{6.3.2}$$

where $\alpha_2 = \theta_2 \alpha_2'$. Keep in mind that the above derivation is just a convenient way of finding θ. The system will not come to equilibrium in our measurements. With a knowledge of the energy levels in a materials and the cross-relaxation parameters, we should be able to calculate the upconversion parameters from our data. These calculations are tabulated in Table 6.3.1 for YLF, BYF, and NYF.

Material	$^5I_5$ τ (μs)	W_{cr} (s^{-1})	a_2' (cm^3s^{-1})	θ_2	a_2 (cm^3s^{-1})
1% Ho:YLF	19±1.5	0	0		
6% Tm, 0.6%Ho:YLF	6.5±1.5	$1.0x10^5$	$1.3x10^{-16}$	0.116	$1.5x10^{-17}$
6% Tm, 1.25% Ho:YLF	6.5±1.5	$1.0x10^5$	$1.3x10^{-16}$	0.116	$1.5x10^{-17}$
10% Ho, 2%Er: YLF	18±2	0	0		
50% Er, 7% Tm, 1.5%Ho: YLF	1.5±1	*	*		
1% Ho: BYF	52±4	0	0		
5% Tm, 1%Ho: BYF	18±2	$3.6x10^4$	$5.5x10^{-17}$	0.157	$8.25x10^{-18}$
8% Tm, 0.8% Ho: BYF	7±1.5	$1.2x10^5$	$1.2x10^{-16}$	0.157	$1.8x10^{-17}$
0.5%Ho:NYF	120±10	0	0		
5%Tm, 0.2%Ho:NYF	55±5	$9.8x10^3$	$1.4x10^{-17}$	0.13	$1.8x10^{-18}$
5%Tm, 0.5%Ho:NYF	55±5	$9.8x10^3$	$1.4x10^{-17}$	0.13	$1.8x10^{-18}$

Table 6.3.1. Lifetimes and energy transfer parameters in BaY_2F_8 at room temperature.

Notice that although the cross-relaxation parameter for BaY_2F_8 is less half that of YLF, the expected upconversion parameter is nearly 65% that of YLF. This difference is due to the energy levels. The expected upconversion parameter for NYF is considerably smaller than that for YLF and BYF; however, we have assumed a value for θ_2 for NYF as complete energy level information for this material is not available. Data for YAG is not included as the cross-relaxation rate for this material is unknown.

6.3.2. Measurement of the 5I5 upconversion.

We now wish to measure the upconversion parameter for $^3F_4$-$^3H_6$, $^5I_7$-$^5I_5$ energy transfer process and see if the measured values correspond to the values predicted by the cross-relaxation measurements. This is a more complicated measurement than Tm $^3F_4$-$^3H_4$ upconversion as many more processes are possible when two different ions are involved. Our method will be to measure the transient response of the Tm-Ho system to square pulse pumping, a technique which has been applied by a number of researchers[136].

---

[136] See, for example, [25], [35], and G. Hansson, A. Callenas, and C. Nelsson, "Upconversion studies in laser-diode-pumped Tm,Ho:$YLiF_4$," in OSA Proc. of the Adv. Sol. State Laser Conf. V16, ed A.A. Pinto and T.Y. Fan, New Orleans, (1993), In press.

Experiment.

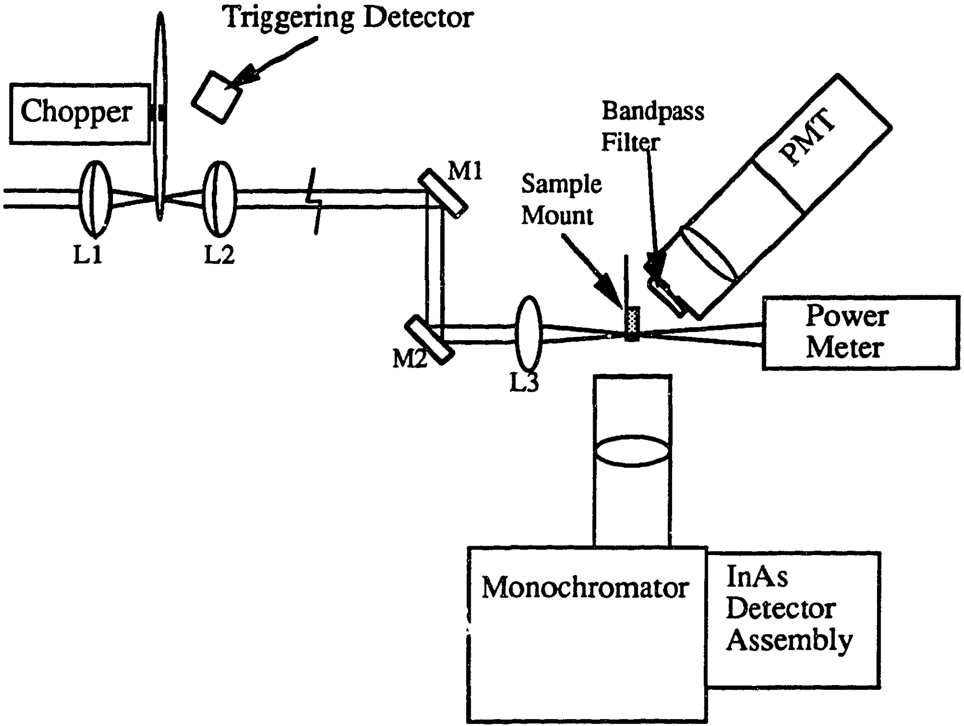

Figure 6.3.5. Experimental arrangement for Tm-Ho upconversion measurements. The Lx's are lenses, the Mx's are mirrors.

Our experimental apparatus is shown in Fig. 6.3.5. In the figure, the pump beam passes through a set of lens and mirrors to be focused on the sample. The power meter is used to monitor the power transmitted through the sample, to measure the incident power, and to profile the pump spot in the sample.

The pump beam comes from a cw Ti:Sapphire laser. Square pulses of pump radiation were obtained by chopping the Ti:Sapphire beam; the assembly composed of the chopper and the lens L1 and L2 was necessary to ensure a short cut-off time for the square pulse. A minimum "dark" time of roughly 80 ms is required between pulses so that the majority of the excitations deposited by a pulse can decay before a second pulse excites that system. This "dark" time requirement limited our chopper frequency to ~16 Hz; at this low frequency the cutoff time of the pulse was long and the pump pulses did not resemble square waves. By using the lens assembly to focus the pump waist to a small spot, we were able to chop the focused spot and achieve a cut-off time for the pump pulse of roughly 40 μs. A small frequency variation was found in the chopper, so a Si detector was required to provide a trigger signal for the sampling system (instead of the triggering signal produced by the chopper).

The lens L3 and the sample mount were 3-axis adjustable as well as having the standard swivel and tilt adjustments. This was necessary as the pump and the sample positions had to be optimized for each set of measurements. The sample was mounted to a razor edge which also allowed precision measurement of the beam waist. The spot size in the sample (and hence the power level) could be adjusted by moving the lens. Each detector was biased so that its measured response time was less than 40 μs. The measured response time included an amplifier used with the InAs detector.

The experiment was conducted in the following manner. The Ti:Sapphire laser was activated and tuned to a wavelength suitable for exciting the $^3H_4$ manifold. The sample was mounted; and the various optics were adjusted.

With the chopper turned off, the beam waist at the front surface of the sample was measured using the razor edge of the sample mount. The power level incident on the sample was measured; and then the sample was inserted into the beam. The position of the sample was adjusted so the pump beam was not visibly distorted from edge effects, and the transmitted power recorded. Following this, the chopper was turned on and allowed to stabilize at the chopping frequency, and the triggering level of the data collection system was adjusted. The transient was then digitized and averaged. The transients at several different power levels were recorded. The power level was adjusted both by varying the output power of the Ti:Sapphire laser and by adjusting the position of the lens L3. The spot size was measured whenever the lens position or the sample position were adjusted.

$^3F_4$ <-> $^5I_7$ Transfer and Back-transfer Data Analysis.

An experiment of this design is capable of generating data which can be analyzed in several different manners. Our initial approach is to fit the rate equations given above to the shapes of the fluorescence transients. We fit only the transient shapes and are not concerned with the relative scale of the different fluorescence signals as the measured magnitude of these signals will depend on many factors. Fitting to the magnitude as well as to the shape introduces many complications since the magnitude depends on the wavelength monitored, the cross-section at a given orientation of the material, and the system response. As we have only a small number of adjustable parameters the relative magnitudes are not necessary to perform a successful fit.

In fitting, it is desirable to minimize the adjustable parameters of the model. We can determine the pump rate (W_p) by measuring the absorbed power. We have previously measured manifold lifetimes in low concentration materials; we have also measured the cross-relaxation parameters for these materials. Additionally, we have shown that the $^3F_4$-$^3H_4$ upconversion parameter is small and its effect can be neglected at most pump intensities. Thus, we are left with only 3 unknowns: the $^3F_4$-$^5I_7$ transfer parameters and the $^5I_5$ upconversion parameter. We first concentrate on the transfer and back-transfer parameters.

At low excitation densities, the shape of both the $^5I_7$ and $^3F_4$ manifolds will be identical if these manifolds are in equilibrium. However, if the equilibration time is long enough to be experimentally resolvable, we may be able to observe a difference in the $^3F_4$ and the $^5I_7$ transients. Measurements discussed earlier imply that the equilibration time is in the range of 10-100 μs in our materials[91, 92]. As our time resolution is roughly 40 μs, this would be on the edge of our experimental resolution; this transfer time is determined by the transfer and back-transfer parameters. Therefore, by measuring the $^3F_4$ and the $^5I_7$ transients as a function of time, we can find these parameters.

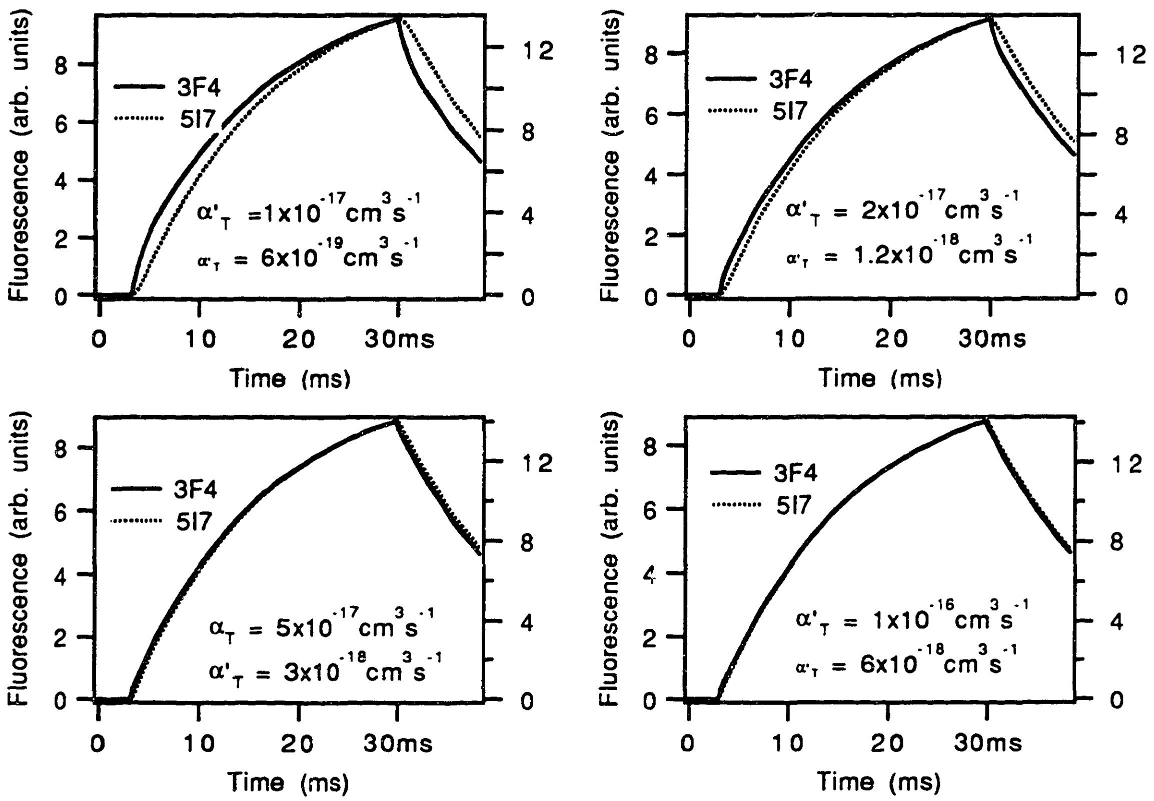

Figure 6.3.6. Predicted fluorescence intensity of the $^3F_4$ and $^5I_7$ manifolds for various values of the transfer parameters.

In Fig 6.3.6 we have numerically solved the rate equations for YLF at low excitation densities for the pulse lengths we will use in the upconversion experiment.

From these plots obvious differences are visible between the two shapes when the transfer parameter α_T is less than $5\text{x}10^{-17}$ cm^{3}s^{-1}.

Observation of a smaller time interval makes the differences between these transients more apparent. However, the need to record a baseline and the limits of our sampling device constrain the maximum pulse length we can use and still resolve the small time interval desired. We must therefore shorten the pump pulse length to improve the time resolution. Unfortunately, we are limited by the signal to noise ratio to pulses of about 10 ms in length. An overlay of the $^3F_4$ and $^5I_7$ fluorescence dynamics is presented in Fig. 6.3.7 for a 12 ms pulse.

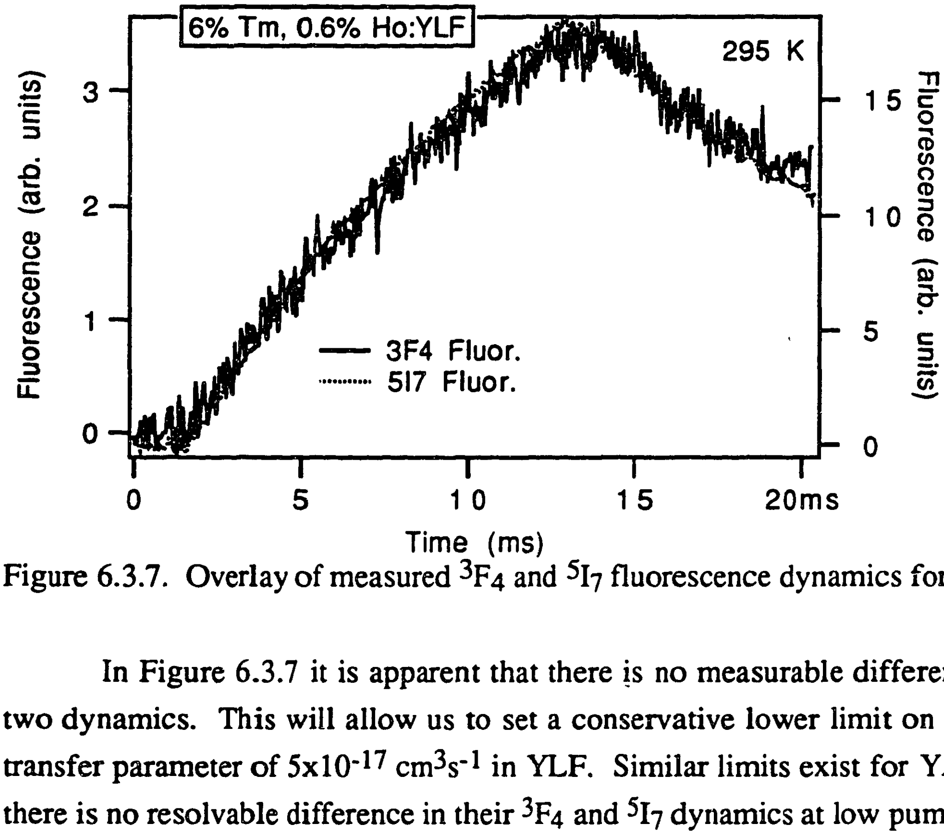

Figure 6.3.7. Overlay of measured $^3F_4$ and $^5I_7$ fluorescence dynamics for Tm, Ho:YLF.

In Figure 6.3.7 it is apparent that there is no measurable difference between the two dynamics. This will allow us to set a conservative lower limit on the value of the transfer parameter of $5\text{x}10^{-17}$ cm^{3}s^{-1} in YLF. Similar limits exist for YAG and BYF as there is no resolvable difference in their $^3F_4$ and $^5I_7$ dynamics at low pump intensities.

Although we have not found the exact values of the transfer parameters, we have shown that the transfer occurs quickly enough that we can not experimentally resolve the process. This implies that, for the time scales of the experiment, we can think of the $^3F_4$ and the $^5I_7$ manifolds as being in equilibrium. This supports the use of the equilibrium approximation generally made when modeling these systems[25]. For the purposes of our modeling, it is sufficient to know only the ratio of the transfer parameters as these will determine the equilibrium distribution. In the preceding chapter, we measured this ratio in the steady state; so the only remaining unknown is the $^5I_5$ upconversion parameter. The above transients support the extension of the equilibrium relations to high excitation densities (Eqs. 3.3.1 and 3.3.2).

$^3F_4$->$^3H_6$, $^5I_7$->$^5I_5$ Upconversion Data Analysis.

To determine the upconversion parameter α_2, we will first use the method generally applied[See, for example, 25]. In this approach, the rate equations for the codoped Tm-Ho system are fit to the transient for the $^5I_7$. Upconversion appears as an additional roll-over in the fluorescence signal with increasing power. This approach will require that we go to slightly higher excitation densities than was used to produce the previous transients. We will also fit to the $^5I_5$ transients as a check on these measurements.

As the $^5I_5$ upconversion rate is the product of the $^3F_4$ and the $^5I_7$ populations with the upconversion parameter, we might expect the $^5I_5$ transient to look like the product of the $^3F_4$ and the $^5I_7$ transients. This is true at low excitation densities; but at higher excitation densities, the measured $^5I_5$ transient does not resemble the product of these transients in most experiments.

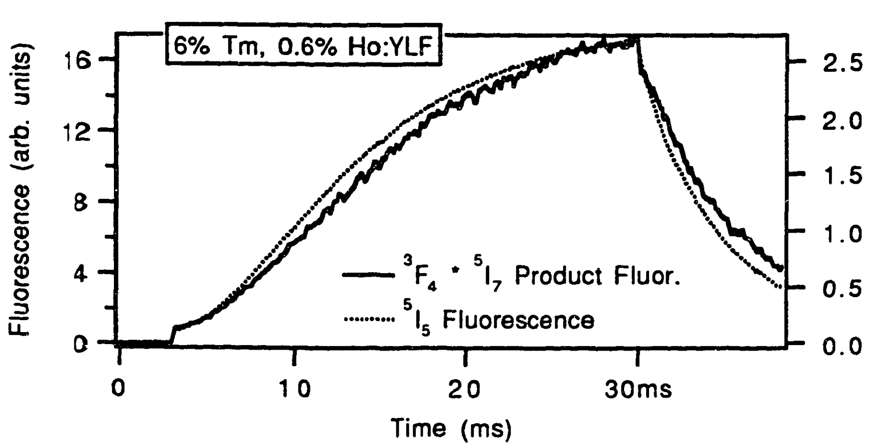

Figure 6.3.8. Plot of $^5I_5$ fluorescence and product of $^5I_7$ and $^3F_4$ fluorescence.

As can be seen from Fig. 6.3.8, there are significant differences in the shapes of the transients. These differences arise from the nature of the pumped spot used in our experiment. The pump beam is Gaussian, and since the excitation density varies as the pump power a range of excitation densities exists in the pumped area. The profile of the beam for our experiment is shown in Fig. 6.3.9.

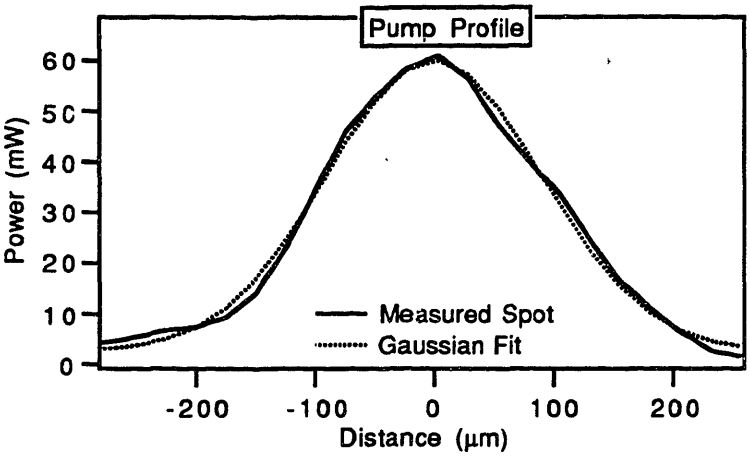

Figure 6.3.9. Profile of pump beam used in upconversion experiments.

The beam profile was determined by adjusting the height of the sample mount so that the razor edge intercepted the beam and then monitoring the transmitted power as the mount was incrementally moved across the beam. The position of the mount could be measured in ~2.5 μm steps with a micrometer-screw drive. Following this measurement, the height was readjusted so the sample intercepted the beam and the transient measurements were performed.

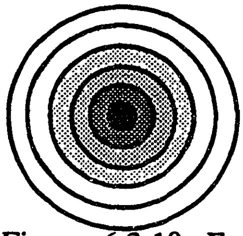

Figure. 6.3.10. Excitation density of spot. The darker the region the higher the excitation density.

Figure 6.3.10 shows a schematic diagram of the excitation density of the pumped spot. Most of the contribution to the $^5I_5$ fluorescence will come from the inner, high excitation region due to the N^2 nature of the upconversion process. Meanwhile, the $^5I_7$ fluorescence will be more representative of the outer regions of lower pump intensities in comparison to the $^5I_5$ signal as the $^5I_7$ fluorescence depends linearly on the excitation density. This is the reason for the correction factor of 2 applied to the Tm upconversion measurements for a Gaussian pump. Here, however, we cannot simply calculate this correction factor as the upconversion parameter is much larger; the $^5I_7$ population is coupled to the upconversion parameter. For any given excitation density and set of transfer parameters, the transient of the $^5I_5$ level is given by the product of the $^5I_7$ and the

$^3F_4$ transients. However, due to the Gaussian spot, the transient we observe is an average of several different transients produced at different excitation densities. At low powers, no difference is observable between the $^5I_5$ and the product transients; when the excitation density becomes high enough, however, the transient shapes will change as some excitations are lost from the $^5I_7$ and $^3F_4$ manifolds to the $^5I_5$ manifold. By proper modeling of the excitation density in the material, the upconversion parameter can be determined from these measurements. We have modeled not only the Gaussian nature of the excitation density but also the exponential excitation density along the length of the material. We will start our analysis with the typical approach of fitting the upconversion parameter to the $^5I_7$ fluorescence transient.

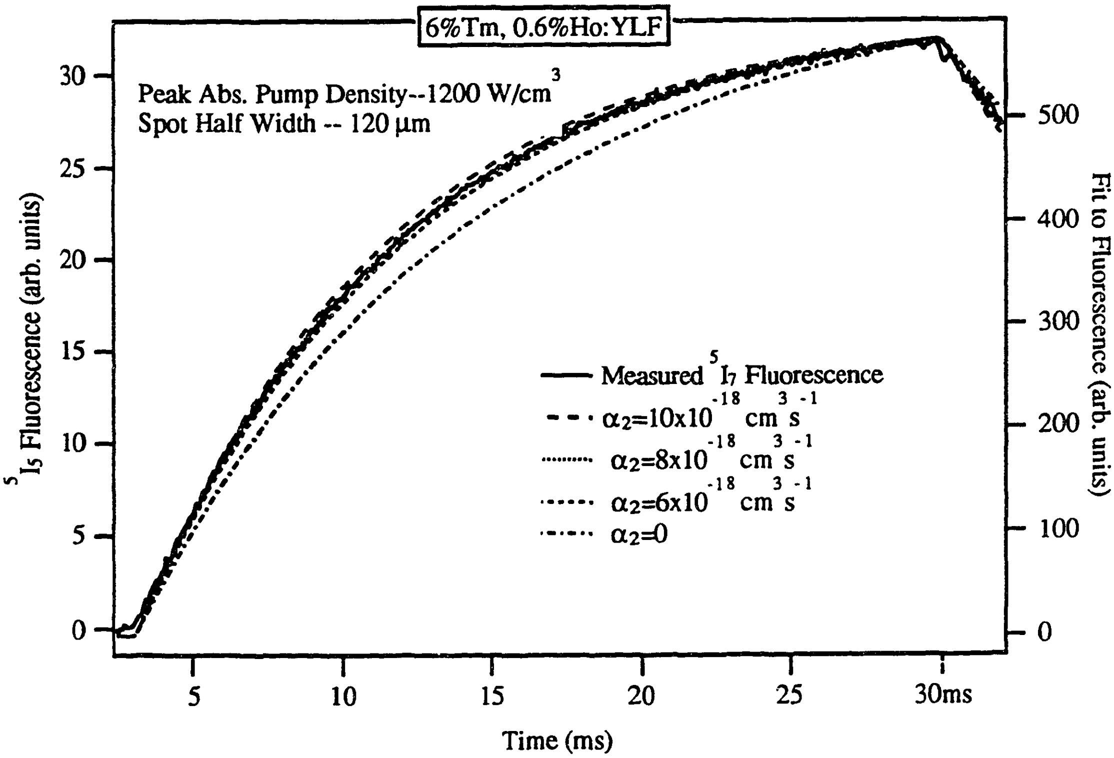

Figure 6.3.11. Experimental $^5I_7$ fluorescence transient with fits for varying values of α_2. All other parameters have been held constant for these fits. The transients resulting from different values of the upconversion parameter have been normalized to overlay the experimental data; as such, only their shapes are considered in the fitting procedure.

Figure 6.3.11 shows the $^5I_7$ transient for 6% Tm, 0.6% Ho:YLF along with solutions to the rate equations for varying values of α_2. As can be seen, the shape of the theoretical transients shows sensitivity to the values of the upconversion parameter. Also displayed is the shape that would be expected if the upconversion parameter were zero (α_2=0). It is clear that the upconversion process causes a distinct change in the shape of the $^5I_7$ transient from what would be expected without upconversion. As expansion of the fitted region is shown in Fig. 6.3.12.

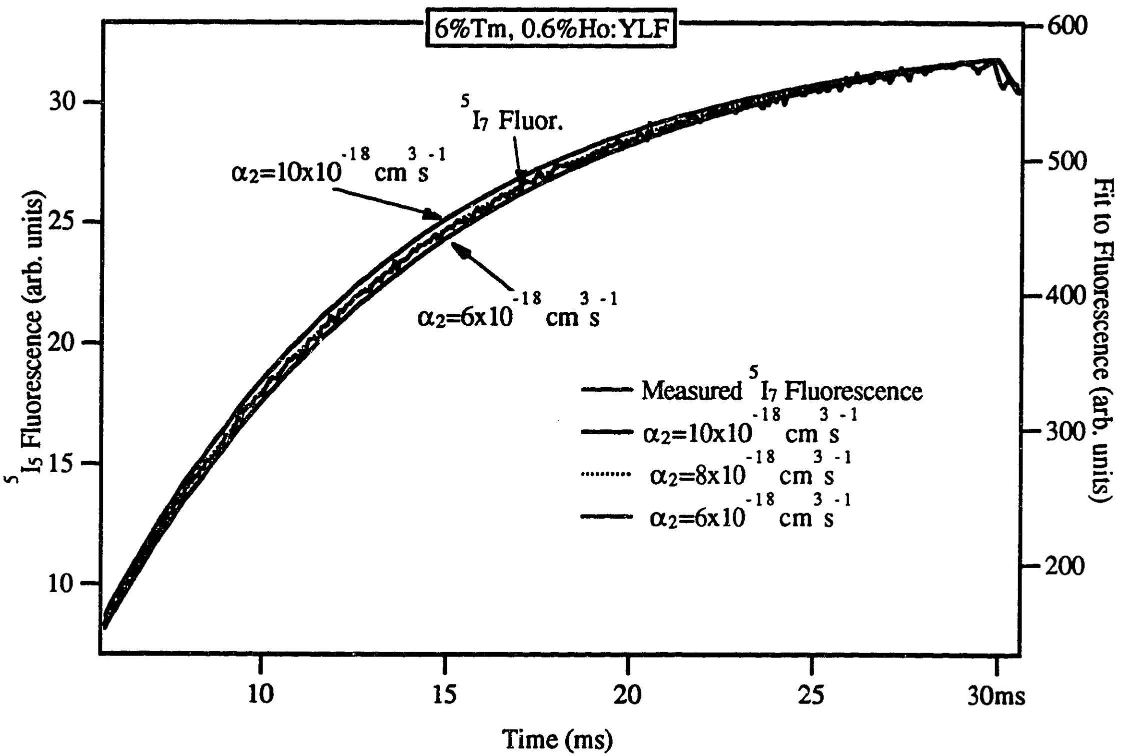

Figure 6.3.12. Expansion of the build-up of the measured $^5I_7$ fluorescence and predictions for the 6% Tm, 0.6% Ho:YLF transients pictured in Fig. 6.3.11.
Note how the transients for the values of α_2=10x10^{-21} cm^{3}s^{-1} and α_2=6x10^{-21} cm^{3}s^{-1} bracket the measured $^5I_7$ fluorescence transient and the prediction for α_2=8x10^{-21} cm^{3}s^{-1}.

From fitting to the above transient, we have determined the value of α_2 to be (8.0±1.5)x10^{-18} cm^{3}s^{-1}. The uncertainty estimate was obtained by varying the previously measured transfer parameters within their experimental uncertainties as well as by varying the pump power used in the fit. The pump intensity was determined by comparing the transmitted power to the incident power and correcting for reflection losses. The absorbed power calculated from these measurements implies an absorption coefficient of 3.2 cm^{-1}; this value is within 3% of the value measured at this wavelength for this sample. The value obtained for any given measurement showed a slight dependence on pump power, which was varied by ±10% in the course of the fitting procedure. The uncertainty listed for α_2 results from this variation as well as the variation of other quantities.

In Figure 6.3.8, we showed that the measured $^5I_5$ fluorescence transient was not the product of the $^5I_7$ and the $^3F_4$ fluorescence transients for our experiments; however, we stated that by compensating for the different excitation densities in the material we should be able to calculate the $^5I_5$ transient as well as the transients of the lower manifolds. This will allow us to check our results for consistency as we can find α_2 by fitting to the $^5I_5$ transient as well as to the $^5I_7$ transient.

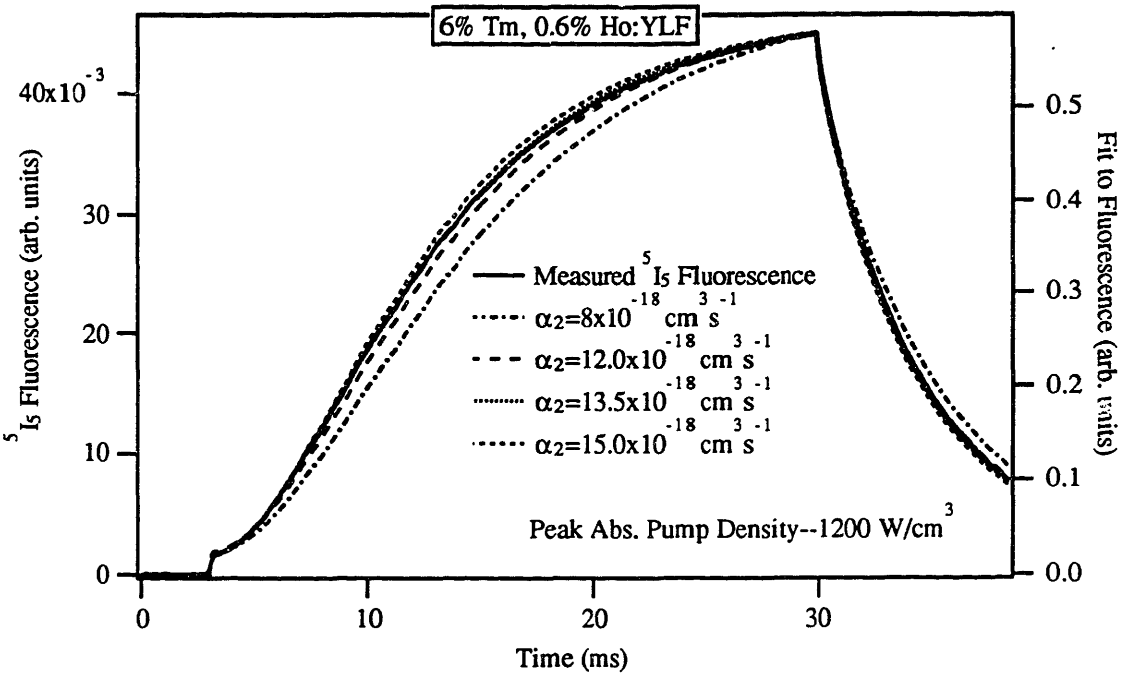

Figure 6.3.13. Experimental $^5I_5$ fluorescence transient for 6% Tm, 0.6% Ho:YLF. The best fit at this power level was obtained with $\alpha_2=13.5\times10^{-18}$ cm^{3}s^{-1}. The transient produced with $\alpha_2=13.5\times10^{-18}$ cm^{3}s^{-1} (the value that produced the best fit to the $^5I_7$ fluorescence) does not fit the $^5I_5$ fluorescence well. The small initial step in the signal results from a direct feeding process that feeds the $^5I_7$ manifold with ≈1.5% efficiency when the $^3H_4$ manifold is pumped at 293 nm.

In Figure 6.3.13, we have shown the measured $^5I_5$ fluorescence and the predictions of the rate equations. Note how the best fit to the fluorescence is obtained with an α_2 of $(13.5\pm1.5)\times10^{-18}$ cm^{3}s^{-1}; although the best fit to the $^5I_7$ fluorescence was obtained with a value for α_2 of $(8\pm1.5)\times10^{-18}$ cm^{3}s^{-1}. These values of α_2 do not agree within the experimental uncertainties, which is surprising as these transients were recorded simultaneously. Uncertainty estimates for both of these values were obtained by varying the measured transfer parameters within their experimental uncertainties as well as by varying the pump power. The value of α_2 produced by any set of transfer parameters changed in the same way for fits to both the $^5I_7$ and the $^5I_5$. Therefore, it is unlikely that the difference between these two values can be explained as a result of larger measurement uncertainties than assumed. The values obtained by fitting to the transients are tabulated in Tables 6.3.2 and 6.3.3 for Tm, Ho: YLF.

Material	(Cr-rel) α_2x10^{-18}	($^5I_7$) α_2x10^{-18}	($^5I_5$) α_2x10^{-18}	(Others) α_2 (x10^{-18})
6%Tm, 0.6%Ho: YLF	(15.0 ± 2.0)	(8.0±1.5)	(13.5±1.5)	5[136]

Table 6.3.2. Values of the upconversion coefficient α_2 in Tm, Ho doped materials produced by fitting to the $^5I_7$. Values of α_2 in the Cr-rel column represent the value of upconversion parameter expected from the cross-relaxation measurements.

What we actually determine from these measurements is the ratio of the upconversion parameter to the cross-relaxation parameter, which we have expected to be θ_2. The $^5I_5$ cross-relaxation rate is much larger than the relaxation rate for the $^5I_7$ manifold; and excitations interacting with this manifold will return very rapidly to the $^3F_4$-$^5I_7$ manifolds by cross-relaxation. As these rates are much faster than the relaxation rate of the $^5I_7$ we will only determine the ratio between the rates for the same reason that the low excitation density $^5I_7$ and $^3F_4$ transients depended only on the ratio of the transfer parameters. In our 6% Tm, 0.6% Ho:YLF sample, we found the best fit to the $^5I_7$ transient was given by a θ_2 ratio of 0.06± 0.01, while the

Material	En. levels θ_2	$^5I_7$ fit θ_2	$^5I_5$ fit θ_2	Others θ_2
6%Tm, 0.6%Ho: YLF	0.116	0.06	0.104	0.06[136]

Table 6.3.3. Ratios between the transfer parameters for the 5I5 upconversion process.

These results indicate that the model used earlier to describe the Tm-Ho system is inadequate. There are two possibilities: (1) we have neglected to include energy transfer or other processes which are active as high-excitation densities and contributes measurably to the dynamics, or (2) we have not correctly modeled the processes involved in the transfer. For this system, we have assumed that we could describe the transfer rate between manifolds with an average transfer parameter α. From energy transfer theory, we know that such a description is not always appropriate; and we suspect that the differences between these two measurements can be explained by the process of migration. We will discuss the implications of energy transfer theory in the next chapter.

Although we suspect that these observed deviations between the transfer microparameters can be explained with energy transfer theory, we have not eliminated other uncertainties as potential causes of the deviation. We now outline our arguments as to why the other transfer processes possible in the codoped system are not probable reasons for the observed deviations.

6.3.3. Additional Processes in Tm-Ho.

One possible explanation for the disagreement between the values of α_2 from transient fitting is that we have not included in our model processes which are active at high excitation densities. Additional loss processes such as excited state absorption from the first excited state manifolds[137], upconversion processes to the $^5I_6$ manifold[50], and upconversion processes to the $^3H_5$ manifolds have been proposed[51, 52]. These processes will add terms to the rate equations presented earlier; this in turn will affect the shape of the fluorescence transients and therefore the value of α_2 found by fitting these transients. We will now discuss why additional processes are not likely to be the source of the large disagreements in the values of α_2. Our arguments will not rule out all other processes; we will just restrict the types of processes which would have large enough effects on the $^5I_5$ and the $^5I_7$ manifolds to cause the observed deviations at these pump intensities.

Any energy transfer process will add terms to the rate equations presented earlier. These terms will act as sources or drains of excitations to the manifolds in whose rate equations the terms appear. As such, they will affect the excitation and time dependence of the manifold's population; these effects will appear as changes in the transients in our experiments. An unidentified process which feeds the $^5I_7$ manifold will act to reduce the apparent value of α_2 resulting from fitting, while a process which removes excitations from the $^5I_7$ will increase the fitted value of α_2. On the other hand, a process which feeds the $^5I_5$ will act to increase the apparent value of α_2, while a process which drains the $^5I_5$ manifold will decrease the apparent value of α_2.

If, in fact, an unidentified process is responsible for the differences between the two values of α_2, we would suspect such a process to be one which feeds either the $^5I_7$ or the $^5I_5$ manifold as the value of α_2 found from $^5I_5$ fitting is larger than the value found from $^5I_7$ fitting. Any process which feeds the $^5I_5$ manifold will also efficiently feed the $^5I_7$ due to cross-relaxation. An unidentified $^5I_7$ feeding process may exist, but is unlikely

---

[137] M. G. Jani, R. J. Reeves, R. C. Powell, G. J. Quarles, and L. Esterowitz, "Alexandrite-laser excitation of a Tm:Ho:Y3Al5O12 laser", J. Opt. Soc. Am. B, V8, N4, (1991), P741.

to cause the observed deviation for the following reason. The $^3H_4$ manifold cross-relaxes to the $^3F_4$ manifold with ~99% efficiency at the Tm concentrations involved (in singly doped Tm); any unidentified $^5I_7$ feeding process will increase the feeding efficiency of the $^3F_4$ and $^5I_7$ manifolds. A change in the feeding efficiency from 99% to 100% will not produce a perceptible change in the $^5I_7$ fluorescence and therefore not change the value of α_2 obtained from fitting this transient. If an unidentified transfer process is the reason for the disagreements between the fitted values of α_2, the most logical process is one which feeds the $^5I_5$ manifold with high efficiency.

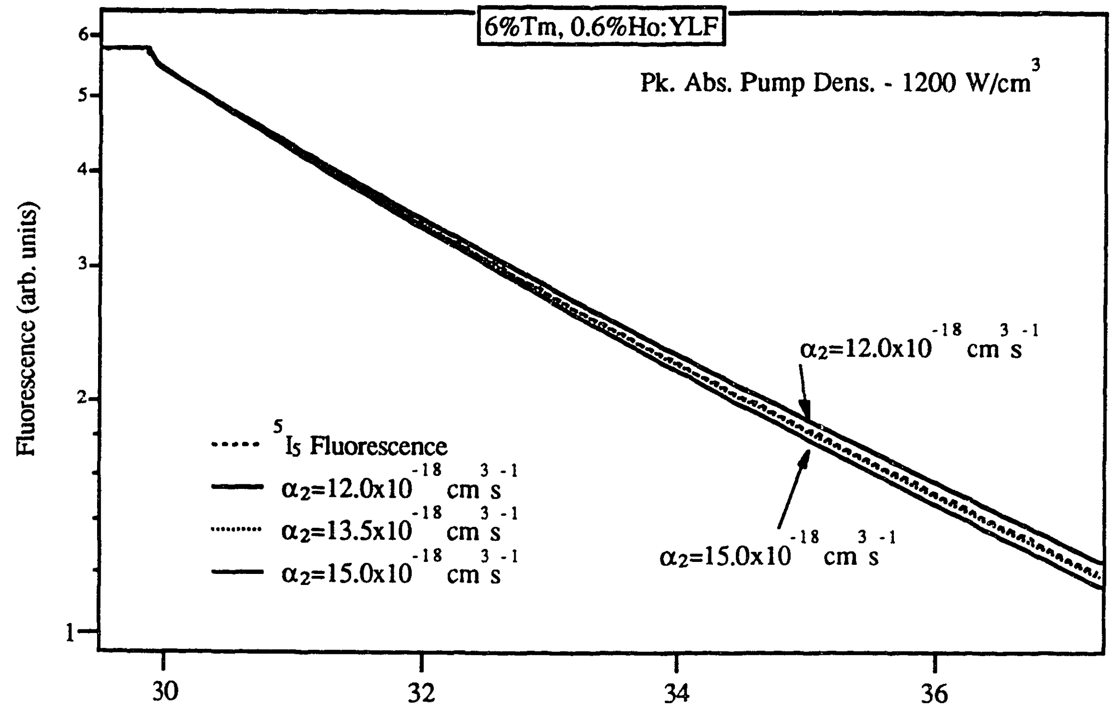

Figure 6.3.14. Logarithmic plot of the $^5I_5$ dynamics following the pump pulse. This is an expansion of the transient shown in Fig. 6.3.13. Notice how the decay is still fit well by the predictions of the rate equations for the same value of α_2 as for build up

By further examining the $^5I_5$ transients, we can restrict the type of possible feeding processes. Figure 6.3.14 shows the dynamics of the $^5I_5$ transient after the pump pulse as well as the predictions of the rate equations. As can be seen, the $^5I_5$ dynamics after the pump pulse are described by the same value of α_2 which described the pulse buildup. This implies that any other transfer processes affecting the $^5I_5$ manifold have the same dependence on excitation density as the $^3F_4$->$^3H_6$, $^5I_7$->$^5I_5$ upconversion process (~lower level excitation density squared). Processes with different dependencies on excitation density build up and decay in different manners with respect to time. This restriction effectively removes from consideration many of the possible energy transfer processes which could affect the $^5I_5$. Excited state absorption processes can also be eliminated from consideration for this reason.

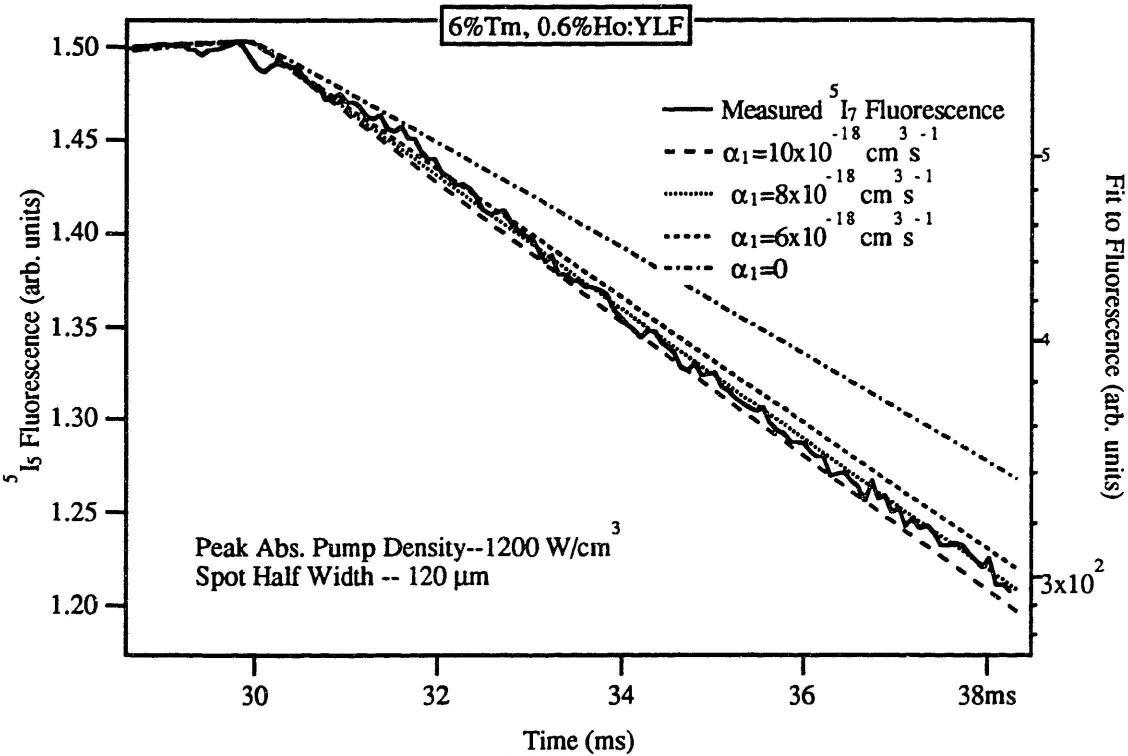

Figure 6.3.15 Logarithmic plot of the $^5I_7$ dynamic following the pump pulse.

Figure 6.3.15 shows the logarithm of the $^5I_7$ fluorescence following the pump pulse. This decay dynamic also appears to be described by the same value of α_2 which described the $^5I_7$ transient build up. The above data severely restrict the type of energy transfer process which could be responsible for the disagreement in the values of α_2; any substantial transfer mechanisms affecting the $^5I_7$ manifold must have a $N_1{}^2$ dependence on excitation density, although these data are slightly noisy and it is difficult to judge the quality of the fit.

One process with a $N_1{}^2$ dependence on excitation density capable of feeding the $^5I_5$ manifold is $^3F_4$->$^3H_6$, $^3F_4$->$^3H_4$ upconversion followed by direct transfer to the $^5I_5$ manifold. Earlier we discussed this upconversion process in singly-doped Tm and dismissed it as a major loss process in the system as the expected value of the upconversion parameter was small relative to the other parameters in the system. We measured the upconversion parameter for 2% Tm:BaY$_2$F$_8$ and found it to be smaller than our predictions from the cross-relaxation measurements discussed in Chap. 6. We did not directly measure the upconversion parameter for the higher-concentration singly-doped Tm samples, however, and therefore had no experimental evidence that the value of the upconversion parameter matched our expectations (from cross-relaxation) in the higher concentration Tm samples. We did measure the $^3H_4$ fluorescence transient in the codoped samples simultaneously with the $^5I_7$ and $^5I_5$ transients; from fitting, we found the parameter for $^3F_4$->$^3H_4$, $^3F_4$->$^3H_6$ upconversion (α_1) to be roughly $(1\pm0.5)\ \mathrm{x}10^{-19}$ $\mathrm{cm}^3\mathrm{s}^{-1}$ in 6% Tm, 0.6% Ho:YLF. The amount of upconversion was too small to determine the upconversion parameter more accurately; however, this implies a ratio between the upconversion and cross-relaxation parameters (θ_1) of ~ 0.003±0.002, which agrees roughly with what we would expect for this process in YLF. A plot of the $^3H_4$ transient is shown in Figure 6.3.16.

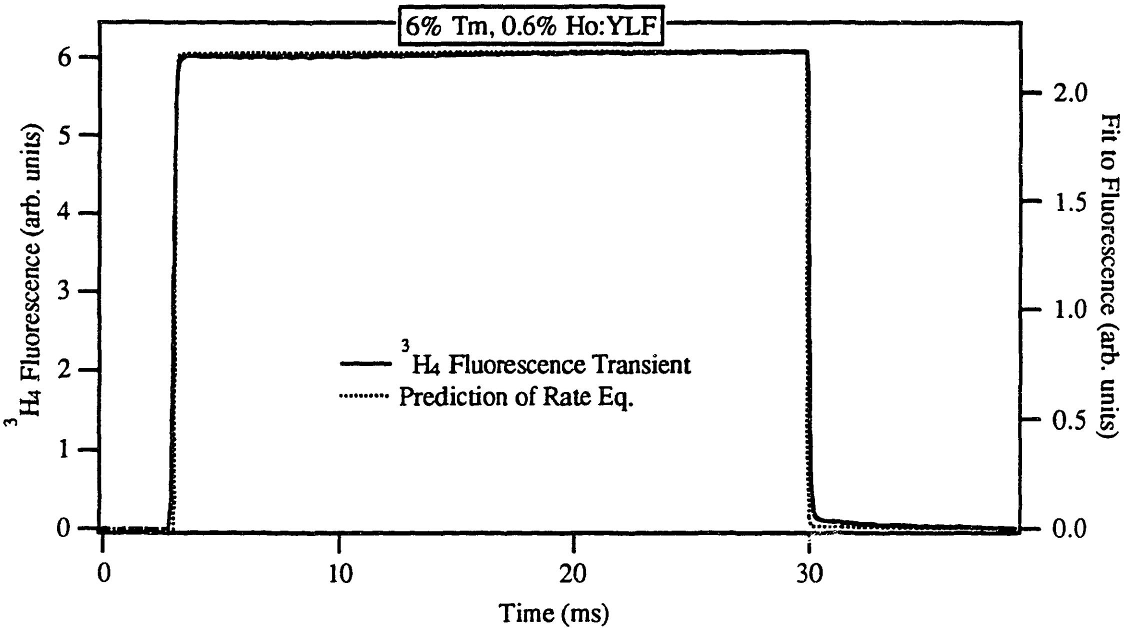

Figure 6.3.16. $^3H_4$ fluorescence transient under direct square pulse pumping.

We can thus discount the Tm $^3F_4$->$^3H_4$, $^3F_4$->$^3H_6$ upconversion as a source of error as it has been included in the rate equation model used for the fits which produced α_2, and, as expected, the value of α_2 is small in comparison to other parameters in the system. The question arises if other processes exist which feed excitations to the $^5I_5$ manifold with an N_1^2 dependence. If these processes exist and occur at high rates, they would affect the apparent value of α_2 produced by fitting to the model. We do not consider the possible 3-body interactions (such as $^3F_4$->$^3H_6$, $^3F_4$->$^3H_6$, $^5I_8$->$^5I_5$ upconversion) for two reasons. These processes are relatively improbable in comparison to two-body processes and have been shown to only contribute measurably to the fluorescence signal at donor concentrations greater than ~15% in rare-earth doped systems. Additionally, these processes would act as loss mechanisms on the $^3F_4$ and $^5I_7$ manifolds and would therefore increase the value of α_2 found by fitting the fluorescence from these manifolds. For now, we rule out additional processes as the reason for the disagreement in the values of α_2 produced by $^5I_5$ and $^5I_7$ transient fitting.

Although we have eliminated other processes from consideration as large deviations observed in our α_2 upconversion measurements, they definitely are active in the system. A process which appears to directly feed the $^5I_5$ manifold is apparent as a small initial step in the signal in the plots of the $^5I_5$ fluorescence (shown in Figure 6.3.13). We have not identified the source of this feeding. This could either be the result of a small direct absorption at the pump wavelength or a direct transfer process from the $^3H_4$ manifold. If this feeding is the result of an unidentified absorption, the absorption coefficient is ~0.03 cm^{-1}. If this process results from direct transfer from the $^3H_4$, the quantum efficiency of the process is only ~1%. This may be the unidentified Tm-Ho feeding process reported in [91].

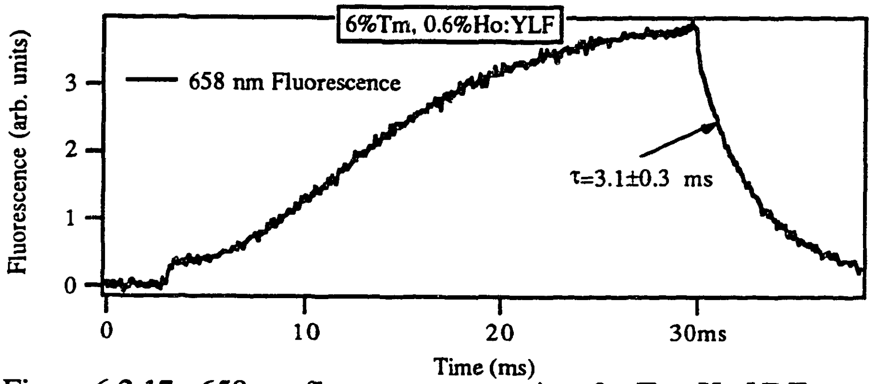

Figure 6.3.17. 658 nm fluorescence transient for Tm, Ho:YLF.

A power dependent 658 nm fluorescence signal was also observed at higher excitation densities. A plot of this transient is shown in Figure 6.3.17. The process is upconversion fed; the decay is much longer lived than any of the manifold which can fluoresce at this wavelength, so the manifold must be fed after the pump pulse has terminated. This eliminates excited state absorption as the source of this process. We suspect that this fluorescence is from the $^5F_5$ manifold as a $^3F_4$->$^3H_6$, $^5I_6$->$^5F_5$ upconversion process is nearly resonant. The energy gap for this process is ≈+1400 cm^{-1} and would therefore be favored.

One parameter which we have not measured is the efficiency of the $^5I_6$->$^3H_5$ transfer process which we postulated based on the position of the system's energy levels. This uncertainty has been accounted for by allowing η (the quantum efficiency of return to either the $^5I_7$ or the $^3F_4$ manifold for an excitation relaxing from the $^5I_5$ by multiphonon relaxation) to vary between 1.0 and 0.7 when fitting the rate equations. The uncertainty produced by this variation has been included in the uncertainty reported for the value of α_2 produced by fitting. This transfer process has been reported to be efficient, which an η that is nearly unity[51]. However, the efficiency of this transfer process has not been determined for YLF. If this process is not efficient, it could allow the population of the $^5I_6$ manifold to develop. A substantial $^5I_6$ population could lead to $^3F_4$->$^3H_6$, $^5I_6$->$^5F_5$ upconversion as well as other processes (for example, a $^3H_5$->$^3F_2$, $^5I_6$->$^5I_8$ upconversion process in Tm). As mentioned previously, these processes will have little effect on the values of α_2 found in these measurements since they do not have a N_1^2 dependence on excitation density.

From these arguments, we conclude that additional transfer processes, while present, will not explain the disparity in the values of α_2 produced by fitting the different transients.

6.4. Chapter Summary

In this chapter, we have discussed several different experiments and presented a great deal of data. However, as mentioned at the start of this chapter, these experiments were designed to provide a good deal of engineering data as well as test certain aspects of our theory. The basic goal of all of these experiments was to check the applicability of the relation $\alpha=\theta\,\alpha'$. We found that this relationship was not applicable in general to the transfer parameters for upconversion and cross-relaxation. We will discuss the reasons for this deviation in the following chapter.

7. Discussion.

In the preceding chapters, we have presented both theoretical predictions for and experimental measurements of the distribution of excitations between the $^3F_4$ and the $^5I_7$ manifolds under quasi-equilibrium conditions. Within experimental uncertainties, our experimental measurements confirmed the predictions of the theory presented in Chapter 3.

We then focused on the rate relationships implied by the existence of an equilibrium distribution. A series of dynamics experiments measured the energy transfer rates between various manifolds. In these measurements we found that the value of the average energy transfer parameters did not agree for different measurement techniques. We now explore possible reasons for the deviations found in the dynamics measurements; following which we address some theoretical and experimental concerns of the general theory. Finally, we end with a discussion of the implications of the theory developed in this thesis for the Tm-Ho laser.

7.1. Concerns of the Dynamics Measurements.

In the dynamics measurements presented in the preceding chapter, we found two areas of disagreement between experimental measurements and the theory and models used to interpret the data. First, we found that the upconversion parameter determined by fitting to the rate equations did not agree with the value predicted from the measurements of the cross-relaxation rates for some measurements. Secondly, we found that the values for the $^3F_4$->$^3H_6$, $^5I_7$->$^5I_5$ upconversion parameter (α_2) found by fitting to different simultaneously-measured transients did not agree. The first observation may indicate a deviation from the expected relationship between the transfer parameters, while the disagreement between the values of α_2 produced by fits to the $^5I_5$ and the $^5I_7$ fluorescence indicate that the model for Tm-Ho presented in Chapter 6 is not adequate to explain this system. We will first concentrate on the reason for differences between the values of α_2 obtained by fitting to the $^5I_5$ and $^5I_7$ transients.

7.1.1. Dependence of the average transfer parameter upon excitation density.

The differences in the fitted values of α_2 can be explained if α_2 is excitation density dependent. Energy transfer theory states that the dynamics of the energy transfer process depends on the manner in which the ensemble of ions involved in the transfer is prepared, i.e., the past history of the system is important.[19, 70] This implies that the average energy transfer parameter (α_2) will depend on both the excitation density and the length of time the system has been pumped; an excitation and time dependence of the upconversion parameters has been found in Cr doped systems[138].

In our experiment, we measure only a single fluorescence transient that is the sum of the fluorescence signals produced throughout the excited volume. The value of α_2 produced by fitting to such a measurement is a weighted average of the energy transfer parameter over the volume contributing to the fluorescence, where the weighting is determined by the fluorescence intensity at a given excitation level. The $^5I_7$ fluorescence is linearly proportional to the excitation density, while the $^5I_5$ fluorescence is proportional to the excitation density squared. Thus, the average parameter obtained from fitting the $^5I_5$ fluorescence intensity will weight the contributions of the regions of high excitation density more than that obtained from fitting the $^5I_7$ fluorescence. Unless the excitation distribution is uniform, we will have different weighting functions over the excited volume for these two transients. The excitation density in the material is proportional to the distribution of energy in the pump. The pump profile has been measured to be approximately gaussian (Chap. 6), so we can assume that the excitation density will be roughly gaussian (as long as the Tm ground state is not depleted). The resulting weighting functions as a function of radial position are illustrated in Figure 7.1.1.

---

[138] M. A. Noginov, H. P. Jenssen, and A. Cassanho, "Upconversion in Cr:LiSGaF and Cr:LiSAF," OSA Proc. Adv. Solid State Lasers, V16, ed E. Pinto and T. Y. Fan, New Orleans, (1993),

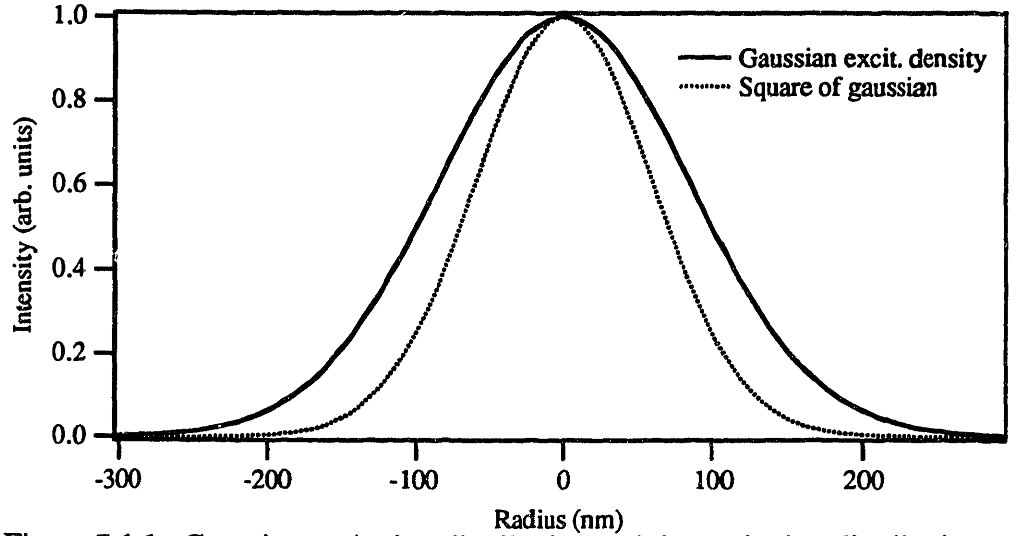

Figure 7.1.1. Gaussian excitation distribution and the excitation distribution squared. The amount of ${}^5I_7$ fluorescence is linearly proportional to the excitation density, while the ${}^5I_5$ fluorescence is proportional to the excitation density squared.

As the weighting functions for the ${}^5I_5$ and ${}^5I_7$ fluorescence are different, it is not surprising that different values of α_2 are found in these measurements. As the value of α_2 determined from fitting the ${}^5I_5$ transient is much greater than that determined by fitting the ${}^5I_7$ transient, we can assume that α_2 will be larger at higher excitation densities. For instance, if α_2 is linearly proportional to the excitation density, the ratio of the measured values for a gaussian excitation distribution would be $\alpha_2({}^5I_7)/\alpha_2({}^5I_5) = 3/4$. Note that the correction that we find here is not a simple correction for the variance of the excitation density with the pump--this was accounted for in Chapter 6 by fitting the transients with a gaussian distribution of excitation densities and there is no need for a correction factor to account for the different contributions to the fluorescence from regions of differing excitation density if the transfer parameters are constant. The correction discussed here results from having an average transfer parameter which is excitation density dependent and having varying excitation densities in an experiment.

7.1.2. Averaging and the role of migration.

Up to now, we have used an average transfer parameter, (α_2, described in Eq. 6.1.5) to describe the transfer process; the approximation of an average transfer parameter is generally made to simplify analysis of laser rate equations[37]. In our discussion of energy transfer theory, we saw that the transfer process for an ensemble of donors and acceptors could be described as a summation over exponentials with differing transfer rates. This description was appropriate when the transfer occurred without migration (static transfer). For migration-assisted transfer, the migration process will average out the different transfer rates resulting from different ion separations and orientations to produce a single transfer rate. As the upconversion process relies on migration, the existence of a single transfer rate is generally used to justify the use of an average transfer parameter in the rate equations. We now discuss how aspects of the migration process will cause the average transfer parameter for upconversion to be excitation density dependent.

There are several reviews of migration-assisted transfer theory available[19, 68, 69, 70, as well as others]. Most of these reviews are directed at finding the proper mathematical description of the dynamics of donors and acceptors for a specific experiments, distributions, etc.; however, we are interested more in the qualitative behave of the average transfer parameter than the details of the microscopic process. Without detailed knowledge of the model used and its parameters, it is extremely difficult to make predictions on the exact manner in which α may vary. However, it is possible to make general statements about the behavior of the average transfer parameter by using only the basic principles of migration-assisted transfer.

In the rate equations of Chapter 6.3, the $^5I_5$ upconversion rate is given by $\alpha_2 N_1 N_1'$. Recalling our discussion of migration-assisted energy transfer, the energy transfer rate per excitation was given by $W_{ma} = k(C_{dd})^m (C_{da})^{1-m} N_d N_a$, where k is a model dependent constant, C_{da} is the microparameter for donor-acceptor transfer, and C_{dd} is the transfer microparameter for donor-donor transfer. In the above expression, m is either 3/4 (for the diffusion model) or 1/2 (for the hopping model). Modeling upconversion as a migration-assisted transfer process, we can relate these two expressions. The number of acceptors, N_a, for migration assisted upconversion is given by the first excited state Ho population, N_1', and not the ground state Ho population ($N_0 \approx N_{Ho}$) as is generally assumed in energy transfer problems. Upconversion to the $^5I_5$ manifold requires a Ho ion in a state belonging to the $^5I_7$ manifold to act as an acceptor for excitations in the Tm $^3F_4$ manifold. The upconversion parameter α_2 can be expressed as

$$\alpha_2 = k(C_{dd})^m (C_{da})^{1-m} N_d . \tag{7.1.1}$$

Notice that the excited state population of Tm (N_1) is <u>not</u> assigned to N_d. In the above relationship, N_d is the total concentration of Tm in the material. Tm ions in the ground state serve as acceptors for migrating excitations as this migration is the result of a $^3F_4$->$^3H_6$, $^3H_6$->$^3F_4$ energy transfer process. Meanwhile, N_1 represents the number of excitations in the $^3F_4$ manifold. As seen in Eq. 7.1.1, the average transfer parameter for migration assisted upconversion (α_2) is determined by not only the transfer microparameter for $^3F_4$->$^3H_6$, $^5I_7$->$^5I_5$ energy transfer, but also by the transfer microparameter for transfer among the $^3F_4$ manifold and the total concentration of Tm. Additionally, we must be concerned with two different types of acceptors -- Ho ions in $^5I_7$ states which act as acceptors for the actual upconversion process and Tm ions in the $^3H_6$ states which act as acceptors for the migration process.

When the distance between an acceptor for upconversion and an excitation donor is large enough that the direct transfer probability between the two ions is small, an excitation deposited in the Tm $^3F_4$ manifold can "hunt" for an acceptor by migrating among Tm ions until the distance between the excitation and an acceptor is reduced and the probability of upconversion transfer has improved. When the acceptor concentration is high, the excitation will require only a few steps before upconversion transfer is possible; on the other hand, if the acceptor concentration is low, the excitation may need to migrate a considerable distance before transfer is probable. If the acceptor concentration is too low, the excitation may decay by spontaneous emission before finding an acceptor. As the excitation density drops, the number of acceptors for upconversion will also decrease; and the average time that an excitation will need to migrate before transferring will increase. This migration will cause a small time lag between when an excitation is deposited in the $^3F_4$ manifold and when it transfers to the $^5I_5$ manifold. This time lag will cause a reduction in the average energy transfer rate as the effective transfer time will be longer than it would be if the excitation transferred directly from a nearby neighbor. As our measurements of α_2 represent a weighted average of the transfer parameters at different excitation levels, it is reasonable that the average values of α_2 differs when measured by observing fluorescence transients from different manifolds in the same sample.

Near the end of Sect. 3.4, we mentioned that limits could be placed on the minimum concentrations of donors and acceptors if an equilibrium distribution between the $^3F_4$ and the $^5I_7$ manifolds was to develop. This is an analogous problem to that just discussed and can also be explained by considering the migration process. Additionally it is a somewhat simpler problem that will illustrate the concerns caused by migration. Several groups have conducted studies of energy transfer between the $^3F_4$ and $^5I_7$

manifolds in different materials when the $^3F_4$ is directly pumped. Payne et al[95] have found that the equilibration time lengthens considerable at lower concentrations. Some of these data are presented in Table 7.1.1.

Tm Conc. ($\times 10^{19}$ cm^{-3})	Ho Conc. ($\times 10^{19}$ cm^{-3})	Equil. Time (ms)
12.6 *	1.25	3.2
37.2 *	1.32	1.3
61.0 *	1.20	<0.1
12.2 *	3.68	2.5
61.0 *	3.64	<0.1
80 £	6.2	≈0.100
80 (in YAG) ç	6.5	0.190
80 (in YAG) ç	13	0.130

Table 7.1.1. Equilibration time for low concentration Tm, Ho doped materials. Date denoted by * is from [95], £ is from[91], and ç is from [92].

These equilibrium times were determined by directly pumping the $^3F_4$ and measuring both the $^3F_4$ and the $^5I_7$ transients. The equilibration time is the time difference between the initial pulse and the point where both the $^5I_7$ and the $^3F_4$ decay with the same rate. The lengthened equilibrium time found at lower ion concentrations indicates that the average energy transfer rate is reduced relative to the higher concentrations. Relating the expression for this transfer process from the rate equations of Chap. 6.3 to the migration-assisted transfer rate given earlier, we find $\alpha_T N_0' N_1 = k'(C_{dd})^m (C_{da}')^{1-m} N_d' N_a N_1$. The concentration of acceptors for migration is simply the number of Tm ions in states belonging to the $^3H_6$ manifold (N_0), while the concentration of acceptors for energy transfer is the number of Ho ions with states in the $^5I_8$ manifold. At low excitation densities, we can approximate N_0 as N_{Tm} and N_0' as N_{Ho}. The transfer parameter α_T can be expressed as

$$\alpha_T = k'(C_{dd})^m (C_{da}')^{1-m} N_{Tm}'. \qquad (7.1.2)$$

For this transfer process, the acceptor for an excitation migrating in the Tm $^3F_4$ manifold is a Ho ion in the ground state; at low excitation densities the number of acceptors can be approximated as the Ho concentration. As the Ho concentration increases, the amount of time that an excitation in the Tm $^3F_4$ manifold needs to migrate to find an acceptor is reduced, and the average transfer time from Tm to Ho will decrease; this implies that for a fixed Tm concentration, the system should come to equilibrium more rapidly with increasing Ho concentration.

If we recognize that the equilibration time is roughly the time required for randomly deposited excitations to diffuse to a position close to an acceptor and transfer, we can find how this process depends on the ion concentrations. Modeling the migration as a standard random walk problem, the average distance x that an excitation will diffuse in time t_0 is

$$\langle x \rangle = \sqrt{6Dt_0}, \tag{7.1.3}$$

where D is the diffusion coefficient. The average distance between acceptor ions is $\approx N_a^{-1/3}$. Assuming that the farthest an excitation would need to diffuse is roughly half the distance between acceptor ions, the equilibrium times above imply a diffusion coefficient for migration on the order of 10^{-12} cm^{2}s^{-1} for $N_{Tm}\approx 12\times10^{19}$ ions/cm^3 and of 10^{-10} cm^{2}s^{-1} for $N_{Tm}\approx 8\times10^{20}$ ions/cm^3 in YLF. The exact value of the diffusion coefficient can not be determined from these measurements alone as the average time of the transfer step between Tm and Ho is also included in the equilibrium times. The time required for this transfer step will be depend on the average distance between a Ho ion and the nearest Tm ion and will therefore also be concentration dependent. There are several different ways of modeling the diffusion process which take into account the structure of the material, the probability of different size steps, and so forth[70], but for our purposes the simple model of diffusion just presented will be sufficient.

There are two different transfer mechanisms active in this transfer process, and each mechanism places constraints on the maximum transfer rate. If the diffusion rate is much slower than the direct transfer step, the transfer time is primarily determined by amount of time that is required for an excitation to migrate to a position close enough to an acceptor to transfer and the transfer process is called "migration-limited", "migration-assisted", or "diffusion-limited" dependent upon the reference. If the direct transfer step is much slower than the time required for diffusion, the process is called "transfer-limited" or the system referred to as being in the "kinetic" limit. Here the rate of the direct transfer process will determine the maximum rate of transfer; this sometimes referred to as a "donor-acceptor bottleneck" as the maximum transfer rate will saturate with increasing concentration. This maximum rate can be calculated with a lattice sum and the energy transfer micro-parameter for the transfer process[138].

One additional point must be mentioned. As can be seen from Eq. 7.1.2, the transfer rate also depends on the number of acceptors for the migration process. At low excitation densities this can be approximated as $N_0 \approx N_{Tm}$, but at higher excitation densities it is not appropriate to approximate the acceptor concentration for migration; $N_0 = N_{Tm} - N_1$ should be used. The result is that the migration rate will be reduced at higher excitation levels.

These processes provide limits on the maximum average transfer rate, R_{max}. Substituting the acceptor concentration into Eq. 7.1.3, the maximum transfer rate in the migration-limited domain will vary as

$$R_{max} \approx BN_a^{2/3}(1 - N_{ex}/N_d), \tag{7.1.4}$$

where N_a is the acceptor concentration, N_d is the donor concentration, and N_{ex} is the excitation concentration. B will be proportional to the value of the transfer microparameters for both donor-donor and donor-acceptor transfer as well as details of the transfer process. This expression is only an approximation as we have not considered back-transfer and other details of the transfer process. In the transfer-limited domain, the maximum transfer rate will be the direct transfer rate for nearest neighbor transfer. Note that we have only developed limits for the maximum rate. The actual rate will be less than this limit and will depend on the relative strength of transfer microparameters.

Returning to the upconversion process, we mentioned earlier that Ho ions in the $^5I_7$ state serve as acceptors for excitations in the Tm. As the acceptor concentration is determined by the excitation level, the transfer rate will be reduced at low excitation densities as excitations must migrate farther to find the acceptors. In this case, Eq. 7.1.4 can be approximated as

$$R_{max} \approx B'N_{ex}^{2/3}(1 - N_{ex}/N_d) \tag{7.1.5}$$

where we have approximated the $^5I_7$ population as directly proportional to $^3F_4$ population. As we are interested in only the limiting behavior at low excitation densities this approximation is sufficient, but for use at higher excitation densities the relationship between the $^5I_7$ and the $^3F_4$ population developed earlier should be used. A plot of this relationship for varying values of B is shown in Fig. 7.1.2.

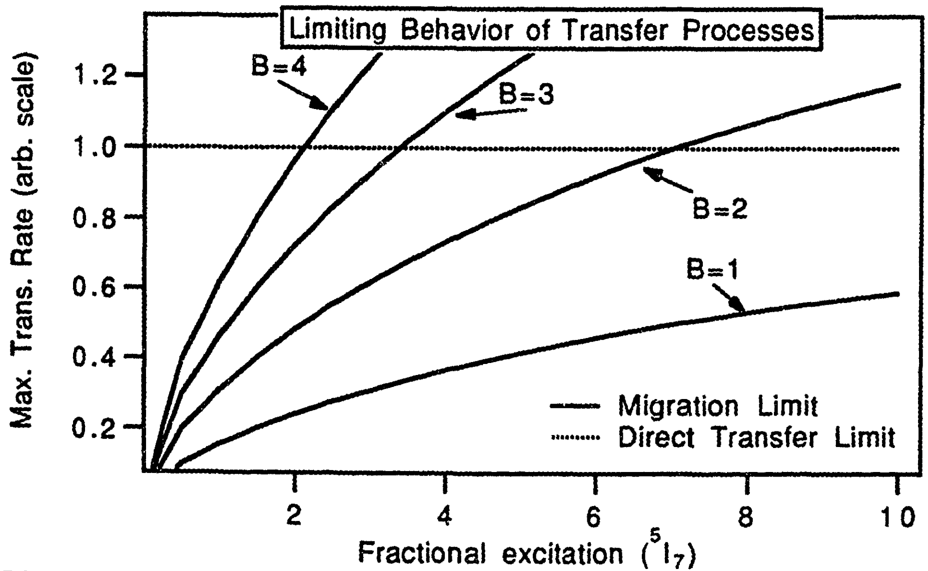

Figure 7.1.2. Plots of the limiting relationships for upconversion transfer rates. The direct transfer rate limit is a constant determined by the rate of transfer to the nearest neighbor, while the migration rate limit is determined by a combination the migration rate and the direct transfer rate.

As can be seen, the behavior of migration-limited transfer is very sensitive to the value of B. The actual rate at any excitation density will be less than the limits presented here. As our upconversion experiment measures the average transfer rate over a range of excitation densities, it is clear that an averaging technique which weights the contribution from the low excitation density regions more than a different technique will also produce a smaller value for the average transfer rate. The difference between the two values will depend on the excitation density where the transfer behavior switches from migration-limited to transfer-limited as well as the details of the averaging technique.

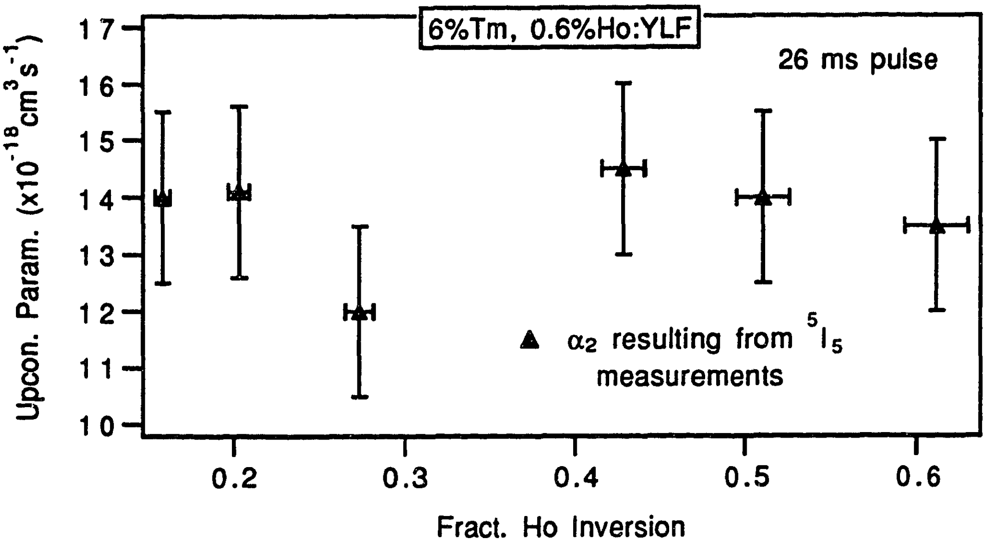

Figure 7.1.3. Measured upconversion parameter as a function of Ho inversion. The values reported are for the value of α_2 produced from fitting to the $^5I_5$ transient.

Figure 7.1.3 presents the values of the upconversion parameter produced by fitting to the $^5I_5$ fluorescence. Within experimental uncertainties, the value of the upconversion parameter is roughly constant; this implies that the upconversion process is in the transfer-limited domain at these inversion densities. It should be noted that the ratio of the upconversion parameters found by fitting to the $^5I_5$ transients and the cross-relaxation parameters yields a value of $\theta \approx 0.11 \pm 0.02$, which agrees within experimental uncertainty with the value of $\theta = 0.116$ predicted from using the chemical potential approach. We can also calculate the ratio between $\alpha_1(^5I_5)$ and $\alpha_1(^5I_7)$ if we know the dependence of the transfer rate upon excitation density. Using the form given in Eq. 7.1.5, we would expect $\alpha_1(^5I_5)/\alpha_1(^5I_7)=1.2$. In our measurements, we found the ratio $\alpha_1(^5I_5)/\alpha_1(^5I_7)=1.6$. If the larger ratio of these parameters is solely the result of the migration process, this would imply that the average rate increases at a higher power of the excitation density than 2/3.

At this point, these arguments are based in theory. The next logical experiment to test the excitation dependence of the transfer parameter which would be to use a uniformly pumped volume to eliminate the problems inherent with a gaussian pump.

7.1.3. Deviation of the average parameters from the predicted values.

In the preceding section, we saw that migration could cause the average value of the transfer parameters to differ in different manners. Migration can also explain why the average transfer parameter for upconversion differs in some measurements from that expected from the measured cross-relaxation parameter and the energy levels. This is partially a result of the manner in which these measurements are conducted. The cross-relaxation measurements were conducted by directly pumping an upper state and observing the shortening of the lifetime as the concentration increased. The average energy transfer rate found in these measurements represents the average rate for a static transfer process, i.e., little to no migration of the excitation occurs before the direct transfer to an acceptor occurs. We established that the cross-relaxation process in Tm was primarily a static transfer process. Upconversion, on the other hand, relies on migration to occur; and therefore the transfer rates for upconversion will always be less than would be predicted from measurements of the cross-relaxation rates in these system. However, this does not mean that the relationship between the transfer microparameters derived in Chapter 3, (Eq. 3.2.5) does not hold.

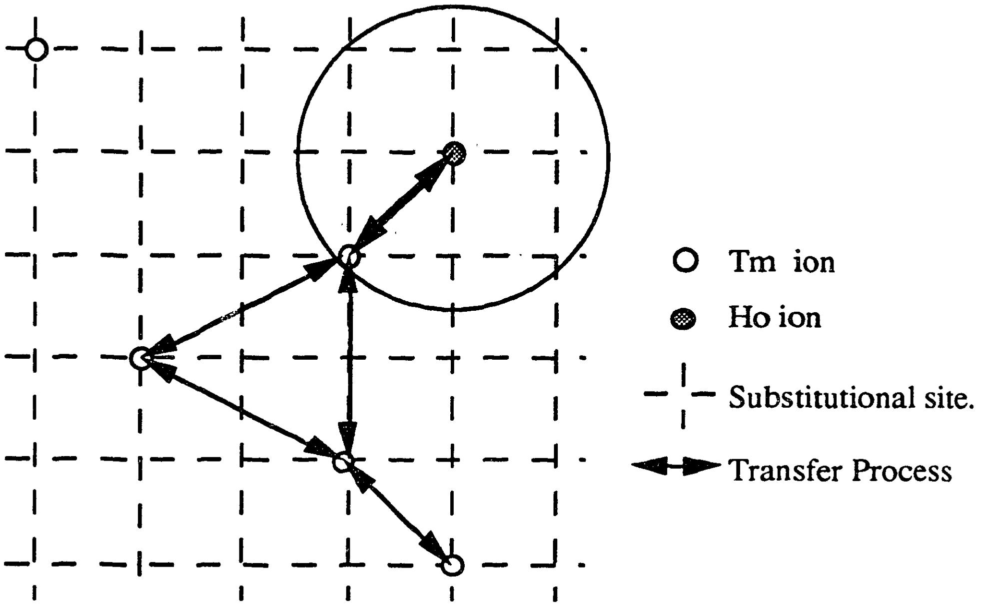

Figure 7.1.4. Schematic of migration and transfer processes on a 2-dimensional lattice. In a Tm-Ho doped material, the probability of $^3F_4$-$^3F_4$ transfer between any two Tm particular ions is equal, while the probabilities of transfer from Tm to Ho and from Ho to Tm will be related by the ratio θ for any particular set of ions.

In Figure 7.1.4, some of the possible transfer steps that can occur in a Tm-Ho doped material are shown. The probability of a step between any two Tm ions is equal for transfer and back-transfer; although the step probability per unit time will depend on the distance between the two ions (and the relative orientation in anisotropic materials). The probability of transfer occurring between any particular Tm ion and the Ho ion is related to the probability of back transfer occurring by the ratio θ <u>if</u> the back transfer exactly retraces the path that the initial transfer followed. However, emission from any Tm ion is indistinguishable, so before the system equilibrates (meaning that all excitations have migrated far enough to have interacted with a Ho ion at least once) the measured ratio of the ion populations will be reduced.

Additionally, if the acceptor concentration is too low, the excitations may decay before finding an acceptor, which would lead to an apparent reduction of the value of θ for systems which have reached equilibrium. This may explain why the value of α_1 measured for the 2%Tm:BaY_2F_8 sample was less than that predicted from the cross-relaxation measurements, although the values of α_1 measured in higher concentration Tm samples at high excitation densities agree within the uncertainty with the expected value. Chou[130], Knowles[131], and Dinerman[139] have measured the rates for both cross-relaxation and upconversion processes in singly-doped Er:YLF and Er:BYF with a steady-state technique. Their measurements imply that the ratio between the upconversion and cross-relaxation parameters ranges from 50% to 20% of the value that would be expected from the known energy level structure of these materials. These measurements were conducted at low excitation densities, so it may be that the acceptor concentrations for upconversion were low. However, it is unclear at this point if an excitation-dependent transfer parameter will explain the deviation in this system. Additional characterization would need to be performed at different excitation levels.

The question that arises is how can we determine if a system will come to equilibrium. It is clear that the migration rate must be high enough that an excitation can travel to an accepting center before it decays. However, this is only part of the problem; the excitation must also transfer to an acceptor before it decays. If the microparameter for direct transfer to an acceptor is small in comparison to the microparameter for migration, it is possible that an excitation will migrate to a donor ion adjacent to an acceptor and continue to migrate without transferring. This is modeled in the hopping model by defining a quenching radius around an acceptor; in this model, if an excitation enters the quenching region around an acceptor, it will become trapped in the region. The excitation will transfer to the acceptor; although it can back-transfer from the acceptor to a donor ion in the region, it will not leave the region as the probability of transfer to the acceptor is much greater than the probability of migrating. This quenching radius R_q can be defined as $R_q = \left(C_{da}/P_{dd}\right)^{1/6}$, where C_{da} is the transfer parameter and P_{dd} is the average probability of donor-donor transfer. Our data imply that R_q for ${}^3F_4 \rightarrow {}^5I_7$ energy

---

[139] B. Dinerman, "A spectroscopic characterization and cw laser operation of Er:GGG and Er:YSGG", PhD dissertation, Boston College, Dec 1993.

transfer is a minimum of 1.4xR_q for upconversion (consistent with the value reported in [140]), so it is reasonable that the $^5I_7$ and $^3F_4$ transfer processes come to equilibrium before the upconversion process. This also means that the coefficient B in Eq. 7.1.4 is considerably larger for $^3F_4$->$^5I_7$ transfer than for upconversion.

In summary, in this section we have discussed how the two different processes of direct transfer and migration can complicate the interpretation of data and can lead to an apparent excitation level dependence of measured parameters. Migration and direct transfer will provide limits on the maximum possible transfer rate that will be observed; these limits will be set by the slowest process. When migration is the limiting process, the measured transfer parameter will be excitation dependent. When direct transfer is the limiting process, the maximum transfer rate will given by $W_{max} = C\sum_{i,j}\frac{1}{r_{ij}^s}$, where C is the transfer microparameter and r_{ij} is the distance between ion i and ion j. The transfer microparameter for upconversion can be calculated from the cross-relaxation microparameter and the chemical potential. The problem becomes how to tell when a system will behave as a migration-limited or transfer limited system.

7.2. Concerns for the General Theory.

We have just discussed how the migration process can change the relationship between the average transfer parameters. There are some other concerns which should be kept in mind when applying the relations connecting the transfer parameters and the equilibrium distributions.

7.2.1. Energy Levels

As discussed earlier, we can calculate the parameter θ and therefore the distribution of excitations between manifolds from a material's energy levels. While this is a relatively simple calculation, the accuracy of this calculation is obviously dependent on how accurately the energy levels of a system are known. Substantial disagreements on the energy level structure of even well characterized materials can be found in the literature.

---

140 S. A. Payne, L. K. Smith, W. L. Kway, J. B. Tassano, and W. F. Krupke, "The mechanism of Tm->Ho energy transfer in LiYF$_4$", J. Phys. Cond. Matter, V4, (1992), P8525.

Discussion

While it may appear to be a fairly straight-forward matter to determine the energy levels of a material, it often takes a large amount of experimental work to accurately determine the positions. The selection rules for transitions are determined by the site symmetry, and quite often transitions to some levels are not allowed. The overall structure is generally inferred by comparing absorption and emission measurements until a self-consistent scheme is developed (See, for instance, [114, 118]. Additional complications can arise from the presence of strong vibronic transitions (which makes identification of the actual energy levels difficult) and the presence of more than one rare-earth substitutional site (as is the case for some materials, such as $NaYF_4$ and KYF_4).

To illustrate the importance of having an accurate energy level scheme, Fig. 7.2.1 presents predictions for the value of θ using two recently reported energy level structures of Ho:YAG, arguably the most well-known 2 μm host. The Tm energy level structure used is the same for both examples.

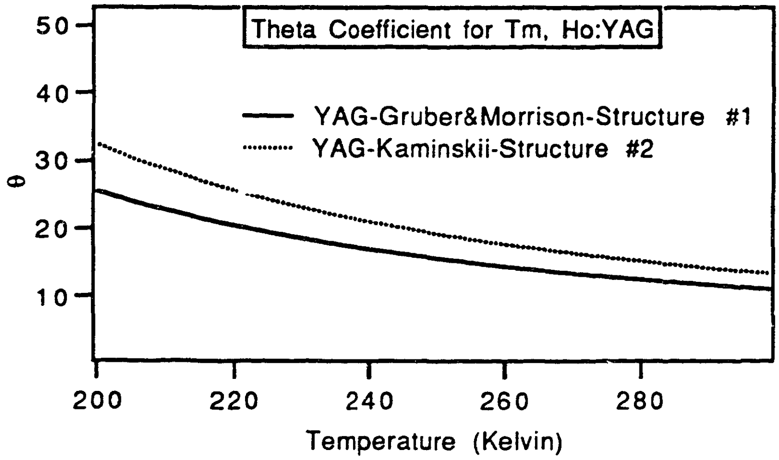

Figure 7.2.1. Temperature dependence θ for YAG for two different Ho energy level structures.

As can be seen, there is a clear difference between the value of θ for these two different structures; at room temperature this difference is roughly 15%. The energy level structures used are shown in Fig. 7.2.2.

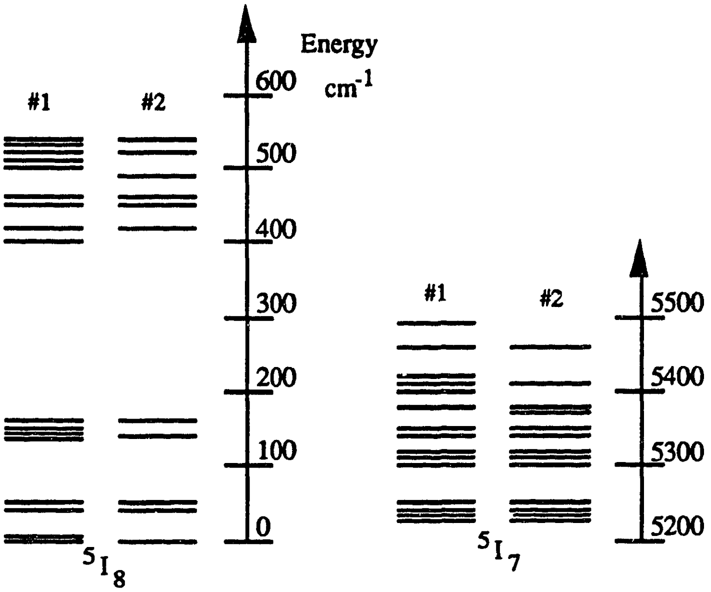

Figure 7.2.2. Different energy level structures for Ho:YAG. The energy level scheme denoted by #1 is from [119] and has been used for calculations throughout the thesis, while #2 is from [141]. There are some missing levels in scheme #2.

It is clear that there are only small differences between the two energy level structures, except for the obvious differences in the location of some higher lying levels. Additionally, the positions of some energy levels are missing one of the structures. The higher lying levels of most manifolds are difficult to identify in many materials due to strong phonon coupling. Although these discrepancies may create only small shifts in the position of the energy levels, any shift in the chemical potential can have a large effect on the value of θ, as θ is given by the exponential difference in the chemical potentials.

One additional point must be mentioned regarding the use of energy levels to predict θ. As the position of a material's energy levels are determined (in part) by the crystal field, it is conceivable that energy levels of a manifold may shift with temperature as the lattice expands or contract. As energy levels are generally determined at low temperatures, θ would be sensitive to any temperature dependent shifts in the positions of the energy levels. However, experimentally observed shifts have been small for the rare earths, roughly 1-10 cm^{-1} over a range of 250K and should pose little problem in the first approximation.

However, for materials where the energy level structure is not well known, it is possible to calculate θ from the emission and absorption cross-sections. These measurements can be performed at any temperature and directly measure the chemical

---

[141] A. A. Kaminskii, Laser Crystals, Optical Sciences, V14, Springer-Verlag, New York, 1981.

potential for the transition, but in practice the resulting chemical potential can be very sensitive to any scaling errors in the magnitude of the cross-sections. This technique must also be applied with care.

7.2.2. Effects of Phonon-electron Coupling

Near the end of Chapter 2, we discussed the effects of the phonon-electron interaction and derived the perturbed "vibronic" wavefunction resulting from this interaction. With these wavefunctions we derived a theoretical expression for the energy level shifts caused by this perturbation and found a non-vanishing second-order correction to the energy which depended on the phonon population. In principle, these shifts would cause shifts in the chemical potential at high phonon populations; but these shifts could be accounted for by determining the chemical potential under the experimental conditions. These shifts have been previously predicted[83], but experimental evidence of the shifts has not been obtained. The question that remains is if the presence of this phonon coupling would cause a shift in the chemical potential with regard to what would be expected from the electronic energy levels.

At the end of Chapter 2 we also derived a relationship between the transition probabilities for forward and reverse transitions between vibronic states (i->j and j->i). This relationship is the basis for McCumber's arguments regarding the applicability of his distribution[77]. However, this relationship assumed that there were no degeneracies between the phonon energies and splittings of the manifold. In many materials the phonon energies are comparable to the manifold splittings, and it is reasonable to assume that degeneracies will exist between these systems. The question is what happens to McCumber's relationship when these degeneracies exist. Aull and Jenssen have shown that there is an apparent break in the reciprocity of these transition probabilities for Nd:YAG[125]. This break may be the result of a shift in the chemical potential (which would affect the entire spectra of the multiplet) or an energy-specific break in reciprocity (which would affect only certain energy transitions). As our first derivation of the equilibrium relationships was based on McCumber's relations, our results would therefore be questionable when there are degeneracies in the system. However, our second derivation does not make any assumption about the transition probabilities, yet it produces the same result. This brings to mind the question of what this implies for non-reciprocal transitions and also for transition rates given by these relations.

7.2.3. Energy transfer in anisotropic materials

Many of the materials used in this thesis are anisotropic; however, energy transfer theory generally treats most materials as isotropic. The lattice-sum technique occasionally employed in more elaborate models takes into account the differences in site location, but does not take into account the differences in the overlap integrals seen at the different sites. These differences result from the projection of the polarized spectra of an ion at one site to an ion at another site. The overlap integrals for transfer between ions will vary with the relative orientation in anisotropic materials. For materials such as YLF or NYF, a weighted average of the overlap integrals for each polarization is generally used to produce C_{da}. This averaging technique has never been justified, and it raises the question if it may be possible to observe two or more different transfer rates in these materials. Such an effect could appear as a faster migration than would be expected from the average parameter. This is currently an unanswered concern when working with these materials.

A second concern emerges when working with monoclinic or triclinic materials. The averaging techniques used in energy transfer theory assume that you have found the principle axes of the system; for these materials, there are no unique principle axes for optical transitions and it may not be appropriate to simply use the standard averaging techniques of energy transfer.

Finally, in the Ho $^5I_7$<->$^5I_8$ spectra, a substantial magnetic dipole component is evident. The proper method for finding the transfer microparameters for spectra with mixed transitions is not clearly established.

7.3. Relation to observed problems

In the introduction, we mentioned that the motivation for exploring this topic came from problems observed in Tm-Ho doped systems that could not be explained with the models generally used. We suggested that one explanation of some of these problems was that the models used to describe this system relied on an incorrect description of the distribution of excitations between the manifolds. We now show how some of the observed measurement inconsistencies can be explained by the use of the proper equilibrium distribution.

7.3.1. Equilibrium times and populations.

A set of measurements by Payne et. al.[140] serves as a good example of the confusion which results from the use of the incorrect distribution. In these measurements, the $^3F_4$ manifold was directly pumped with a short pulse and the resulting fluorescence decays of the $^5I_7$ and $^3F_4$ manifolds were monitored. A fast initial decay of the $^3F_4$ fluorescence and fast initial build-up of the $^5I_7$ fluorescence is observed, following which both signals decay with the same lifetimes. The fast initial transients are the result of the initial transfer from Tm to Ho which leads to equilibrium.

The two transients are scaled and summed to produce a decay that is completely linear. The scaling factors required to produce a linear decay yield the fractional population of each manifold. Results of these measurements are tabulated in Table 7.3.1.

Tm Conc. ($\times 10^{19}$ cm^{-3})	Ho Conc. ($\times 10^{19}$ cm^{-3})	Equilibration Time (ms)	Measured Population	Fractional Ho Population: Castleberry's Method	Fractional Ho Population: Chemical Potential
12.6	1.25	3.2	0.62	0.75	0.64
12.2	3.68	2.5	0.84	.90	0.84
37.2	1.32	1.3	-	0.51	0.38
61.0	1.20	<0.1	0.36	0.37	0.26
61.0	3.64	<0.1	0.63	0.64	0.51

Table 7.3.1. Equilibration time and fractional populations for low concentration Tm, Ho doped materials. Data from Payne et al[140]. The fractional Ho population predicted by a canonical summation over only the $^5I_7$ and $^3F_4$ manifold is tabulated for each sample under the heading "Castleberry's Method", while the predictions of a canonical summation including the ground states are tabulated under the heading "Chemical Potential."

At low excitation densities, the fractional population of Ho, f_{Ho}, is given by the following relation,

$$f_{Ho} = \frac{\theta N_{Ho}}{\theta N_{Ho} + N_{Tm}}. \qquad (7.3.1)$$

where the other terms keep their earlier definitions. In Table 7.2.1, we have tabulated the fractional Ho population predicted by Castleberry's method(Section 3.2.1) and for our distribution. As can be seen, for low concentrations of Tm, the measured fractional Ho population is less than the value predicted Castleberry's method but agrees well with the value predicted by our distribution.

At higher concentrations of Tm, the measured distribution appears to correspond with that predicted by Castleberry. An examination of Payne's technique, however, reveals that the data are determined by the fast initial transient of the signals. As can be seen in the data, the equilibrium times for the higher concentration Tm samples (and therefore the initial transient signals) are faster than the stated resolution of the equipment; therefore, the values of f_{Ho} for these two samples are somewhat suspect.

Payne has used Castleberry's method to calculate his values of f_{Ho} and argues that the difference observed between his measurements of the low concentration samples and the predicted values of f_{Ho} results from details of the migration-assisted transfer process. Based on these differences, he concludes that the migration theory of energy transfer theory does not adequately explain this problem and that a new conceptual framework is required to understand this problem.

This is a questionable argument as the equilibrium times measured for the low concentration samples are considerably less than the lifetimes of the manifolds; which implies that the manifolds have come to equilibrium. This equilibrium distribution should be independent of the details of the transfer processes which bring about equilibrium as the predictions of statistical mechanics do not rely on detailed knowledge of the processes. Therefore, the conclusions which can be drawn concerning the kinetic natures of the processes involved are very limited.

By using the our distribution, we see that the predicted values of f_{Ho} are in close agreement with the values of f_{Ho} measured in the lower Tm concentration samples. We find no reason to question the validity of migration-assisted energy transfer theory at these concentration levels.

7.3.2 Upconversion Measurements

As has been discussed, measurements of the upconversion parameter can be very sensitive to the manner in which the experiment is conducted. Measurements of the upconversion parameter detailed in the literature often neglect the prescence of the cross-relaxation process. The result of neglecting the upconversion parameter is that an effective upconversion parameter is obtained. This parameter would be power dependent even without the complicating effects of migration. Cross-relaxation measurements can provide an upper bound on the value of the upconversion parameter and can serve as a useful check on the value of the upconversion parameter.

8. Summary

This thesis was motivated by problems observed in codoped 2 µm Tm-Ho laser systems. In this system, the $^3H_4$ manifold of Tm can be optically pumped with efficient laser diodes currently available. An energy transfer process cross-relaxes this manifold and populates the $^3F_4$ manifold with two for one quantum efficiency. At the concentrations of Tm used in these lasers, the process is very efficient and nearly all the excitations deposited in the $^3H_4$ manifold will cross-relax to the $^3F_4$ manifold. Following this cross-relaxation process, energy will migrate among the Tm ions and eventually transfer to the Ho $^5I_7$ manifold. Due to the close proximity in energy of the $^3F_4$ to the $^5I_7$, back-transfer from excited Ho ions will also occur. These transfer and back-transfer processes occur rapidly enough compared to the relaxation times of these manifolds that an equilibrium distribution of excitations develops between these manifolds. This distribution has generally been described with a canonical summation over the energy levels of the $^5I_7$ and the $^3F_4$ manifolds.

These lasers do not operate as efficiently as expected from the current models. The deviations are generally attributed to a $^5I_7$-$^5I_5$, $^3F_4$->$^3H_6$ upconversion energy transfer process which acts as a loss on the system. However, models which include the upconversion process still do not adequately predict the behavior of the system at high excitation densities. In this thesis, we have explored both the equilibrium distribution and upconversion processes active in this system.

8.1. General comments

We have rigorously derived the distribution of excitations between manifolds of interacting rare-earth ions for quasi-equilibrium situations. We have found that the distribution of excitations between excited manifolds is not described by a canonical summation over only the energy levels of the excited manifolds as has commonly been assumed (Castleberry's method). Instead, the energy levels of the lower manifolds must be included in the summation as these manifolds are also involved in the transfer process. We have used the Tm-Ho doped system to explore this problem; in this system, the distribution of excitations between the $^3F_4$ and the $^5I_7$ manifolds is described by the following relation:

$$\theta = \frac{\sum_{i}^{5I7} g_i e^{-\beta\varepsilon_i} \sum_{k}^{3H6} g_k e^{-\beta\varepsilon_k}}{\sum_{j}^{3F4} g_j e^{-\beta\varepsilon_j} \sum_{l}^{5I8} g_l e^{-\beta\varepsilon_l}} = \frac{N_1'}{N_0'}\frac{N_0}{N_1},$$

where N_1 is the $^3F_4$ population, N_0 is the $^3H_6$ population, N'_1 is the $^5I_7$ population, and N'_0 is the $^5I_8$ population. Here, ε_i is the energy and g_i the degeneracy of level i; $\beta=1/kT$, where k is Boltzmann's constant. Our steady-state measurements confirm this relation at low excitation densities, and our dynamics experiments confirm the relationship at higher excitation densities.

This description of the distribution is valid as long as the average transfer rates are considerably faster than the relaxation rates of the manifolds. This requirement will set a limit on the maximum energy gap that can exist between the manifolds since non-resonant energy transfer rates decrease as the energy gap increases. Additionally, as the average transfer rates decrease with decreasing population, this requirement will effectively set limits on the minimum dopant concentrations required for a qausi-equilibrium distribution to develop. The limits for any system will be determined by the competition between the energy transfer rates and the relaxation rates of the manifolds.

The equilibrium distribution can also be found from simple spectroscopic measurements. Using generalizations of the Einstein relations, we have shown that the equilibrium distribution can be related to the cross-sections for absorption and emission. Additionally, the distribution can be determined from the ratio of the energy transfer microparameters. These relations are useful as they allow the distribution to be determined when the energy levels of a material are not known. The relationships have been experimentally confirmed for the Tm, Ho:YLF system.

The existence of this equilibrium distribution implies that relationships exist between the transfer parameters. However, these relationships can not be directly applied to the transfer processes for time scales short compared to the equilibration time of the system. Complications arise from the random distribution of dopants in the material as well from migration. The average transfer parameter used to approximate an energy transfer process is generally not the same as the transfer microparameter for that process, even when the rate equations for the system are linear.

8.2. Implications for transfer theory

We have established a theoretical connection between incoherent transfer processes and generalized Einstein relations. This link can be used as a tool to explore energy transfer processes. We have shown that the transfer microparameters for reverse processes are related by the expression

$$\frac{C_{ij}}{C_{ji}} = e^{\beta(\mu_i - \mu_j)},$$

where μ_i is the chemical potential for the manifold i, μ_j is the chemical potential for the manifold j, and C_{ij} is the microparameter for transfer from i to j. The chemical potential, μ_i, must be calculated in reference to the lower-lying manifold of the two manifolds (for each ion) involved in the transfer process. For example, for the $^3F_4$->$^3H_6$, $^5I_7$->$^5I_5$ upconversion process, the chemical potential for the Tm manifolds involved in the transition is given by

$$e^{-\beta\mu_i} = \frac{\sum_{1}^{3F4} g_l e^{-\beta\varepsilon_l}}{\sum_{k}^{3H6} g_k e^{-\beta\varepsilon_k}},$$

and for the Ho manifolds by

$$e^{-\beta\mu_j} = \frac{\sum_{1}^{5I5} g_l e^{-\beta\varepsilon_l}}{\sum_{k}^{5I7} g_k e^{-\beta\varepsilon_k}}.$$

These relations will allow different energy transfer measurements to be related. For instance, we should be able to find the energy transfer microparameter for an upconversion process by finding the cross-relaxation microparameter and using this relation. As cross-relaxation measurements are generally easier to perform than upconversion measurements, this is a useful relation. However, the relation of the cross-relaxation and the upconversion microparameters to the observed average transfer parameters is complicated by the migration process. We find that the transfer micro-parameter measured for the static process (such as cross-relaxation) will give an upper limit on the maximum parameter for the reverse transfer process. This limit will apply when the migration is fast and the system is in "kinetic" or "transfer-limited" regime. When migration is slow compared to the transfer process, the migration process provides the limit on the maximum transfer rate and the transfer rate measured will be less than that predicted from the static measurements with the chemical potentials.

This relation also gives us a tool to study the migration process. One of the chief complications in determining the migration microparameters is that migration is generally studied by observing the change in the donor lifetimes caused the migration-assisted transfer to acceptor ions. The migration assisted transfer rate is given by

$$W_{ma} = k(C_{dd})^{m}(C_{da})^{1-m}N_dN_a,$$

where m and k are determined by the model. As can be seen, two unknowns (the microparameters for donor-donor transfer <u>and</u> for donor-acceptor transfer) must be considered when interpreting migration-assisted transfer measurements. By using the relation between the transfer parameters, it should be possible to determine the donor-acceptor microparameter with a second measurement and therefore eliminate one of the unknowns of the transfer process. An example, earlier we discussed measurements of the transfer process from the Tm $^3F_4$ manifold to the Ho $^5I_7$ manifold in which migration played an essential role. We could not determine the $^3F_4$ migration rate since we did not know the microparameter for transfer from Tm to Ho. By directly pumping the Ho $^5I_7$ manifold, we could determine the microparameter for transfer from Ho to Tm (As the Ho concentration is low, we would not need to be concerned with Ho to Ho migration.), and, using the relation above, find the unknown Tm->Ho microparameter.

Lastly, the existence of the equilibrium distribution yields a limiting relationship for the energy transfer process. When integrated versus time, microscopic theories of energy transfer should yield the equilibrium distribution for times long in comparison to lifetimes of the manifolds involved in the processes. This may serve as a good check for some of the many theories of energy transfer and migration.

8.3. Practical implications for lasers

As has been mentioned, the examination of this problem was motivated by questions concerning the performance of Tm, Ho doped 2 μm lasers. We now discuss what conclusions we can draw for the Tm, Ho system based on the results of this thesis.

First of all, we have established that the distribution of excitations between the $^3F_4$ and the $^5I_7$ manifolds is not described by Castleberry's approach and that the levels of the $^3H_6$ and the $^5I_8$ manifold must be included in the canonical summation. For Tm, Ho: YLF and YAG, the resulting distribution yields lower values of the $^5I_7$ inversion for a given total excitation density than would be expected from including only the levels of the $^5I_7$ and $^3F_4$ manifolds. This in turn sets a more conservative limit on the energy that can be extracted from the $^5I_7$ manifold at a given excitation density than the limits imposed by current models for this system. For Tm-Ho:YLF, we found that $\theta = 17.8$ in contrast to 31 as predicted with Castleberry's method. For Tm-Ho:YAG, we measured θ to be 11.3 as opposed to the value of 22 as expected using Castleberry's method. At room temperature, the Castleberry's method yields a ratio of Ho to Tm excitations 50%-100% larger than the ratio predicted by our description of the distribution.

We have measured the cross-relaxation process ($^3H_6$->$^3F_4$, $^5I_5$->$^5I_7$) which effects the $^5I_5$ manifold when Tm is codoped with Ho. We find that many authors neglect this process when fitting to find the upconversion parameter. Measurements such as this determine an effective upconversion constant which can appear to be excitation-density dependent.

We have measured the upconversion parameters for Tm, Ho:YLF and found that the measured $^5I_5$ upconversion parameter depends on the manner in which the experiment is conducted. The values of the upconversion parameter found by independently fitting simultaneously measured $^5I_7$ and $^5I_5$ transients differ. This indicates that the model used for the Tm-Ho system is not complete, even when modified to include the proper equilibrium distribution and the cross-relaxation process. We suspect that these differences arise as a result of migration. We find a value of $\alpha_2=8\times10^{-18}$ cm^{3}s^{-1} when fitting the $^5I_7$ fluorescence and $\alpha_2=13.5\times10^{-18}$ cm^{3}s^{-1} when fitting the $^5I_5$ fluorescence. Both of these values are less than the limiting value of $\alpha_2=15.0\times10^{-18}$ cm^{3}s^{-1} implied by the cross-relaxation measurements.

Based on our measurements of the $^5I_5$, $^5I_7$, $^3F_4$, and $^3H_4$ transients, we can reject some proposed additional loss mechanisms for this system. Specifically, we have shown that excited state absorption does not substantially affect the $^3F_4$ or the $^5I_7$ manifolds in the Tm, Ho:YLF system at moderate excitation levels. Additionally, we can reject the Tm $^3F_4$->$^3H_6$, $^3F_4$->$^3H_4$ upconversion process ($\alpha_{up}<10^{-19}$ cm^{3}s^{-1}) and the Ho $^5I_7$->$^5I_8$, $^5I_7$->$^5I_5$ upconversion process ($\alpha_{up}<10^{-19}$ cm^{3}s^{-1}) in YLF as substantial loss mechanisms. We have observed an upconversion fed fluorescence at 658 nm, but have not identified the manifolds involved in this process.

We have measured the upconversion parameters for Tm, Ho:YLF and found that the measured $^5I_5$ upconversion parameter depends on the manner in which the experiment is conducted. The values of the upconversion parameter found by fitting simultaneously measured $^5I_7$ and $^5I_5$ transients differ. This indicates that the model used for the Tm-Ho system is not complete, even when modified to include the proper equilibrium distribution and the cross-relaxation process. We suspect that these differences arise as a result of migration.

One assumption in our model which has not been assessed is the efficiency of $^5I_6$->$^3H_5$ energy transfer. In other materials (YSGG, YSAG) the $^5I_6$ transfer process has been reported to be nearly 100% efficient. Other energy transfer processes may affect the $^5I_6$ manifold and may cause higher than expected losses at high excitation densities; however, additional processes affecting $^5I_6$ will not explain the disagreement in the measured $^5I_5$ upconversion parameters.

These disagreements in the transfer parameter values may arise from approximating the upconversion parameter as constant. Excitation migration in the $^3F_4$ manifold can cause the upconversion parameter to have an excitation dependence. Migration-assisted energy transfer theory predicts that the upconversion parameter should increase as a function of excitation density and eventually saturate at some maximum value (when the process becomes transfer-limited). The rate of increase and the excitation density where saturation occurs will depend on details of the microscopic energy transfer process and has not been determined. The maximum value of the upconversion parameter will occur when the transfer process is transfer-limited; this limiting value can be determined from the cross-relaxation parameter with relations given earlier. Measurements of the upconversion parameter have been performed at a variety of excitation levels. We find that the value of the upconversion parameter found by fitting the $^5I_5$ fluorescence agrees with this limit within experimental error at high excitation densities. An excitation dependence of this parameter may explain some of the disagreements between measurements reported in the literature.

Extension of the steady state analysis techniques used in Chapter 3 to include the $^5I_5$ manifold will set a limit on the maximum $^5I_7$ inversion that can be achieved. For Tm, Ho:YLF, this limit is ≈85% of the total Ho concentration. As a summary, we have included a tabulation of some of measured parameters in Table 8.3.1.

Parameter	YAG	YLF	BYF	NYF
θ (293 K)	11.3	17.8	≈23	?
α_2 (cm^3s^{-1})	?	1.5×10^{-17}	8.3×10^{-18}	$\approx 2 \times 10^{-18}$
α'_2 (cm^3s^{-1})	?	1.3×10^{-16}	5.5×10^{-17}	1.4×10^{-17}

Table 8.3.1. Summary of measured parameters of the materials used in this thesis. α_2 is the $^5I_5$ upconversion parameter and α'_2 is the cross-relaxation parameter. Values were not obtained for YAG as the $^5I_5$ lifetime was smaller than our instrumental resolution. The θ for BYF has been determined from energy level data only.

Appendix A. Mathematical Derivations

In this Appendix, we present the mathematical derivations for some of the relations presented in the text. These derivations are presented only when different from the standard relations found in the literature. We detail the assumptions and the approximations made in these derivations.

A.1. Derivation of the static transfer decay relations

As mentioned in the main body of the text, an energy transfer experiment does not measure the transfer rate between isolated pairs of ions, but instead produces an ensemble averaged measurement over all the different ion environments in the material.

The proper way to do this is, of course, to average the different local environments; the resulting average will produce a summation of exponential decays containing all possible combinations of transfer and decay rates. However, it is useful to approximate this process in order to get a physical understanding of the system that can be compared with physical measurements. We will derive the standard relation for the transfer dynamics when the transfer occurs without any migration among the donor ions. This is generally referred to as "static" transfer.

The total relaxation rate from an excited donor ion separated from an acceptor ion by $\vec{r}_{ij}$ is given by

$$P_{ij} = \left(\frac{1}{\tau_0} + f(\vec{r}_{ij})\right), \tag{A.1.1}$$

where τ_0 is the intrinsic lifetime of the donor manifold and $f(\vec{r}_{ij})$ is a relation describing the energy transfer probability between the two ions.

We now restrict ourselves to only one interaction process. The single ion relaxation processes as well as additional transfer processes can be solved for independently and added to produce the final solution as we consider only linear type processes. The total transfer probability for an ion i can be expressed as

$$P_i = \sum_{k}^{N_a} f(\vec{r}_{ik}), \tag{A.1.2}$$

where the index k represents a summation over the number of acceptors. The transfer dynamics of the donor ion now appear as

$$\rho_i(t) = \prod_{k}^{N_a} \exp(-tf(\vec{r}_{ik})) \tag{A.1.3}$$

Now, averaging this relation over a number of different donors to find the experimentally observable transient, we find

$$\bar{\rho}_i(t) = \frac{1}{N_d} \sum_{i}^{N_d} \prod_{k}^{N_a} \exp(-tf(\vec{r}_{ik})). \tag{A.1.4}$$

The above relationship will in principle describe the energy transfer accurately if the distribution of ions and the interaction rates are known. However, it is useful to approximate this relation as we generally do not know these quantities. The first step is to exchange the summation and multiplication operators in Eq. A.1.4. We now have

$$\bar{\rho}_i(t) = \frac{1}{N_d} \prod_{k}^{N_a} \sum_{i}^{N_d} \exp(-tf(\vec{r}_{ik})). \tag{A.1.5}$$

To proceed further theoretically, it is necessary to make some assumptions about the distribution of ions. We start with the assumption that the ions are distributed with constant density in the material. This is a glassy or amorphous model and neglects the discrete nature of the crystalline structure. It is also useful to restrict the interaction as this will simplify the derivation. For now we assume that the transfer probability has no orientation dependence. Transforming the summation of Eq. A.1.5 to an integral over volume, we find

$$\bar{\rho}_i(t) = \frac{1}{N_d} \prod_{k}^{N_a} \sum_{\Delta V}^{V} \Delta V \frac{\Delta N_d}{\Delta V} \exp(-tf(r)). \tag{A.1.6}$$

Letting the volume increase to infinity but keeping the total number of donors constant, we find

$$\bar{\rho}_i(t) = \prod_{k}^{N_a} \int_0^\infty 4\pi r^2 dr \exp(-tf(r)) = \left[\int_0^\infty 4\pi r^2 dr \exp(-tf(r)) \right]^{N_a} \qquad (A.1.7)$$

To get this relation from Eq. A.1.4, we have made only two approximations: (1) that the interaction depends only on distance, not orientation, and (2) that the distributions of donors and acceptors are completely random and can be described as a constant density distribution. Thus, we have neglected the discrete nature of sites in a crystal. Now, assuming an interaction of the form $f(r) = C / r^s$. This relation will then yield a the time-dependent decay of the form

$$I(t) = I_0 \exp\left(-\frac{t}{\tau} - \frac{4\pi}{3}\Gamma\left[1 - \frac{3}{s}\right] N_a \left(C^s t\right)^{3/s} \right) \qquad (A.1.8)$$

for directly pumped, "short"-pulse excitation. The length of a "short" pulse must be considerably shorter than the time scale of any of the transfer or relaxation processes affecting the system. The dynamics following a "long" pulse can be found by adding a time-dependent source term to Eq. A.1.8 and integrating with respect to time.

The first obvious correction to this relation for a crystalline material is to restrict the minimum transfer distance to be the distance between nearest neighbors. This can be accomplished by setting the lower limit of the integral in Eq. A.1.7 to be the minimum transfer distance instead on zero. With this restriction, Eq. A.1.8 becomes

$$I(t) = I_0 \exp\left(-\frac{t}{\tau} - \frac{4\pi}{3}\Gamma\left[1 - \frac{3}{s}\right] N_a (Ct)^{3/s} + B\,\mathrm{erf}[Dt] \right), \qquad (A.1.9)$$

where erf is the error function. The coefficients B and D will depend on the order of the interaction. Relations for the exchange interaction can be found by using the appropriate interaction form in Eq. A.1.7.

A.2. Migration-assisted transfer relations

As the donor concentration is increased excitations can also transfer between donor ions as well as from donor ions to acceptor ions. These interactions allow an excitation to move or "migrate" among the donor ions before transferring to an acceptor or decaying. This process partially averages the different local environments of each donor ion. In the limiting case where donor-donor transfer rates are much greater than donor-acceptor transfer rates, the donor ions see only one effective transfer rate and measured decay becomes a simple exponential, i.e.

$$I(t) = I_0 \exp(-W_{tot}t), \tag{A.2.1}$$

where $W_{tot} = W_{ma} + 1/\tau_0$. W_{tot} is the total decay rate seen by manifold and W_{ma} is the migration assisted rate. In this situation, donors with nearby acceptor ions decay by static quenching, but before a donor can transfer to farther-lying acceptors it transfers to another donor. Under these circumstances, the decay can be described as

$$I(t) = I_0 \exp\left[-W_{tot}t - B\sqrt{t}\right] \tag{A.2.2}$$

for the case of dipole-dipole coupling. With a dynamic decay such as this, it is possible to find interaction micro-parameters for not only C_{da}, but also C_{dd}. C_{dd} can be found from the migration assisted transfer rate. The general approach is to model the migration process as a random walk (or diffusion) process with various complications.

A.2.1. The diffusion model.

Modeling migration as a diffusion process, the migration assisted transfer rate is given by

$$W_{ma} = \frac{dn}{dt} = -D\nabla^2 n - n\sum_i \frac{C_{da}}{|\vec{r} - \vec{r}_i|^6}. \tag{A.2.3}$$

With a few assumptions this relation can be solved to yield

$$W_{ma} = 4\pi N_a D\rho. \tag{A.2.4}$$

Here ρ is a physically significant length scale defined to be the characteristic distance where the average time required to directly transfer is equal to the time required to reach the acceptor by diffusion. Effectively, ρ is the distance at which an excitation is more likely to directly transfer than to diffuse. We can solve for ρ in terms of D and C_{da}. We have $\tau \approx \frac{\rho^2}{6D}$, for diffusion, and $\tau \approx \frac{\rho^6}{C_{da}}$ for direct transfer. These lead to

$$\rho = k\left(\frac{C_{da}}{D}\right)^{1/4}, \tag{A.2.5}$$

where k is a constant that is determined by the actual details of the modeling.

We can relate the diffusion constant to C_{dd} in the same manner that we related ρ. We can express the average transfer time for a diffusion step as

$$\tau = \frac{R^2}{6D}. \tag{A.2.6}$$

Here R is the size of one step and τ is the average time between steps. If we make the assumption that the dipole-dipole interaction is responsible for migration, we can then say $\tau = R^6/C_{dd}$. We can now say

$$D \approx \frac{C_{dd}}{6R^4}, \tag{A.2.7}$$

for dipole-dipole coupling. If we make the assumption that the average distance is merely given by the average spacing between donors, we can approximate $R \approx N_d^{-1/3}$. D is now given by the expression

$$D = \gamma C_{dd} N_d^{4/3} \tag{A.2.8}$$

where γ is a constant that depends on the exact structure of the crystal. Combining Eqs. A.2.4, A.2.5, and A.2.8, we see that the migration assisted rate can be expressed as

$$W_{ma} = kN_a N_d C_{da}^{1/4} C_{dd}^{3/4}, \tag{A.2.9}$$

where we have lumped the various model depend constants into the leading constant k. This is the general relation for diffusion assisted transfer. Implicit in this model is the assumption that transfer to the acceptor can occur from anywhere in the lattice. The migration process merely allows the transfer distance between the donor and acceptor to change. This implies that C_{da} is much larger that C_{dd} for the concentrations of donors and acceptors generally used.

A.2.2. The hopping model

Another model has been developed by Burshtein which may be appropriate in situations where the probability of donor-donor transfer is much greater than that for donor-acceptor transfer. This model models the migration process in the same manner as above, but restricts the transfer to an acceptor to occur only in a small volume around the acceptor. A diffusing excitation can pass through this volume in only a step in the limiting case examined. In this case, the transfer to the acceptor must before the acceptor steps again. In the literature, this model is referred to as the "hopping" model.

For dipole-dipole transfer, it can be shown that the migration-assisted transfer rate will be

$$W_{ma} = \frac{2\pi}{3} N_a \left(\frac{C_{da}}{\tau_s} \right)^{1/2} . \tag{A.2.10}$$

Assuming that the migration interaction is dipole-dipole and applying the same relations used above, this relation becomes

$$W_{ma} = k' N_d N_a C_{da}^{1/2} C_{dd}^{1/2}, \tag{A.2.11}$$

where k' is a constant that is dependent on the exact details of the modeling.

A.3. Phonon-electron coupling

We now briefly derive some of the relations used in our discussion of the electron phonon interaction. This treatment differs from the approaches summarized in the reference articles regarding vibronic transitions as we have performed the derivation for an arbitrary number of phonons in each mode, whereas the typical approach is for only one phonon in a single mode. As our derivation is slightly more general, we have briefly summarize it. We start by deriving the perturbed wavefunction for the system.

A.3.1. The coupled electron-phonon wavefunction

We start by expressing the hamiltonian for the entire crystal. We work in the adiabatic approximation and model the coupling as a perturbation. Here Ψ is the complete state of the system and can be expressed as $\Psi=\psi\phi$, where ψ is the electronic state and ϕ is the lattice state. The total hamiltonian for the system is

$$H_{tot}=H_0+H_{vib}+H_P, \tag{A.3.1}$$

where H_P represents the interaction responsible for the electronic-phonon coupling. The unperturbed states for this system are given by $H_0|\psi_i\rangle=E_i|\psi_i\rangle$ and $H_{vib}|\phi_n\rangle=E_n|\phi_n\rangle$.

Using non-degenerate time-independent perturbation theory, we can express the effect of H_P upon the states of the system as

$$|\chi_{ix}\rangle=|\Psi_{ix}\rangle+\sum_{\substack{j\neq i\\ r\neq x}}\frac{|\Psi_{jr}\rangle\langle\Psi_{jr}|H_P|\Psi_{ix}\rangle}{E_{ix}-E_{jr}} \tag{A.3.2}$$

where χ_{ix} are the states resulting from the perturbation. Here the i refers to the electronic state of the system and x to the state of the lattice. The interaction H_P arises because the crystal field is treated as static in the adiabatic approximation when in fact it is dynamic. The dynamic crystal field, V, can be expanded in a Taylor series,

$$V=V_0+\frac{\partial V}{\partial x_\alpha}dx_\alpha+\frac{1}{2}\frac{\partial V}{\partial x_\alpha \partial x_\beta}dx_\alpha dx_\beta+\cdots. \tag{A.3.4}$$

where the Einstein summation convention for repeated indices is applied. The summation here is over the three independent crystallographic directions. H_0 is defined to be $H_{free}+V_0$ and can be seen to contain a zeroth order approximation to the crystal field. The remaining terms of the Taylor's expansion can be assigned to H_P. We can now say

$$H_P=\frac{\partial V}{\partial x_\alpha}dx_\alpha+\frac{1}{2}\frac{\partial V}{\partial x_\alpha \partial x_\beta}dx_\alpha dx_\beta+\cdots \tag{A.3.5}$$

As can be seen, this expression for H_P couples the ionic motion to the electronic hamiltonian. Note that we are still working in the Born-Oppenheimer (adiabatic) approximation--although we allow the ions to move, we still assume that the electronic motion is much faster; what effectively occurs is that the electrons continue to move in eigenstates of changing potential caused by the ion motion.

For the present time we will just analyze the first order correction to the static crystal field model and drop all higher order terms from H_P. H_P is now

$$H_P \equiv \frac{\partial V}{\partial x_\alpha} dx_\alpha = v_\alpha dx_\alpha,$$

where v_α represents the correction to the electrostatic potential due to ion motion and dx_α represents the relative ion motion. In linearizing this perturbation, we have left out effects such as lattice expansion and higher-order phonon effects, but in principle their effects would be similar to what we find for the linearized perturbation.

As the unperturbed wavefunction is separable, we can say

$$|\chi_{ix}\rangle = |\Psi_{ix}\rangle + \sum_{\substack{j\neq i \\ r\neq x}} \frac{|\Psi_{jr}\rangle\langle\Psi_{jr}|H_P|\Psi_{ix}\rangle}{E_{ix}-E_{jr}} = |\psi_i\rangle|\phi_x\rangle + \sum_{\substack{j\neq i \\ r\neq x \\ \alpha}} \frac{|\psi_j\rangle|\phi_r\rangle\langle\psi_j|v_\alpha|\psi_i\rangle\langle\phi_r|dx_\alpha|\phi_x\rangle}{(E_i+E_x)-(E_j+E_r)} \quad \text{(A.3.6)}$$

by separating the electronic and ionic portions of the hamiltonian. This separation can be accomplished as the v_α will effect only the electronic portion of the wavefunction (to first order) and the dx_α will act only on the ionic portion of the wavefunction. Here $E_i+E_x=E_{ix}$ as we can break up the energy of the unperturbed system to an electronic contribution and an ionic contribution. We can express the state ϕ_x as a product over the normal vibrational modes of the system, i.e., $|\phi_x\rangle = \prod_q |q,n_q^x\rangle$, where $|q,n\rangle$ is the state corresponding to n phonons in a mode q and n^x_q is the phonon occupation number for state q when the total wavefunction is ϕ_x. Expressing ϕ_x and ϕ_r as a product of normal mode components, we can transform Eq. A.3.6 into

$$|\chi_{ix}\rangle = |\psi_i\rangle\prod_q |q,n_q^x\rangle + \sum_{\substack{j\neq i \\ q,q' \\ r\neq x \\ \alpha}} \frac{|\psi_j\rangle\langle\psi_j|v_\alpha|\psi_i\rangle\langle q',n^r_{q'}|dx_\alpha|q,n^x_q\rangle}{(E_i+E_x)-(E_j+E_r)} \prod_{q''\neq q'} |q'',n^r_{q''}\rangle. \quad \text{(A.3.7)}$$

This is a very general expression for the vibronic state χ_i. It is desirable to have an expression for a vibronic state that corresponds to a particular number of phonons in the system. The approximate expression for $H_P = \sum v_\alpha dx_\alpha$ can be expressed in the normal mode basis as $\sum v_q \Omega_q$, where Ω_q is an operator corresponding to the amplitude of vibration of the normal mode q. The v_q's are now derivatives of the crystal field with respect to the normal mode coordinates. Ω_q can be expressed as

$$Q_q = \sqrt{\frac{\hbar}{2\omega_q}}\left(b_q^\dagger + b_q\right)$$

where $b_q^\dagger$ and b_q are respectively the creation and destruction operators for the phonon state q. Remembering that $b_q^\dagger|q,n\rangle = \sqrt{n+1}|q,n+1\rangle$, $b_q|q,n\rangle = \sqrt{n}|q,n-1\rangle$, and $\langle q,n|q',n'\rangle = \delta_{qq'}\delta_{nn'}$ for the phonon normal-mode expansion, we can re-express Eq. A.3.7 as

$$|\chi_{ix}\rangle = |i\rangle\prod_q|q,n_q^x\rangle + \sum_{\substack{j\neq i\\ r\neq x\\ q}}\sqrt{\frac{\hbar}{2\omega_q}}\frac{|j\rangle|q,n_q^r\rangle\langle j|v_q|i\rangle\langle q,n_q^r|\left(b_q^\dagger + b_q\right)|q,n_q^x\rangle}{\left(E_i + E_x\right)-\left(E_j + E_r\right)}\prod_{q'\neq q}|q',n_{q'}^r\rangle, \quad \text{(A.3.8)}$$

where we have represented $|\psi_i\rangle$ by $|i\rangle$ for notational simplicity. We can eliminate the summation over r (and therefore n^r_q) by using the properties of creation and destruction operators to get

$$|\chi_{ix}\rangle = |i\rangle\prod_q|q,n_q^x\rangle + \sum_{\substack{j\neq i\\ q}}\sqrt{\frac{\hbar}{2\omega_q}}|j\rangle\langle j|v_q|i\rangle\left[\frac{\sqrt{n_q^x+1}|q,n_q^x+1\rangle}{E_i - E_j - \hbar\omega_q} + \frac{\sqrt{n_q^x}|q,n_q^x-1\rangle}{E_i - E_j + \hbar\omega_q}\right]\prod_{q'\neq q}|q',n_{q'}^x\rangle. \quad \text{(A.3.9)}$$

We also have replaced the E_x-E_r term with $\pm\hbar\omega_q$ by consideration of the energy differences between states which differ only by one phonon. We now have an expression for the vibronic wavefunction corresponding to the electronic state ψ_i coupled to the lattice state ϕ_x. Note that these states are not necessarily orthogonal; transitions may occur between these due only to the electron-phonon interaction.

A.3.2. Energy level shifts resulting from phonon coupling

The first item we analyze is the change in the energy of the state i. As mentioned previously (Chapter 2), the first order correction to the energy will vanish, but the second-order correction will not. The second-order correction can be expressed as

$$E_{ix}^{(2)} = \sum_{q,q'} \frac{\hbar}{2\omega_q} \left|\langle i|v_q|j\rangle\right|^2 \frac{\langle q,n_q^x|(b_q^\dagger + b_q)|q',n_{q'}^r\rangle\langle q',n_{q'}^r|(b_q^\dagger + b_q)|q,n_q^x\rangle}{E_i - E_j \pm \hbar\omega_q}. \qquad \text{(A.3.10)}$$

The sign in front of the phonon energy can be determined by examining Eq. A.3.9. This relation can be expressed as

$$E_{ix}^{(2)} = \sum_{q} \frac{\hbar}{2\omega_q} \left|\langle i|v_q|j\rangle\right|^2 \left(\frac{n_q + 1}{E_i - E_j - \hbar\omega_q} + \frac{n_q}{E_i - E_j + \hbar\omega_q} \right) \qquad \text{(A.3.11)}$$

As can be seen, there will be a shift in the energy of the level which will be dependent upon the phonon mode occupation numbers. As the occupation number will be temperature dependent, we know from this relationship that the energy levels of the crystal will have a temperature dependence.

A.3.3. Vibronic transition probabilities

We now examine electronic transition between two vibronic states. Although this is in some sense this is a second-order effect, it is conceptually different from a standard second-order perturbation calculation as we are not concerned with the second-order correction of a single interaction hamiltonian but rather the first order corrections of two-different interactions. In other words, we are examining coupled phonon-photon transitions as opposed to 2-photon processes.

Our approach is to use the vibronic wavefunctions given by Eq. A.3.9 and then solve for transition probabilities between these new eigenstates caused by the interaction H_M. A second approach would be to treat both the phonon-electron and electron-applied field perturbation simultaneously; i.e., as a coupled phonon-photon transition occurring between unperturbed states of the initial system. We will analyze the interaction in the manner first described; where H_P is taken to be a perturbation which shifts the energy levels and produces new eigenstates, and H_M is the interaction which causes transitions between them. This can be justified as the two interactions occur on very different time scales for the rare earths. The proper way to handle these perturbations is with time-dependent perturbation theory; however, to simplify analysis we use time-independent perturbation theory and point out the relevant differences.

The matrix elements for transitions with no net change in the phonon occupation numbers have been analyzed; the relations for these transitions can be found in Chapter 2.

We now evaluate the transition probability when a transition occurs with a net change in the phonon occupation number. Starting with the matrix element between the vibronic state χ_{ix} with $n^x{}_q$ phonons in mode q and the vibronic state χ_{jr} with $n^x{}_q+1$ phonons in mode q, we have

$$\langle \chi_{ix}^{n} | M | \chi_{kx}^{n+1} \rangle = \sum_{j \neq i} \langle i | f_q | j \rangle \langle j | M | k \rangle \sqrt{\frac{\hbar}{2\omega_q}} \frac{\sqrt{n_q + 1}}{E_i - E_j - \hbar\omega_q} + \sum_{j \neq k} \langle i | M | j \rangle \langle j | f_q | k \rangle \sqrt{\frac{\hbar}{2\omega_q}} \frac{\sqrt{n_q + 1}}{E_k - E_j + \hbar\omega_q} \tag{A.3.12}$$

where we have dropped terms which vanish due to the orthogonality of the phonon states. Each term in the above relationship corresponds conceptually to a different process. The first term corresponds to the situation where the ion in state i emits a phonon and then makes the transition to the state k, while the second term corresponds to the situation where the ion makes the transition and then emits a phonon.

Now, squaring the matrix elements to find transition probabilities, we have

$$p_{ik}^{n_q, n_q+1} = \left| \sum_{j \neq i} \langle i | f_q | j \rangle \langle j | M | k \rangle \sqrt{\frac{\hbar}{2\omega_q}} \frac{\sqrt{n_q + 1}}{E_i - E_j - \hbar\omega_q} + \sum_{j \neq k} \langle i | M | j \rangle \langle j | f_q | k \rangle \sqrt{\frac{\hbar}{2\omega_q}} \frac{\sqrt{n_q + 1}}{E_k - E_j + \hbar\omega_q} \right|^2 \tag{A.3.13}$$

for the probability of a transition between vibronic states i and k coupled with the emission of a phonon into the mode q. Now by making the assumption of no degeneracies between the phonon energies and energy differences of any of the ion's electronic states, we can drop the cross-terms from this relationship. This condition is <u>necessary</u> as the quantum mechanical phases associated with each matrix element will in general cause cross-terms to vanish over time and therefore not contribute to the transition probability; however, for degenerate energies these phase differences will cancel each other out--resulting in cross terms between matrix elements which do not vanish over time. This is the condition which we must keep in mind as we have not used time-dependent, degenerate perturbation theory to derive these results. Making the approximation that phases are unimportant, we can say

$$p_{ki}^{n_q+1, n_q} = \frac{\hbar}{2\omega_q} (n_q + 1) \left[\sum_{j \neq k} \frac{|\langle k | f_q | j \rangle \langle j | M | i \rangle|^2}{(E_k - E_j + \hbar\omega_q)^2} + \sum_{j \neq i} \frac{|\langle k | M | j \rangle \langle j | f_q | i \rangle|^2}{(E_i - E_j - \hbar\omega_q)^2} \right]. \tag{A.3.14}$$

It is clear from the mathematics that this process is clearly reciprocal, i.e., $p_{ik}^{n_q,n_q+1} = p_{ki}^{n_q+1,n_q}$. It is tempting to say that the probability of transitions from i to k is equal to the probability of transitions from k to i. However, this is not true as the above relationship holds for a certain number of phonons in the mode q, namely n when the ion is in state i and n+1 when the ion is in the state k. However, the number of phonons initially in the mode q will be independent of the ionic state (for incoherent processes). In this case, the probability for a transition between i and k coupled with a q phonon emission will be proportional to n_q+1, while the probability for the reverse process will be proportional to n_q. The relationship which we now have between transition probabilities for this process is

$$p_{ki}^{n_q,n_q-1} = \frac{n_q}{n_q+1} p_{ik}^{n_q,n_q+1} \tag{A.3.15}$$

We have discussed how McCumber in his theory has accounted for this by using the Bose-Einstein distribution to find values for n, subsequently proven his theorem in the non-degenerate case. We also discussed how degeneracies may affect this relationship and pointed out the results of Aull and Jenssen (See Chapter 7). These degeneracies also affect the probabilities of transitions with no net change in phonon occupations.

B. Steady-State Relations between Manifold Populations

Recalling our derivations of the equilibrium distribution established earlier (Chap. 3), we established relationships between the manifold populations and the transfer parameters at low excitation densities. We considered only $^3F_4$ and $^3H_6$ manifolds in Tm and the $^5I_7$ and $^5I_8$ manifolds in Ho. We then presented a relationship between the excited state manifold populations at high excitation densities. We will now derive that relationship and extend the derivation to include other manifolds. We start with the equilibrium relationship

$$\frac{N_1'}{N_1} = \theta_0 \frac{N_0'}{N_0} \qquad \text{(B.1.1)}$$

where θ_0 is that derived earlier for the $^3F_4$->$^3H_6$, $^5I_8$->$^5I_7$ energy transfer process and its reverse.

$$\theta_0 = e^{\beta(\mu_1 - \mu_1')} = \frac{z_1' \, z_0}{z_1 \, z_0'} = \frac{\sum_i^{5I7} e^{-\beta\varepsilon_i}}{\sum_j^{3F4} e^{-\beta\varepsilon_j}} \frac{\sum_k^{3H6} e^{-\beta\varepsilon_k}}{\sum_l^{5I8} e^{-\beta\varepsilon_l}} \qquad \text{(B.1.2)}$$

This relationships should be applicable to any set of manifolds with energy transfer rates that are much faster than the relaxation rates. We now examine the implications of this relations at high pump intensities.

B.1. Distribution of excitations between $^3F_4$ and $^5I_7$ at high excitation densities.

We first consider the $^3F_4$ and $^5I_7$ manifolds at high excitation densities. We initially approximated N_0 by N_{Tm} and N'_0 by N_{Ho}, where N_0 and N'_0 are respectively the total concentrations of Tm and Ho. By keeping the exact values for N_0 and N'_0, we can obtain a relationship between the excitation density and the amount of excitation stored in each species. Constraining the Ho ions to be either in the first excited state or the ground state, we have $N_0' = N_{Ho}' - N_1'$. Substituting this constraint into Eq. B.1.1, we get the following relationship.

Steady State Relations

$$\frac{N_1'}{N_1} = \theta_0 \frac{N_0'}{N_0} = \theta_0 \frac{N_{Ho} - N_1'}{N_0} \qquad \text{(B.1.4)}$$

Solving this expression for N'$_1$, we find

$$\frac{N_1'}{N_{Ho}'} = \theta_0 \frac{N_1}{N_0 + \theta_0 N_1}. \qquad \text{(B.1.5)}$$

By constraining the Tm ions to be in either the $^3F_4$ or the $^3H_6$ manifolds, ($N_{Tm}=N_1+N_0$), we find

$$\frac{N_1'}{N_{Ho}} = \theta_0 \frac{N_1}{N_{Tm}} \frac{1}{1+(\theta_0 - 1)^{N_1}\!/\!_{N_{Tm}}} = \frac{\theta_0 r}{1+(\theta_0 - 1)r} \qquad \text{(B.1.6)}$$

where $r=N_1/N_{Tm}$ is the fraction of Tm ions excited. Plots of this relationship for values of θ corresponding various temperatures in Tm-Ho:YLF are shown in Figure B.1.1 and B.1.2.

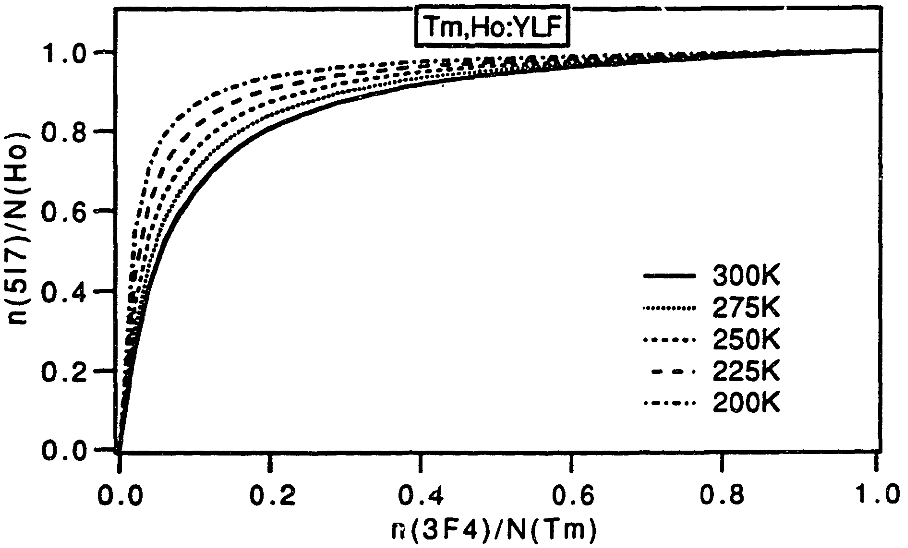

Figure B.1.1. Fraction of Ho ions inverted vs the fraction of Tm ions inverted.

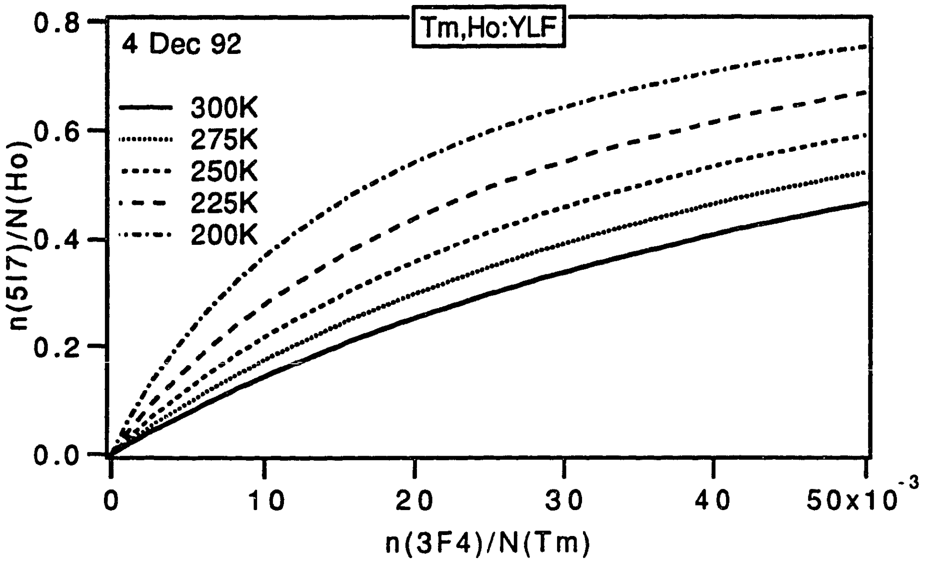

Figure B.1.2. Expansion of Fig. B.1.1 showing the differences in the initial slope.

Although the essential physics of this model is contained in Eq. B.1.6, it is useful to convert this relationship to explicitly contain the concentration and the excited state density. In our present model, all excitations will be in either the Tm $^3F_4$ level or the Ho $^5I_7$ level, so we can have an additional constraint $N_{ex}=N_1+N'_1$. Combining this with Eq. B.1.6, we can solve for N_1. We begin with

$$N_{ex} = N_1 + N'_1 = N_1 + \frac{N'_{Ho}\theta_0 r}{1 + r(\theta_0 - 1)}. \tag{B.1.7}$$

Substituting for r, we can transform this relation to

$$(\theta_0 - 1)N_1^2 + \left[N_{Tm} + N'_{Ho}\theta_0 - N_{ex}(\theta_0 - 1)\right]N_1 - N_{Tm}N_{ex} = 0. \tag{B.1.8}$$

n_1 can be expressed in terms of the dopant concentrations, the level of excitation, and θ_0 by using the well-known quadratic formula .

$$N_1 = \frac{-\left[N_{Tm} + N_{Ho}\theta_0 - N_{ex}(\theta_0 - 1)\right]}{2(\theta_0 - 1)} + \frac{\sqrt{\left[N_{Tm} + N_{Ho}\theta_0 - N_{ex}(\theta_0 - 1)\right]^2 + 4(\theta_0 - 1)N_{Tm}N_{ex}}}{2(\theta_0 - 1)} \tag{B.1.9}$$

Taking the positive branch of the square root (We know that N_1 cannot be negative), we now the relationship desired. We can find the value of N'_1 from the relationship $N_{ex}=N_1+N'_1$.

B.2. The distribution of excitations between the $^3F_4$, $^5I_7$, and $^5I_5$ manifolds.

This simple model can be extended to include the effects of $^5I_5$ upconversion and cross-relaxation. We can apply the same relations used to find the equilibrium distribution to energy transfer to the $^5I_5$ manifold. When the both the cross-relaxation and upconversion rates are equal, we should have an equilibrium distribution between this manifold and the lower manifolds. The model is illustrated in Figure B.2.1.

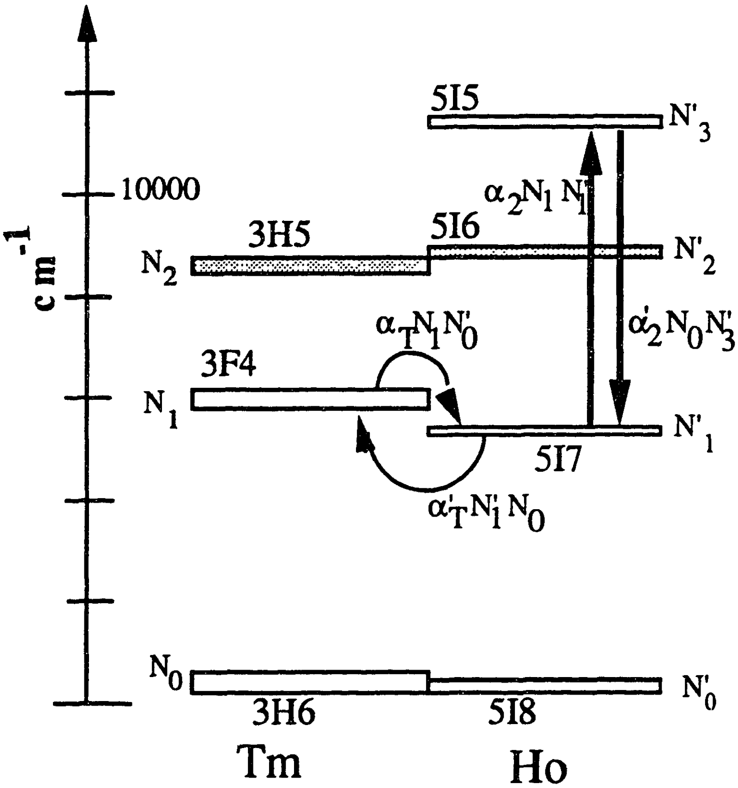

Figure B.2.1. Energy transfer processes in Tm,Ho. No losses are shown and energy transfer processes to higher-lying levels have not been considered.

In this model, all other relaxation and transfer mechanisms have been neglected; while this is a good approximation for the $^5I_7$ and the $^3F_4$ manifolds due to their long lifetimes, it is not so good for the $^5I_5$ level as there is generally rapid multiphonon relaxation to the $^5I_6$ level. This rapid relaxation acts as a loss on the system, so under most conditions the $^5I_5$ level will not be in true "equilibrium" with the lower levels unless the cross-relaxation rate is much greater than the non-radiative relaxation. However, this model is useful if we keep in mind that while the system is not in equilibrium, it is being driven towards it.

What we can find from this model is the distribution of excitations between these three manifolds. The $^5I_5$ multi-phonon relaxation acts as a loss on the system and therefore will reduce the total amount of energy stored in the system, while the upconversion and cross-relaxation processes will tend to lead an equilibrium distribution of excitations which results in different distribution of stored energy than would otherwise occur .

Using N'_1 as an elevated ground state, the equilibrium conditions connecting the $^5I_5$, $^5I_7$, and $^3F_4$ manifolds become

$$\frac{N_3'}{N_1} = \theta_2 \frac{N_1'}{N_0}. \qquad \text{(B.2.1)}$$

where N'_3 is the population of the Ho $^5I_5$ level, θ_2 is the ratio of the energy transfer coefficients ($\theta_2=\alpha_2/\alpha'_2$); and the other symbols keep their previously definitions.

The constraint for Ho is now, $N_{Ho}=N'_0+N'_1+N'_3$, where we have assumed that a Ho ion will be only in one of these three manifolds. Solving Eq. B.1.1 for N'_1 and substituting our constraint for N'_0, we get

$$N_1' = \theta_0 \frac{N_1}{N_0}\left(N_{Ho} - N_3' - N_1'\right). \qquad \text{(B.2.2)}$$

Rearranging terms, we can produce an expression for N'_1,

$$N_1' = \theta_0\left(\frac{N_1}{N_0+\theta_0 N_1}\right)\left(N_{Ho}-N_3'\right). \qquad \text{(B.2.3)}$$

Rearranging Eq. B.2.1 and substituting into the above expression, we find

$$N_3' = \frac{\theta_2\theta_0 N_1{}^2}{N_0\left(N_0+\theta_0 N_1\right)}\left(N_{Ho}-N_3'\right). \qquad \text{(B.2.4)}$$

Solving for N'_3, and rearranging ,we find

$$\frac{N'_3}{N_{Ho}} = \frac{\theta_2\theta_0 N_1^2}{N_0(N_0+\theta_0 N_1)+\theta_2\theta_0 N_1^2}. \tag{B.2.5}$$

We have now solved for the Ho $^5I_5$ population in terms of the ground state and excited state populations of Tm. Constraining the Tm ions with the relation $N_0=N_{Tm}-N_1$, we can simplify this relationship to find

$$\frac{N'_3}{N'_{Ho}} = \frac{\theta_2\theta_0 N_1^2}{(N_{Tm}-N_1)(N_{Tm}-N_1+\theta_0 N_1)+\theta_2\theta_0 N_1^2}. \tag{B.2.6}$$

Pulling N_{Tm} out of the denominator and replacing the value of N_1/N_{Tm} by r, we get

$$\frac{N'_3}{N'_{Ho}} = \frac{\theta_2\theta_0 r^2}{(1-r)\big(1+(\theta_0-1)r\big)+\theta_2\theta_0 r^2}, \tag{B.2.7}$$

an expression for the fraction of Ho ions in the $^5I_5$ state as a function of the fraction of excited Tm ions. With this relationship, we can solve for the fraction of Ho ions in the $^5I_7$ state. Recalling Eq. B.2.4, we substitute N_{Tm}-N_1 for N_0, rearrange, and find

$$N'_1 = \theta_0\left(\frac{r}{1+(\theta_0-1)r}\right)(N_{Ho}-N'_3). \tag{B.2.8}$$

Substituting Eq. B.2.7 for N'_3 in the above equation, we find

$$N'_1 = \theta_0\left(\frac{r}{1+(\theta_0-1)r}\right)\left(N_{Ho}-\frac{\theta_2\theta_0 r^2 N_{Ho}}{(1-r)\big(1+(\theta_0-1)r\big)+\theta_2\theta_0 r^2}\right). \tag{B.2.9}$$

With a few mathematical steps, we can find the relation for the population of the $^5I_7$ manifold,

$$\frac{N'_1}{N_{Ho}} = \theta_0\left(\frac{(1-r)r}{(1-r)\big(1+(\theta_0-1)r\big)+\theta_2\theta_0 r^2}\right). \tag{B.2.10}$$

This relationship, along with the relationship for N'_3/N_{Ho} (Eq. B.2.7), can be used do describe the behavior of the Tm-Ho system under the conditions. A plot of N'_1/N_{Ho} (Eq. B.2.10) is shown in Fig. B.2.2.

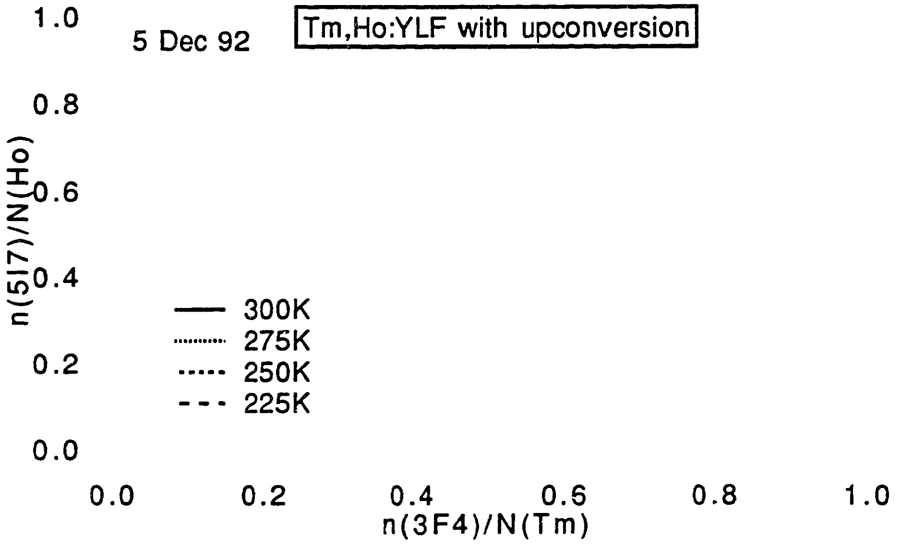

Figure B.2.2. Fractional population of the $^5I_7$ level as a function of the fractional population of the $^3F_4$ level. The presence of upconversion to the 5I5 manifold has been included.

In Fig. B.2.2, notice how the maximum fractional population of the $^5I_7$ is less than unity. The value of this maximum is inversely proportional to the θ_2; this means that even without consideration of the losses associated with the $^5I_5$ manifold, there is a limit on the maximum fraction of Ho ions that can be in the $^5I_7$ manifold. The larger the ratio of the upconversion parameter to the cross-relaxation parameter (θ_2), the less energy you will be able to store in the Ho $^5I_7$ at higher excitation densities. Additionally, the roll-off of the $^5I_7$ fractional population occurs at lower fractional Tm population from that predicted without upconversion as the value of θ_2 is increased. In other words, the greater the value of θ_2, the earlier the deviation from simple model presented earlier.

It is possible to re-express these relations as a function of excitation density in the same manner as we did for the system without upconversion (Eq. B.1.9) by using the constraint relation $Nex=N_1+N'_1+2N'_3$; however, these resulting equation is a fairly complicated cubic equation, and in practice it is simpler to use Eqs. B.2.7 and B.2.10 and reconstruct the excitation density by addition.

C. Selection, Design, and Operation of Pump Sources.

This section details the various laser sources which were assembled in support of this thesis as well as other projects. It has been written to provide some documentation on these sources as well as for the purposes of thesis support. In this section, we describe in brief some of the design considerations and alignment procedures for some of these systems as well as their performance.

C.1. CW Titanium:Sapphire laser.

A cw Ti:Sapphire laser was constructed based on the design of Schwartz Electro-optics. Our initial design yielded sub-standard performance and several iterations of re-design were required to optimize the system. We will now detail the various laser designs which yielded acceptable performance. The basic set-up of the system is diagrammed in Fig C.1.1.

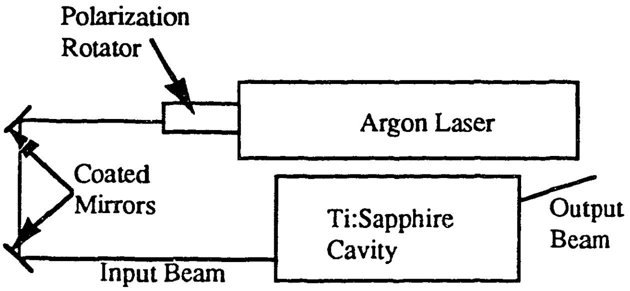

Figure C.1.1. Arrangement of Ti:Sapphire laser and pump.

This initial design of the laser was a 4 mirror design roughly duplicated from the commercial designs of Shwartz Electro-optics[1]. When this system was initially assembled and aligned, the Ti:Sapphire laser performance displayed the following characteristics. With a 5% output coupler, the system threshold was approximately 2 W with a slope efficiency of approximately 10%. The mirrors used were mid-range mirrors, allowing tuning from ≈760 nm to 850 nm. The peak reflectance was near 800 nm, and the maximum tuned output power was ≈500 mW. Over a period of a few months, the performance of the laser degraded constantly until operation was no longer possible, despite repeated system realignments. Under inspection it was observed that the mirror

---

[1] The initial design, calculations, and mirror specification were performed by D. S. Knowles and M. Tonelli.

coatings had acquired a mottled appearance, which indicated coating degradation. The mirrors were replaced with a set optimized for short wavelengths and the laser was re-aligned. Laser action was again possible, although the maximum output power was limited to ≈300 mW and the tuning range to ≈740 nm to 770 nm. Over a period of approximately 3 months the laser performance again degraded to inoperability; this also coincided with the appearance of mottling on the mirror surfaces.

As we waited to acquire new mirrors, we performed a design check on the system as the extractable power in similar systems is generally exceeds one W. We verified the stability of our cavity design, and found the figure of merit of our Sapphire crystal to be ≈80. The nominal Ti^{3+} concentration of our crystal was 0.1% and the crystal was Brewster cut. With these parameters, our system should be able to produce over one W with our pumping conditions.

We cleaned our degraded mirrors with a molecular-level coating-type cleaner which appeared to remove most of the blemishes; following this treatment, the laser could again be operated. We also acquired a set of mirrors from Schwartz Electro-Optics in Concord, MA. With two sets of mirrors, we could compare of slope efficiencies and thresholds to optimize the system as well as identify losses. Using the Schwartz high-reflectors, the laser threshold was unchanged (≈2 W) but a higher slope efficiency than earlier was achieved (≈15%). However, the laser would saturate at approximately 250-300 mW dependent on alignment procedures and pump mode size. Both a three-mirror and a four-mirror scheme were used in an attempt to identify the cause of this saturation. The losses of the sapphire crystal were estimated to be approximately 1%. Under further investigation, it was discovered that our Ar laser mode was degraded at higher pump powers; this degradation is thought to a result of heating in the polarization rotator. This degradation destroyed the pump mode - laser mode overlap.

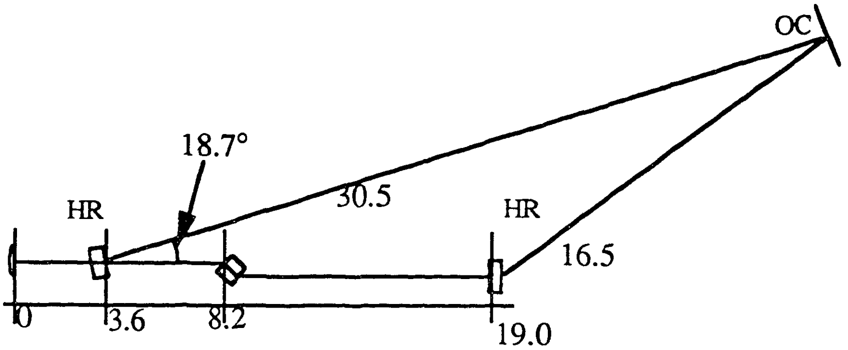

Figure C.1.2. Schematic of the three mirror configuration. All reported numbers are the distance between elements in cm.

To overcome this problem, a polarization rotator was constructed out of 2 coated optics. This provides us with a polarization rotation of 90°, which is sufficient for our purposes. Following this change, the system was realigned and the performance immediately improved. We then tried different output couplers to see if we could determine the loss of our material. We used the three-mirror design (Fig C.1.2) for most of this work as it simplified alignment. Fig A.4.3 displays plots of these measurements for the 3 mirror system.

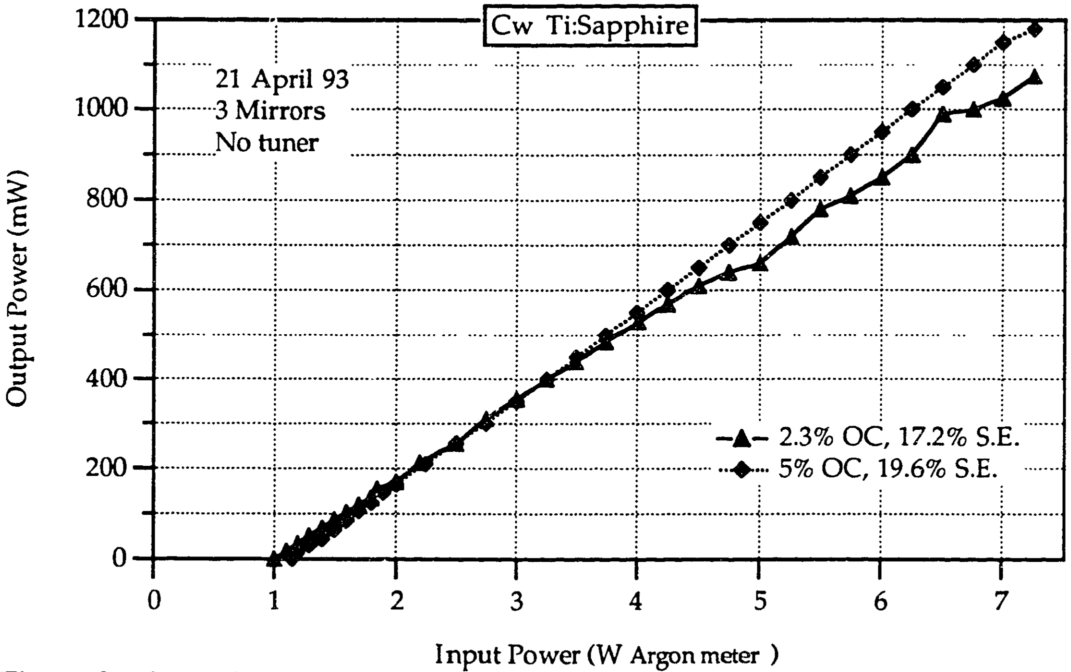

Figure C.1.3. Performance of 3 mirror Ti:Sapphire system (No tuner) with different output couplers.

Here we have reported the slope efficiencies as read from the Ar laser power monitor. The power incident on the crystal is roughly 90% of the readings on this meter. Therefore, the x axis in the figures should be scaled by roughly 0.9, and the slope efficiencies divided by 0.9 to get the actual slope efficiencies.

Although this system now met our expectations as far as slope efficiency for the untuned system was concerned, we found two problems with this set-up: (1) the slope efficiency fell to roughly 12% when the tuning element was introduced, and (2) the output mode was observed to have a rectangular shape instead of gaussian distribution. For these reasons we returned to the 4 mirror configuration.

With this configuration, we repeated the slope efficiency measurements. We found that the tuner insertion loss was reduced and the mode quality improved so that the output was nearly gaussian. The threshold decreased slightly in this configuration. A comparison of the three-mirror and four-mirror configurations is presented in Fig. C.1.4.

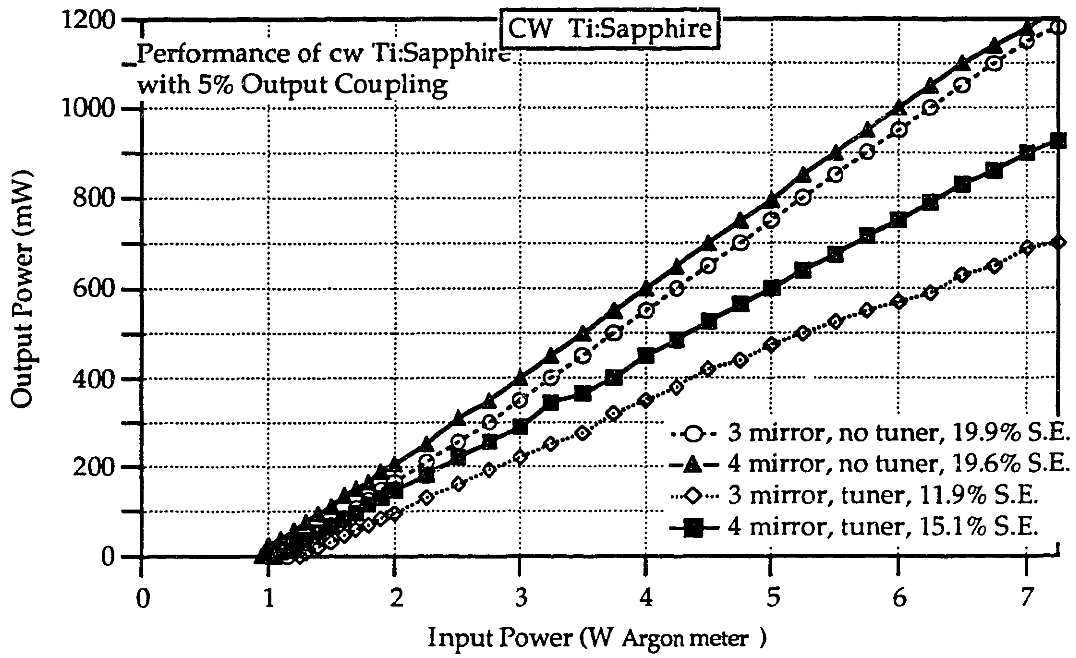

Figure C.1.4. Comparison of Ti:Sapphire performance with different configuration cavitites with 5% Output Coupling.

As this performance was sufficient to meet our experimental needs at the time, we discontinued our experimentation with Ti:Sapphire designs and moved on to actual experiments. The schematic diagram of the configuration which produced the best performance is shown in Fig. C.1.5.

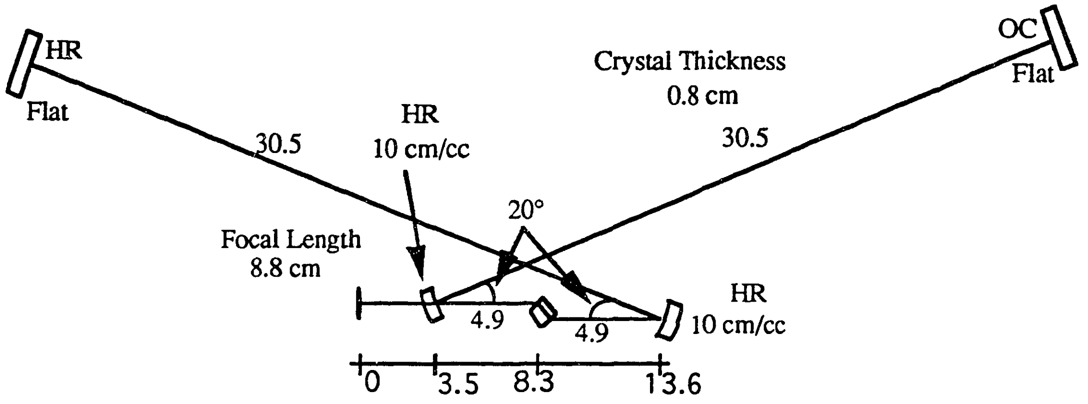

Figure C.1.5. Schematic diagram of 4 mirror Ti:Sapphire configuration. The birefrigent tuner was inserted into the output coupling arm. All reported distances are in cm.

Although the system is usable in its current configuration, it could be improved with a few changes. These changes would be to find a crystal with a higher figure of merit (and possibly a higher Ti concentration), reduce the insertion loss of the birefrigent tuner (theoretically this should be zero), and to match the mirror sets. We are currently operating the laser with the output coupler and the high reflecting mirrors optimized at different wavelengths. It would be preferable to optimize these at the same wavelength.

D. Spectral Measurement of the Chemical Potential.

If both the emission and absorption cross-section of a material are known for the same experimental conditions (temperature, orientation, etc.), it is possible to extract the chemical potential for transitions between the manifolds involved with simple math and McCumber's theory of transitions. Starting with McCumber's relation, we have

$$\sigma_{ab}(\lambda) = \sigma_{em}(\lambda) e^{\beta(E(\lambda)-\mu)},$$

where σ_{ab} is the absorption cross-section, σ_{em} is the emission cross-section, E is the energy of a transition at a given wavelength, and μ is the chemical potential. Here $\beta = 1/kT$, where T is the temperature and k is the Boltzmann constant. By taking the logarithm of the ratio of the emission cross-section to the absorption cross-section we get

$$\frac{1}{\beta}\ln\left(\frac{\sigma_{ab}(\lambda)}{\sigma_{em}(\lambda)}\right) = E(\lambda) - \mu$$

or

$$\frac{1}{\beta}\ln\left(\frac{\sigma_{em}(\lambda)}{\sigma_{ab}(\lambda)}\right) = \mu - E(\lambda)$$

depending on which spectra you choose to use as the divisor.

The chemical potential can now be read by simply plotting out the logarithm of the ratio versus the wavelength (or any other units in which the spectra are expressed.) The chemical potential is found by noting the energy at the point where the plot crosses the zero line. An example plot is shown below in Fig. 1.

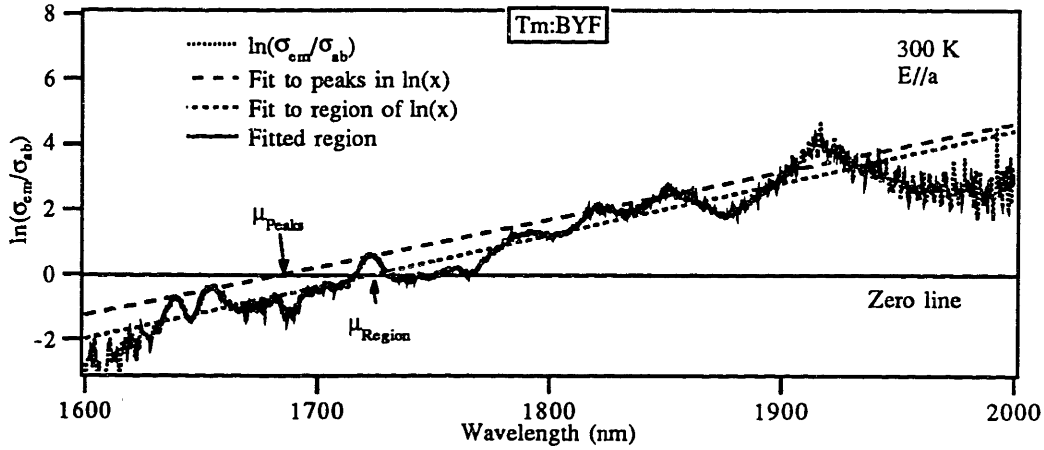

Figure 1. Illustration of method used to find the chemical potential from the absorption and emission cross-sections.

Additional accuracy can be gained by fitting an appropriate function to the logarithm and noting the point where the fit crosses the zero line. The appropriate function will depend upon the units against which the logarithm is plotted. If the units are those of energy, the appropriate function will simply be linear; while for units of wavelength, the function is slightly more complicated, but can sometimes be approximated with a simple linear function. This will be dependent upon the region with which you are working and the accuracy which you desire to know the potential.

There are two important considerations when fitting to find the chemical potential. First, regions where very small numbers are in the divisor (in Figure 1, regions of very small absorption) must be eliminated from the fit when possible as ratios derived from these values are often noisy and will skew the fit. A second more subtle consideration is the resolution of the two spectra. If the spectra were taken at exactly the same resolution, then the fit can be done simply by using ratios of peak values; if, however, the spectra were taken at different resolutions, the measured peak values will be different than predicted by the relation above. (The intensity, in a sense, is distributed over a broader spectral range in peaks taken at lower resolution in comparison to those taken at high resolution.) In this case, it is more accurate to fit an entire regions of spectra where the absorption and emission are of sufficient strength to ensure that the data are not too noisy. This is graphically illustrated in Fig. 1 where a fit to the peaks yields a μ of 5936 cm^{-1} and a fit to the selected region yields a μ of 5801 cm^{-1}. The calculated value of μ is this material at 300K is 5740 cm^{-1} based on our current knowledge of the energy level structure. As the spectra shown in Fig. 1 are preliminary data, this is acceptable accuracy at the present time. Of course, once the chemical potential is known you can generate either emission or absorption spectra from the complementary spectra.

This method is susceptible to any errors in the scaling of the spectra. For instance, if we have take the absorption cross-section to be $A\sigma_{ab}(\lambda)$ instead of $\sigma_{ab}(\lambda)$ (where A is a scaling factor), this will appear in the above equation as an offset in the zero crossing; and thus will lead to an inaccuracy in the chemical potential. Mathematically this is illustrated below.

$$\frac{1}{\beta}\ln\left(\frac{A\sigma_{ab}(\lambda)}{B\sigma_{em}(\lambda)}\right)=E(\lambda)-\mu+\frac{1}{\beta}\ln\left(\frac{A}{B}\right)$$

where A and B are scale factors for the absorption and emission spectra. This leads to an uncertainty in μ of

$$\Delta\mu\approx\frac{1}{\beta}\left[\ln\left(1-\frac{\Delta\sigma_{ab}}{\sigma_{ab}}\right)+\ln\left(1-\frac{\Delta\sigma_{em}}{\sigma_{em}}\right)\right].$$

where $\Delta\sigma$ is the uncertainty in the respective spectra. For instance, if both the absorption and emission cross-sections are known to 5% accuracy, the uncertainty in μ at room temperature is roughly $kT^*[\ln(.95)+\ln(.95)]=21\ \mathrm{cm}^{-1}$.

References

1 A. L. Schalow and C. H. Townes, Phys. Rev., V112, (1958), P1940.

2 T. H. Maiman, Nature, V187, (1960), P493.

3 B. G. Wybourne, Spectroscopic Properties of the Rare-Earths, Wiley, New York, 1965.

4a G. J. Quarles, L. Esterowitz, G. Rosenblatt, R. Uhrin, and R. Belt, in OSA Proc. of the Advanced Solid State Laser Conference (V 13), Ed. Chase and Pinto, Santa Fe, 1992, P 306-309,

4b P. P. Sorokin and M. J. Stevenson, "Stimulated Infrared Emission from Trivalent Uranium," Phys. Rev. Lett. 5, (1960), P 557-559.

5 S. Hufner, Optical Spectra of Transparent Rare Earth Compounds, Academic Press, New York, 1978.

6 E. U. Condon and G. H. Shortley, The Theory of Atomic Spectra, Cambridge University Press, Cambridge, 1957.

7 L. M. Falicov, Group Theory and Its Physical Applications, University of Chicago Press, Chicago, 1989.

8 H. M. Crosswhite and H. M. Moos, Optical Properties of Ions in Crystals, Interscience, New York, 1967.

9 C. A. Morrison, Host Materials for Transition-Metal Ions, Harry Diamond Laboratories, US Army Electronics Research and Development Command, Pub. HDL-Ds-89-1, 1989.

10 C. A. Morrison, Lectures on Crystal Field Theory, Harry Diamond Laboratories, US Army Electronics Research and Development Command, Pub. HDL-SR-82-8, 1982.

11 C. J. Ballhausen, Introduction to Ligand Field Theory, McGraw-Hill, New York, 1962.

12 E. D. Filer, C. A. Morrison, G. A. Turner, and N. P. Barnes, "Theoretical Branching Ratios for the 5I7->5I8 Levels of Ho3+ in the Garnets A3B2C3O12," OSA Proc. on Advanced Solid-State Lasers, Santa Fe, Ed. L. L. Chase and A. A. Pinto, V13, 1992, P354.

13 Y. R. Shen, The Principles of Nonlinear Optics, Wiley, New York, 1984.

14 J. H. Van Vleck, J. Phys. Chem., V4, (1937), P67.

15 L. A. Riseberg and M. J. Weber, "Relaxation Phenomena in Rare-Earth Luminescence," Progress In Optics, V14, Ed. E. Wolf, North-Holland, Amsterdam, 1976, P91-159.

16 M. Wagner, "Vibronic Spectra in Ionic Crystals," Optical Properties of Ions in Crystals, Ed. H. M. Crosswhite and H. W. Moos, Interscience, New York, 1967, P349-356.

17 H. P. Jenssen, "Phonon Assisted Laser Transitions and Energy Transfer in Rare Earth Crystals," PhD Dissertation, Mass. Inst. of Tech., 1971.

18 H. W. Moos, "Spectroscopic Relaxation Processes of Rare Earth Ions in Crystals," J. Lumin, V1, N2, (1970), P106.

19 J. C. Wright., in Radiationless Processes in Molecules and Condense Phases, Ed. F.K. Fong, Topics in Applied Physics Series, V15, Springer-Verlag, Berlin, 1976, P. 239.

20 V. M. Agranovich and M. D. Galanin, Electronic Excitation Energy Transfer in Condensed Matter, Modern Problems in Condensed Matter Sciences Series, V3, North-Holland, Amsterdam, 1982.

21 D. S. Knowles and H. P. Jenssen, "Upconversion versus Pr-deactivation for Efficient 3 μm Laser Operation in Er", IEEE J. Quant. Elect., V28, N4, (1992), P1197.

22a R. Buisson and J. Q. Liu, "Fluorescence quenching of Nd3+ in LaF3 studied by direct measurement of pairs," J. Physique, V45, (1984), P1523.

22b V. Lupei, A. Lupei, S. Georgescu, and W. M. Yen, "Effects of energy transfer on quantum efficiency of YAG:Nd," J. Appl. Phys., V66, N8, 1989, P3792.

23 B. J. Dinerman and P.F. Moulton, "CW Laser Operation from Er:YAG, Er:GGG and Er:YSGG," OSA Proc. on Advanced Solid-State Lasers, Santa Fe, Ed. L.L. Chase and A.A. Pinto, V13, 1992, P152.

24 T. Herbert, W. P. Risk, R. M. Macfarlane, and W. Lenth, "Diode-Laser-Pumped 551-nm Upconversion Laser in YLiF4:Er3+," OSA Proc. on Advanced Solid-State Lasers, Salt Lake City, ed. H. P. Jenssen and G. Dube, V6, 1990, P379.

25 T. Y. Fan, G. Huber, R. L. Byer, and P. Mitzscherlich, "Spectroscopy and Diode Laser-Pumped Operation of Tm, Ho:YAG," IEEE J. Quant. Elect., V24, N6, (1988), P924.

26 M. J. Weber, "Luminescence Decay by Energy Migration and Transfer: Observation of Diffusion-Limited Relaxation", Phys. Rev. B, V4, N9, (1971), P2932.

27 S. W. Henderson, C. P. Hale, J. R. Magee, M. J. Kavaya, and A. V. Huffaker, "Eye-safe coherent laser radar system at 2.1 mm using Tm,Ho:YAG lasers," Optics Letters, V16, N 10, (May 1991), P 773-775.

28 M. E. Storm and W. W. Rohrbach, "Single-longitudinal-mode lasing of Ho:Tm:YAG at 2.091 mm", Applied Optics, V 28, N 23, (Dec 89), P 4965.

29 P. A. Budni, P. G. Schunemann, M. G. Knights, T.M. Pollak, and E.P. Chicklis,"Efficient, High Average Power Optical Parametric Oscillator Using ZnGeP2.", in OSA Proc. of the Advanced Solid State Laser Conference (V 13), Ed. Chase and Pinto, Santa Fe, 1992, P 380-383.

30 K. L. Schepler, M. D. Turner, and P. A. Budni, "High-Average-Power Nonlinear Frequency Conversion in AgGaSe2", OSA Proc. on Adv. Sol. State Laser, V10, ed G. Dube and L. Chase, Hilton Head, (1991), P325.

31 T. Y. Fan and R. L. Byer, "Diode Laser-Pumped Solid State Lasers," IEEE J. Quant. Elect., V24, N6, (1988), P 895.

32 P. F. Moulton, "An Investigation of the Co:MgF2 Laser System," IEEE J. Quant. Elect., V21, (1985), P1582.

33 D. M. Rines, G. A. Rines, D. Welford, and P. F. Moulton, "High-Energy Operation of a Co:MgF2 Laser," in OSA Proc. of the Advanced Solid State Laser Conference (V 13), Ed. Chase and Pinto, Santa Fe, 1992, P 161.

34 G. J. Quarles, A. Rosenbaum, C. L. Marquardt, and L. Esterowitz, "Efficient room-temperature operation of a flash-lamp-pumped Cr,Tm:YAG laser at 2.01 μm," Optics Letters, V15, N1, (1990), P42.

35 S. R. Bowman, G.J . Quarles, and B. J. Feldman, "Upconversion Studies of Flashlamp-Pumped Cr,Tm:YAG," in OSA Proc. of the Advanced Solid State Laser Conference (V 10), Ed. G. Dube and L. Chase, Hilton Head, 1991, P 169.

36 L. F. Johnson, G. D. Boyd, and K. Nassau, "Optical maser characteristics of Ho3+ in CaWO4," Proc. IRE, V 50, (1962), P 87.

37 A. Yariv, Quantum Electronics, Wiley, New York, 1967, P245.

38 R. L. Remski and D. J. Smith, "Temperature dependence of pulsed laser threshold in YAG: Er3+, Tm3+, Ho3+," IEEE J. Quant. Elect., V6, (1970), P750.

39 E. P. Chicklis, C. S. Naiman, R. C. Folweiler, D. R. Gabbe, H. P. Jenssen, and A. Linz, "High-Efficiency Room-Temperature 2.06-μm Laser Using Sensitized Ho3+:YLF," App. Phys. Let., V19, N4, (1971), P119.

40 G. J. Quarles, A. Rosenbaum, C. L. Marquardt, and L Esterowitz, "High-efficiency 2.09 μm flashlamp-pumped Tm:Ho:YAG laser," Appl. Opt., V24, (1985), P940.

41 N. P. Barnes, M. E. Storm, P. L. Cross, and M. W. Skolaut, Jr., "Efficiency of Nd laser materials with laser diode pumping," IEEE J. Quant. Elect., V26, (1990), P558.

42 L. E. Holder, C. Kennedy, L. Long, and G. Dube, "One Joule per Q-Switched Pulse Diode-Pumped Laser," IEEE J. Quant. Elect., V28, N4, (1992), P986.

43 T. S. Kubo and T. J. Kane, "Diode-Pumped Lasers at Five Eye-Safe Wavelengths," IEEE J. Quant. Elect., V28, N4, (1992), P1033.

44 R. C. Stoneman and L. Esterowitz, "Intracavity-pumped 2.09-µm Ho:YAG Laser," OSA Proc. on Adv. Sol. State Lasers, V13, ed. L. L. Chase and A. A. Pinto, Santa Fe, (1992), P115.

45 D. E. Castleberry, "Energy transfer in sensitized rare earth lasers," Ph.D. dissertation, Mass. Inst. of Tech, Cambridge, MA, 1975.

46 R. Allen, L. Esterowitz, L. Goldberg, J. F. Weller, and M. Storm, "Diode-pumped 2 µm holmium laser," Electron. Lett., V22, (1986), P947.

47 T. Y. Fan, G. Huber, R. L. Byer, and P. Mitzscherlich, "Continuous wave operation at 2.1 µm of a diode laser pumped, Tm-sensitized Ho:Y3Al5O12 laser at 300K," Opt. Lett., V12, (1987), P678.

48 S. R. Bowman, M. J. Winings, R. C. Y. Auyeung, J. E. Tucker, S. Searles, and B. J. Feldman, "Upconversion Studies of Flashlamp-Pumped Cr,Tm,Ho:YAG," in OSA Proc. of the Advanced Solid State Laser Conference (V 13), Ed. L. Chase and E. Pinto, Santa Fe, 1992, P 172.

49 M. G. Jani, R. R. Reeves, R.C . Powell, G. J. Quarles, and L. Esterowitz, "Alexandrite-laser excitation of a Tm:Ho:$Y_3Al_5O_{12}$ laser," J. Opt. Soc. Am. B, V8, N4, (1991), P741.

50 L. B. Shaw, X.B . Jiang, R. S. F. Chang, and N. Djeu, "Upconversion of 5I7 to 5I6 and 5I5 in Ho:YAG and Ho:YLF," in OSA Proc. of the Advanced Solid State Laser Conference (V 13), Ed. L. Chase and E. Pinto, Santa Fe, 1992, P 174.

51 M. A. Noginov, G. K. Sarkissian, V. A. Smirnov, and I. A. Shcherbakov, "Cross-relaxation depletion of the ground state of rare-earth ions in crystals", OSA Proc. of the Adv. Solid State Laser Conf. V6, Ed. H. P. Jenssen and G. Dube, Salt Lake City, (1990), P375.

52 C. Hauglie-Hanssen and N. Djeu, "Pump saturation for the 2 µm Tm laser", OSA Proc. of the Advanced Solid State Laser Conference, Ed. E. Pinto and T. Y. Fan, New Orleans, 1993, In press.

53 A. S. Davydov, "The Radiationless Transfer of Energy of Electronic Excitation Between Impurity Molecules in Crystals," Phys. Stat. Sol., V30, (1968), P357.

54 O. K. Alimov, M. K. Ashurov, T. T. Basiev, E. O. Kirpichenkova, and V. B. Murav'ev, in Selective Laser Spectroscopy of Activated Crystals and Glasses, Ed. by V.V. Osiko, Proc. of the Inst. of Gen. Phys. Acad. of Sciences of the USSR, Vol. 9., Nova, New York, (1990), P69.

55 L. D. Landau and E. M. Lifshitz, Quantum Mechanics, 3rd Ed., Pergamon, Oxford, 1977.

56 J. J. Sakurai, Modern Quantum Mechanics, Addison-Wesley, Redwood City, (1985), P320.

57 R. Loudon, The Quantum Theory of Light, 2nd Ed., Oxford Science, New York,1983.

58 D. L. Dexter, T. Forster, and R. S. Knox, Phys. Stat. Sol., V34, (1969), K159.

59 T. Forster, Ann. Physik, V2, (1948), P55.

60 D. L. Dexter, "A Theory of Sensitized Luminescence in Solids," J. Chem. Phys., V21, N5, (1953), P836.

61 R. J. Birgeneau, "Mechanisms of energy transport between rare-earth ions," App. Phys. Lett., V13, N5, (1968), P193.

62 R. J. Birgeneau, M.T. Hutchings, J.M. Baker, and J.D. Riley, "High-Degree Electrostatic and Exchange Interactions in Rare-Earth Compounds," J. Appl. Phys., V40, N3, (1969), P1070.

63 N. Krasutsky and H. W. Moos, "Energy transfer between the low-lying energy levels of Pr3+ and Nd3+ in LaCl3", Phys. Rev. B, V8, N3, (1973), P1010.

64 C.H. Edwards, Jr. and D.E. Penney, Elementary Differential Equations with Applications, Prentice-Hall Englewood Cliffs, (1985).

65 R. A. Cellarius, "Excitation Energy Transfer in Systems of Many Molecules," Photochemistry and Photobiology, V6, (1967), P91.

66 D. S. Knowles, "Energy Transfer Under Strong Pumping in High Concentration Rare Earth Doped Laser Crystals", PhD dissertation, MIT, Sept 1991.

67 W.J.C. Grant, "Role of Rate Equations in the Theory of Luminescent Energy Transfer," Phys. Rev. B, V4, N2, (1971), P648.

68 H. C. Chow, and R. C. Powell, "Models for energy transfer in solids," Phys. Rev. B, V21, N9, (1980), P3785.

69 M. Yokota and O. Tanimoto, "Effects of diffusion on energy transfer by resonance", J. Phys. Soc. of Japan, V22, N3, (1967), P779.

70 A. I. Burshtein, "Concentration quenching of noncoherent excitation in solutions," Sov. Phys. Usp., V27, N8, (1984), P579.

71 A. I Burshtein, "Hopping Mechanism of Energy Transfer," Sov. JETP Phys., V35, N5, (1972), P882.

72 W. Koechner, Solid-State Laser Engineering, 2nd Ed., Springer-Verlag, New York, 1985.

73 A. Einstein, Phys. Zeits. V18, (1917), P121.

74 See, for example, J.J. Sakurai, Advanced Quantum Mechanics, Addison-Wesley, Redwood City, 1967.

75 H. P. Christensen, D.R. Gabbe, and H.P. Jenssen, "Fluorescence lifetimes for neodymium-doped yttrium aluminum garnet and yttrium oxide powders," Phys. Rev. B, V25, N3. (1982), P1467.

76 D. E. McCumber, "Theory of Vibrational Structure in Optical Spectra of Impurities in Solids. I. Singlets," J. Math. Phys., V5, N2, (1964), P221.

77 D. E. McCumber, "Theory of Vibrational Structure in Optical Spectra of Impurities in Solids. II. Multiplets," J. Math. Phys., V5, N4, (1964), P508.

78 D. E. McCumber, "Einstein relations connecting broadband emission and absorption spectra", Phys. Rev., V136, (1964), PA954.

79 K. Gottfried, Quantum Mechanics I, Fundamentals, Addison-Wesley, Redwood City, 1989.

80 F. Reif, Fundamentals of Statistical and Thermal Physics, McGraw-Hill, New York, 1965.

81 J. C. Walling, O. G. Peterson, H. P. Jenssen, R. C. Morris, and E. W. O'Dell, "Tunable Alexandrite Lasers," IEEE J. Quant. Elect., V16, N12, (1980), P1302.

82 Y. B. Band and D. F. Heller, "Relationships between the absorption and emission of light in multilevel systems," Phys. Rev. A, V38, N4, (1988), P1885.

83 E. Cohen and H. W. Moos, "Vibronic Transitions of Hexagonal Rare-Earth Trichlorides. I. Pr^{3+} and Nd^{3+} in $NdCl_3$," Phys. Rev., V161, N2, (1967), P258.

84 See, for example, K. Gottfried, Quantum Mechanics I, Fundamentals, Addison-Wesley, Redwood City, 1989.

85 L. A. Riseberg, H. W. Moos, and W. D. Partlow, "Multiphonon Relaxation in Laser Materials and Applications to the Design of Quantum Electronic Devices," IEEE J. Quant. Elect., V4, N10, (1968), P609.

86 H. W. Moos, "Spectroscopic Relaxation Processes of Rare Earth Ions in Crystals", J. Lumin, V1, N2, (1970), P106.

87 See, for example, E.D. Reed, Jr. and H.W. Moos, "Multiphonon Relaxation of Excited States of Rare-Earth Ions in YVO_4, $YAsO_4$, and YPO_4," Phys. Rev. B, V8, N3, (1973), P980.

88 T. Miyakawa and D. L. Dexter, " Phonon sidebands, multiphonon relaxation of excited states, and phonon-assisted energy transfer between ions in solids", Phys. Rev. B, V1, N7, (1970), P2961.

89 For example, contrast the results of N.S. Yamada, S. Shionoya, and T. Kushida, J. Phys. Soc. Japan, V32, (1972), P1577 and H.P. Jenssen in [17].

90 D. E. McCumber, "Theory of phonon-terminated optical masers", Phys. Rev., V134, (1964), PA299.

91 A. Brenier, J. Rubin, R. Moncorge and C. Pedrini, "Excited-state dynamics of the Tm^{3+} ions and Tm^{3+}->Ho^{3+} energy transfers in $LiYF_4$", J. Phys. France, V50, (1989), P1463.

92 G. Armagan, A. M. Buoncristiani, A. T. Inge, and B. DiBartolo, "Comparison of Spectroscopic Properties of Tm and Ho in YAG and YLF Crystals", OSA Proc. on Adv. Sol. State Lasers, V10, Ed. G. Dube and L. Chase, Hilton Head, (1991), P222.

93 See, for example, G. Armagan, A. M. Buoncristiani, A. T. Inge, and B. Di Bartolo, "Comparison of Spectroscopic Properties of Tm and Ho in YAG and YLF Crystals", OSA Proc. on Adv. Sol. State Lasers, V10, Ed. G. Dube and L. L. Chase, Hilton Head, (1991), P222.

94 D. A. Zubenko, M. A. Noginov, S. G. Serenkov, V. A. Smirnov, and I. A. Shcherbakov, Sov. J. Quant. Elect., V22, N2, (1992), P133-138.

95 S. A. Payne, L. K. Smith, W. L. Kway, and W. F. Krupke, "Tm->Ho Energy Transfer in $LiYF_4$," Proc. Adv. Solid State Lasers, Sante Fe, 1992, Ed. Chase and Pinto, P166.

96 K. Lark-Horovitz and V. A. Johnson, Solid State Physics, Methods in Experimental Physics Series, V6, Ed L. Marton, Academic Press, New York, 1959.

97 C. Kittel, Introduction to Solid State Physics, 6th Ed, Wiley, Brisbane, 1986.

98 H. P. Christensen, H. P. Jenssen, and D. R. Gabbe, "BaY_2F_8 as a Host For Ln Ions, I: Optical Properties of the Crystal and Spectroscopic Results for Pr, Dy, Ho, and Er Doping", Unpublished.

99 A. A. Kaminskii, S. E. Sarkisov, F. Below, and H. J. Eichler, "Spectroscopic and laser properties of Er^{3+}-doped monoclinic BaY_2F_8 single crystals," Optical and Quant. Elect., 22, S95,(1990).

100 L. F. Johnson and H. J. Guggengeim, "Laser emission at 3 μm from Dy^{3+} in BaY_2F_8," Appl. Phys. Lett., V23, N2, P96, (1973).

101 A. A. Kaminskii and B. N. Sobolev, Neorg.Mat., V19, N11, (Nov 83), P1947-1950.

102 A. A. Kaminskii, and S. E. Sarkisov,"Stimulated-Emission Spectroscopy of Pr^{3+} Ions in Monoclinic BaY_2F_8 Flouride", Phys. Stat. Sol. (a) 97, K163 (1986).

103 L. F. Johnson and H. J. Guggenheim, "Electronic- and Phonon- Terminated Laser Emission from Ho^{3+} in BaY_2F_8," IEEE J. of Quant. Elect., V10, N4, P442, (1974)

104 A. A. Kaminskii, B. P. Sobolev, S. E. Sarkisov, G. A. Denisnko, V. V. Byabchenkov, V. A. Fedorov, and T. V. Uvarova, "Physiochemical Aspects of the Preparation, Spectroscopy, and Stimulate Emission of Single Crystals of $BaLn_2F_8$-Ln^{3+}," Neorg. Mat., V18, N3, P482, (1982).

105 O. E. Izotova and V. B. Aleksandrov, "The Crystal Structure of $BaTm_2F_8$," Sov. Phys. Doklady, V15, N6, P525, (1970).

106a M. Born and E. Wolf, Principles of Optics, 6th ed., (Pergamon, 1980), P667-679, P708.

106b J.J. Nye, Physical Properties of Crystals, (Oxford, London, 1960), P3-49, P305-309.

107 W. L. Bond, J. Apple. Phys., 36, P1674, (1965).

108a M. Born and E. Wolf, Principles of Optics, 6th ed., (Pergamon, 1980), P667-679, P708.

108b J.J. Nye, Physical Properties of Crystals, (Oxford, London, 1960), P3-49, P305-309.

109 K. M. Dinndorf, D. S. Knowles, M. Gojer, C. J. Taylor, and H. P. Jenssen, "Where are the principal axes for transitions in monoclinic crystals?", Proc. of the Adv. Solid State Laser Conf., Santa Fe, NM, Feb 17-19, 1992.

110 I. N. Kurkin, K. P. Chernov, and Yu. K. Chirkin, Sov. Phys. Solid St., V21, P521, (1979).

111 A. Linz, H. P. Jenssen, C. S. Naiman, and E. P. Chickliss, "$LiYF_4$ (YLF): A Spectrally Diverse Laser Host and Electro-Optical Material", unpublished, 1980.

112 D. R. Gabbe, A. Linz, M. Douma, C. S. Naiman, and R. C. Folweiler, "Growth of single crystals of pure and rare earth doped $LiYF_4$ for laser applications", presented and 169th ACS Nat. Meet., Philadelphia, Apr 6-11, 1975.

113 A. L. Harmer, A. Linz, and D. R. Gabbe, "Fluorescence of Nd3+ in Lithium Yttrium Fluoride", J. Phys. Chem. Solids, V30, (1989), P1483.

114 H. P. Jenssen, A. Linz, R. P. Leavitt, C. A. Morrison, and D. E. Wortman,"Analysis of the optical spectrum of Tm^{3+} in $LiYF_4$, " Physical Review B, V 11, N 1, (Jan 1975), P 92-101.

115 N. Karayianis, D.E. Wortman, and H.P. Jenssen, "Analysis of the optical spectrum of Ho^{3+} in $LiYF_4$, " J. Phys. Chem. Solids, V 37, (1976), P675-682.

116 G. A. Bogomolova, L. A. Bumagina, A. A. Kaminskii, and B. Z. Malkin, "Crystal field in laser garnets with TR^{3+} ions in the exchange charge model", Sov. Phys. Solid State, V19, N8, (1977), P1428.

117 C. A. Morrison, E. D. Filer, and N. P. Barnes, "Energy levels and branching ratios of Tm^{3+} in ten garnet laser materials", Harry Diamond Laboratories, Adelphi MD, HDL-TR-2196, (1991).

118 J. B. Gruber, M. E. Hills, R. M. Macfarlane, C. A. Morrison, G. A. Turner, G. J. Quarles, G. J. Kintz, and L. Esterowitz, "Spectra and Energy Levels of Tm3+:Y3Al5O12", Phys. Rev. B, V40, (1989), P9464.

119 J. B. Gruber, M. E. hills, M. D. Seltzer, S. B. Stevens, C. A. Morrison, G. A. Turner, and M. R. Kokta, "Energy levels and crystal quantum states of trivalent holmium in yttrium aluminum garnet", J. Appl. Phys., V69, N12, (1991), P8183.

120 S. Aleonard, M. Labeau, Y. Le Fur and M. Gorius, Mat. Res. Bull., V8, (1973), P605.

121a J. H. Burns, "Crystal Structure of Hexagonal Sodium Neodymium Fluoride and Related Compounds", Inorg. Chem., V4, (1965), P1005.

121b B. P. Sobolev, D. A. Mineev, and V. P. Pashutin, "Low-temperature hexagonal modification of NaYF4 having the gagarinite structure", Dokl. Akad. Nauk. SSSR, V150, (1963), P791.

121c A. A. Voronkov, N. G. Shumyatskay, and Y. A. Pyatenko, "Crystal Structure of Gagarinite", Zh. Strukt. Khim., V3, (1962), P691.

122 Y. Yamaguchi, K. M. Dinndorf, H. P. Jenssen, and A. Cassanho, "Spectroscopy of $Nd:KYF_4$", OSA Proc. of Adv. Solid State Laser Conf., Ed. E. Pinto and T. Y. Fan, New Orleans, (1993), In press.

123a D. S. Knowles, A. Cassanho, and H. P. Jenssen, OSA Proc. on Tunable Solid State Lasers, (1989), V5. P139.

123b M. F. Joubert, C. Linares, B. Jacquier, A. Cassanho, and H. P. Jenssen, J. Lumin., V51, (1992), P175.

124 H. Chou, "Energy Transfer in Codoped Ho, Er:YLF and Its Potential for Improving the Efficiency of 3 Micron Lasers", S. M. Dissertation, Mass. Inst. of Tech., May 1983.

125 B. F. Aull and H. P. Jenssen, "Vibronic Interactions in Nd:YAG Resulting in Nonreciprocity of Absorption and Stimulated Emission Cross Sections", IEEE J. Quant. Elect., V18, N5, (1982), P925.

126 S. A. Payne, L. L. Chase, L. K. Smith, W. L. Kway, and W. F. Krupke, "Infrared cross-section measurements for crystals doped with Er^{3+}, Tm^{3+}, and Ho^{3+}", IEEE J. Quant. Elect., V28, N11, (1982), P2619.

127 M. E. Storm, "Holmium YLF amplifier performance and the prospects for multi-joule energies using diode-laser pumping", IEEE J. Quant. Elect., V29, N2, (1993), P440.

128 D. L. Dexter and J. H Schulman, "Theory of Concentration Quenching in Inorganic Phosphors", J. Chem. Phys., V22, N4, (1954), P1063.

129 G. La Rosa, "Spectroscopy of Tm^{3+}:YLF as a Laser Material for Diode Laser Pumping," M.S. dissertation, Mass. Inst. of Tech., Aug. 1988.

130a H. Chou and H.P. Jenssen, in OSA Proceedings on Tunable Solid State Lasers, Vol. 5, ed. M.L. Shand and H.P. Jenssen, Cape Cod, (1989), P167.

130b H. Chou, Upconversion Processes and Cr-sensitization of Er- and Er, Ho-activated Solid State Laser Materials, Ph.D. dissertation, Mass. Ins. of Tech, Feb. 1989.

131 D.S. Knowles, Energy Transfer Under Strong Pumping in High Concentration Rare Earth Doped Laser Crystals, Ph.D. dissertation, MIT, Sept. 1991.

132 Stoneman, Pinto, and L. Esterowitz,OSA annual conference, Boston, 1992.

133 F. E. Auzel, "Materials and Devices Using Double-Pumped Phosphors with Energy Transfer", Proc. of the IEEE, V61, N6, (1973), P758.

134 K. H. Kim, Y. S. Choi, R. V. Hess, C. H. Blair, P. Brockman, N. P. Barnes, G. W. Henderson, and M. R. Kokta, "Experiments and Theory for Tm:Ho:YAG Laser End Pumped by a Cr:GSAG Laser", OSA Proc. Adv. Sol. State Lasers, V6, Ed. H. P. Jenssen and G. Dube, Salt Lake City, (1990), P155.

135 K.M. Dinndorf, M. Tonelli, A. Cassanho, Y. Yamaguchi, and H.P. Jenssen, "Relative Upconversion Rates in Tm-Ho doped crystals," in OSA Proc. of the Adv. Sol. State Laser Conf, V16, ed A.A. Pinto and T.Y. Fan, New Orleans, (1993), P.

136 G. Hansson, A. Callenas, and C. Nelsson, "Upconversion studies in laser-diode-pumped Tm,Ho:$YLiF_4$," in OSA Proc. of the Adv. Sol. State Laser Conf, V16, ed A.A. Pinto and T.Y. Fan, New Orleans, (1993), In press.

137 M. G. Jani, R. J. Reeves, R. C. Powell, G. J. Quarles, and L. Esterowitz, "Alexandrite-laser excitation of a Tm:Ho:Y3Al5O12 laser", J. Opt. Soc. Am. B, V8, N4, (1991), P741.

138 M. A. Noginov, H. P. Jenssen, and A. Cassanho, "Upconversion in Cr:LiSGaF and Cr:LiSAF," OSA Proc. Adv. Solid State Lasers, V16, ed E. Pinto and T. Y. Fan, New Orleans, (1993),

139 B. Dinerman, "A spectroscopic characterization and cw laser operation of Er:GGG and Er:YSGG", PhD dissertation, Boston College, Dec 1993.

140 S. A. Payne, L. K. Smith, W. L. Kway, J. B. Tassano, and W. F. Krupke, "The mechanism of Tm->Ho energy transfer in $LiYF_4$", J. Phys. Cond. Matter, V4, (1992), P8525.

141 A. A. Kaminskii, Laser Crystals, Optical Sciences, V14, Springer-Verlag, New York, 1981.